Displacement Based Seismic Assessment of Earth Retaining Structures

Rohit Tiwari

A thesis submitted in total fulfilment of the requirements for the degree of Doctor of Philosophy

March 2020

Department of Infrastructure Engineering

The University of Melbourne

ABSTRACT

The present study deals with the displacement based seismic assessment of earth retaining structures. Detailed shaking table experiment has been performed on two different scaled down retaining wall models. The first set of shaking table experiment has been performed on base restrained retaining wall model, and the second set of shaking table experiment has been performed on a rotational base retaining wall model. It was observed from the shaking table experiment that inertial forces from backfill profoundly influence the seismic displacement of the earth retaining structures. Different dynamic properties of scaled down retaining wall models have also been studied with the shaking table experiment results. Significant amplification of horizontal acceleration in the backfill has also been observed during all shaking table experiments.

A detailed geotechnical investigation has also been performed on the backfill used for scaled down retaining wall model construction. Characterization of the backfill has been achieved based on different geotechnical experiments. The hardening/softening behaviour of backfill has also been studied from the consolidated drained (CD) triaxial test results and the Mohr Coulomb material model. A detailed process for the finite element (FE) modelling of seismic actions on earth retaining structures has been explained. Capability of the FE models has also been verified by replication of the shaking table experimental results.

A detailed and rigorous FE investigation has been performed on different earth retaining structures. The base restrained retaining wall, the free straining retaining wall, and the cantilever retaining wall founded on rock-socketed pile foundation have been considered for the FE investigations. Earthquake induced displacement behaviour of the earth retaining structures has been studied against different synthetic and historical accelerograms. The effects of different backfill type on the seismic response of earth retaining structures has also been

studied. Significant amplification of the horizontal acceleration in the backfill has been observed for all cases. Simplified hand calculations have also been proposed for estimating the seismic displacement of the base restrained retaining wall.

It was observed that the earthquake induced displacement of earth retaining structures mainly depends on the severity of ground shaking, inertial forces from the backfill, and hardening/softening behaviour of the backfill. In the case of a free-standing retaining wall and a retaining wall founded on rock socketed pile foundation, granular backfill shows better seismic performance than natural sand backfill. In the case of a retaining wall founded on the rock socketed pile foundation, high displacement of the rock-socketed piles has been observed.

DECLARATION

This is to certify that:

(i) This thesis comprises only my original work,

(ii) Due acknowledgement has been made in the text to all other material used,

(iii) This thesis is fewer than 100,000 words in length, exclusive of tables, maps, bibliographies, and appendices.

Rohit Tiwari

March 2020

Dedicated to my grandfather late Mr. Hira Ballabh Tewari.

ACKNOWLEDGEMENTS

First of all, I would like to express my sincere gratitude to my Ph.D. advisor Professor Nelson Lam for his continuous guidance, motivation, and support during the Ph.D. candidature. I am also thankful to Professor Nelson Lam for funding the shaking table experiment program, numerical computation program, 6 conference travels, and research scholarship. My sincere thanks to Dr. Elisa Lumantarna for her guidance and support as Ph.D. co-advisor. I would also like to thank Dr. Lihai Zhang for chairing the Ph.D. advisory committee.

My sincere thanks to Dr. Mahdi Miri Disfani for supporting the geotechnical experiment program and providing geotechnical expertise for Ph.D. research work. I am also thankful to my friends Mr. Babar Nasim Khan Raja, Dr. Ryan, Dr. Alireza Mohammadinia, Mr. Philip, Dr. Arnold, Dr. Jude and Ms. Sanchari for the help and support they provided during the shaking table experiment and geotechnical experiment program.

My sincere thanks to all my Ph.D. colleagues especially Dr. Alireza Mehdipanah, Dr. Anita, Dr. Naveen, Dr. Mehair, Dr. Yuxiang, Mr. Tu and Dr. Jing for their support and help. Also, I would like to thank Dr. Tanusree Chakraborty, Mr. Arnab Sur, Dr. Sandeep Saha, Mr. Anurag Misra, Mr. Vijay Rawat, and Mr. Rohit John for motivating me before and during the Ph.D. candidature.

I am also thankful to the IT Department of Melbourne School of Engineering for supporting my numerical computation program. Also, I would like to express my sincere gratitude to Ms. Pauline, Ms. Eileen and Ms. Jemma for helping me with administrative works.

I would also like to express my thankfulness to my parents, who always supported and motivated me during my Ph.D. research time. My special thanks to all my family members and friends for their constant support and encouragement.

At last, I would like to thank my wife Anjali Binwal, for her support, love and care.

LIST OF PUBLICATIONS

In Refereed Conferences:

1. Tiwari, R., Lam, N., & Lumantarna, E. (2019). *Modelling of seismic actions on earth retaining structures*. In the proceedings of 7th International Conference of Computational Mechanics and Simulation, Dec, 11th - 13th, IIT Mandi, India. **(Selected for the special edition by Springer)**

2. Tiwari, R., & Lam, N. (2019). *Displacement based estimate of seismic actions on earth retaining structures*. In the proceedings of Australian Earthquake Engineering Society Conference, Nov, 29th – Dec, 1st, Newcastle, Australia.

3. Tiwari, R., Lam, N. T., & Lumantarna, E. (2018). *Displacement based seismic assessment of cantilever retaining walls*. In the proceedings of Australian Earthquake Engineering Society Conference, Nov, 16th -18th, Perth, Australia **(*Best student paper award*)**.

4. Tiwari, R., Lam, N. T., & Lumantarna, E. (2017). *Assessment of displacement demand for earth retaining structures*. In the proceedings of Australian Earthquake Engineering Society Conference, Nov, 24th -26th, Canberra, Australia.

5. Tiwari, R., Lam, N. T., Lumantarna, E., & Au, F. T. (2017). *A drift and displacement based seismic assessment method for bridge abutments*. In the proceedings of Austroads Bridge Conference, April 3rd -6th, 2017, Melbourne, Victoria, Australia.

6. Tiwari, R., Lam, N. T., & Lumantarna, E. (2016). *Displacement based design of bridge abutments*. In the proceedings of Australian Earthquake Engineering Society Conference, Nov, 25th -27th, Melbourne, Australia.

In Refereed Journals:

1. Tiwari, R., & Lam, N. *Modelling of Seismic Actions in Earth Retaining Walls and Comparison with Shaker Table Experiment*. (Communicated)

2. Tiwari, R., Lam, N., & Lumantarna, E. *Earthquake Induced Displacement Response of Base Restrained Retaining Walls*. (in preparation)

TABLE OF CONTENTS

List of Figures

LIST OF TABLES

List of Notations

Notation	Description
K_A	Lateral earth pressure coefficient for active case
K_P	Lateral earth pressure coefficient for passive case
$k_{h\text{-critical.}}$	Critical acceleration value to initiate sliding
ϕ'	Angle of internal friction of the backfill soil (effective stress)
θ	Angle of inclination of wall surface from the vertical plane
Δ	Angle of friction between the backfill soil and the retaining wall
B	Angle of inclination of the backfill soil from the vertical plane
H_w	Retaining wall height
Δ	Displacement
K_h	Horizontal seismic coefficient
K_v	Vertical seismic coefficient
γ_{soil}	Unit weight of the backfill soil
G	Shear modulus
f	Frequency
f_s	Frequency of elastic soil column
V_{SH}	Shear wave velocity of the elastic soil column
V_{sf}	Shear wave velocity of the foundation soil
$d_{residual}$	Permanent outward displacement of the retaining wall
V	Maximum ground velocity.
k_y	Yield acceleration.
k_{max}	Maximum seismic coefficient.
W_W	Weight of the wall
A_{max}	Maximum ground acceleration
L	Length
M	Mass
T, t	Time
λ	Dimensionless ratio
L_s	Scaled down model height
L_p	Prototype model height
N	Rank of the dimensionless matrix
σ	Stress
F	Force
A	Area
g, g_p, g_s	Acceleration due to gravity
ρ	Mass density
V	Velocity
E	*Stiffness*
F_I	Inertial Force
A_p , a_p	Acceleration in prototype model
A_s , a_s	Acceleration in scaled model

Notation	Description
ω	Circular frequency
E	Young's modulus
E_{p}	Young's modulus of prototype model
E_{s}	Young's modulus of scaled down model
V_{p}	Velocity in the prototype model
V_{S}	Velocity in the scaled model
ρ_{P}	Density of prototype model
ρ_{S}	Density of scaled model
λ_{E}	Ratio of Stiffness
λ_{ρ}	Ratio of density
λ_{l}	Ratio of length
λ_{ω}	Ratio of frequency
$\lambda_{\Delta t}$	Ratio of time step
ω_{P}	Frequency of prototype model
ω_{s}	Frequency of scaled model
λ_{V}	Ratio of velocity
λ_{A}	Ratio of acceleration
α_m, α	Mass dependent parameter
α_{k}, β	Stiffness dependent parameter
$\lambda_{\mathrm{K}_{\theta}}$	Ratio of rotational stiffness
$\mathrm{K}_{\theta_{\mathrm{p}}}$	Rotational stiffness of prototype model
$\mathrm{K}_{\theta_{\mathrm{s}}}$	Rotational stiffness of scaled model
M_{Toe}	Moment about toe
θ	Rotation
Δ_{Top}	Displacement at top
Δ_{Base}	Displacement at base
H_{stem}	Height of RW stem
Δ_{rel}, Δ_{R}	Relative Displacement
M_{g}	Magnitude
R	Distance
PGA	Peak ground acceleration
RSA	Response spectral acceleration
RW	Retaining wall
CRW	Concrete retaining wall
D_{60}	Particle size of the crushed rock (backfill) at 60 % finer
D_{30}	Particle size of the crushed rock (backfill) at 30 % finer
D_{10}	Particle size of the crushed rock (backfill) at 10% finer
C_{u}	Coefficient of uniformity
C_{c}	Coefficient of curvature
M_{s}	Constrained modulus
σ_{v} , σ_{22}	Vertical stress

Notation	Description
$\sigma_{d,el}$	Elastic deviatoric stress
ε_v	Vertical strain
D_r	Relative density
1-D	One dimensional
2-D	Two dimensional
FE	Finite element
RC	Reinforced concrete
$\varepsilon_{v,el}$	Volumetric elastic strain
$\varepsilon_{v,pl}$	Volumetric plastic strain
ε_{el}	Elastic strain
ε_{pl}	Plastic strain
ε_{11}^{p}	Plastic strain in vertical direction
ε_{22}^{p}	Plastic strain in lateral direction
$\bar{\varepsilon}^{pl}$	Equivalent plastic strain
R_{mc}	Function depending on the deviatoric polar and friction angle
C	Cohesion
θ_P	Polar angle
p, σ_d	Deviatoric stress
q	Principle stress
Q	Mises equivalent stress or deviatoric stress
G_p	Flow potential
ψ	Dilation angle of soil
$c\|_0$	Yield stress in cohesion
ε	Eccentricity on the meridional stress plane
E	Deviatoric eccentricity
$[C]$	Damping matrix
$[M]$	Mass matrix
$[K]$	Stiffness matrix
D, ξ	Damping ratio
ξ_i	Initial viscous damping ratio (ξ_i)
ξ_{max}	Maximum viscous damping ratio (ξ_{max})
γ	Shear strain in soil
γ_{ref}	Reference shear strain
CDP	Concrete damaged plasticity
L_{min}	Smallest element dimension
V_{SV}	Stress wave velocity
Δt	Smallest stable time interval
σ_t	Stress vector for the tensile stresses
σ_c	Stress vector for the compressive stresses
σ_{22}	Stress in vertical direction
ε_t^{pl}	Equivalent plastic strains in tension

Notation	Description
ε_c^{pl}	Equivalent plastic strains in compression
E_0^{el}	Initial undamaged elastic modulus
d_t	Damage variable in CDP
d_c	Damage variable in CDP
f_{cu}	Maximum compressive strength of concrete
f_t	Tensile strength of concrete
G_f	Fracture energy
d_a	Maximum aggregate size
ν	Poisson’s ratio
f_{st}	Maximum tensile strength
δ_{max}	Maximum elastic displacement
AF	Amplification factor
$W1_{AE}$	Body force at unit height of RW
I	Moment of Inertia of the RW
$W2_{AE}$	Seismic force per unit width of the RW
$\ddot{u}(t)$	Acceleration at time t
Δt_p	Time step in prototype model
Δt_s	Time step in scaled down model
Δt	Time step
A_X	Acceleration in “x” direction
τ_{xy}	Shear stress
K_0	Lateral earth pressure coefficient at rest
μ	Coefficient of friction
α_i , β_i	Coefficients of equation 4.2

Chapter 1. INTRODUCTION

1.1.Background

Earth retaining structures are an essential part of a modern infrastructure system. The primary function of earth retaining structures is to retain and support the backfill/ground behind it. The earth retaining structures are highly prevalent in highway, railway, building and harbour infrastructure. In highway and railway infrastructure, retaining walls and bridge abutments are widely used to support the vertical cuts and unstable slopes (figure 1-1). In building and harbour infrastructure, the base/top restrained retaining walls are more common (figure 1-2). The retaining wall/bridge abutment constructed on firm ground is known as free-standing retaining wall/bridge abutment. In the absence of firm strata or weak subsoil profile, the retaining wall/bridge abutment could be constructed using the piled foundation (figure 1-3). Therefore, satisfactory performance of earth retaining structures during an earthquake is desirable for ensuring a safe and uninterrupted highway, railway, building and harbour infrastructure.

Earth retaining structures are massive and have high stiffnesses; therefore, structural failure occurs mainly due to excessive sliding and rotation of the earth retaining structure. In the case of quay walls and base restrained retaining walls, flexural failure can also occur. The backfill plays a vital role in the seismic performance of earth retaining structures. Existing methods of seismic design of earth retaining structures follow the conventional force based seismic design, in which the factor of safety in sliding and overturning is estimated based on the seismic backfill pressure.

Seismic response of retaining wall founded on rock socketed piled foundation is complicated. The seismic performance of piled foundation profoundly influences the displacement and rotation of the retaining wall. Seismic pressure generated on the retaining wall by the backfill also transfers to the rock socketed piles. Therefore, the seismic performance of retaining wall founded on rock socketed pile foundation depends on displacement and rotation of both the retaining wall and rock socketed piles.

Experiments could be performed on scaled down/large scale models of the earth, retaining structures for understanding their seismic response. However, large scale experiments are subjected to several limitations and generally requires high experimental costs. On the other hand, scaled down models of earth retaining structures are profoundly used for studying the effects of earthquake actions on them.

The finite element (FE) investigations are widely used for investigating the linear and non-linear behaviour of complicated boundary value problems. However, verification of the FE modelling technique with experimental results should be performed in order to ensure the accuracy of FE results.

Practising engineers generally prefer simple hand calculations or simplified models for estimating the seismic displacement of the earth retaining structures. The hand calculations or simplified models should require lesser computational time and should be able to estimate the seismic displacement of earth retaining structures with a reasonable degree of accuracy.

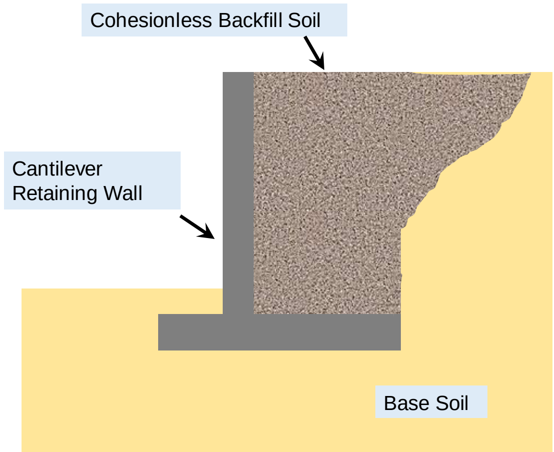

(a) Free-standing cantilever retaining wall

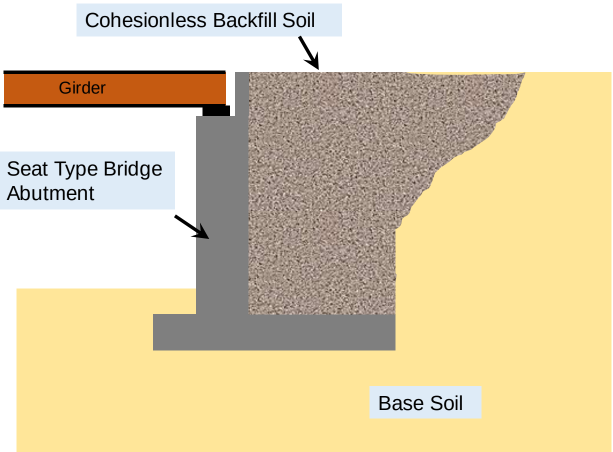

(b) Free-standing seat type bridge abutment

(c) Retaining wall for highway infrastructure
(Image courtesy: Tenax Corporation)

(d) Seat type bridge abutment
(Image courtesy: Mark Rossow)

Figure 1-1 Retaining walls and seat type bridge abutment.

(a) Diaphragm wall for building basement
(Image source: PT Indonesia Pondasi Raya Tbk)

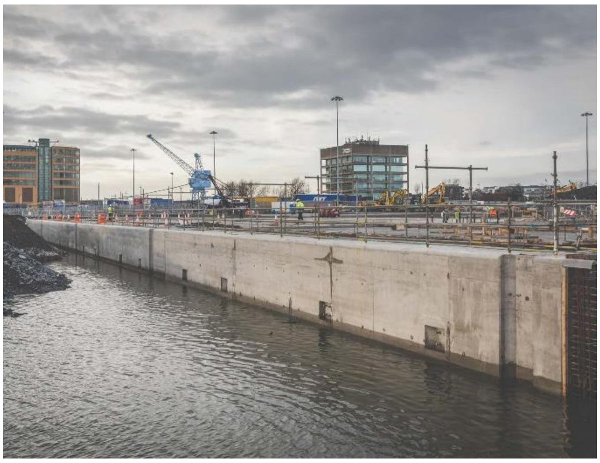

(b) Quay wall for harbour infrastructure
(Image source: Roadbridge ltd)

Figure 1-2 Diaphragm wall for building basement (left) and quay wall for harbour infrastructure (right).

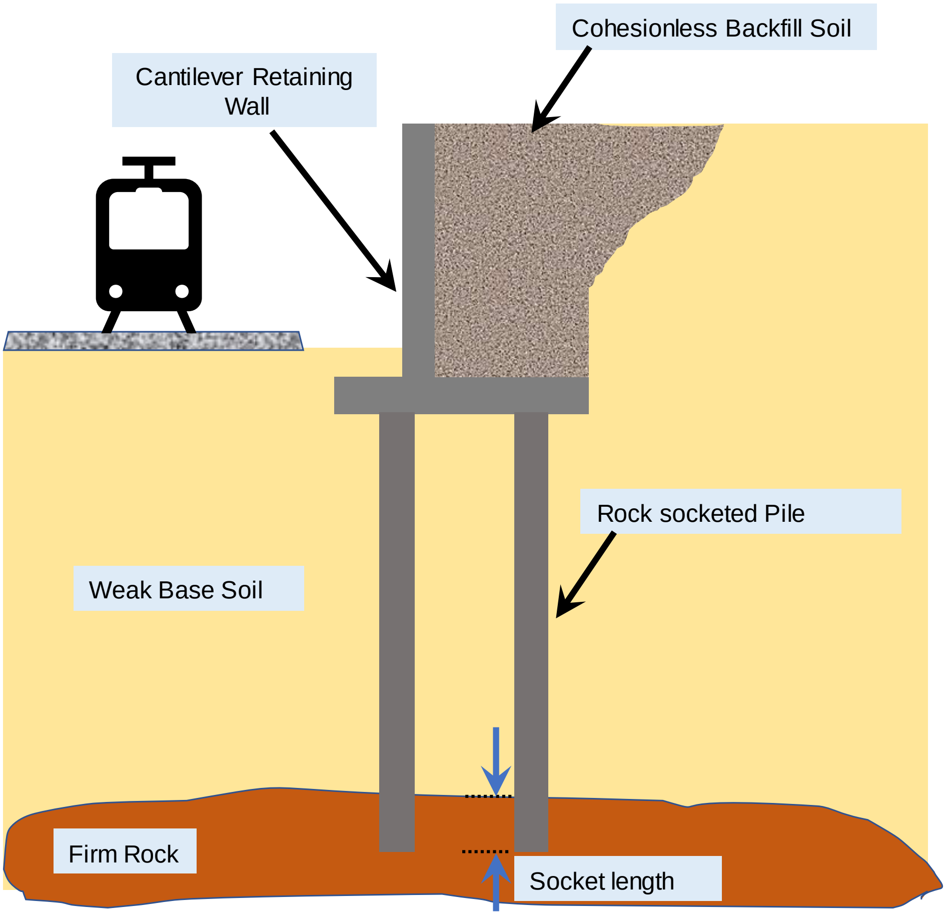

Figure 1-3 Cantilever retaining wall founded on rock socketed pile foundation.

1.2.Problem Statement

A detailed literature review is presented in chapter 2. It has been observed that the satisfactory performance of the earth retaining structures during an earthquake could be ensured by an accurate and realistic assessment of the earthquake induced displacement and rotation of earth retaining structures. Whereas most of the experimental, numerical and analytical investigations focused on the seismic backfill pressure. A detailed experimental investigation is required for understanding the earthquake induced displacement response behaviour of the earth retaining structures.

It was observed by several researchers that the backfill profoundly influence the earthquake induced displacement and rotation of earth retaining structures. However, detailed characterization of backfill for understanding its hardening/softening behaviour and its influence on the seismic performance of the earth retaining structures has not been presented in the literature. Therefore, a detailed geotechnical investigation is required for characterization of the backfill and understanding its constitutive behaviour.

Several researchers have discussed the FE modelling of seismic actions on earth retaining structures. However, the capability of the FE models should be verified by replication of realistic and accurate seismic response of earth retaining structures. Moreover, a detailed process for the FE modelling of seismic actions on earth retaining structures considering the hardening/softening behaviour of the backfill has not been addressed in the literature.

A limited number of studies reported the seismic behaviour of base restrained earth retaining structures. However, reports on a detailed and rigorous FE investigation considering the hardening/softening behaviour of backfill and different backfill type can not be found in the literature. Moreover, a simplified hand calculation is required for estimating the earthquake induced displacement demand of base restrained retaining walls.

Several researchers have studied the earthquake induced displacement demand behaviour of free-standing gravity and cantilever retaining wall. One-block models, two-block models, limited equilibrium and moment equilibrium studies are some of the conventional approaches for analyzing the seismic response of free-standing gravity or cantilevered retaining wall. However, a detailed parametric investigation considering the effects of backfill domain size, hardening/softening behaviour of backfill and different backfill type on the seismic behaviour of free-standing cantilever retaining wall has not been addressed in the literature.

Several experimental investigations have been performed on large scale/scaled down models of earth retaining structures to study their seismic response. However, seismic performance of earth retaining structures founded on the rock socketed pile foundations has not been addressed in the literature. Therefore, an experimental and numerical investigation is required in order to understand the earthquake induced displacement and rotation of earth retaining structures founded on the rock socketed piled foundation.

1.3.Research aims and objectives and the significance of research

1.3.1. Research aims

Several studies indicated that the damage and failure of earth retaining structures highly depends on the earthquake induced displacement and rotation of earth retaining structures. Studies have also highlighted that the backfill influence the seismic performance of earth retaining structures. Therefore, a detailed experimental and numerical investigation is required for understanding the earthquake induced displacement of earth retaining structures considering different support conditions. Therefore, the aim of the present research is to observe displacement behaviour of the earth retaining structures considering different support conditions under earthquake loading by experimental and numerical methods.

1.3.2. Research objectives

The present research work is focused on addressing the following research objectives:

1.3.2a Experimental Investigations:

(i) Understanding the seismic performance of scaled down models of earth retaining structures with different support conditions by conducting a detailed shaking table experiment on them.

(ii) Characterization of the backfill by conducting a detailed geotechnical investigation.

1.3.2b. Numerical Investigations:

(i) Calibration of the Mohr Coulomb material model with consolidated drained triaxial tests results for simulating hardening/softening behaviour of the backfill.

(ii) Development of FE model of earth retaining structure, considering the hardening/softening behaviour of backfill.

(iii) Verification of the capability of FE models in order to replicate the shaking table experiment results.

(iv) FE investigation of seismic actions on base restrained retaining wall.

(v) FE investigations of seismic actions on free standing retaining wall.

(vi) FE investigation of seismic actions on retaining wall, founded on the rock socketed pile foundation.

1.3.2c. Simplified hand calculation:

Development of hand calculations for estimation of earthquake induced displacement of base restrained retaining wall.

1.3.3. Significance of research:

Assessment of the earthquake induced displacement is one of the primary objectives of modern performance based design. The present research work provides a realistic and accurate assessment of earthquake induced displacement of earth retaining structures. Observations from the shaking table experiments and results from the FE simulations have been used for developing simple hand calculations and design guidelines for displacement based seismic assessment of the earth retaining structures, which could help the practising engineers for the seismic design of earth retaining structures.

1.4.Research methodology and framework for Ph. D. research

1.4.1. Research methodology

The doctoral research work has been carried out in three major steps: (i) shaking table investigation on scaled down models of earth retaining structures, (ii) characterization of backfill, and (iii) development of FE models of earth retaining structures. Figure 1-4 shows the research methodology followed in the present research work.

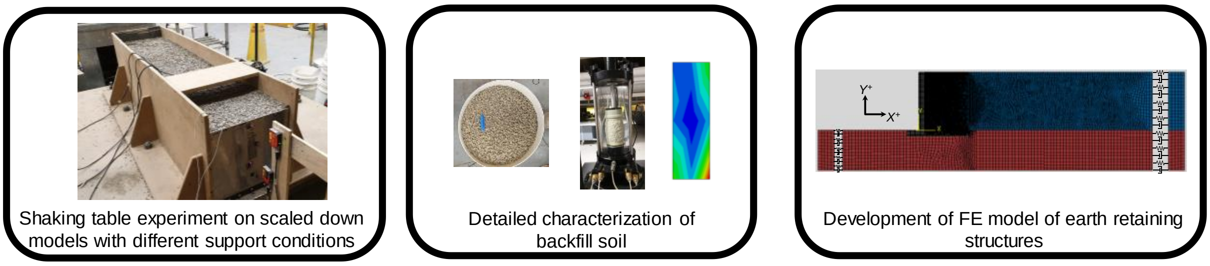

Figure 1-4 The research methodology used for Ph. D. research work.

1.4.2. Framework for Ph. D. research

The focus of the Ph. D. research is to understand the earthquake induced displacement of earth retaining structures. A detailed and rigorous experimental and finite element investigation has been performed on different earth retaining structures. Figure 1-5 shows the detailed framework for Ph. D. research.

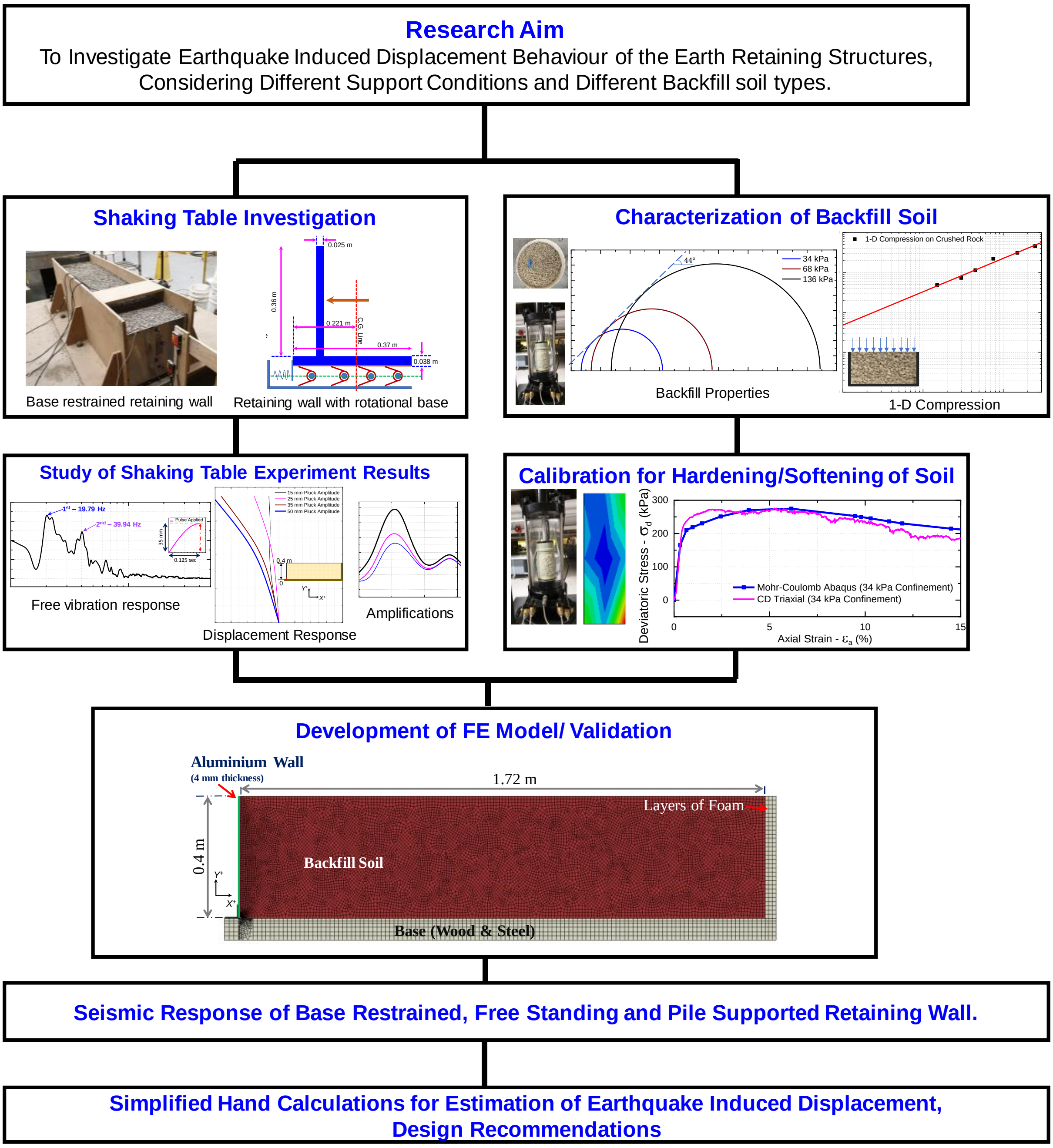

Figure 1-5 Framework for the Ph. D. research work.

1.5.Thesis organization

The present thesis has nine chapters, a summary of all the chapters is discussed below:

Chapter 1 outlines the introduction of Ph. D. research work. A detailed background of earth retaining structures has been presented. The earthquake induced actions on earth retaining structures have also been discussed. The objectives of Ph. D. research work have been presented along with the research methodology and framework.

Chapter 2 presents the detailed literature review of earthquake actions on earth retaining structures. Different experimental, analytical and numerical investigations performed for understanding the effects of seismic actions on earth retaining structures have been reviewed. The research gaps identified based on the extensive literature review have also been summarized.

Chapter 3 presents the details of scale down modelling of earth retaining structures. A brief description of the theory of similitude has been presented. A detailed process for scaling down the retaining wall models has been explained. The capability of the scaled down retaining wall models has been verified for replicating the earthquake induced displacement behaviour of prototype retaining wall models.

Chapter 4 presents the shaking table experiment performed on scaled down models of earth retaining structures considering different support conditions. The detailed process for scaled down model construction has also been explained. The earthquake induced displacement response of scaled down models against different base excitations has been presented. The results of the shaking table experiment have been studied for understanding the free vibration response, and displacement response of earth retaining structures. Amplification of the horizontal acceleration in backfill has also been studied. The results of the shaking table experiment have also been studied for estimation of shear wave velocity in the backfill.

Chapter 5 presents the characterization of backfill material. Detailed geotechnical investigation performed on the crushed rock (backfill) have been presented. The capability of FE models has also been verified for replicating the accurate and realistic seismic response of earth retaining structures. The hardening/softening of crushed rock has also been stimulated by calibrating the Mohr Coulomb material model with triaxial test results.

Chapter 6 presents the seismic response of base restrained earth retaining structures. A detailed and rigorous FE investigation has been performed for understanding the seismic behaviour of base restrained earth retaining structures. A parametric investigation has been performed for different backfill type. The results of FE investigations have been studied for the earthquake induced displacement behaviour of earth retaining structures. The dynamic backfill pressure and amplification of horizontal acceleration in the backfill have also been studied. Simplified hand calculations have been proposed for estimating earthquake induced displacement of base restrained earth retaining structures. Accuracy of proposed simplified hand calculations has been examined by comparing the hand calculations results with the shaking table experiment and the FE investigation results.

Chapter 7 presents the seismic response of free standing earth retaining structures. Similar to chapter 6, a detailed parametric FE investigation has been performed on free standing cantilever retaining wall (CRW) model. The results of FE analyses have been studied for earthquake induced displacement of free standing CRW. The dynamic backfill pressure on CRW and amplification of horizontal acceleration in the backfill have also been studied.

Chapter 8 presents the seismic response of cantilever retaining wall founded on rock socketed pile foundation. A detailed and rigorous FE investigation has been performed on cantilever retaining wall founded on rock rocketed pile foundation. A detailed parametric investigation has also been performed for different backfill type. The results of finite element analyses have been studied for seismic displacement and rotation of retaining wall and rock socketed piles. Effect of backfill on seismic performance of rock socketed piles has also been discussed. Dynamic backfill pressure and amplification of horizontal acceleration in the backfill have also been studied.

Chapter 9 presents the conclusion of Ph. D. research work and scope for future research.

Chapter 2. LITERATURE REVIEW

2.1. Introduction

The earth retaining structures are an essential part of the modern infrastructure system, i.e. retaining walls, sheet pile walls, basement walls, and bridge abutments. Retaining walls and bridge abutments are the critical elements of the highway infrastructure, whereas, sheet pile walls and basement walls are more prevalent in the building and the harbour infrastructure. Moderate to severe damage to the earth retaining structures have been observed during the past earthquakes. It was also observed from past earthquakes that the seismic performance of earth retaining structures mainly depends on their support conditions. Satisfactory performance of the earth retaining structures against a design level seismic event could be ensured by the accurate assessment of the seismic actions on them. Several researchers studied the effects of earthquake actions on the earth retaining structures by performing experimental, analytical and numerical investigations on them. A detailed literature review has been performed in order to understand the seismic loading and backfill pressure on the earth retaining structures. A review of the seismic design guidelines from different design standards has also been performed.

2.2. Performance of the earth retaining structures during past earthquakes

Several researchers studied the performance of the earth retaining structures during past earthquakes. During the Northridge earthquake (1994, 0.94g PGA); significant damage to the earth retaining structures was observed. High vertical ground accelerations (up to 1.8g) were also observed at sites where the earthquake epicenter was close to the ground (Shakal et al. 1994). Excessive outward displacement and rotation of the conventional retaining walls were observed during the Northridge earthquake. On the other hand, reinforced soil and geogrid reinforced soil slopes show satisfactory performance during the Northridge earthquake (Sandri, 1997; Matasovic, 2004).

Damage to many earth retaining structures during the Kobe earthquake has been reported (1995, 0.8g PGA). Conventional gravity retaining walls showed excessive outward displacement and tilting, leading to failure of the retaining walls. On the other hand, reinforced concrete retaining walls founded on piled foundation caused limited damage. (Koseki et al., 1995; Koseki, 2002; Koseki et al., 1998; Tatsuoka et al., 1996). During the Chi-Chi earthquake of Taiwan (1999, >1g PGA) severe damage and collapse of unreinforced retaining walls were observed. Conventional gravity retaining walls experienced excessive outward displacement and tilting (Shayo and Cheng, 2009; Yazdani et al., 2013).

During the Wenchuan earthquake (2008, 0.98g PGA); sliding and rotation of bridge abutments were observed. Unseating of the bridge deck/girders was also observed in some bridges. Noticeable settlement of the approach slab; due to excessive sliding and rotation of abutments was also observed (Qiang et al. 2009). Satisfactory performance of some retaining walls was also observed during the Wenchuan earthquake.

During the Bhuj earthquake (2001, 0.37g PGA); flexural failure of the anchored quay wall was observed. High deflection at the quay wall top and settlement of backfill behind the quay wall were also observed. Due to the lateral spreading and liquefaction, damage to the bridge abutment, retaining walls and piled foundations were observed (Madabhushi and Haigh, 2005).

2.3. Lateral earth pressure on the earth retaining structures

Lateral earth pressure behind the retaining wall for the static case mainly depends on the movement of earth retaining structure. The earth retaining structure can translate or rotate, depending on the structural type and boundary conditions. Three different states of the lateral earth pressure could be considered; based on the movement of the retaining wall (Bowles, 1982).

(i) At rest state, no movement of the retaining wall $\left(\frac{\Delta}{H\text{w}} = 0\right)$.

(ii) Active state, movement of the retaining wall away from the backfill.

(iii) Passive state, movement of the retaining wall towards the backfill.

Figure 2-1 shows the different states of lateral earth pressure. The usual range of lateral earth pressure coefficients has also been shown in figure 2-1 (Bowles, 1982).

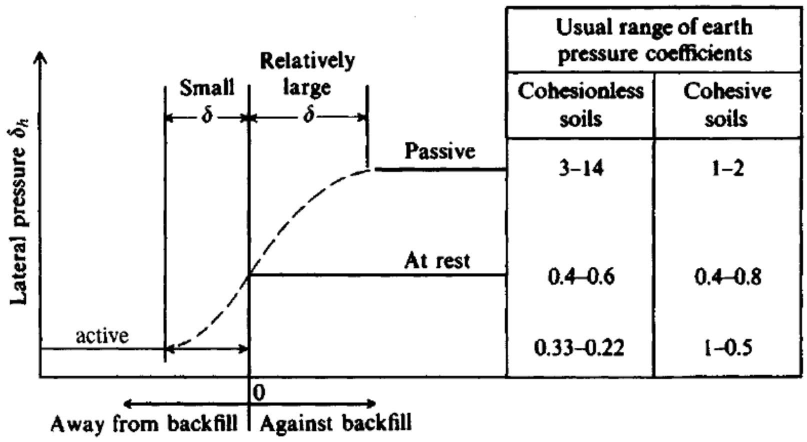

Figure 2-1 Different states of lateral earth pressure against the movement of the retaining wall (Bowles, 1982).

Coulomb's earth pressure theory (1776) and Rankine earth pressure theory (1857) have been used widely for estimating the lateral earth pressure on the earth retaining structures. Coulomb's earth pressure theory considers a failure wedge formed in the backfill behind the retaining wall; due to the retaining wall movement. Depending upon the lateral stress state, the failure wedge could slide downwards/upwards and towards the wall/backfill. Coulomb's earth pressure theory was based on total stress conditions (Bakr, 2018). Figure 2-2 shows Coulomb's active state condition due to the movement of the retaining wall.

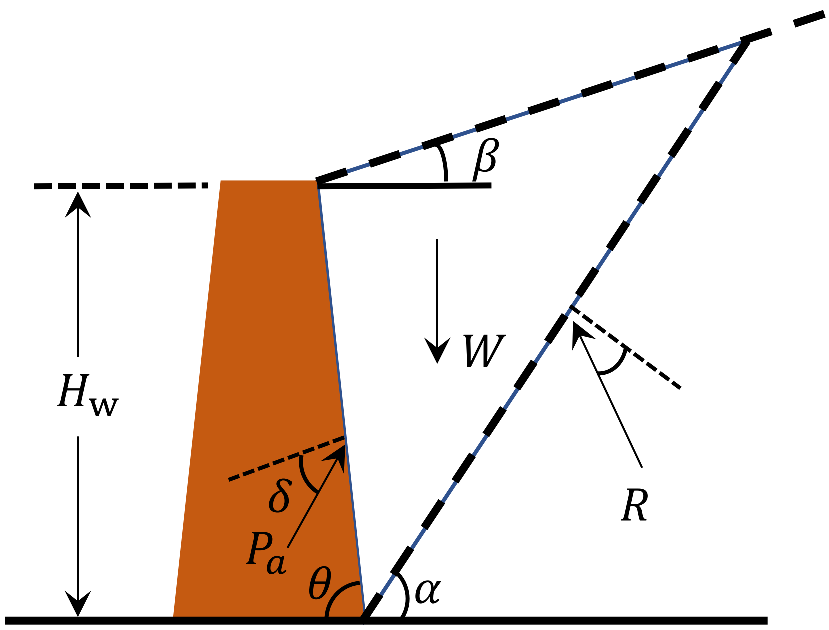

Figure 2-2 Coulomb's active state condition for the cohesionless soil.

Equation 2.1 and 2.2 show the lateral earth pressure coefficient for the active and passive state; derived using Coulomb's earth pressure theory (Das and Sivakugan, 2016; Bakr, 2018).

$$K_{\mathrm{A}} = \frac{\mathrm{Cos}^2(\phi' - \theta)}{\mathrm{Cos}^2\theta \cos(\delta + \theta)\left[1 + \sqrt{\frac{\sin(\delta + \phi')\sin(\phi' - \beta)}{\cos(\delta + \theta)\cos(\beta - \theta)}}\right]^2} \tag{2.1}$$

$$K_{\mathrm{P}} = \frac{\mathrm{Cos}^2(\phi' + \theta)}{\mathrm{Cos}^2\theta \cos(\delta - \theta)\left[1 + \sqrt{\frac{\sin(\delta + \phi')\sin(\phi' + \beta)}{\cos(\delta - \theta)\cos(\beta - \theta)}}\right]^2} \tag{2.2}$$

where,

ϕ' = Angle of internal friction of the backfill

θ = Angle of inclination of wall surface from the vertical plane (0 for vertical walls).

δ = Angle of friction between the backfill and the retaining wall

β = Angle of inclination of the backfill from the vertical plane (0 for horizontal backfill)

It should be noted herein that the Coulomb's theory overestimates the passive pressure resistance from the backfill, which could lead to an unsafe design of the earth retaining structures (Das and Sivakugan, 2016).

2.4. Seismic actions on the earth retaining structures

Earthquake induced ground excitations may generate forces and deformation in the longitudinal, transverse and vertical directions; depending on the direction of the ground motion (Whitman and Liao 1985). Figure 2.3 shows the seismic loading on a gravity retaining wall with different orientations.

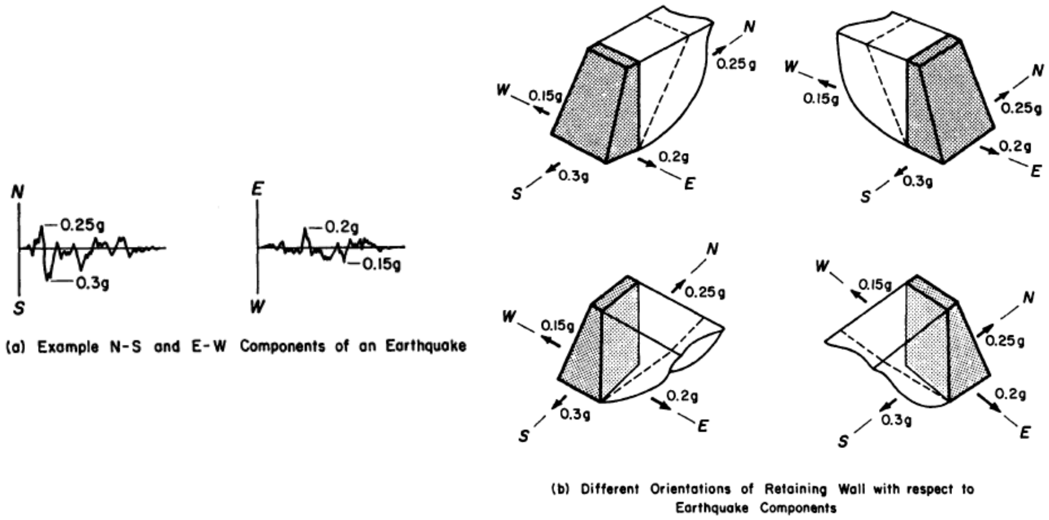

Figure 2-3 Seismic loading on the gravity retaining wall with different orientations (Whitman and Liao 1985).

Earthquake induced base excitations generate the inertial forces on the earth retaining structures and the backfill. Due to the inertial forces in the backfill, an additional thrust starts acting on the earth retention wall from the backfill (Seed and Whitman, 1970; Siddharthan et al., 1994). The additional thrust from the backfill can significantly influence the seismic response of the earth retaining structures (Siddharthan et al., 1994).

2.4.1. Earthquake induced pressure on the earth retaining structures

Due to the inertial forces and lateral displacement of the earth retaining structures, an active or passive state could be formed in the backfill. The amount and the duration of earthquake induced backfill pressure depends on the severity of earthquake shaking. Therefore, backfill pressure during an earthquake is also known as dynamic soil pressure (Sherif and Fang, 1984). Several researchers studied the seismic pressure on the earth retaining structures by performing experimental, analytical and numerical investigations on the earth retaining structures, out of which the most relevant work is being discussed hereafter.

Pseudo-static backfill pressure based on the study of Okabe (1926) and Mononobe & Matsuo (1929)

S. Okabe, N. Mononobe and H. Matsuo studied the dynamic backfill pressure on earth retaining structures. They modified Columb's active and passive earth pressure coefficient by introducing a new parameter ψ, to account the inertial forces at a given peak ground acceleration (PGA). Equation 2.1 and 2.2 show the lateral earth pressure coefficient for seismic active (K_{AE}) and passive (K_{PE}) conditions, respectively.

$$K_{\mathrm{AE}} = \frac{\mathrm{Cos}^2(\phi' - \theta - \psi)}{\cos\psi \mathrm{Cos}^2\theta \cos(\delta + \theta + \psi)\left[1 + \sqrt{\frac{\sin(\delta + \phi')\sin(\phi' - \beta - \psi)}{\cos(\delta + \theta + \psi)\cos(\beta - \theta)}}\right]^2} \tag{2.3}$$

$$K_{\mathrm{PE}} = \frac{\mathrm{Cos}^2(\phi' + \theta - \psi)}{\cos\psi \mathrm{Cos}^2\theta \cos(\delta - \theta + \psi)\left[1 - \sqrt{\frac{\sin(\delta + \phi')\sin(\phi' + \beta - \psi)}{\cos(\delta - \theta + \psi)\cos(\beta - \theta)}}\right]^2} \tag{2.4}$$

$$\psi = \tan^{-1}\frac{K_{\mathrm{h}}}{1 - K_{\mathrm{v}}} \tag{2.5}$$

where,
K_{h} = Horizontal seismic coefficient

K_{v} = Vertical seismic coefficient

The earthquake induced dynamic thrust from the backfill could be estimated using the lateral earth pressure coefficient (active/passive) obtained from the Mononobe-Okabe (MO) method.

$$P_{\mathrm{AE}} = \frac{1}{2}K_{\mathrm{AE}}\gamma_{\mathrm{soil}}(H_{\mathrm{W}})^2 \tag{2.6}$$

where,

γ_{soil} = Unit weight of the backfill

H_{W} = height of the earth retention wall

The MO method assumes a cohesionless backfill behind the retaining wall, and a rigid backfill failure wedge has been assumed for the lateral movements of the retaining wall. The inclination angle for the failure wedge (critical plane) can also be estimated (Bakr 2018).

Analytical investigations by Matsuo and O'hara (1960)

Matsuo and O'hara (1960) performed analytical investigations for finding the earthquake induced lateral pressure on the quay walls. Their study considers the seismic pressure from the backfill and water. The general assumptions made by Matsuo and O'hara includes the reduction in the hydrostatic force from the seaside and increment in water pressure from the backfill side. The combined lateral force (soil + water), depends on the height of the quay wall and the lateral seismic coefficient.

Analytical investigations by Veletsos and Younan (1997)

Veletsos and Younan (1997) developed analytical solutions for finding the seismic response of the flexible retaining wall restrained at its base. The retaining wall - soil system was analyzed against different base excitations. Seismic response of the retaining wall was studied for the dynamic backfill pressure, retaining wall displacement, and dynamic moment. Veletsos and Younan observed that the retaining wall flexibility could decrease the backfill pressure significantly. The analytical results for the flexible retaining wall showed a good agreement with the pseudo-static MO method; when amplification effects were neglected.

Moment equilibrium by Chen (2014)

Chen (2014) used Coulomb's limit equilibrium method for finding active earth pressure on the rigid retaining wall. The moment equilibrium method was used for finding the horizontal seismic coefficient for the selected portion of the failure wedge. Earthquake induced sliding of the retaining wall was considered by Chen (2014). The mobilized values of the friction angle of the backfill and the wall backfill interface were used for finding the seismic earth pressure coefficient for the active state. The dynamic pressure obtained from the moment equilibrium method was compared with the experimental results.

Numerical investigations by Bakr (2018)

Bakr (2018) performed the finite element investigations on the free-standing gravity and the cantilever retaining walls. The parametric investigations were performed for different retaining wall heights and relative densities of the backfill. The finite element models of the retaining walls were also analyzed against the different base excitations. It was observed by Bakr that the maximum seismic thrust from the backfill and the maximum base acceleration does not occur at the same time. The relative density of the backfill profoundly influences the seismic performance of the retaining walls. The backfill with higher relative density shows good seismic performance. Lesser seismic pressure was observed for the backfill with low relative density, because of higher sliding of the free-standing retaining wall.

Apart from the studies mentioned above, several other researchers have also studied the seismic loading on earth retaining structures. Table 2-1 shows a summary of different investigations performed for understanding the earthquake loading on the earth retaining structures.

Numerical investigations by Yang et al. (2012)

Yang et al. (2012) studied the hardening softening behaviour of backfill using a finite element model. They reported that the behaviour of reinforced backfill mainly influenced by the stress levels. Failure plane could be developed in the backfill as soon as stress levels in backfill reaches to soils peak strength. Mobilization of soil strength along the failure plane is irregular. Formation of failure plane in backfill is usually followed by irregular softening of backfill along the failure plane. During the finite element analysis Yang et al. (2012) also observed extensive deformation and tensile stresses in the backfill located at the failure plane.

Table 2-1. Summary of different investigations for earthquake loading on the earth retaining structures.

Sr. No.	Investigation performed by	Investigation type	Model type	Major outcomes
1	Wood (1973)	Analytical investigations	Rigid retaining wall	(i) Maximum seismic thrust for the harmonic base excitations. (ii) Minimum dynamic amplification for $\frac{f}{f_s} < 0.5$, where f = frequency of base excitation, f_s = frequency of elastic soil column
2	Iai and Kameoka. (1993)	Finite element investigation	Anchored quay wall	(i) Performance of the sheet pile quay wall highly influenced by the softening behaviour of the soil and exiting stress conditions. (ii) The low magnitude of the shear strain in the backfill behind the quay wall
3	Stadler (1996)	Centrifuge investigations	Scaled down retaining wall model	(i) MO method overestimates the dynamic backfill pressure (ii) Triangular to rectangular distribution of backfill pressure behind the retaining wall.
4	Li and Aguilar (2000)	Analytical investigations	Rigid retaining wall	(i) Deformation of the retaining wall foundation can significantly affect the seismic performance of the rigid retaining walls (ii) Point of application of backfill thrust as a function of $\frac{V_s}{V_{sf}}$, where V_s = shear wave velocity of the elastic soil column, V_{sf} = shear wave velocity of the foundation soil
5	Choudhury et al. (2006)	Analytical investigation	Rigid retaining wall	(i) Seismic earth pressure coefficients for the active and passive states (ii) Lesser passive resistance for backfill than MO method, passive pressure was found sensitive for the retaining wall - backfill interface friction

2.4.2. Earthquake induced displacement of the earth retaining structures

One block model from Richards and Elms (1979)

Newmark (1965) studied the seismic behaviour of the dams and the embankments and suggested a sliding block model for estimating the earthquake induced slip of the dams and the embankments. Richards and Elms (1979) modified Newmark's sliding block model for estimating the seismic displacement of the gravity retaining walls. Richards and Elms considered a rigid failure wedge of backfill behind the retaining wall. Richards and Elms suggested formulation for finding the yield acceleration (critical acceleration at which the retaining wall starts moving away from backfill). It should be noted herein that Richards and Elms used the MO method for finding the backfill pressure on the gravity retaining wall. They also suggested reducing K_h as the backfill pressure should reduce with sliding of the retaining wall. Richards and Elms also gave formulations and design charts for finding the seismic displacement of the gravity retaining walls. Equation 2.5 shows the formulation suggested by Richards and Elms to estimate the earthquake induced displacement of the gravity retaining walls.

$$d_{\text{residual}} = 0.087\left(\frac{V^2}{\text{g}k_{\text{max}}}\right)\left(\frac{k_{\text{y}}}{k_{\text{max}}}\right)^{-4} \qquad (2.7)$$

where, d_{residual} is the permanent outward displacement of the retaining wall.

V is the maximum ground velocity.

k_y is the yield acceleration.

k_{max} is the maximum seismic coefficient.

Study by Wu and Prakash (2001)

Wu and Prakash investigated the earthquake induced displacement behaviour of the gravity retaining walls by using one block model. The foundation stiffness and degradation of the shear modulus of the foundation soil were also considered in their study. The time dependent seismic pressure from the backfill was computed using the MO method. The effect of the hydrostatic pressure on seismic displacement and rotation of the gravity retaining wall was also considered. Wu and Prakash observed from their one block model that the backfill properties do not influence the seismic displacement of the gravity retaining wall. Tilting mode of failure could become critical in the gravity retaining wall with increased flexibility of the foundation soil.

Study by Steedman (1998)

Steedman studied different aspects of the traditional seismic retaining wall design. Steedman also discussed the limitations of the MO method and observed that the seismic behaviour of the earth retaining structures highly dependent on the foundation stiffness and seismic behaviour of the backfill. Steedman proposed a design chart for the performance based seismic design of the earth retaining structures.

Analytical investigations by Veletsos and Younan (1997)

Veletsos and Younan studied the seismic response of the flexible and rigid retaining walls using the analytical approach. The backfill behind the retaining wall was modelled as an elastic shear beam. The displacement of the base restrained flexible retaining wall was found highly influenced by the base flexibility and wall flexibility itself. The displacement obtained by the analytical elastic solutions were also compared with the retaining wall movement limits for mobilization of the failure wedge in the backfill.

2.5. Review of experimental investigations performed on the earth retaining structures

Several researchers studied the seismic behaviour of the earth retaining structures by conducting centrifuge/shaking table experiments on the retaining wall models. A brief summary of some significant contributions is provided in below:

Experimental investigations by Mononobe and Matsuo (1929)

Mononobe and Matsuo performed the shaking table experiments on the scaled down retaining wall model for understanding the dynamic backfill pressure behind the scaled down retaining wall. Backfill behind the retaining wall was constructed using dry cohesionless soil. A sinusoidal base excitation was than applied to the scaled down model. Different frequencies of the sinusoidal excitation were used to increase the intensity of applied excitations. Backfill pressure was then measured by using a pressure gauge at the top of the retaining wall.

Experimental investigations by Sherif and Fang (1984)

Sherif and Fang performed shaking table experiments on a rigid retaining wall rotating about the top. They observed nonlinear distribution of the dynamic earth pressure along the retaining wall height. Sherif and Fang also reported that the point of application of the dynamic backfill thrust is about 0.55m above the retaining wall base. Figure 2-4 shows the nonlinear backfill pressure behind the rigid retaining wall observed by Sherif and Fang during the shaking table investigations.

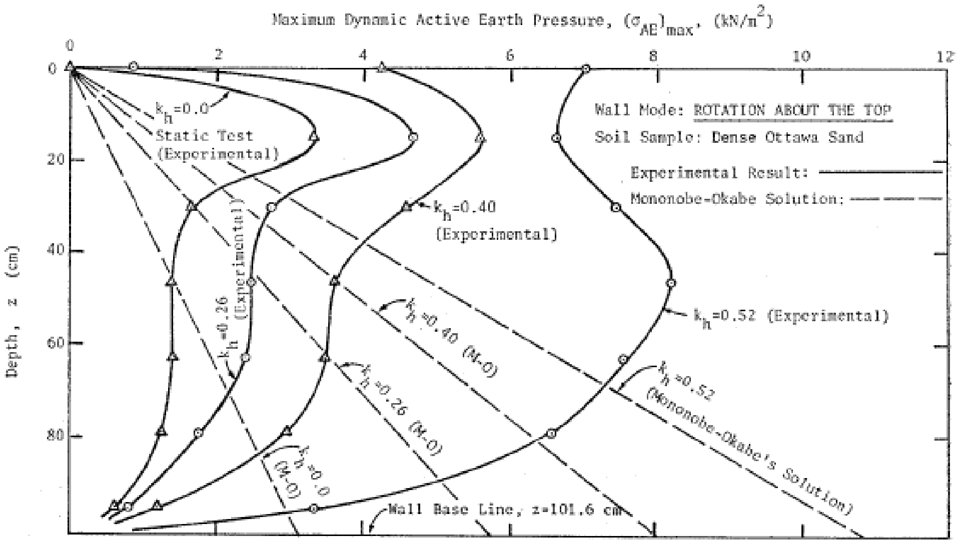

Figure 2-4 Nonlinear distribution of the maximum backfill pressure along the retaining wall height for different input base excitations (Sherif and Fang, 1984).

Experimental investigations by Wilson and Elgamal (2009, 2015)

Wilson and Elgamal (2009) performed a large scale shaking table experiment on the bridge abutment. They observed a significant reduction in the passive resistance of the backfill against the applied earthquake excitation. Later, Wilson and Elgamal (2015) performed the shaking table experiments on a large scale retaining wall with the $c - \phi$ backfill. Results from the shaking table experiment were compared with the limit equilibrium analyses results. Wilson and Elgamal observed that the MO method overestimates the dynamic pressure (when $c = 0$) on the retaining wall. The dynamic backfill pressure behind the retaining wall was found to act in a parabolic manner. The amplitude, and direction of the dynamic backfill pressure was also found to change with the applied base excitations.

Experimental investigations by Mikola and Sitar (2013)

Mikola and Sitar performed centrifuge experiments on scaled down models of the earth retaining structures. The experimental investigation was focused on the seismic performance of different earth retaining structures. Mikola and Sitar observed that the MO method could adequately estimate the dynamic backfill pressure along the height of the earth retention wall. It was also observed by Mikola and Sitar that the dynamic backfill pressure behind the earth retaining structures was highly influenced by the backfill density, severity of earthquake shaking, and displacement of the earth retaining structures.

Several other researchers have also studied the seismic response of the earth retaining structures by performing shaking table/centrifuge experiments on the scaled down /large scale models of the earth retaining structures. Table 2-2 shows a summary of different experiments performed on earth retaining structures.

Table 2-2 Summary of different shaking table/centrifuge experiments performed on the earth retaining structures.

Sr. No.	Investigation performed by	Investigation type	Model type	Major outcomes
1	Bolton and Steedman (1982)	Centrifuge investigations	Scaled down micro concrete retaining wall	(i) Importance of the retaining wall inertial forces. (ii) Permanent displacement of the retaining wall should be accounted for the seismic design
2	Ortiz et al. (1983)	Centrifuge investigations	Scaled down flexible retaining wall	(i) Nonlinear distribution of the dynamic soil pressure along the retaining wall stem height (ii) MO method can estimates the dynamic backfill pressure on the retaining wall
3	Koseki et al. (1998)	Shaking table investigations	Scaled down retaining wall model	(i) Steeper angle of the failure plane for $k_{h\text{-critical}}$. (ii) High vulnerability for the tilting mode of failure.
4	Watanbe et al. (2003)	Shaking table investigation	Scaled down retaining wall models	(i) Better seismic performance by the reinforced soil retaining wall (ii) MO method overestimates the seismic force (for peak ϕ)
5	Ling et al. (2005)	Shaking table investigation	Full scale modular retaining wall	(iii) Better seismic performance by the reinforced soil retaining wall (iv) High amplification towards the backfill top (v) High values of the residual backfill pressure
6	Kloukinas et al. (2015)	Shaking table investigation	Scaled down retaining wall model	(i) The base soil behavior controls the tilting of the retaining wall (ii) Higher values of the active state displacements of the retaining wall

2.6. Seismic design of earth retaining structures according to design codes

The design guidelines and recommendations for the seismic design of the earth retaining structures have been given in several design codes. Section 6 of the AASTHO guide specifications for LFRD seismic bridge design (2011) provides a detailed overview of the site investigations and design parameters. A brief overview of the geotechnical investigations (in-situ and laboratory) has also been suggested; for the site characterization. The standard also recommends conducting a detailed geotechnical investigation for the assessment of subsoil liquefaction potential, seismic induced settlement, lateral spreading, slope instability, and dynamic earth pressure on a particular site. The MO method has been suggested for finding the dynamic earth pressure. In case of the freestanding retaining wall; the permissible displacement has been suggested as $250A_{max}$ (mm), where A_{max} was the maximum ground acceleration. (AASTHO guide specifications for LFRD seismic bridge design 2002).

A site investigation based seismic design guidelines is not available in Eurocode 8. Section 6.7 of the Eurocode 8 deals with the designing of abutment and retaining walls. It recommended that the bridge abutment should remain elastic during a design level seismic event. In the case of flexible abutments; the guidelines recommend considering the following forces: (i) seismic earth pressure, (ii) inertial forces due to the abutment mass and the mass of the backfill at the top layer of the abutment, and (iii) reactions from the bearings. However, as mentioned earlier, a behaviour factor of 1.5 has been suggested for the monolithic abutments. A table has also been given for limiting the design displacement for the monolithic abutments. For finding the seismic earth pressure; it has been suggested to use EN 1998-5:2004. Section 7 of EN 1998-5: 2004 deals with the design of the earth retaining structures. The MO method was suggested for finding the dynamic earth pressure. Equations have also been proposed for finding the horizontal and vertical seismic coefficients. It was suggested to consider the point of application of dynamic earth pressure at $\frac{H_W}{2}$.

The AS 4678-2002 suggests considering 475 years return period earthquake for seismic design of earth retaining structures. In the case of free-standing retaining walls; 50 % reduction in the peak acceleration is recommended. The AS 4678 specifies a permissible displacement of $250A_{max}$ (mm) for free-standing gravity retaining walls. The MO method has been suggested for finding the pseudo-static backfill pressure on the earth retaining structures. The range for point of application of the lateral thrust has been specified as 0.4H to 0.55H. It was also recommended to consider the site specific analysis for finding the amplified acceleration at the ground surface. The AS 4678 recommends applying the inertial forces ($K_{\mathrm{h}}W_{\mathrm{W}}$)at $\frac{H_{\mathrm{W}}}{2}$.

Figure 2-5 shows the flow charts for the forced based and displacement based seismic design of earth retaining structures. The conventional forced based seismic design of the earth retaining structures profoundly used in the engineering practice. However, it does not assess the performance of the earth retaining structures during a design level seismic event. On the other side, the displacement based design of earth retaining structures assess all aspects of modern performance based seismic design, which makes it a robust process for the seismic design of the earth retaining structures.

Figure 2-5 Flow chart for the force based and displacement based seismic design of the earth retaining structures.

Flow chart for the force based seismic design

Flow chart for the displacement base seismic design

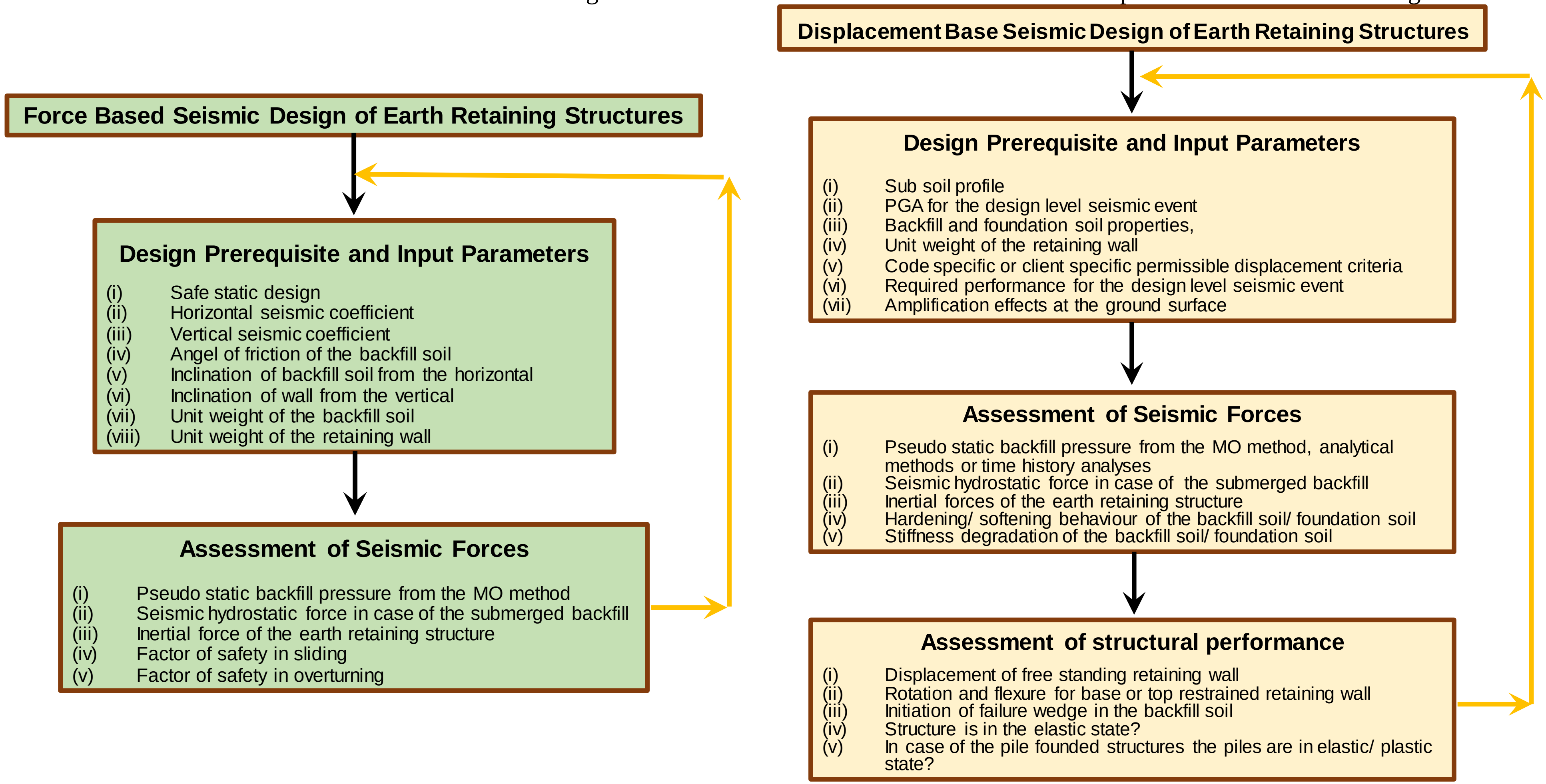

2.7. Summary of literature review

A detailed review of earthquake induced actions on the earth retaining structures has been presented along with the performance of the earth retaining structures during the past earthquakes. Seismic performance of the earth retaining structures during the past earthquakes indicates that the damage and failure of the earth retaining structures highly depends on the severity of the earthquake shaking and behaviour of the backfill/base soil. It was also observed that the earth retaining structures performed well against low to moderate earthquakes (Clough and Fragaszy, 1977).

In order to understand the seismic performance of the earth retaining structures, several experimental investigations have been performed on scaled down and large scale models of earth retaining structures. However, most of the investigations were focused on the backfill induced dynamic pressure on the earth retaining structures. It should be noted herein that a small amount of displacement and rotation of the earth retaining structures is required for generating an active failure wedge in the backfill (Clough and Duncan, 1991). Moreover, for the base restrained structures, flexural displacement may significantly influence the seismic response of the earth retaining structures (Steedman, 1998). It was observed that a detailed experimental investigation for understanding the seismic performance of a retaining wall that is founded on a piled foundation has not been reported in the literature.

Several experimental, analytical, and numerical investigations have been performed for understanding the role of the backfill on the seismic performance of the earth retaining structures. It was observed by Wu and Prakash (2001) that in the case of gravity retaining walls, the type of backfill does not influence the seismic displacement demand on the retaining wall. However, several experimental and numerical investigations reported that the backfill type, mobilization of backfill's friction angle, the flexibility of base/backfill, and the inertia of backfill can profoundly influence the seismic performance of the earth retaining structures (Bolton and Steedman, 1982; Steedman, 1998; Huang et al. 2009; Mikola and Sitar; 2013; Kloukinas et al., 2015; Bakr, 2018). Moreover, a detailed characterization of the backfill and the effects of hardening and softening behaviour of the backfill on the seismic performance of the earth retaining structures have not been reported in the literature.

Rock socketed piled foundations have been commonly used to support earth retaining structures. However, the seismic performance of earth retaining structures founded on rock socketed piled foundation considering hardening/softening behaviour of the backfill has not been reported in the literature.

Design recommendations for the seismic design of earth retaining structures have been provided in several design codes. However, most of the design recommendations have been provided for the seismic design of free-standing earth retaining structures. Limited design recommendations are available for the seismic assessment of base restrained earth retaining structures and pile founded earth retaining structures. Performing non linear time history analyses on finite element models of earth retaining structures requires high computational costs and background in finite element modelling. Therefore, simple hand calculations or design charts are required in order to estimate the earthquake induced elastic displacement of earth retaining structures.

Chapter 3. SCALE DOWN MODELLING OF EARTH RETAINING STRUCTURES

3.1. Introduction

Accurate assessment of earthquake induced actions on earth retaining structures is important for ensuring their satisfactory performance during a design level seismic event. Several researchers performed experimental investigations on full scale and scaled down models of earth retaining structures, in order to understand their seismic behaviour. Full scale experiments can effectively replicate the seismic behaviour of earth retaining structures. However, full scale experiments are constrained to a limited choice of ground accelerations and backfill type. Moreover, full scale experiments are costly and require a longer time for construction than scaled down models. Hence, a detailed parametric investigation on full scale models of earth retaining structures is difficult (Ertugrul and Trandafir, 2014). On the other hand, scaled down models of earth retaining structures are famous for replicating effects of seismic actions on earth retaining structures. Similitude analyses are useful for scaling down prototype models (Moncarz and Krawinkler, 1981). Scaled down models of earth retaining structures could be analyzed experimentally either using a centrifuge or using a shaking table (Ertugrul and Trandafir, 2014).

Present chapter outlines scale down modelling of earth retaining structures. Theory of dynamic similitude and details of scale down modelling of earth retaining structures is presented. The capability of scaled down retaining wall (RW) models has also been verified for replication of the seismic behaviour of prototype RW. Different support conditions have also been considered for scaled down RW models, and scaling down of rotational stiffness of rock socketed pile foundation using torsional springs is also presented. It was observed that scaled down RW models can effectively replicate the seismic response of prototype RW models.

3.2. Scaled down modelling of retaining wall soil system and theory of dynamic similitude

Scaled down models of retaining wall (RW), Quay wall, basement wall and bridge abutment were used by various researchers to examine their response against different loading conditions. Matuo and Ohara, 1960; Bolton and Steedman, 1982; Sherif and Fang, 1984; Sitar and Mikola, 2013; Oldecop and Zabala, 1996; Simonelli et al. 2000; Latha and Krishna, 2006, used scaled down RW models, to understand their response against earthquake loading. Similitude laws should be followed for scaling down prototype models, in the case of dynamic loading scenarios such as an earthquake or blast loading, dynamic similitude modelling approach should be used for scaling down prototype models (Moncarz and Krawinkler, 1981).

Theory of similitude is used to establish a relationship between the fundamental quantities of scaled down and prototype models. Theory of similitude is based on laws of similarity, which is also known as dimensional analysis (Moncarz and Krawinkler, 1981; Wood et al. 2002). Dimensional analyses are performed in two major steps; the first step is to identify relevant material and structural properties of prototype model, and the second step is to establish a valid relationship between structural and material properties of scaled down and prototype models. Table 3-1 shows the basic quantities for dimensional analysis (Moncarz and Krawinkler 1981, Jha 2004).

Table 3-1 Basic quantities for dimensional analysis.

Sr. No.	Basic quantity	Basic abbreviations
1	Length	*L*
2	Mass	*M*
3	Time	*T*

The relationship between basic quantities (L, M and T) of prototype and scaled down model can be expressed by a ratio (λ). For example, if scaled down model height (L_s) is 1/10th of prototype model height (L_p), the dimensionless ratio of heights could be written as:

$$\lambda_l = \frac{L_p}{L_s} = 10 \tag{3.1}$$

Basics for dimensional analysis can be obtained by using Buckingham Pi theorem (Buckingham, E. 1914). The Buckingham Pi theorem gives a dimensionless number "π" as a power to any basic physical quantity "*A*".

For example, if a physical quantity "*A*" depends on other quantities such as A_1, A_2, A_3……A_n, then this relationship can be expressed in the form of equation no. (3.2),

$$A = f(A_1, A_2, A_3 \dots \dots A_n) \tag{3.2}$$

Equation 3.2 can be written with a dimensionless number "π" as follows;

$$\pi_A = f\left(\pi_{A1}, \pi_{A2}, \pi_{A3} \dots \dots \pi_{A(n-N)}\right) \tag{3.3}$$

where, N is rank of the dimensionless matrix,

It should be noted here that, the scaled down model will produce similar results to the prototype model if,

$$\pi_{1p} = \pi_{1s} \tag{3.4}$$

$$\pi_{(n-N)p} = \pi_{(n-N)s} \tag{3.5}$$

Use of Buckingham Pi theorem for the generation of the homogeneous equation for stress (σ) is shown below; σ mainly depends on force (*F*) and the applied area (*a*), dimensionally homogeneous equation for stress can be written as:

$$\sigma = f(M, L, T) \tag{3.6}$$

where, "*M"* is the system mass, "*L"* is length and "*T"* is time.

In the above expression σ is a dependent quantity which depends on the value of *m*, *g* and *l*. According to Buckingham Pi theorem; equation (3.6) can be rewritten using the dimensionless number "π" which is the power of the corresponding physical quantity,

$$\pi_\sigma = f(\pi_m, \pi_l, \pi_t) \tag{3.7}$$

The dimensionless form of equation (3.6) is presented as equation (3.7), which is valid for a true scaled down model.

The dimensional analysis starts with the identification of significant physical quantities, which can influence the behavior of the prototype model when subjected to the stipulated loading conditions. Relaxation on some physical quantities is possible provided that the prototype model behaviour has not been altered to a certain extent. In earthquake engineering; geometry, material properties and boundary conditions of the prototype model can profoundly influence dimensional analysis. Depending on the type and nature of the investigation (such as structural response/material failure), relaxation on physical quantities can be decided.

Table 3-2 shows the summary of different measurement quantities and corresponding dimensional details for two sets of scale factors; (i) force (*F*), length (*L*), Time (*T*).and (ii) mass (*M*), *L* and *T* (Moncarz and Krawinkler 1981).

Table 3-2 Details of different measurements considered for dimensional analysis

Measurement	Abbreviations	Related Formulation	Dimensional Details						
			F	L	T		M	L	T
Length	L	l	0	1	0		0	1	0
Time	T	t	0	0	1		0	0	1
Frequency	ω	1/t	0	0	-1		0	0	-1
Acceleration, acceleration due to gravity	A, g	$\frac{l}{t^2}$	0	1	-2		0	1	-2
Force, Inertial Force	F, F_I	$\frac{ml}{t^2}$	1	0	0		1	1	-2
Stress, Stiffness	σ, E	$\frac{m}{lt^2}$	1	-2	0		1	-1	-2
Mass density	ρ	$\frac{\gamma}{g}, \frac{F_g}{gl^3}$	1	-4	2		1	-3	0
Mass	M	$\rho l^3, \frac{F_g}{g}$	1	-1	2		1	0	0
Velocity	V	$\frac{l}{t}$	0	1	-1		0	1	-1

Scaled down models are classified as true replica / adequate and distorted models. Adequate models are those which satisfy all aspects of dimensional analysis. In the case of the distorted models, some similarity laws could be relaxed, depending on their effects on the desired response of the scaled down model.

As mentioned in Chapter 1, shaking table experiments have been performed on scaled down RW models. In the case of a shaking table experiment, the acceleration ratio of the prototype and scale down model is equal to one,

$$\frac{a_{\mathrm{p}}}{a_{\mathrm{s}}} = \frac{\mathrm{g_p}}{\mathrm{g_s}} = 1 \tag{3.8}$$

where,

a_{p}= acceleration in prototype model = $\mathrm{g_p}$= gravitational acceleration

a_{s}= acceleration in scaled down model = $\mathrm{g_s}$= gravitational acceleration

In the case of a true replica model; Hooke's law can be expressed by the following design conditions:

$$E = \frac{\sigma}{\varepsilon} = \frac{Fl}{l^2 \Delta l} = \frac{m\mathrm{g}l}{l^3} = \rho \mathrm{g} l \tag{3.9}$$

$$\lambda_{\mathrm{E}} = \frac{E_{\mathrm{p}}}{E_{\mathrm{s}}} = \frac{(\rho \mathrm{g} l)_{\mathrm{p}}}{(\rho \mathrm{g} l)_{s}} = \lambda_{\rho} \lambda_{\mathrm{l}} \tag{3.10}$$

$$\frac{\lambda_{\mathrm{E}}}{\lambda_{\rho}} = \lambda_{\mathrm{l}} \tag{3.11}$$

The above expression can be used to form the dimensionless one-dimensional wave propagation equation using Cauchy condition:

$$V = \sqrt{\frac{E}{\rho}} \tag{3.12}$$

$$\lambda_{\mathrm{V}} = \frac{V_{\mathrm{p}}}{V_{\mathrm{s}}} = \sqrt{\frac{\lambda_{\mathrm{E}}}{\lambda_{\rho}}} = \sqrt{\lambda_{\mathrm{l}}} \tag{3.13}$$

In the case of distorted models, one or more dimensional analysis conditions are not satisfied. This can result in the distortion of dimensionless quantities, and ultimately the response of the scaled down model is different from the prototype model. However, the distorted models can be used after accounting for the distorted quantities and choice of output results. As mentioned earlier, it is difficult to satisfy all similitude criteria for a 1-g shaking table experiment, as gravitational acceleration is the same for the prototype and scale down model. However, errors could be minimized with suitable dimensional analysis and suitable choice of output results (Murphy, 1950; Moncarz and Krawinkler, 1981; Crosariol, 2010).

It should be noted here that the shaking table experiment is performed in a 1-g environment, which implies a restriction on gravitational acceleration for scaled down models. As mentioned earlier, the ratio of prototype and scaled model acceleration is 1 for a shaking table experiment ($A = \frac{A_{\mathrm{p}}}{A_{\mathrm{s}}} = 1$). Therefore, in the case of scaled down models of earth retaining structures, the assumption of the same material (as prototype model) can result in a high additional (nonstructural) mass requirement for the scaled down model.

Figure 3-1 shows the schematic procedure of scaled down modelling for 1-g shaking table experiment. The scale down process starts with the identification of the basic physical quantities of the prototype model and their effects on desired output response, e.g., in case of earth retaining structures; stiffness of the structure is generally very high. During an earthquake; structural and backfill failure can occur because of excessive displacement and rotation of the earth retaining structures, and not because of structural damage. Therefore, scaled down and prototype (full scale) model are not required to be of the same material as material failure is not desired from the scaled down model. This condition is further explained in section 3.4 of the present chapter.

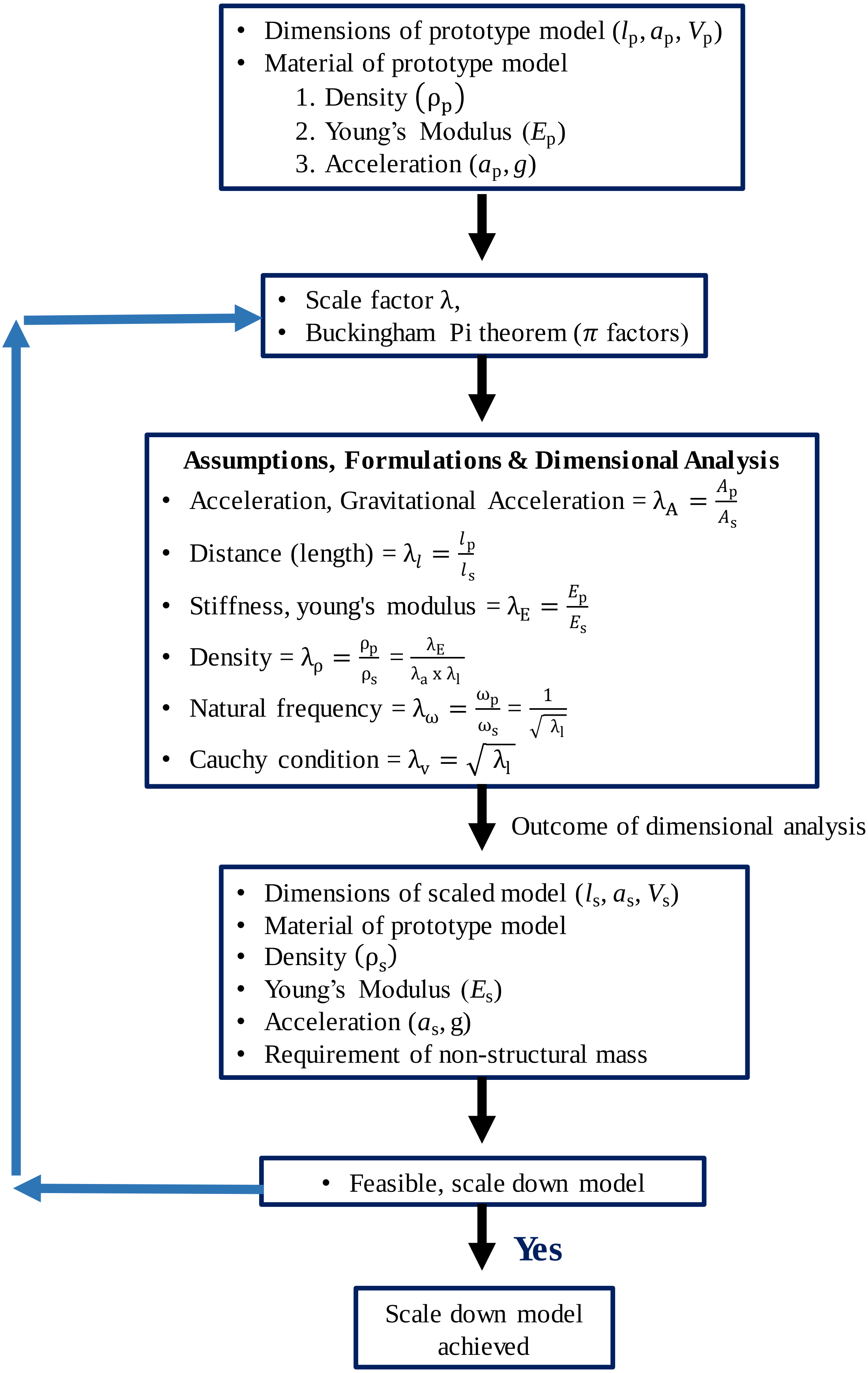

Figure 3-1 Flow chart for finding scale down model properties.

3.3. Understanding the capability of scaled down models of earth retaining structures

The capability of scaled down RW models has been evaluated for replication of earthquake response of prototype RW models. Similitude analyses have been performed for finding scaled down RW model properties. Figure 3-2 (a) and (b) shows geometrical details and finite element (FE) mesh of prototype RW model; considered for similitude analysis, respectively.

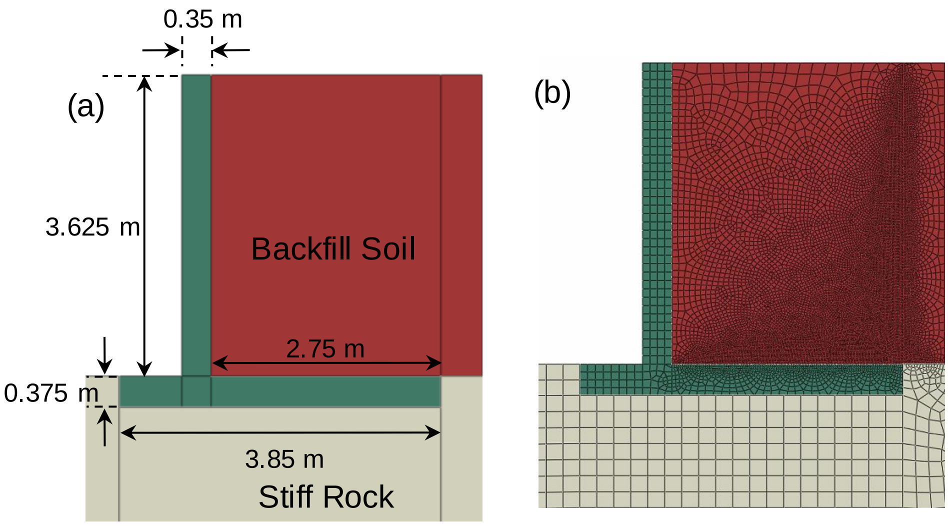

Figure 3-2 Geometrical details and finite element (FE) mesh of prototype RW model.

Dynamic similitude calculations have been performed for 10 scale down factor (λ). Identical material of the scaled down and prototype RW model at 1 g acceleration level was assumed. Dimensional details of physical quantities are presented in table 3-2. RW is modelled using concrete material, and crushed rock is considered as backfill type for both scaled down and prototype RW models. The Mohr-coulomb model (details are presented in section 5.3.3 of chapter 5) has been used to model the backfill. Concrete was modelled using the concrete damaged plasticity (CDP) model, which is an inbuilt material model in FE software Abaqus. Details of the CDP model are presented in section 6.3.2). Damping in the backfill has been modelled using Rayleigh damping parameters (details are presented in section 5.3.5 of chapter 5). Table 3-3 shows details of material properties considered for the prototype RW model.

Table 3-3 Material properties considered for prototype RW (only for section 3.3.)

Sr. No.	Material	Property	
1.	Concrete	Density	2400 kg/m^3
		Elastic modulus	32 GPa
		Poisson's ratio	0.3
		Maximum compressive strength	40 MPa
		Plasticity Model	Concrete damaged plasticity
2.	Crushed rock	Density	1790 kg/m^3
		Constrained modulus	15.5 MPa
		Poisson's ratio	0.45
		Friction angle	44^o
		Dilation angle	19^o
		Damping (α_m)	0.89
		Damping (α_k)	0.000167
		Plasticity Model	Mohr coulomb plasticity
3.	Stiff rock	Density	2800 kg/m^3
		Elastic modulus	100 GPa

Figure 3-3 shows the finite element mesh, and boundary conditions for the base constrained RW model. The RW and the backfill have been modelled over firm rock. The base of the firm rock has been restrained for vertical ("*y*") direction movement and free to translate in horizontal ("*x*") direction. Springs and dashpots system have been adopted at lateral boundaries for minimizing boundary effects. A deailed study has also been performed for finding optimum length of backfill domain behind RW (section 6.4 of chater 6). Details of the spring and dashpot system are presented in section 6.4 of chapter 6.

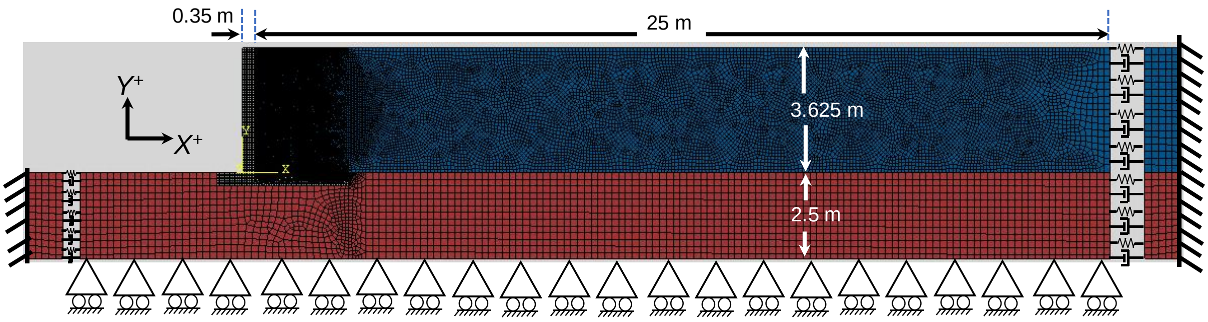

Figure 3.3 Two dimensional (2D) plane strain FE model of prototype RW, adopted boundary conditions.

Prototype and scaled down RW models have been analyzed using FE software Abaqus, and non-linear time history analyses have been performed in the dynamic explicit module of Abaqus. Two base excitations (multiple pulses and Tabas, Iran accelerogram) have been used as input ground motions to excite the prototype and the scaled down RW models; both accelerograms are shown in figure 3-4. It should be noted here that the time domain of applying base excitation for scaled down RW model is scaled down by $\sqrt{\lambda_1}$, to satisfy similitude criteria and Cauchy conditions.

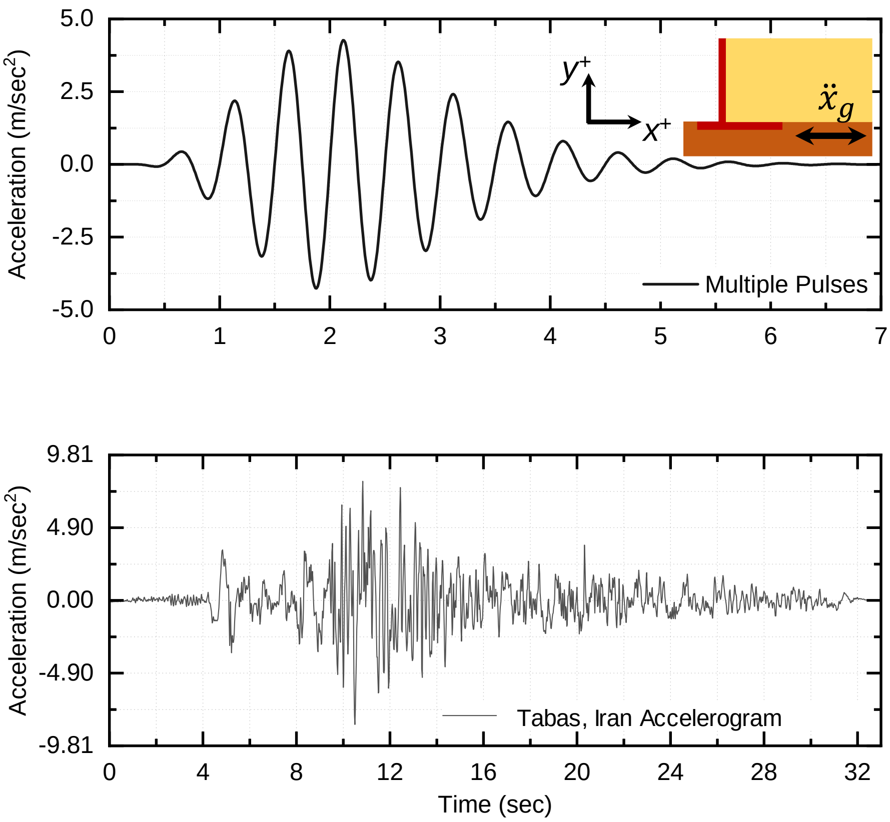

Figure 3-4 Applied base excitations for prototype FE RW models.

FE analysis has been performed in two steps. During the initial step, geostatic stresses and gravity loading have been applied to FE models for satisfying the equilibrium conditions in the soil. Earthquake loading has been applied in the dynamic explicit step. Details of the dynamic explicit step of Abaqus are presented in section 5.4 of chapter 5.

Figure 3-5 shows a comparison of relative displacement at RW top (relative to base); obtained from scaled down and prototype RW models. It should be noted here that results of scaled down RW model need to be scaled up (time and displacement). A good agreement has been observed between relative displacement obtained from the scaled down and prototype RW models. Therefore, it can be concluded that the scaled down RW models of earth retaining structures can effectively replicate seismic behavior of the prototype RW models.

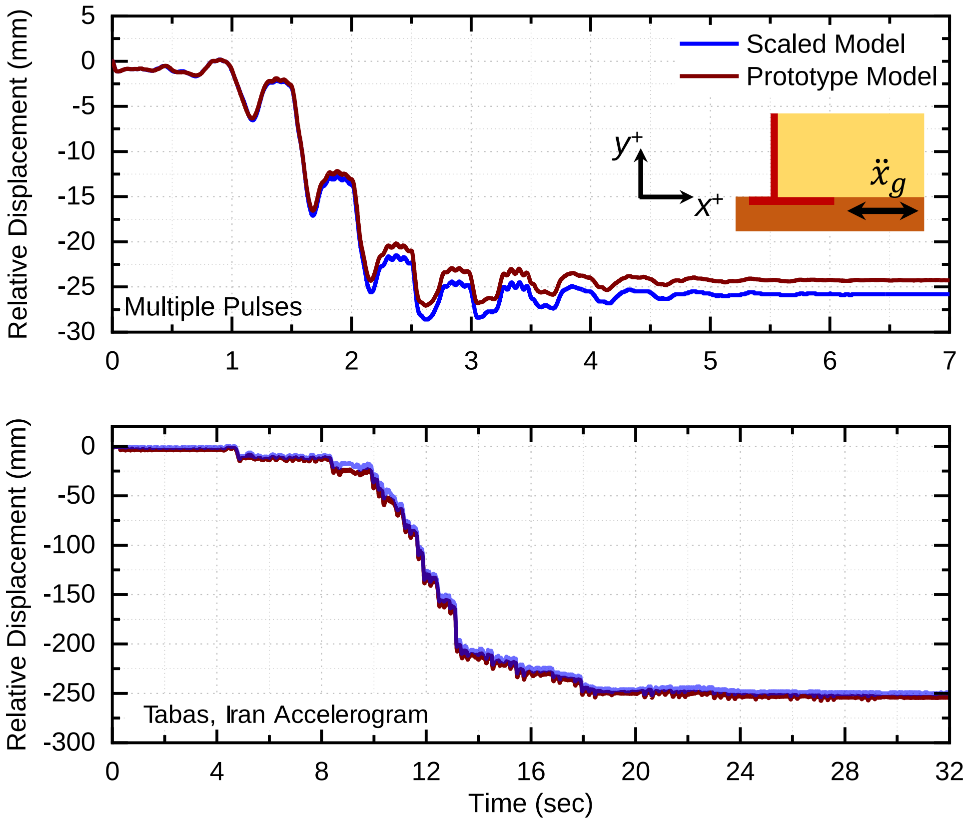

Figure 3-5 Comparison of relative displacement at RW top observed from prototype and scaled down RW models.

3.4. Selection of scaled down RW model material and RW model fabrication

Once dimensional analysis (finding scaled down RW model properties) is completed, the next step is to find materials for the scaled down model. As mentioned earlier, shaking table experiments performed in 1-g environment (same acceleration and material assumption) requires an additional non-structural mass in scaled down models, to satisfy weight similitude criteria when the π number is equal to 1. However, in the case of concrete structures; the required amount of non-structural mass is generally very high, and assemblage of such high non-structural mass in scaled down model could change material behavior completely. Hence, it is not possible for most of the reinforced concrete (RC) members to satisfy weight similitude criteria (Moncarz and Krawinkler, 1981). As explained earlier, earth retaining structures generally have high strength and mass. Therefore, failure of earth retaining structures occurs mainly as a result of excessive displacement and rotation, and not because of the failure of structural material (cracking, crushing) (Seed and Whitman, 1970). Moreover, a small amount of active state displacement of RW is enough to generate an active failure wedge behind the RW (Gamal, 1996; Choudhury and Chatterjee, 2006). Therefore, the most important criteria for scaled down RW model is to replicate realistic seismic displacement and rotation of the prototype RW model. Hence, in the present study requirement of the same material in the scaled down RW model is relaxed (Crosariol, 2010). As explained earlier, the scale down factor (λ) in the present study is 10. Therefore, target elastic modulus of the scaled down RW was selected as 2-3 GPa. Achieving low elastic modulus is not possible with most of the metals. However, some plastics with high density range satisfy low modulus criteria. Based on rigorous search on possible options for scaled down RW model material, polycarbonate sheets have been selected as scaled down RW model material. Figure 3-6 shows the fabricated cantilever RW model. Dimensional details of scaled down RW model is also shown in figure 3-7c. Sandpaper has been used on the inner surfaces and the base of the fabricated cantilever RW model as shown in figure 3-7a and 3-7b, (for initiating initiate friction between RW and backfill).

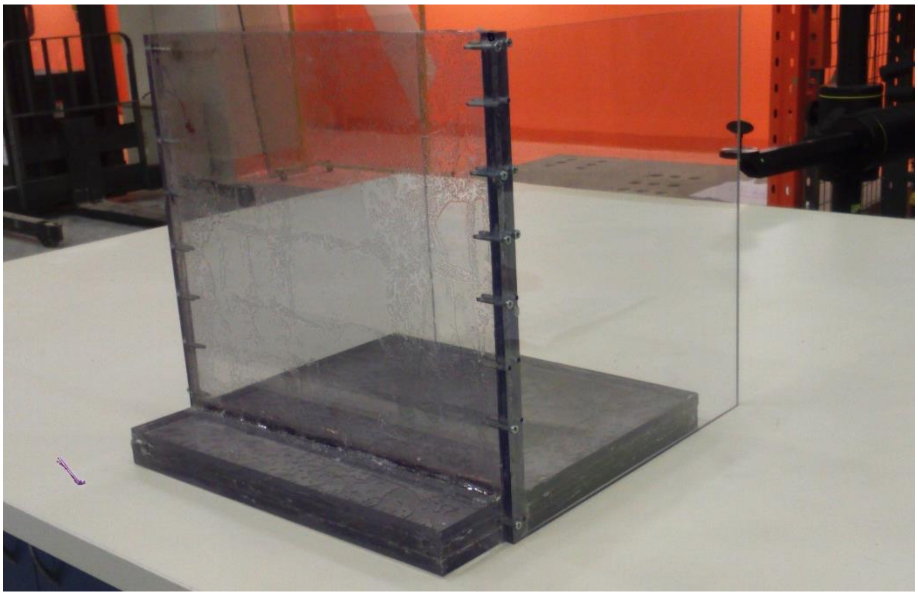

Figure 3-6 Scaled down RW model, fabricated using Polycarbonate sheets.

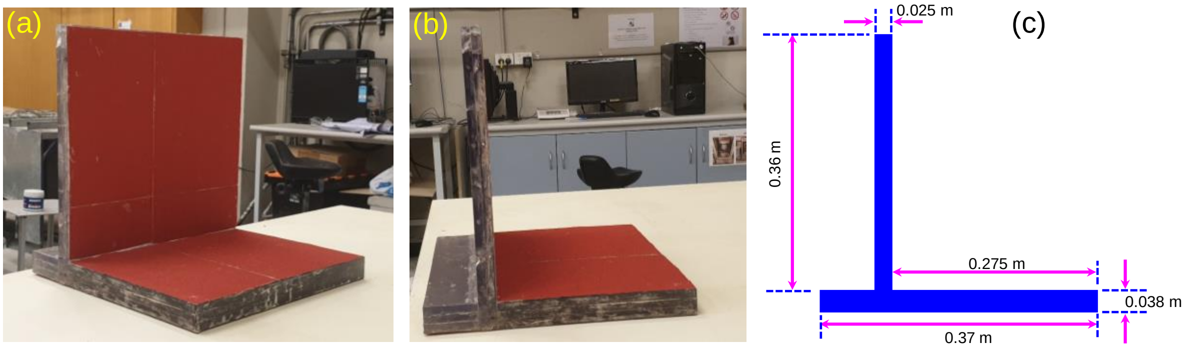

Figure 3-7 Fabricated polycarbonate RW model with sandpaper to initiate friction.

3.4.1. Support conditions for scaled down (polycarbonate) RW model

Selection of accurate and realistic boundary conditions for the scaled down RW models is highly important in order to replicate the realistic seismic response of the prototype RW models. Several researchers performed shaking table and centrifuge experiments on scaled down free-standing gravity wall models. Ichihara and Matsuzawa (1973) and Ishibashi and Fang (1987) performed a shaking table experiment on rigid RW with movable and rotational base by introducing a constant sliding and rotation at the RW base. However, experimental investigations for understanding seismic rotational behaviour of RW; founded on rock socketed pile foundation has not been investigated in the past. Therefore, a series of shaking table experiments have been performed on scaled down RW model with a rotational base in this study. Rotational springs have been selected to replicate the rotational response of rock socketed pile foundation system. Rotational stiffness of the pile foundation (a group of four piles), has been estimated with the help of 2D plane strain FE model. It should be noted herein that the rock socketed pile foundation is not of plane strain geometry. However, the 3D response of the pile group can effectively represent by 2D plane strain FE model after simple alterations with pile rigidity as explained below:

3.4.2. Seismic response of 3D and 2D RW models, founded on rock-socketed pile foundation

FE analyses have been carried out, in order to understand the capability of the 2D plane strain RW model (founded on rock-socketed pile foundation) for replication of seismic behavior of similar 3D RW model. For simplicity and reduction in computational time, backfill behind the RW and foundation soil surrounding piles is not considered (only in this section). Figure 3-8 and 3-9 shows geometrical details of 2D and 3D finite element RW models, which are founded on rock-socketed piles. Elastic RW and pile foundation is modelled using concrete material with young's modulus of 26 GPa and Poisson's ratio of 0.3. It was assumed that the pile was socked 2 m into the rock. Fixity has been modelled between the base of the RW and top of the pile cap. It should be noted herein that the pile foundation is not a plane strain problem. However, Young's modulus of 2D rock-socketed piles has been recalculated to match the axial rigidity of the 3D rock-socketed piles. The base of the rock domain has roller boundary conditions for ensuring free lateral displacement, but no vertical displacement of the rock base. Multiple pulses, as shown in figure 3-10 have been used as the input base motion for both the 2D and 3D FE models. FE Analyses have been performed in the dynamic explicit module of the FE software Abaqus (Abaqus/Explicit User's Manual, 2013). Comparison of the relative displacement at the RW top (relative to pile cap top) as observed from 2D and 3D FE analysis is shown in figure 3-11. Good agreement has been observed between the 2D and 3D FE analysis results. Therefore, it can be concluded that the 2D FE model of RW founded on a rock-socketed pile foundation can replicate the seismic behaviour of a similar 3D RW-Pile model.

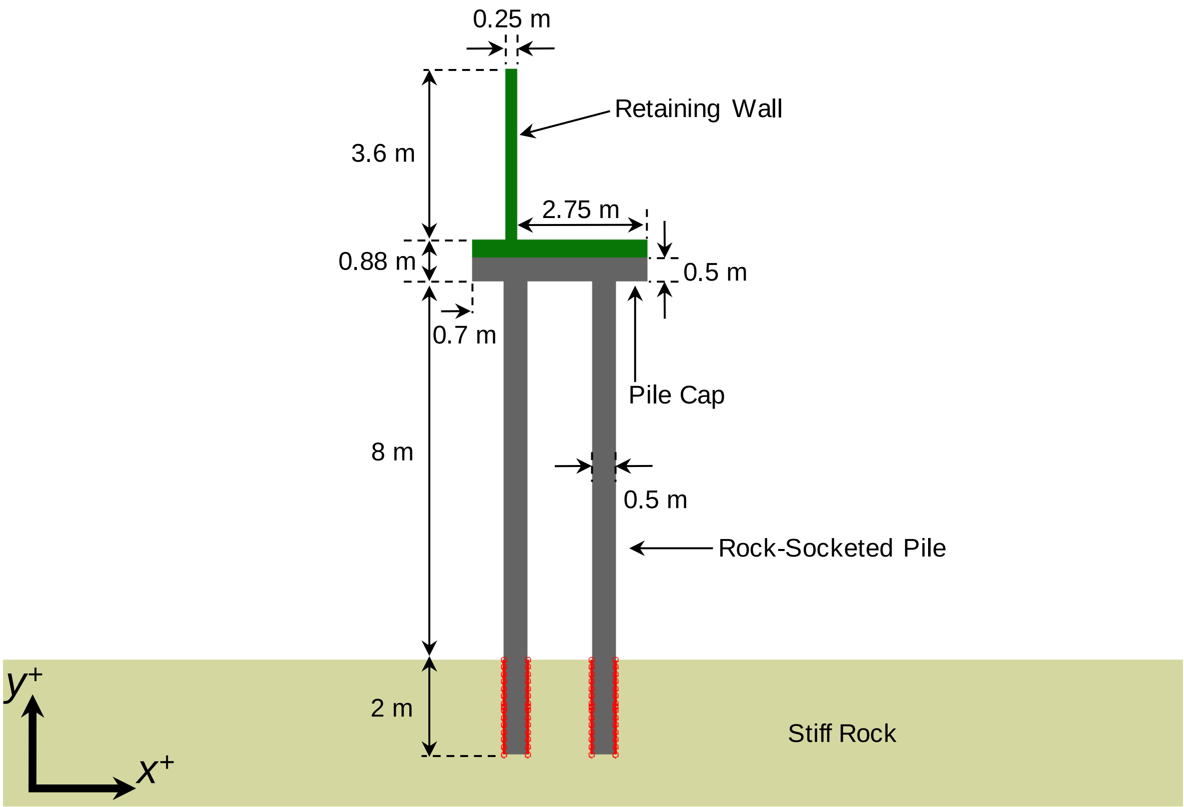

Figure 3-8 Geometrical details of 2D FE model of RW, supported with rock-socketed pile foundation.

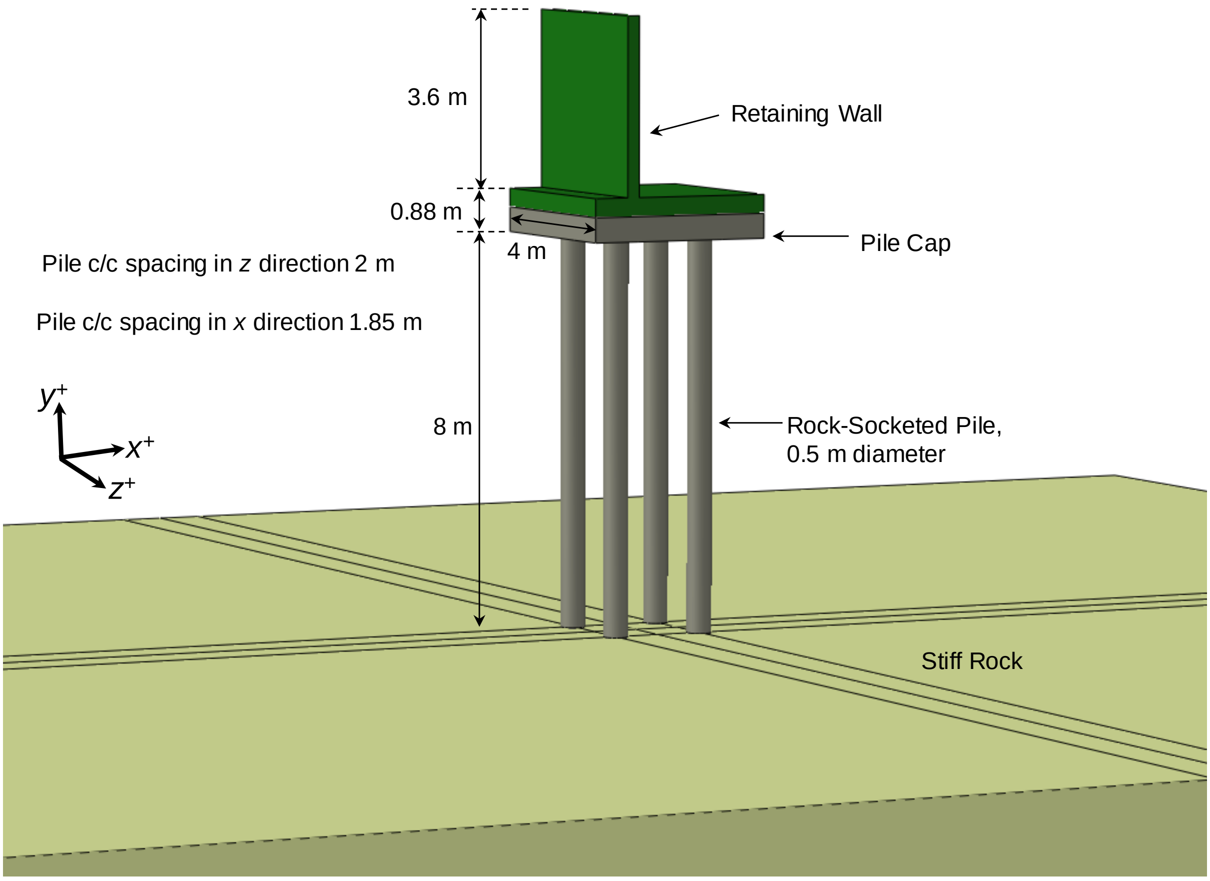

Figure 3-9 Geometrical details of 3D FE model of RW, supported with rock-socketed pile foundation.

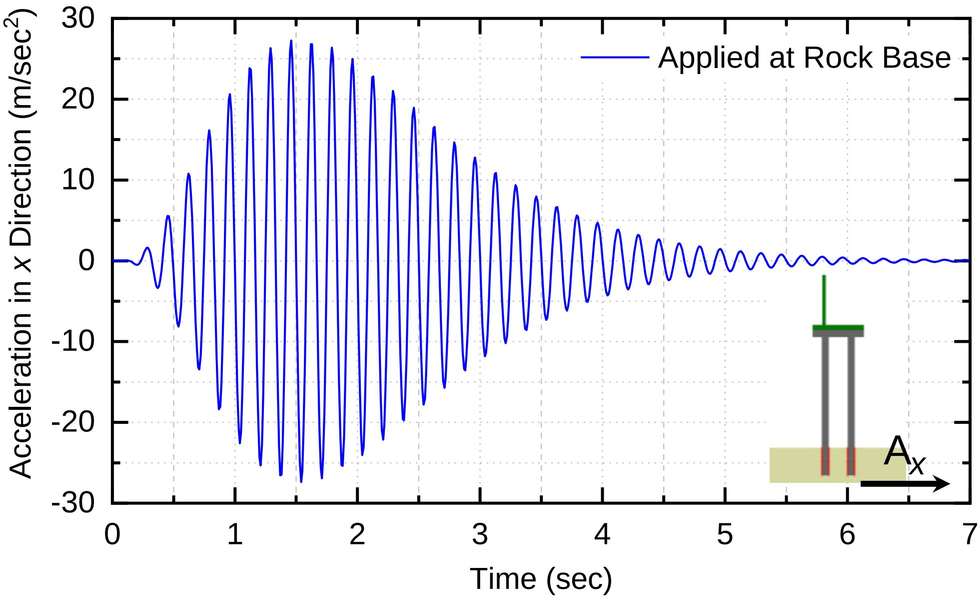

Figure 3-10 Applied acceleration at FE model (2D and 3D) base.

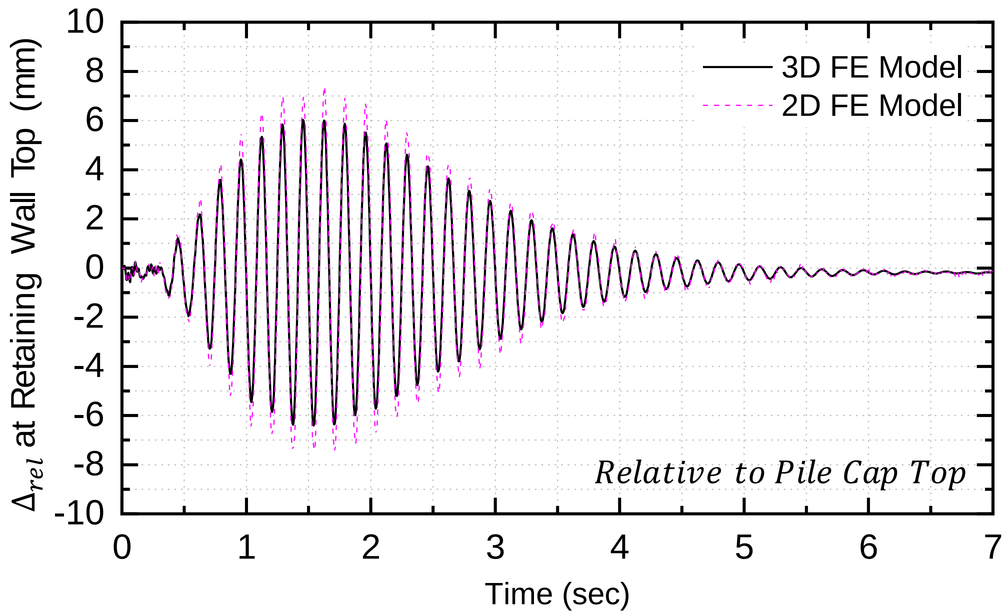

Figure 3-11 Comparison of relative displacement at RW top obtained from 2D and 3D FE model of RW on rock-socketed pile foundation (no backfill/ foundation soil).

3.4.3. Evaluation of scaled down rotational stiffness of rock-socketed pile foundation

The rotational stiffness of the rock-socketed pile foundation has been evaluated based on FE analysis of the 2D plane strain prototype RW model. Figure 3-12 shows the 2D plane strain FE model of the prototype RW, which was supported on a rock-socketed pile foundation. Geometrical details and boundary conditions of the 2D plane strain model is also shown in figure 3-12. The RW, pile cap and pile foundation were modelled using an elastic concrete material with Young's modulus and Poisson's ratio equal to 26 GPa and 0.3 respectively. Backfill behind the RW is modelled as crushed rock. Mohr coulomb model is used to model backfill. Details of the crushed rock and Mohr coulomb model is presented in Chapter 5. The foundation soil underneath the RW is modelled as Brown Clay (A1.1.). The Mohr Coulomb model was used to model Brown Clay. Rayleigh damping was used to model damping in crushed rock and Brown Clay. Details for finding the value of the Rayleigh damping parameters are presented in section 5.3.5 of chapter 5. Both piles are socketed 2 m into rock (IRC 78:2014). Springs and dashpots are used in vertical boundaries of the FE model (as shown in figure 3-12), for reducing boundary effects. Gravity loading has been applied to the FE model, and geostatic stresses have also been defined to maintain equilibrium conditions in soils. Artificial accelerogram, as shown in figure 3-13 (PGA 0.74g), generated on the rock outcrop by program GENQKE (Lam, 1999), has been applied at the base of the rock domain. The FE model domain between spring and dashpot system was free to translate in the lateral ("*x*") direction but restrained in the vertical ("*y*") direction. Nonlinear FE analysis has been performed in the dynamic explicit module of the FE software Abaqus (Abaqus/Explicit User's Manual, 2013).

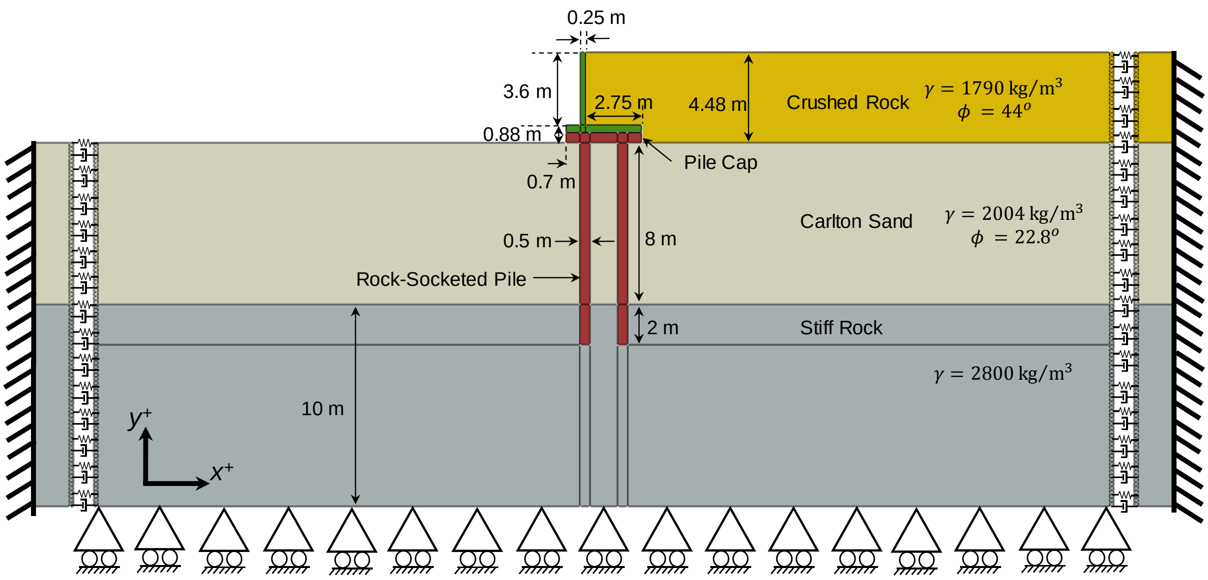

Figure 3-12 Geometrical details and boundary conditions of 2D plain strain FE RW model supported with rock-socketed pile foundation.

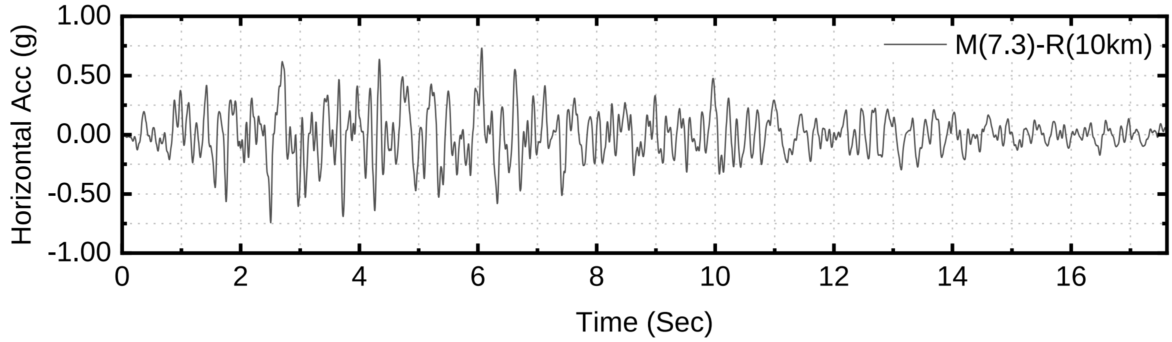

Figure 3-13 Acceleration time history applied at FE model base.

Results of FE analysis were used for determining the bending moment at the base of pile cap (RW toe side). Figure 3-14 shows applicable stresses (lateral or vertical) and their path used for determining bending moment at the pile cap base.

$$\text{Moment } (M)_{\text{n}^{\text{th}}\text{ element}} = \sum \text{Stress } \times \text{Element Area} \times \text{ Leverarm} \qquad (3.14)$$

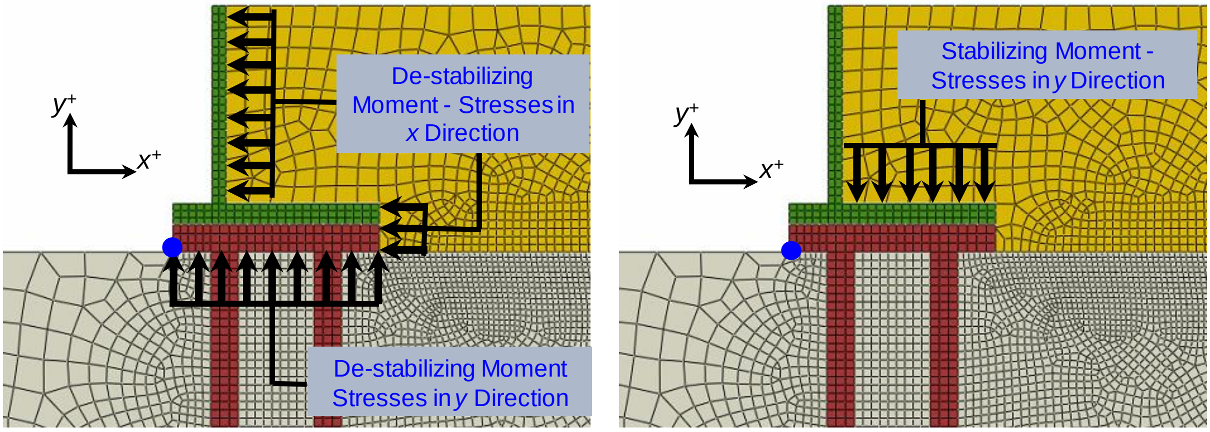

Figure 3-14 Horizontal and vertical stresses considered for finding moment along pile cap toe.

Equation 3.14 shows the overturning moment (calculated using lateral and heel slab base stresses) and the stabilizing moment (calculated using heel slab top vertical stresses). The final moment about the toe of the pile cap has been obtained by subtracting the stabilizing moment from the overturning moment.

Rotation (θ) at the top of the RW is calculated using relative displacement ($\Delta_{\mathbf{rel}}$) at the RW top (relative to the base) divided by the RW height (*H*). Figure 3-15 shows the rotation time history at the RW top when subjected to M(7.3)-R(10km) accelerogram.

$$\tan\theta = \frac{\Delta_{\text{Top}} - \Delta_{\text{Base}}}{H_{\text{stem}}} \qquad (3.15)$$

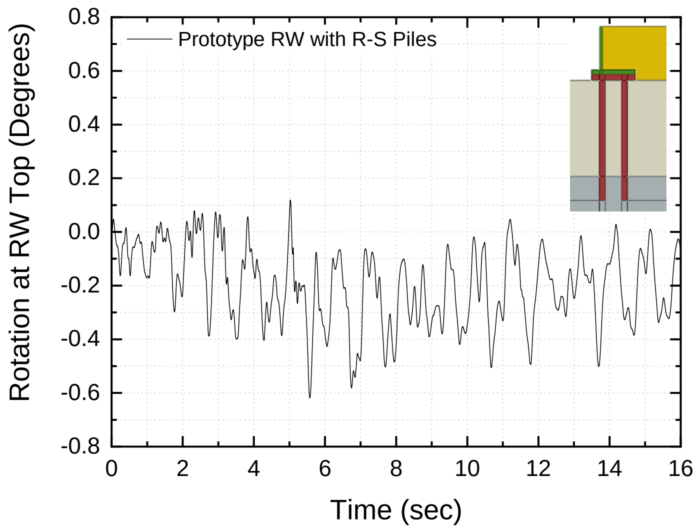

Figure 3-15 Rotation time history at RW top.

The rotational stiffness of the pile foundation is then calculated as the moment required for unit rotation of the pile cap using the following formulations:

$$K_{\theta} = \frac{M_{\mathrm{Toe}}}{\theta} \tag{3.16}$$

By FE analyses the rotational stiffness of the prototype RW which was founded on the rock-socketed pile foundation was estimated as 91.47 kNm/m-degree.

3.4.4. Scaling of rotational stiffness of rock-socketed pile foundation

Scaling down of the physical piles for the 1-g shaking table experiment is complicated. Obtaining realistic behaviour of the pile rotation with the scale down model of the piles is also doubtful. Therefore, it was decided to replicate scaled rotational stiffness of the pile foundation with rotational (torsion) springs. Dimensional analyses were then performed for finding scaled rotational stiffness of the pile foundation. The following relationship was obtained for scaling rotational stiffness of the pile foundation:

$$\lambda_{\mathrm{K}_{\theta}} = \frac{K_{\theta_{\mathrm{p}}}}{K_{\theta_{\mathrm{s}}}} = \left(\frac{L_{\mathrm{p}}}{L_{\mathrm{s}}}\right)^{4} = \left(\lambda_{\mathrm{L}}{}^{4}\right) \tag{3.17}$$

It should be noted herein that same material has been assumed for the prototype and scaled down rock socketed pile, for the finding rotational stiffness of the scaled down rock socketed pile foundation (K_{θ_s}).

$K_{\theta_s}$was further used to decide on the rotational stiffness of the single spring, as the prime objective of modelling the rotational response behaviour of the scaled down RW model. The scaled rotational stiffness of the rock socketed pile foundation was calculated as 9147 N-mm/m-degree.

The rotational stiffness of the single rotational spring and spring's position is determined by a uniform distribution of rotational springs over the RW base. Participation of the entire RW width (0.4 m) was assumed for calculation of the total rotational stiffness. Symmetry in the rotational spring distribution over the toe and heel of the scaled RW is achieved by distributing them uniformly on both sides of the centre of gravity (C.G.). Figure 3-16 shows the plan and elevation of the scaled down RW with positions of the rotational springs. A total of 16 rotational springs were used at the RW base. The rotational stiffness of the single rotational spring is calculated as 229 N-mm/degree. Figure 3-17 shows the mild steel rotational springs which were fabricated at The University of Melbourne.

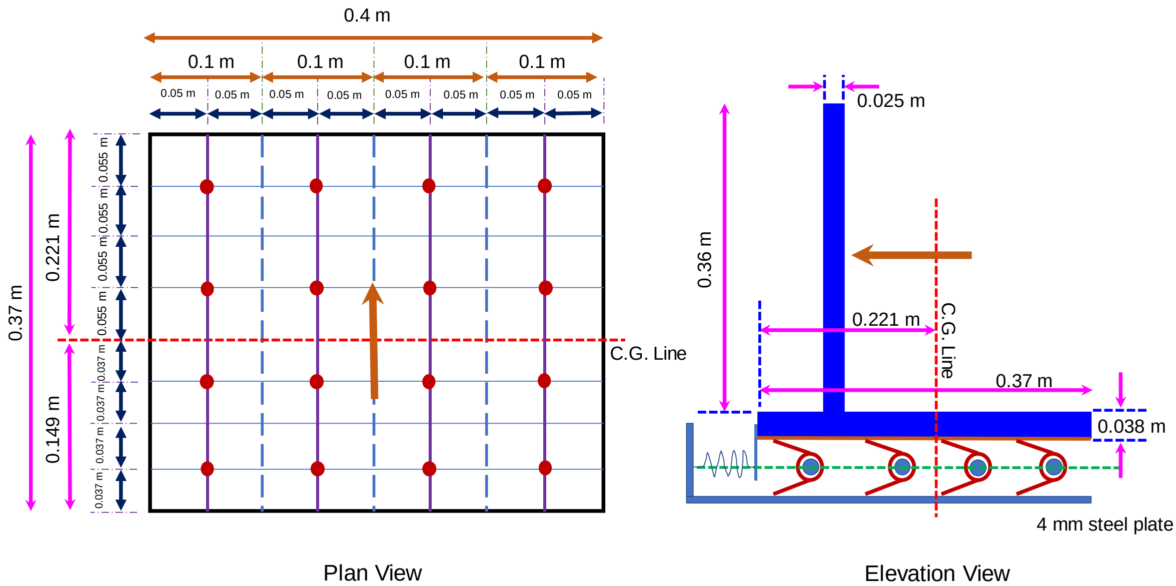

Figure 3-16 Distribution of rotational springs at scale down RW model base.

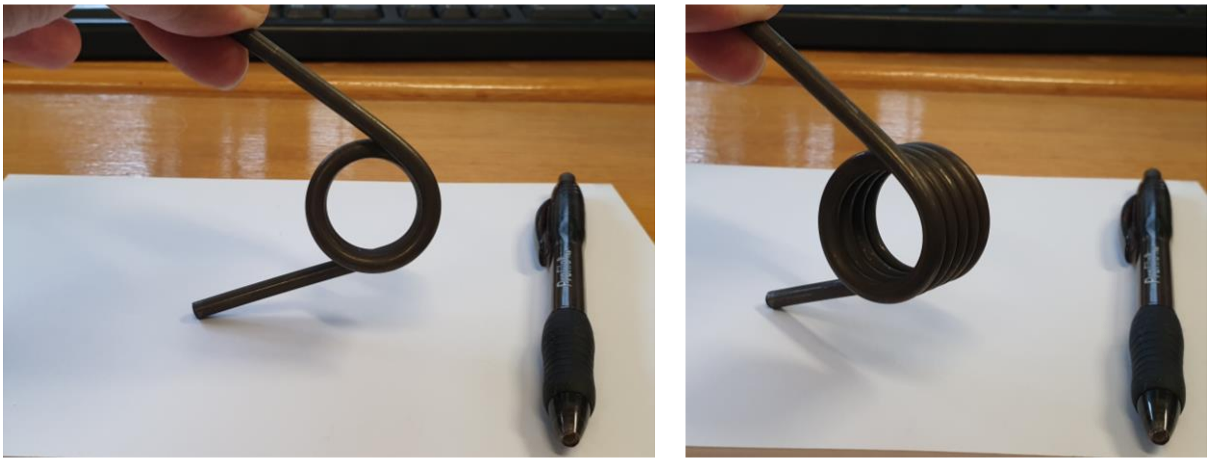

Figure 3.17 Fabricated mild steel rotational springs at The University of Melbourne.

3.4.5. Understanding the capability of scaled down Retaining wall model with rotational springs

The capability of the scaled down RW model founded on rotational springs has been evaluated for replication of the rotational response of the prototype RW founded on the rock-socketed pile foundation. Figure 3-18 shows the 2D plane strain finite element model of the scaled down RW, which was resting on four rotational springs. RW was modelled using a ***polycarbonate material*** with Young's modulus of 2.6 GPa and Poisson's ratio of 0.3. Backfill behind the RW is modelled as crushed rock (details presented in chapter 5). One dimensional compression test has been performed on crushed rock (details presented in section 5.2.2 of chapter 5), for finding the constrained modulus against given confinement, based on which the constrained modulus of crushed rock was estimated as 18.8 MPa (for backfill of prototype FE model). The Mohr Coulomb model was also used to model the hardening and softening behaviour of the backfill (crushed rock). Damping of the backfill is modelled with Rayleigh damping parameters. All details of geotechnical testing and material models are presented in chapter 5. Rotational springs underneath the RW have been modelled as elastic steel material using beam elements. Load deformation FE analyses have been performed on a single elastic steel spring to calibrate its rotational stiffness with the scaled rotational stiffness obtained from dimensional analysis (229 N-mm/degree). Contact between RW and backfill is simulated using frictional contact in the tangential direction with a friction coefficient of 0.56, and "hard contact" in the normal direction to avoid mesh penetration. The base of the finite element model was modelled as stiff steel material to avoid any base deformation.

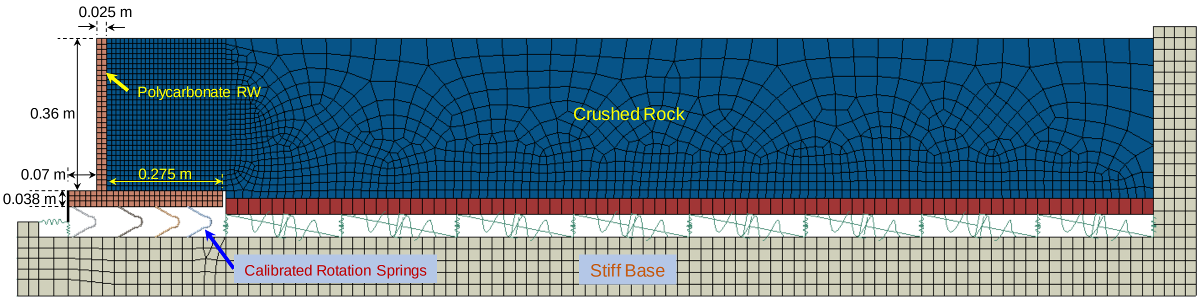

Figure 3-18 Scaled down 2D plain strain FE model of polycarbonate RW supported by four rotational springs.

Figure 3-19 shows a comparison of the rotation at the RW top observed from the prototype RW, which was founded on the rock-socketed pile foundation and the scaled down RW which was supported on rotational springs. Good agreement has been observed between rotation obtained from the prototype and scaled down RW model. Therefore, the scaled down RW with rotational springs can effectively replicate earthquake induced rotation of the prototype RW founded on a rock socketed pile foundation.

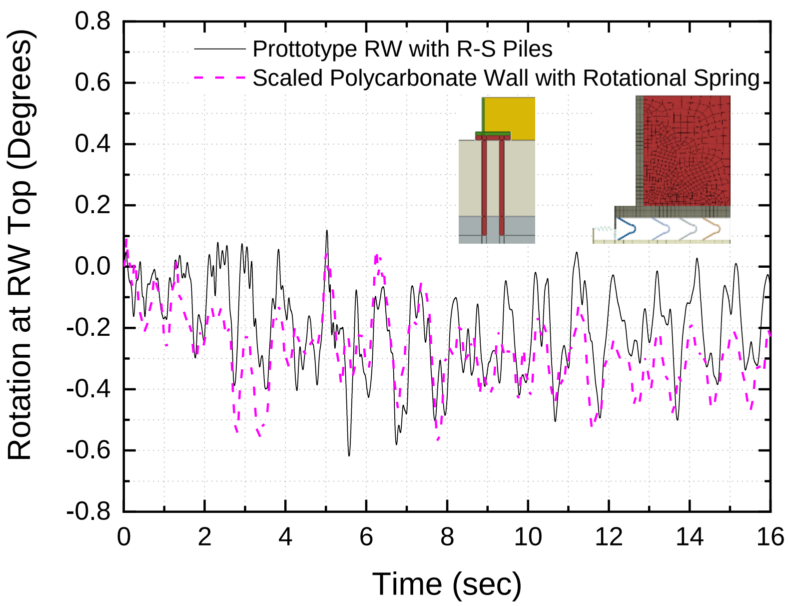

Figure 3-19 Comparison of rotation at RW top obtained from prototype RW (R-S pile foundation) and scaled RW (rotational springs).

3.5. Base restrained cantilever RW wall

As mentioned earlier, a true scaled down model is one which satisfies all similitude conditions. However, the accomplishment of all similitude criteria is difficult, especially for a 1-g scaled down model (Ertugrul and Trandafir, 2014). Moreover, distorted models are also useful for understanding the important responses of prototype structure, and to calibrate the numerical models with 1-g shake table tests (Prasad et al., 2004). Therefore, during the initial phase of a shaking table investigation, a base restrained Aluminum cantilever RW must be used (Kloukinas et al., 2015; Di Santolo et al., 2012; Keykhosropour and Lemnitzer, 2019). The primary purpose of using scaled down Aluminum RW is to facilitate observation of the displacement response of the base restrained cantilever RW against different base excitations and to observe free vibration response of the base restrained earth retaining structures along with amplification of the horizontal acceleration. Observations and skills achieved from the shaking table experiments have also been used to calibrate the FE model of base restrained cantilever RW. Details and findings of the shaking table experiments performed on base restrained cantilever RW are presented in chapter 4. Figure 3-20 shows the base restrained cantilever RW used for the first set of shaking table experiment. Details of the model fabrication and shaking table experiment has been presented in Chapter 4.

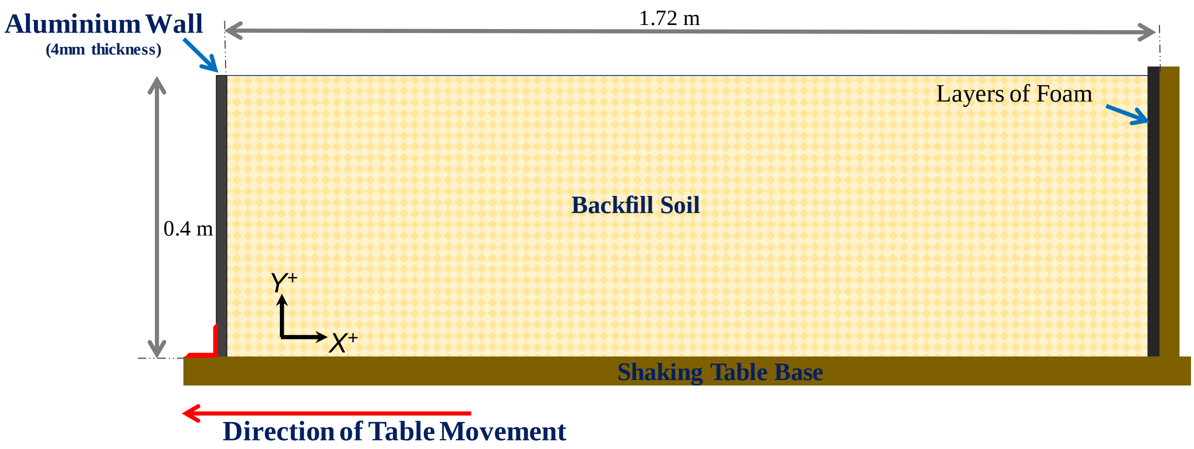

Figure 3-20 base restrained cantilever RW.

3.6. Chapter closure

Details of dimensional analyses have been presented for the scaling down of RW models. The capability of the scaled down RW model has been evaluated for replication of seismic response of full scale RW models. It was observed that a scaled down RW model could effectively replicate the seismic response of a full scale RW model. The capability of the torsional springs for replicating the rotational response of rock-socketed pile foundation has also been evaluated. It was found that rotational/ torsional springs can replicate the seismic rotation of the rock socketed pile foundation.

Chapter 4. THE SHAKING TABLE EXPERIMENT ON SCALED DOWN RETAINING WALL MODELS

4.1. Introduction

In order to understand the effects of earthquake actions on the earth retaining structures, a detailed shaking table experiment has been performed on scaled down retaining wall (RW) models. Primary objectives of the shaking table experiment include the study of free vibration response of RW, seismic displacement and rotational behaviour of RW, and amplification of horizontal acceleration in the backfill. The shaking table experiment has been performed on base restrained cantilever RW model and rotational base RW model, respectively. The crushed rock has been used to construct the backfill behind the scaled down RW models.

Free vibration response of the base restrained RW model has been investigated by conducting a series of pluck tests on them, based on which the natural periods of the scaled down RW model, and the shear wave velocity in the backfill was estimated. The earthquake response of scaled down RW models has also been investigated against different base excitations such as multiple pulses, synthetic and historical accelerograms. It was observed that the inertia of backfill profoundly influences the seismic performance of the scaled down RW models. Amplification of horizontal acceleration in backfill was also observed. Permeant displacement of the RW and settlement of backfill at the interface of RW and backfill was also observed.

4.2. Construction of the scaled down base restrained RW model

4.2.1. Fabrication of backfill container

The backfill material was contained by an assembly of 15 mm thick plywood sheets held firmly on the shaker table (Figure 1). To resemble the boundary conditions of a wide RW the plywood-backfill interface on the sides had a smooth finish (to minimise frictional interference from the sides) whereas the base of the backfill was covered by sand papers to prevent any sliding movement which is unlikely in real conditions. The back-face of the plywood assembly was covered by a 20 mm thick foam material to minimise wave reflections. The aforementioned features were consistent with those adopted in shaker table tests carried out by Watanbe et al. (2003). Figure 4-1c shows a photograph of the wooden container used to retain the backfill. The wooden container was constrained with the shaking table platform with the help of six 24 mm diameter bolts.

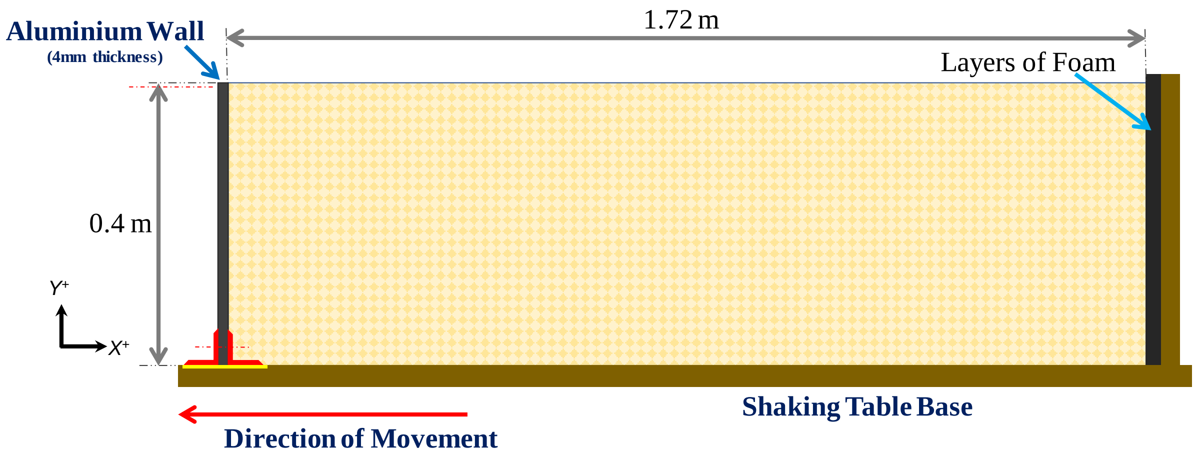

(a) Fabricated backfill container dimensions and wall position (not to scale).

(b) Sandpaper placed at wooden container base.

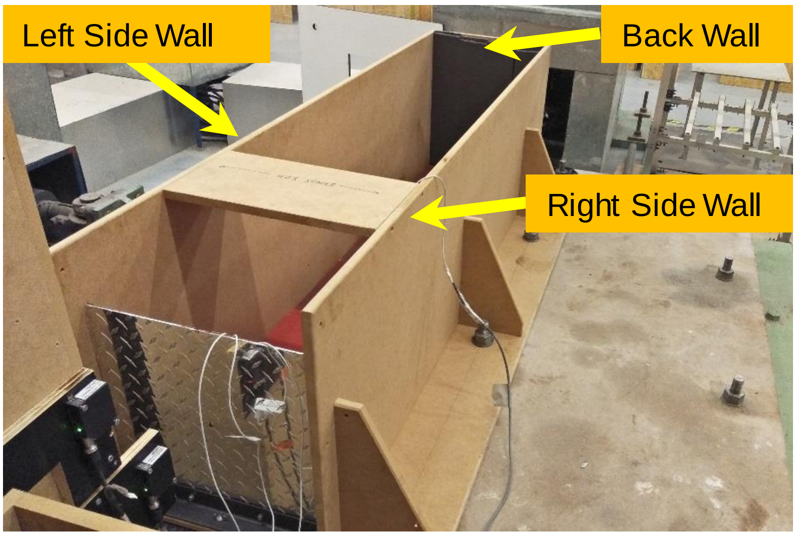

(c) Wooden Container with base restrained cantilever RW.

Figure 4-1 Details of the scaled down RW (base restrained) model fabrication.

4.2.2. Backfill construction behind the scaled down base restrained RW

Backfill plays an essential role in the seismic performance of earth retaining structures (Huang et al., 2009). In the present study, a detailed and rigorous shaking table experiment investigation has been carried out. Therefore, the selection of backfill type has been made based on easiness with backfill construction and classification. Crushed rock has been chosen as the backfill material for the scaled down RW models because of the easiness of compaction in achieving the desired dry density. This presents advantages in an experimental program involving repetitive shaking of the specimen. Thus, poorly graded backfill has been used in previous investigations (Munoz & Kiyota 2020; Earth Mechanics 2005). Figure 4-2a shows crushed rocks used for the backfill construction. Geotechnical classification and detailed geotechnical testing of backfill (crushed rock) have been presented in chapter 5. The sieve size analyses have been performed for gradation of the backfill. The maximum dry density of crushed rock was estimated as 1790 kg/m^3. It should be noted herein that the scaling of soil material in1-g environment highly depends on its modulus and in the case of backfill (retained medium), the constrained modulus has outmost importance (Monaco and Marchetti, 2004; Kim and Santamarina, 2008). The constrained modulus of soil depends on the degree of confinement and increases linearly with increasing confinement (Kim and Santamarina, 2008). A similar process has been used in section 3.3 of chapter 3, for scaling the constrained modulus of the backfill. The backfill behind the RW (base restrained) has a uniform height of 0.4 m. The backfill has been constructed in four layers with 100 mm single layer height (figure 4-2b). The required weight of the backfill has been calculated for each soil layer against the maximum dry density of the soil (1790 kg/m^3). The crushed rock then dropped from a constant height for all layers to achieve a uniform soil distribution. Every layer of backfill was compacted with the help of the shaking table in order to level the backfill surface and to compact the backfill up to its maximum dry density. Wooden planks were used to support the RW face during compaction of the backfill. Figure 4-2 (c) shows the photograph of the fabricated scaled down RW (base restrained) model. It should be noted herein that deformation of RW and over compaction of backfill has been examined after completion of every test. Moreover, backfill has been reconstructed once over compaction and deformation of RW has been observed.

(a) crushed rock used as the backfill (b) Placement of backfill in the model container

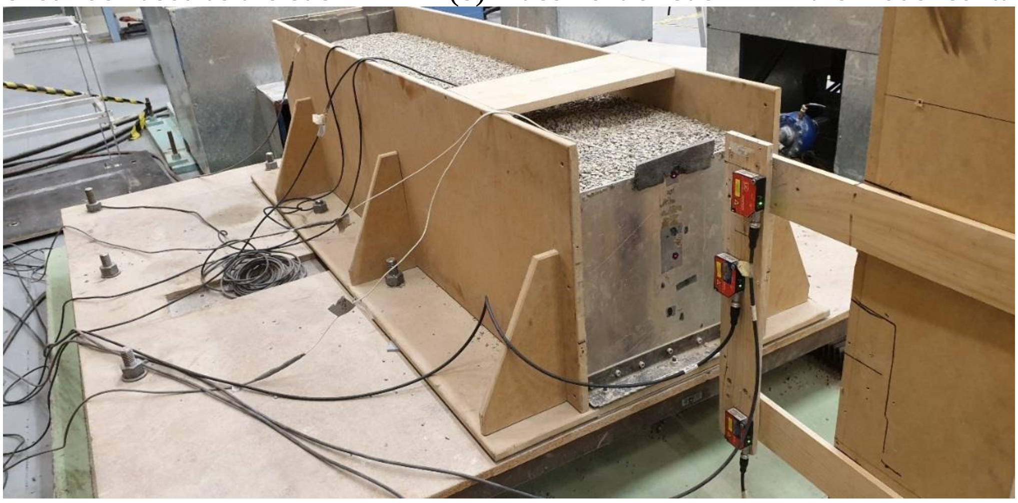

(c) Fabricated scaled down RW (base restrained) model.

Figure 4-2 Fabricated scaled down RW (base restrained) model, placed on the shaking table at The University of Melbourne.

4.2.3. The shaking table experiment at The University of Melbourne

The shaking table facility of The University of Melbourne has been used for performing the shaking table experiments on the scaled down RW models. The shaking table platform was 2 m x 2 m size with a maximum load capacity of 2 tones. The shaking table has two actuators, for uni-directional or bi-directional base excitations, with 180 mm maximum stroke capacity. It should be noted herein that only uni-directional base excitation has been considered in the present study. The hydraulic pump system was used to supply power and to control the movement of the actuators. Figure 4-3 shows the shaking table facility at The University of Melbourne.

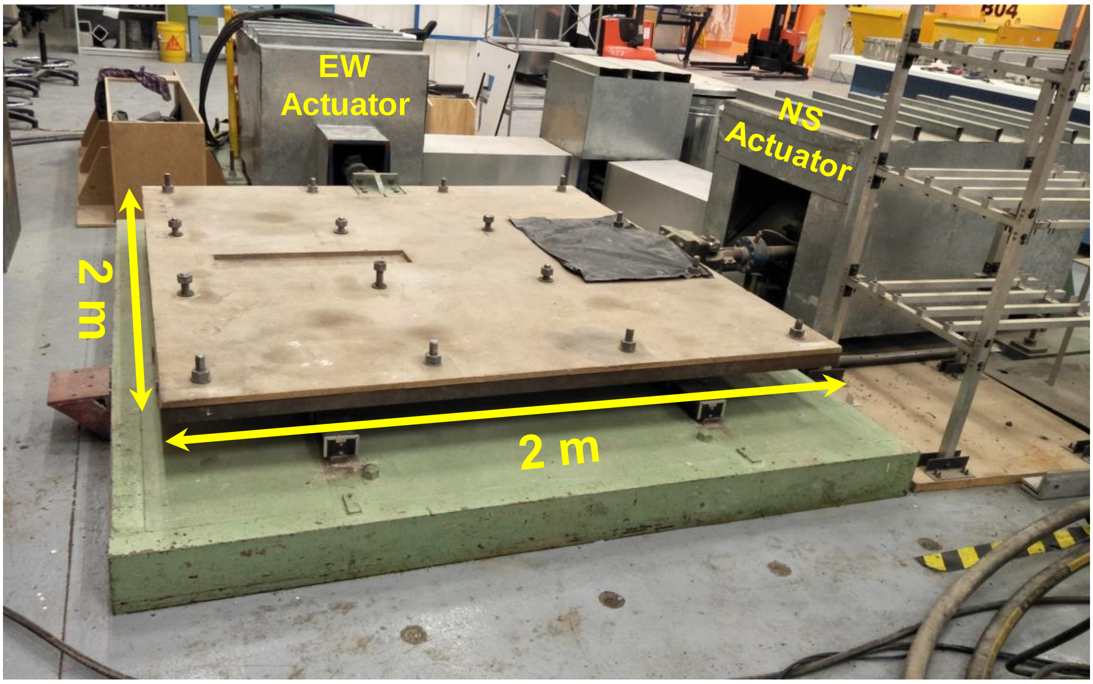

Figure 4-3 The shaking table facility at The University of Melbourne.

4.2.4. Instrumentation setup for the shaking table experiment (base restrained RW)

Instrumentation setup was crucial in order to capture dynamic response of scaled down models during the shaking table experiment. Intelligent laser-optical displacement transducers were used to capture the displacement of the RW and the shaking table base. Uniaxial, biaxial and triaxial accelerometers have been used to capture acceleration of the RW and the backfill. Figure 4-4 shows the locations of the laser transducer and accelerometers.

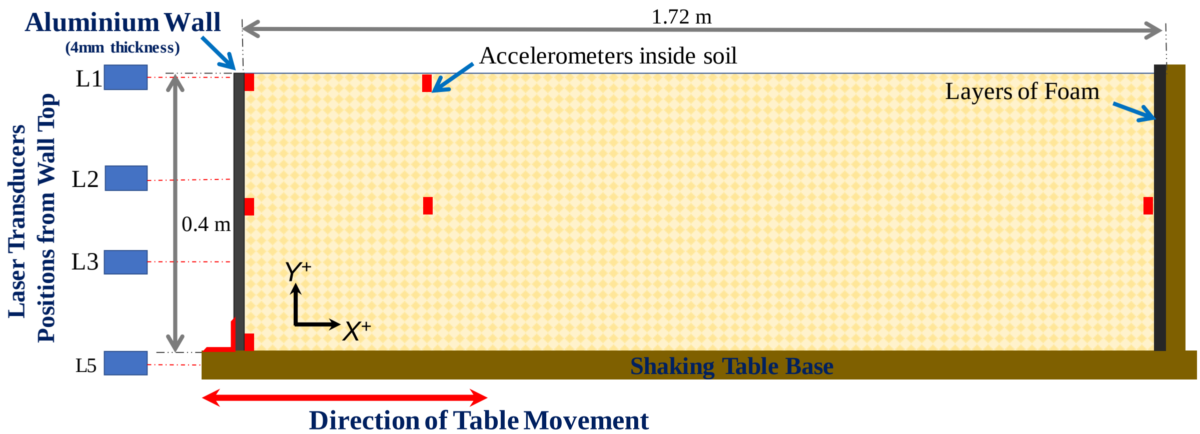

Figure 4-4 Locations of laser transducer and accelerometers in the scaled down RW (base restrained) model.

4.2.5. Intelligent laser-optical displacement transducers

Intelligent laser-optical displacement transducers (laser transducers) of 20 mm, 100 mm, 200 mm and 600 mm range were used for capturing the displacement of the RW and the shaking table base. The choice of the displacement range (laser type) depends on the amplitude of the applied motion. The sampling frequency of laser transducers has been kept at 750 Hz, to ensure high accuracy of captured displacement response of the RW. Calibrations for all laser transducers have been performed prior to conducting the shaking table experiments, for ensuring accurate output displacement. Figure 4-5 shows the photograph of the laser transducers used in the present study.

Figure 4-5 Laser transducer used for capturing displacement response of scaled down RW model.

4.2.6. Uni-axial and Tri-axial accelerometers

Uni-axial and tri-axial accelerometers have been used to capture the acceleration response of the RW and the backfill. Three uni-axial accelerometers were attached with RW back face (backfill side) at RW base, middle and top respectively. Two uni-axial accelerometers were inserted into the backfill, 300 mm away from the RW, at the height of 200 mm and 400 mm (backfill top) respectively. One triaxial accelerometer was placed at the end of the backfill (1.72 m away from RW) at height of 200 mm, for observing the reflection of stress waves from the backend of the wooden container. Measurement range of all accelerometers was +/- 5g, which was enough for the shaking table experiments conducted on the scaled down RW models. The sampling frequency of accelerometers was kept at 1000 Hz, to ensure capturing of necessary accelerations of the scaled down RW and the backfill. Figure 4-6 shows photographs of accelerometers used in the shaking table experiments.

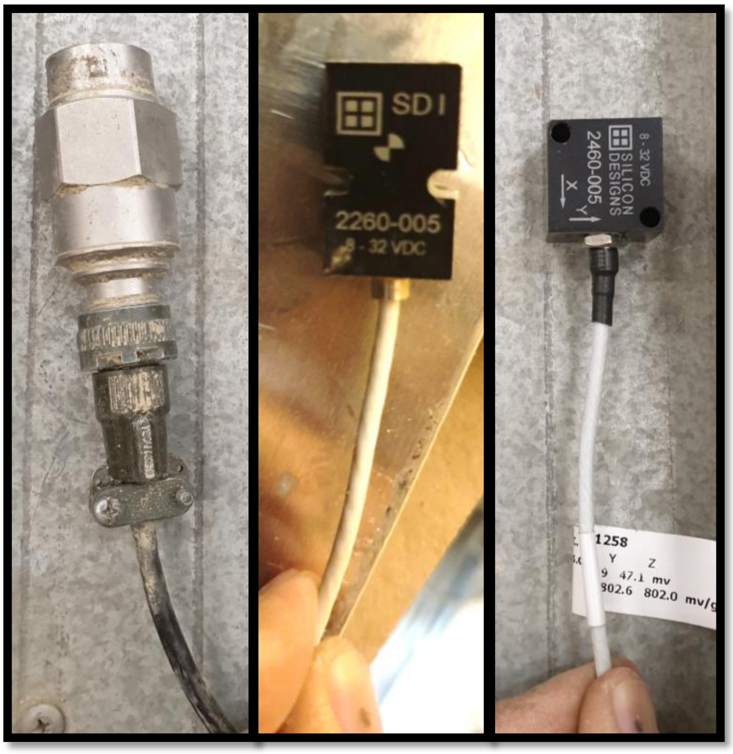

Figure 4-6 Uniaxial (left side two) and triaxial accelerometers (right side) used for capturing acceleration.

4.3. Pluck Test on scaled down RW (base restrained) model

A series of pluck tests were performed on the scaled down RW (base restrained) model. The shaking table facility was used to generate pulses for the pluck tests. Figure 4-7 shows pulses used for the pluck tests and the direction of movement of the shaking table. Laser transducers and accelerometers were used for capturing the displacement and acceleration of the scaled down RW (base restrained). A high-speed camera was also been used for capturing the slow motion movement of the RW and the backfill.

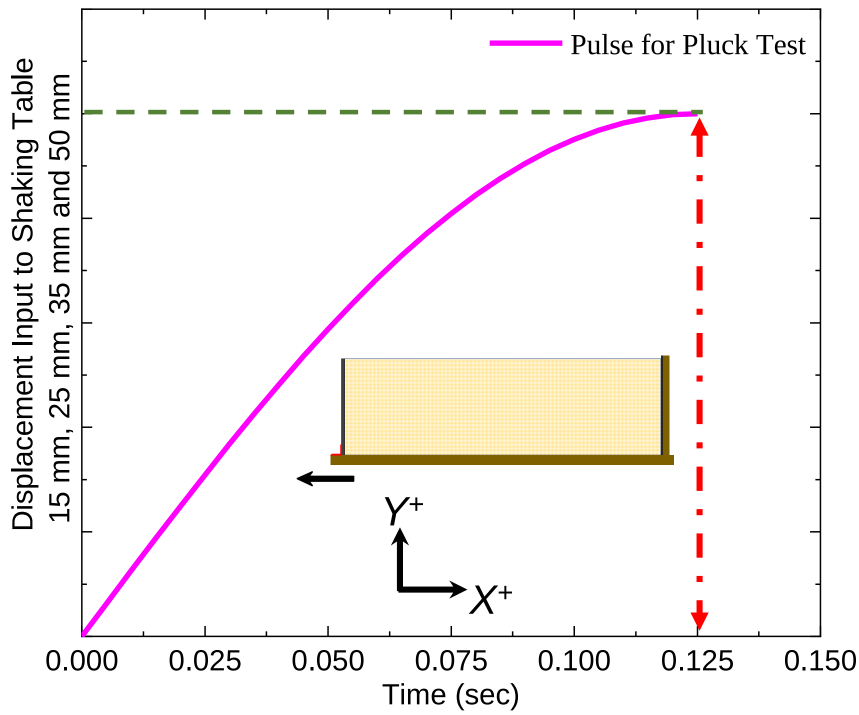

Figure 4-7 Quarter cycle pulse used for pluck test on scaled down RW (base restrained) model.

4.3.1. Displacement behaviour of the scaled down RW (base restrained) model during the pluck test

Figure 4-8 to 4-11 shows the absolute and relative (to base) displacement time histories of the base restrained cantilever RW for different pluck tests. The following formulation has been used for finding the relative displacement at the top of the RW.

$$\Delta(t)_{\text{relative}} = \Delta(t)_{\text{Retaining wall Top}} - \Delta(t)_{\text{Retaining wall Base}} \tag{4.1}$$

The first pluck test was performed using a quarter cycle sine pulse of 15 mm maximum in amplitude and 0.125 sec in duration, followed by a series of three similar pulses of 25 mm, 35 mm and 50 mm in amplitude and 0.125 sec in duration respectively. Increase in relative displacement (towards the top of the RW) was observed with increasing pulse amplitude. A hike in the relative displacement at the top of the RW was also observed during the end phase of the applied pulse. Separation of the RW from the backfill was also observed during this phase. The pluck tests with 15 mm, 25 mm, 35 mm and 50 mm maximum amplitude shown a maximum relative displacement to RW base (Δ_R) = 1.26 mm (0.32H%), 3.09 mm (0.77H%), 7.23 mm (1.81H%) and 8.35 mm (2.09H%) respectively.

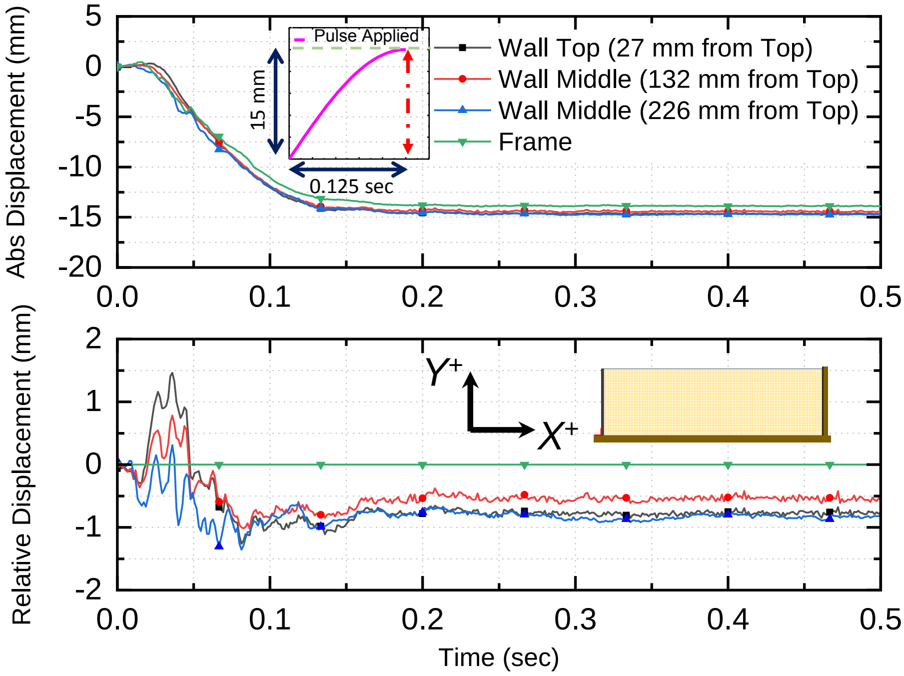

Figure 4-8 Displacement time history for pluck test (15 mm maximum amplitude), at various heights of scaled down RW (base restrained).

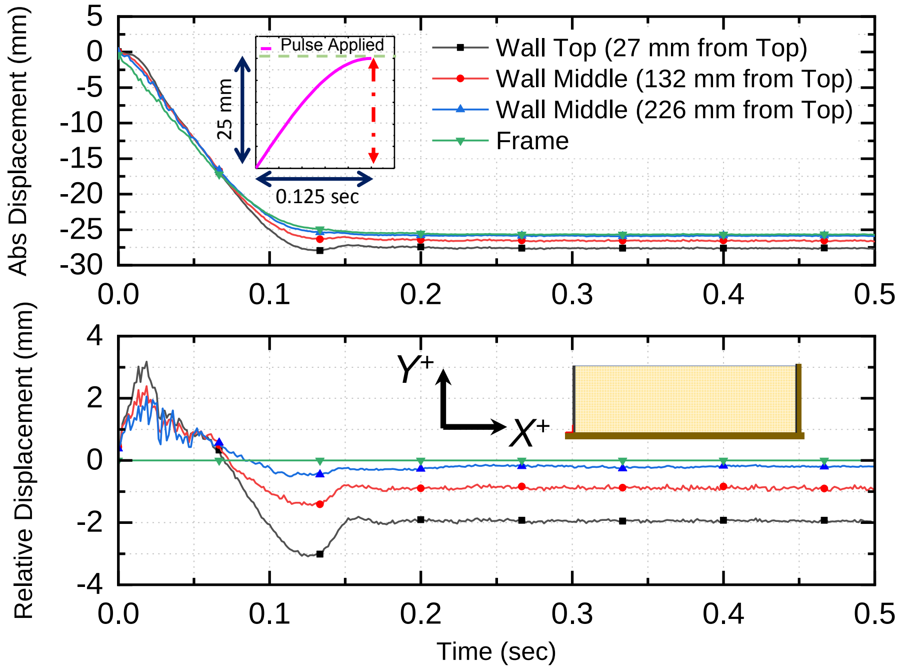

Figure 4-9 Displacement time history for pluck test (25 mm maximum amplitude), at various heights of scaled down RW (base restrained).

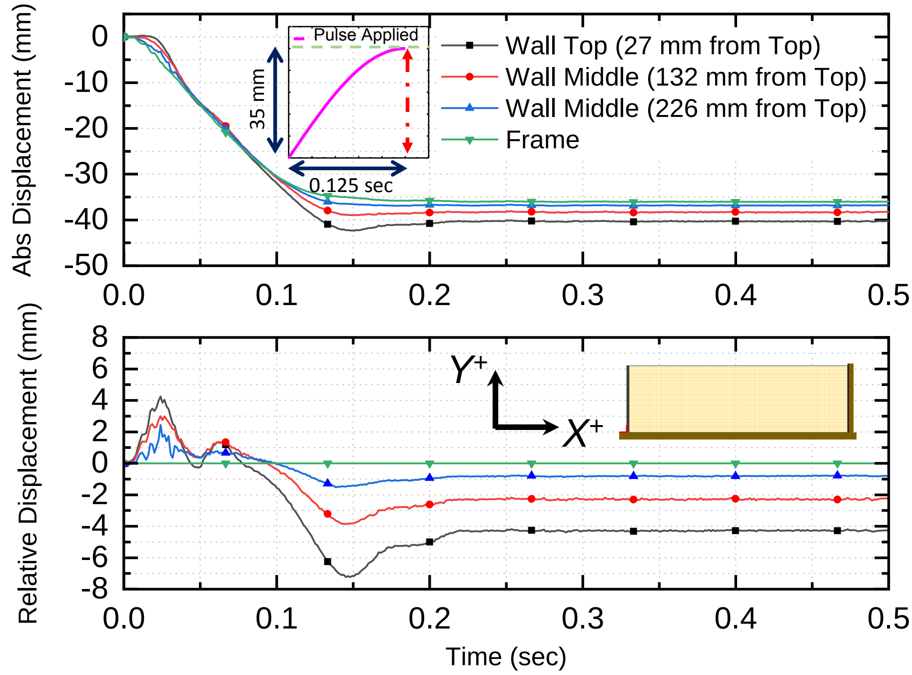

Figure 4-10 Displacement time history for pluck test (35 mm maximum amplitude), at various heights of scaled down RW (base restrained).

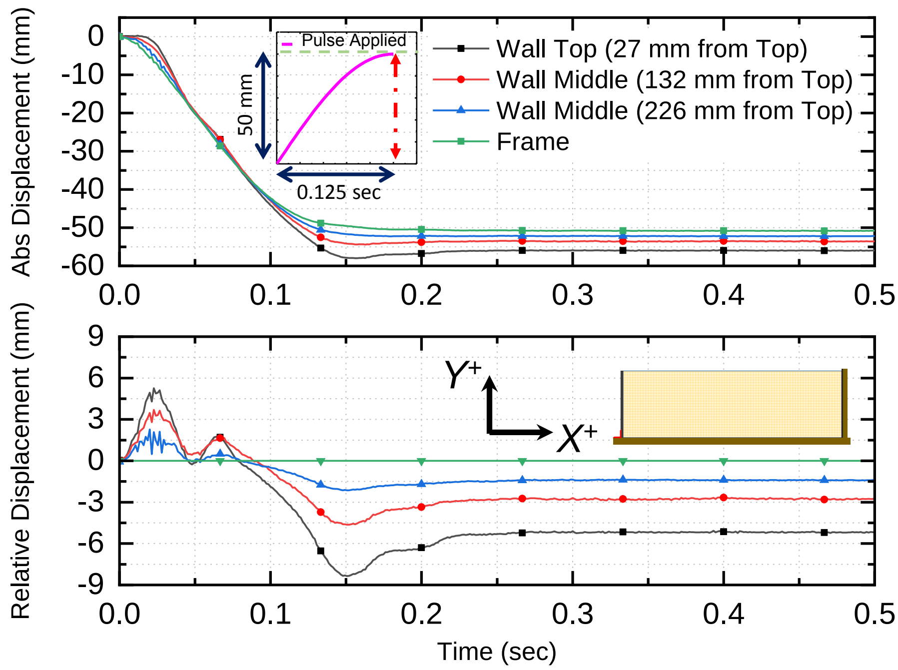

Figure 4-11 Displacement time history for pluck test (50 mm maximum amplitude), at various heights of scaled down RW (base restrained).

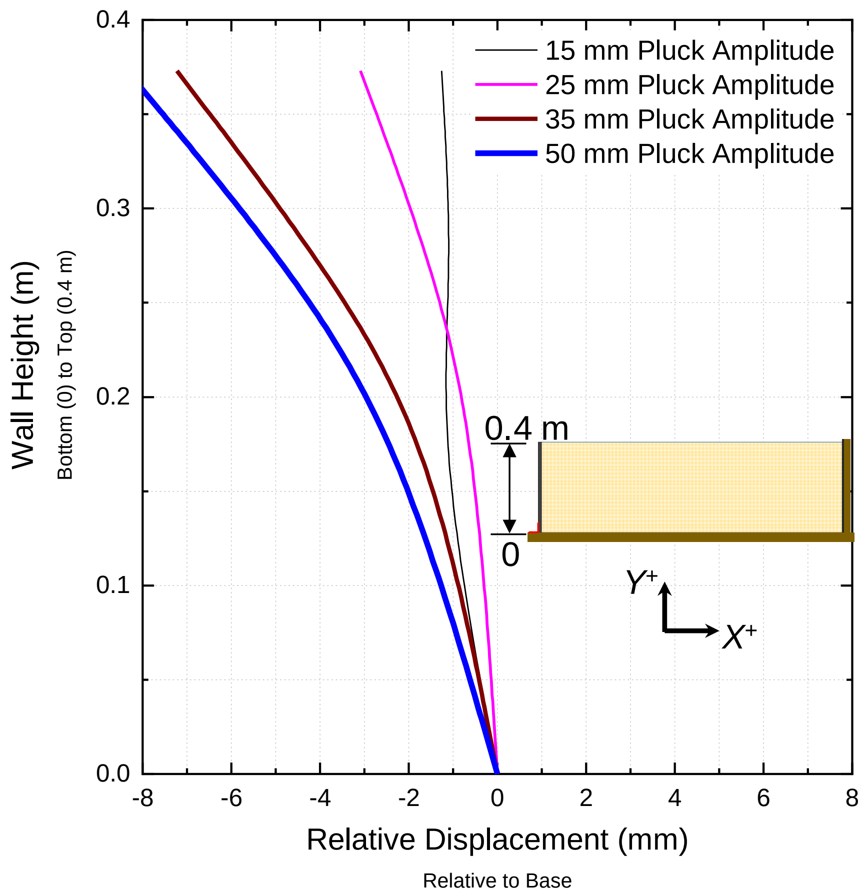

Figure 4-12 Relative displacement (to base) along the scaled down RW (base restrained) height, observed during different pluck tests.

Figure 4-12 shows relative displacement along the RW height (*H*) for different pluck tests. Linear deflection pattern was observed up to 0.15 m RW height (from base), beyond which the curvilinear displacement pattern was observed.

4.3.2. Free vibration response of the scaled down RW (base restrained) model

Free vibration response of the scaled down RW (base restrained) model has been studied based on pluck test results. Displacement and acceleration of the base restrained RW captured during the pluck test have been input into frequency domain analyses. It should be noted herein that the frequency domain analyses have been performed on the free vibration response of the base restrained RW. Figure 4-13 shows the loading and free vibration phase of a sample pluck test performed during the shaking table experiment.

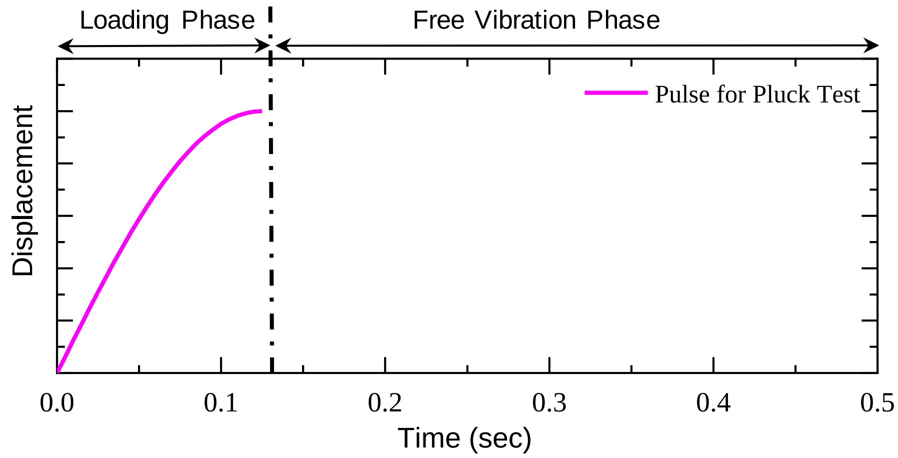

Figure 4-13 Loading and free vibration phase for a sample pluck test.

The natural periods/frequencies of base restrained RW have been estimated based on frequency domain analyses results. Figure 4-14 shows the result of frequency domain analysis and the observed natural frequencies of the RW model for 35 mm and 50 mm amplitude pluck tests, respectively. Based on the frequency domain analysis the 1st natural frequency for the RW model was observed as 19.79 Hz and 20.02 Hz for 35 mm and 50 mm amplitude pluck test, respectively. The 2nd natural frequency for the RW model was observed as 39.94 Hz and 39.06 Hz for 35 and 50 mm amplitude pluck test, respectively.

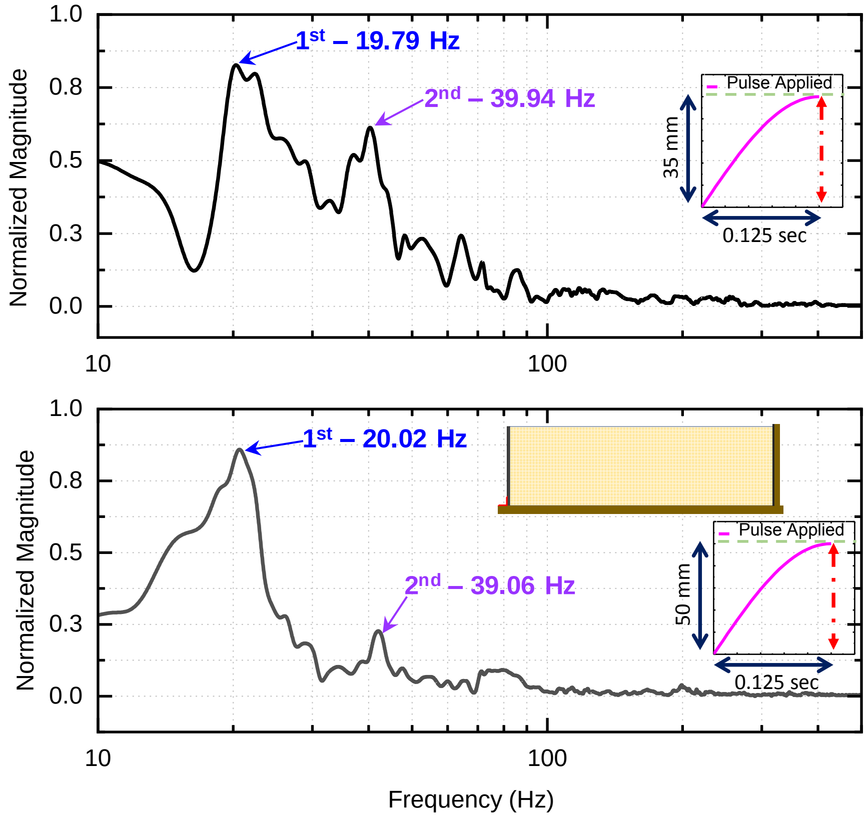

Figure 4-14 Frequency domain analysis for 35 mm and 50 mm amplitude pluck tests.

Based on the pluck test results, the natural frequencies of the scaled down RW (base restrained) was estimated around 20 Hz (1st mode) and 40 Hz (2nd mode).

4.3.3. Amplification of the horizontal acceleration based on pluck test

Figure 4-15 shows the response spectral acceleration (RSA) of the horizontal acceleration (A_x), for the free vibration phase. A_x was captured using uni-axial accelerometers placed at the base of the backfill, at the middle (0.2 m above base) and at the top (0.4 m above base). The positions of the uniaxial accelerometers used for capturing the A_x have been shown in the inset diagram of figure 4-15. Amplification of horizontal accelerations was observed during the pluck tests. Maximum amplification of the horizontal acceleration at the top of the backfill was observed to be 52 %, 195 % and 116 % of base A_x for 15 mm, 25 mm, and 35 mm amplitude pluck test, respectively. It should be noted herein that for the 50 mm amplitude pluck test the uni-axial accelerometer placed at the top of the backfill accidentally titled downwards into the backfill and hence could not capture the horizontal acceleration. Highly non-linear behaviour of the backfill was observed during the pluck test of the RW model.

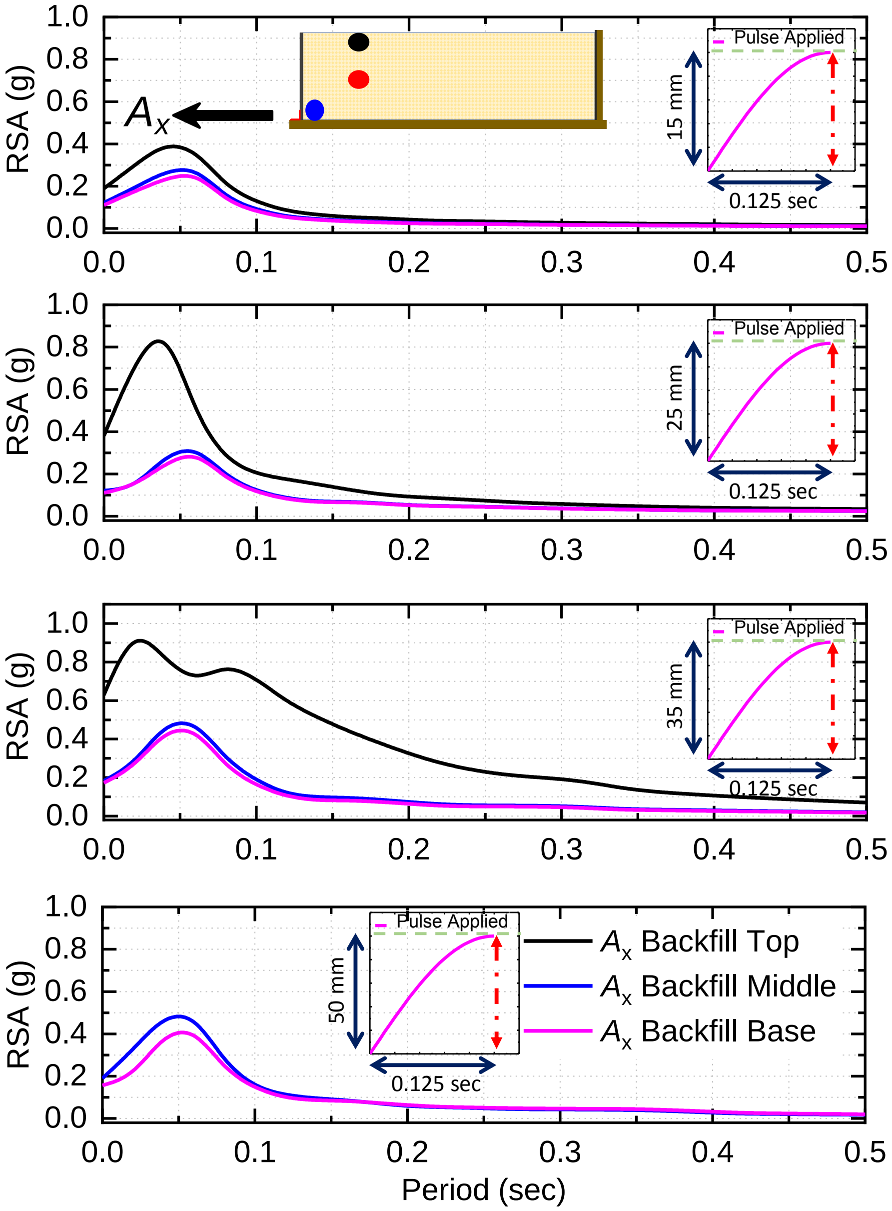

Figure 4-15 Response spectral acceleration (RSA) at backfill base, middle and top for different pluck tests.

4.4. The shaking table experiment using the half cycle sine pulse, one cycle sine pulse and multiple pulses

In order to understand the seismic behaviour of the scaled down RW (base restrained) model, different pulses have also been used as base excitations. Moreover, pulses are often used by researchers to understand the seismic behaviour of scaled down models. Pulses can be used to reduce high stiffness effects of distorted models, and meaningful structural response could be obtained (Yazdandoust, 2017). Figure 4-16 shows the half cycle sine pulses of 0.25

sec in duration with amplitude of 20 mm (left) and 50 mm (right), respectively. Figure 4-17 shows one cycle sine pulse of 0.5 sec duration with 35 mm (left) and 50 mm (right) maximum amplitude, respectively. Pulses shown in figure 4-16 and 4-17 were applied to the shaking table platform.

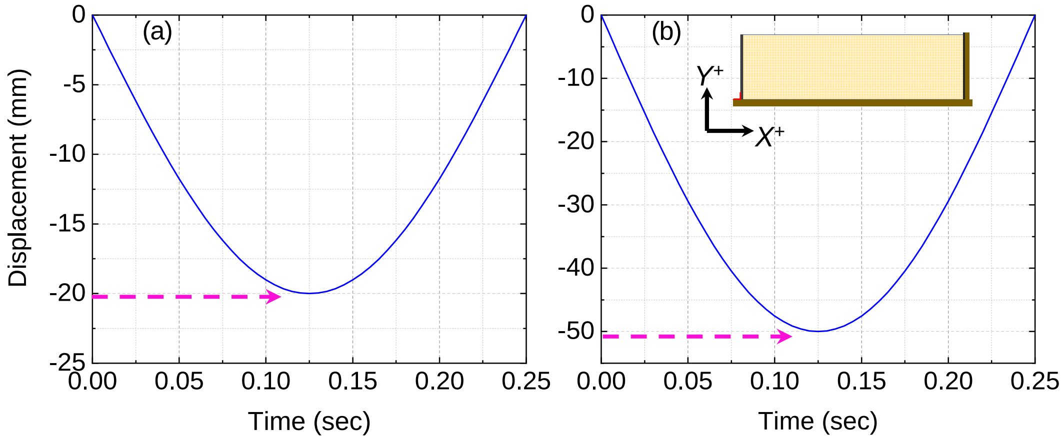

Figure 4-16 Applied half cycle sine pulse with 20 mm (left) and 50 mm (right) maximum amplitudes and 0.25 sec duration.

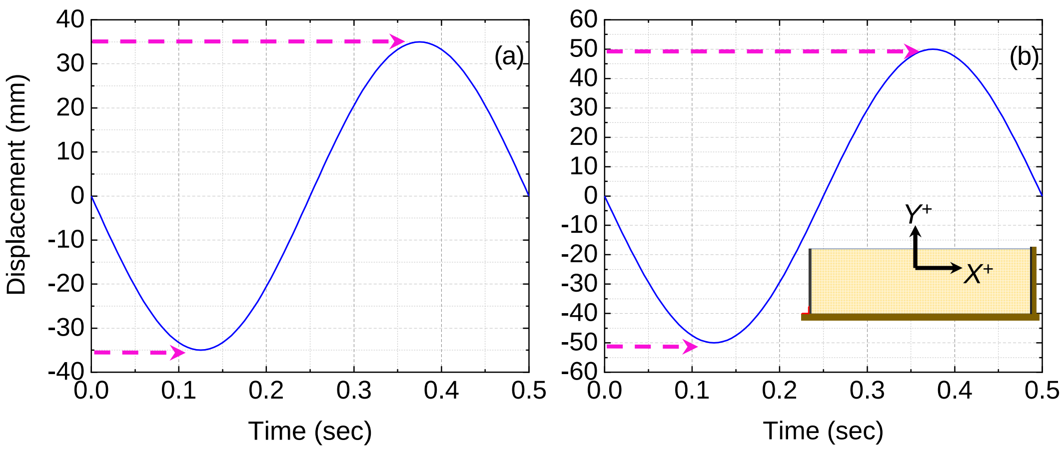

Figure 4-17 Applied one cycle sine pulse with 35 mm (left) and 50 mm (right) maximum amplitudes and 0.5 sec duration.

4.4.1. Displacement response of the scaled down RW (base restrained)model against half cycle and single cycle sine pulse

Figure 4-18 shows relative (to base) displacement time history for both half cycle sine pulses at various RW heights. The input pulse has also been shown in the inset diagram of figure 4-18a and 4-18b, respectively. Maximum outward displacement (wall moves away from the soil) was observed at the top of scaled down RW (base restrained). The outward displacement of RW increases up to 0.125 sec (half duration of input pulse – active phase).

A gap formation has also been observed at the interface of the RW and the backfill. Soon after the gap formation, the backfill fell on the RW, thereby increasing the outward wall displacement. During the second half phase of the applied pulse when the RW started moving towards the backfill (passive phase), the high inertia forces from the backfill pushed the RW away from it. Residual displacement (increasing towards the RW top) at the end of 20 mm amplitude half cycle sine pulse was also observed. The boundary effects have been observed for the 50 mm amplitude half cycle sine pulse, and no residual displacement was observed. The pulse tests with half cycle sine pulse of 20 mm and 50 mm maximum amplitude shown a maximum relative displacement at RW top (relative to RW base) (Δ_R) = 1.87 mm (0.47H%) and 10.73 mm (2.68H%), respectively.

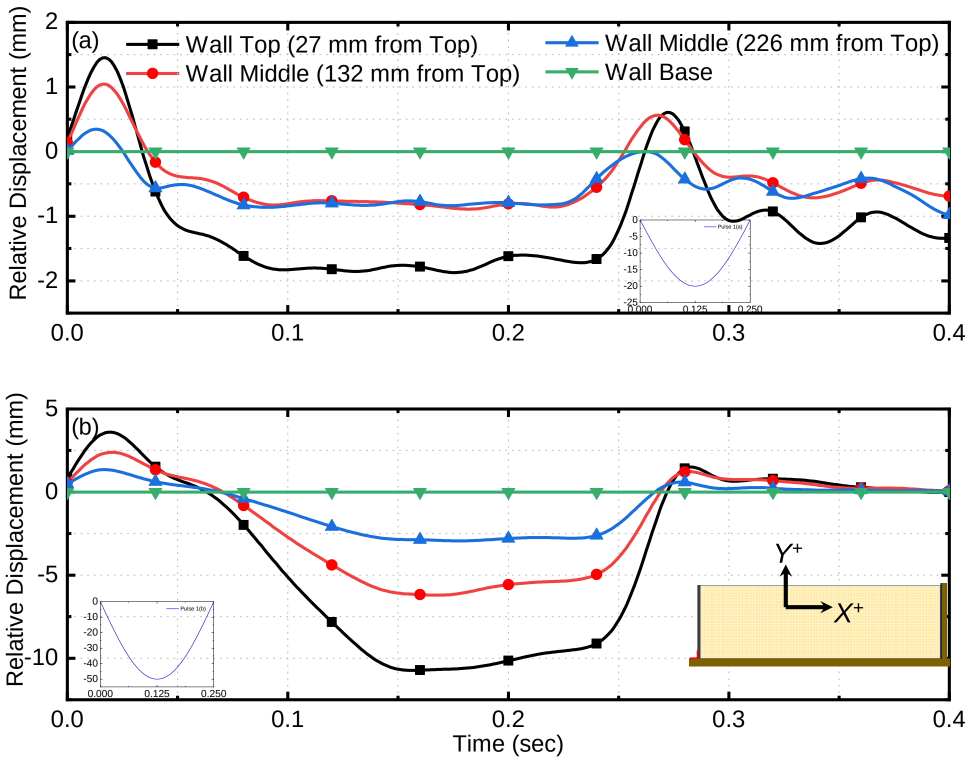

Figure 4-18 Relative (to base) displacement time history at various RW (base restrained) heights, when subjected to half cycle sine pulses (20 and 50 mm maximum amplitude).

Figure 4-19 shows the relative displacement time history at various RW heights for single cycle sine pulse of 35 mm and 50 mm maximum amplitude, respectively. Increasing the amount of relative displacement up the height of the RW was observed for both the 35 mm and 50 mm amplitude one cycle sine pulse. The gap formation between the RW and the backfill was also observed during the initial phase of the wall movement (active phase). During the passive phase (the wall moving back towards the backfill) due to the inertia of the backfill, higher relative displacement (active state) was observed for the one cycle pulses. Moreover, residual displacement (increasing up the height of the RW) was also observed for the one cycle sine pulses. The pulse tests with single cycle sine pulse of 35 mm and 50 mm maximum amplitude shown a maximum relative displacement at RW top (relative to RW base) (Δ_R) = 11.44 mm (2.86H%) and 13.48 mm (3.37H%), respectively.

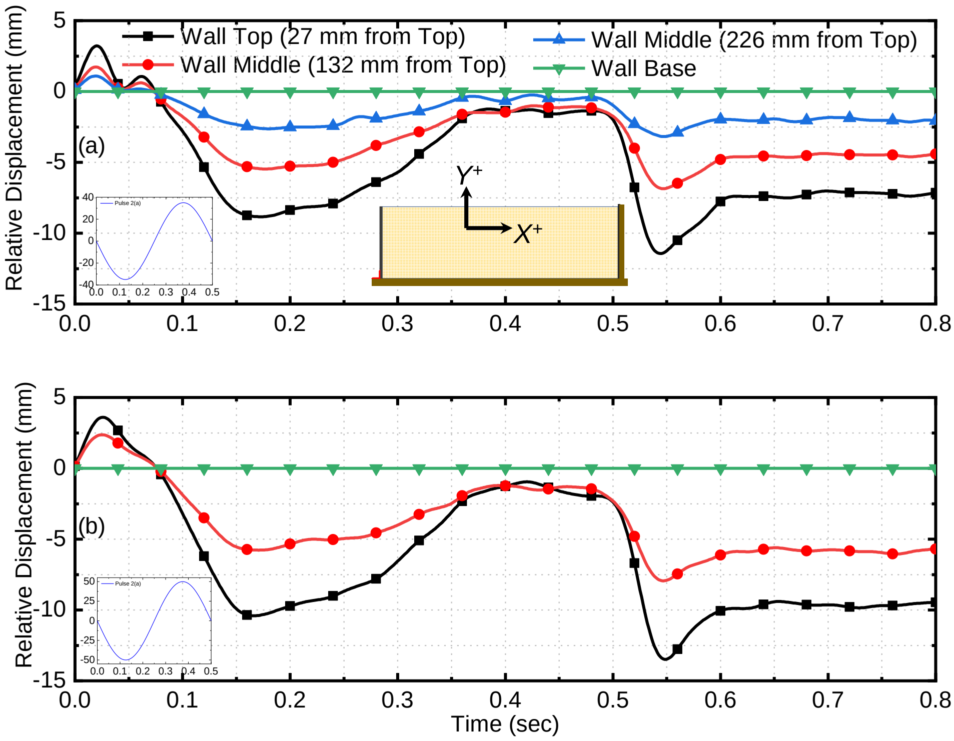

Figure 4-19 Relative (to base) displacement time history at various RW (base restrained) heights, when subjected to one cycle sine pulses (35 and 50 mm maximum amplitude).

4.4.2. Response of scaled down RW (base restrained) model against multiple pulses

Pulses are often used to evaluate the earthquake response of scaled down models during the shaking table investigations (Yazdandoust, 2017). The formulation shown in equation 4.2, has been used for the generation of different types of pulses (Yazdandoust, 2017).

$$\ddot{u}(t) = \sqrt{\beta_{\mathrm{i}} e^{-\alpha_{\mathrm{i}} t} t^{\xi}} Sin(2\pi f t) \tag{4.2}$$

Earthquake response of scaled down RW (base restrained) model has been analyzed against two base excitations with PGA = 0.75g and 0.95g, respectively. Multiple pulses (3 Hz frequency) have been applied at the RW base. Figure 4-20 shows multiple pulses that were used to excite the scaled down RW (base restrained) model. The first pulse has a 20 mm maximum amplitude, and the second pulse has a 25 mm maximum amplitude.

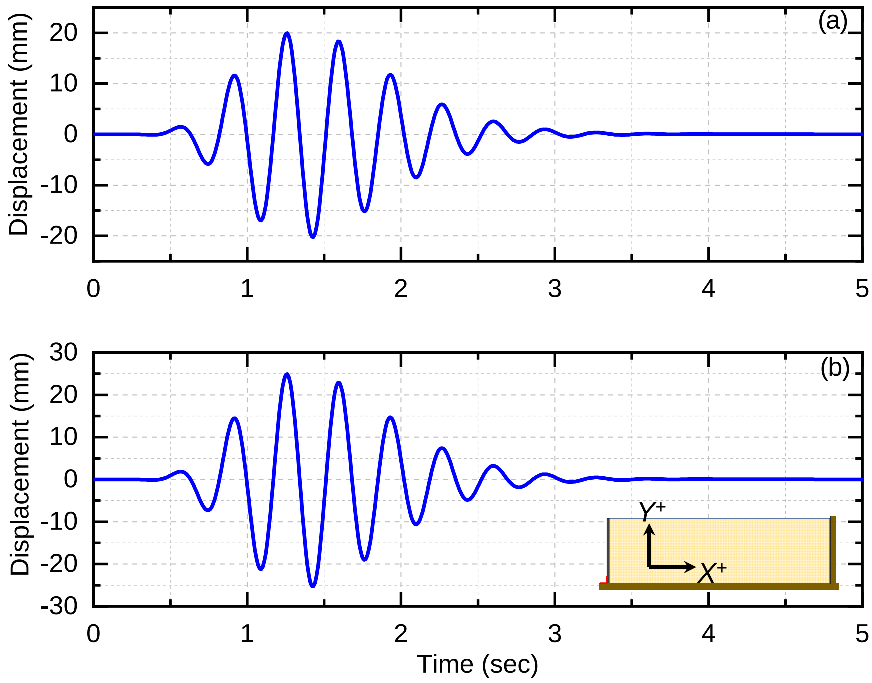

Figure 4-20 Applied multiple pulses on scaled down RW (base restrained) model during the shaking table experiment.

Figure 4-21 shows the relative displacement time history at RW top, middle and base. Higher relative and residual displacement were observed for the pulse with 25 mm maximum amplitude. Active state movement was observed for both set of multiple pulses, which further highlights the importance of understanding active state seismic response of the base restrained earth retaining structures. Testing's with multiple pulses of 20 mm and 25 mm maximum amplitude shown a maximum relative displacement at RW top (relative to RW base) (Δ_R) = 7.55 mm (1.89H%) and 10.24 mm (2.56H%), respectively.

Figure 4-22 shows the RSA for both multiple pulses. Amplification of horizontal acceleration was also observed in both cases. Pulse with 20 mm maximum amplitude (as shown in figure 4-22(a) shows 19 % amplification in the horizontal acceleration of the backfill at the top and 6 % amplification at the middle (relative to the base), respectively. Pulse with 25 mm maximum amplitude (as shown in figure 4-22(b) shows 23 % amplification in the horizontal acceleration at the top and 8 % amplification at the middle (relative to the base), respectively.

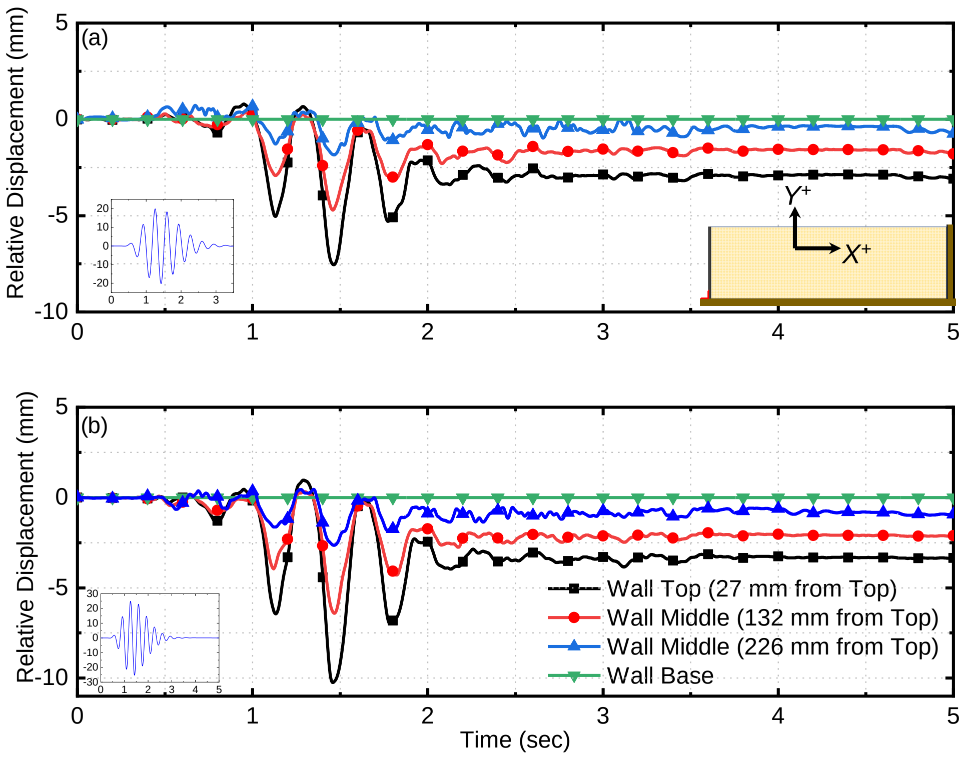

Figure 4-21 Relative (to base) displacement time history at various RW heights against applied multiple pulses (20 mm and 25 mm maximum amplitude, 3 Hz frequency).

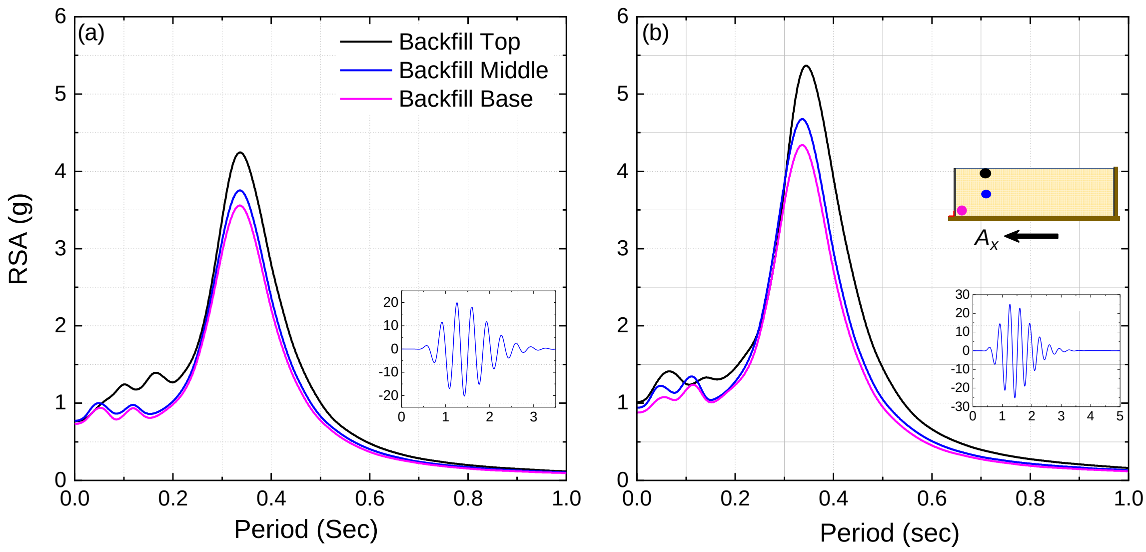

Figure 4-22 RSA of horizontal acceleration at backfill top, middle and bottom for applied multiple pulses.

4.5. Earthquake response of the scaled down RW (base restrained) model

4.5.1. Ground motion selection

Selection of ground motions for shaking table input excitation was an important task. It was decided to use a combination of synthetic (artificial) and historical accelerograms. Artificial accelerograms were obtained on rock outcrop; using program GENQKE (Lam, 1999). The program GENQKE assumes a seismic source model for different magnitude (M_g) and distance (R) combinations of the intraplate region. Artificial accelerograms have been proven to be very useful for analyzing the seismic response of structures located in a low to moderate seismicity regions like Australia (Lumantarna et al. 2010, Shahi et al. 2017). Five artificial accelerograms (in the order of increasing Peak Ground Acceleration) have been selected as input ground motions for the shaking table experiments. Figure 4-23 shows acceleration time history for the artificial accelerograms.

Earthquake response of the scaled down RW (base restrained) model has also been investigated against historical accelerograms recorded at the rock outcrop. The PEER ground motions database was used for searching historical earthquake records with reverse fault mechanism, to represent seismological scenario identical to Australian earthquakes (Brown and Gibson, 2004a; Amirsardari et al., 2017). In order to search accelerograms on the rock outcrop, the shear wave velocity (V_{SH}) range was kept from 600 to 1800 m/sec. For all accelerograms, source to site distant was kept at 5 km (minimum) to 50 km (maximum). Figure 4-24 shows acceleration time histories for all five historical accelerograms (in the order of increasing Peak Ground Acceleration).

It should be noted herein that the displacement-controlled movement has been chosen for the shaking table actuators. Therefore, the displacement time history of accelerograms has been used for the input motion. The time and displacement domains of all accelerograms have been scaled down for satisfying the similitude criteria (Huang et al., 2009). Scaling in the time-domain is explained in section 3.3 of chapter 3.

Three sets of shaking table experiments were conducted with earthquake base excitations. The first set of experiments has been conducted with five artificial and five historical accelerograms ($\boldsymbol{\lambda}_{\Delta t} = \sqrt{\boldsymbol{\lambda}_{l}}$ & $\boldsymbol{\lambda}_{l} = \mathbf{10}$). The second and third set of shaking table experiments has been performed for five historical accelerograms with reduced time-steps ($\boldsymbol{\lambda}_{\Delta t} = \mathbf{2}\sqrt{\boldsymbol{\lambda}_{l}}$ & $\boldsymbol{\lambda}_{l} = \mathbf{10}$ & $\boldsymbol{\lambda}_{\Delta t} = \mathbf{4}\sqrt{\boldsymbol{\lambda}_{l}}$ & $\boldsymbol{\lambda}_{l} = \mathbf{10}$). Reduced time step accelerograms were more intense and can be used to excite high stiffness structures such as scaled down miniature models.

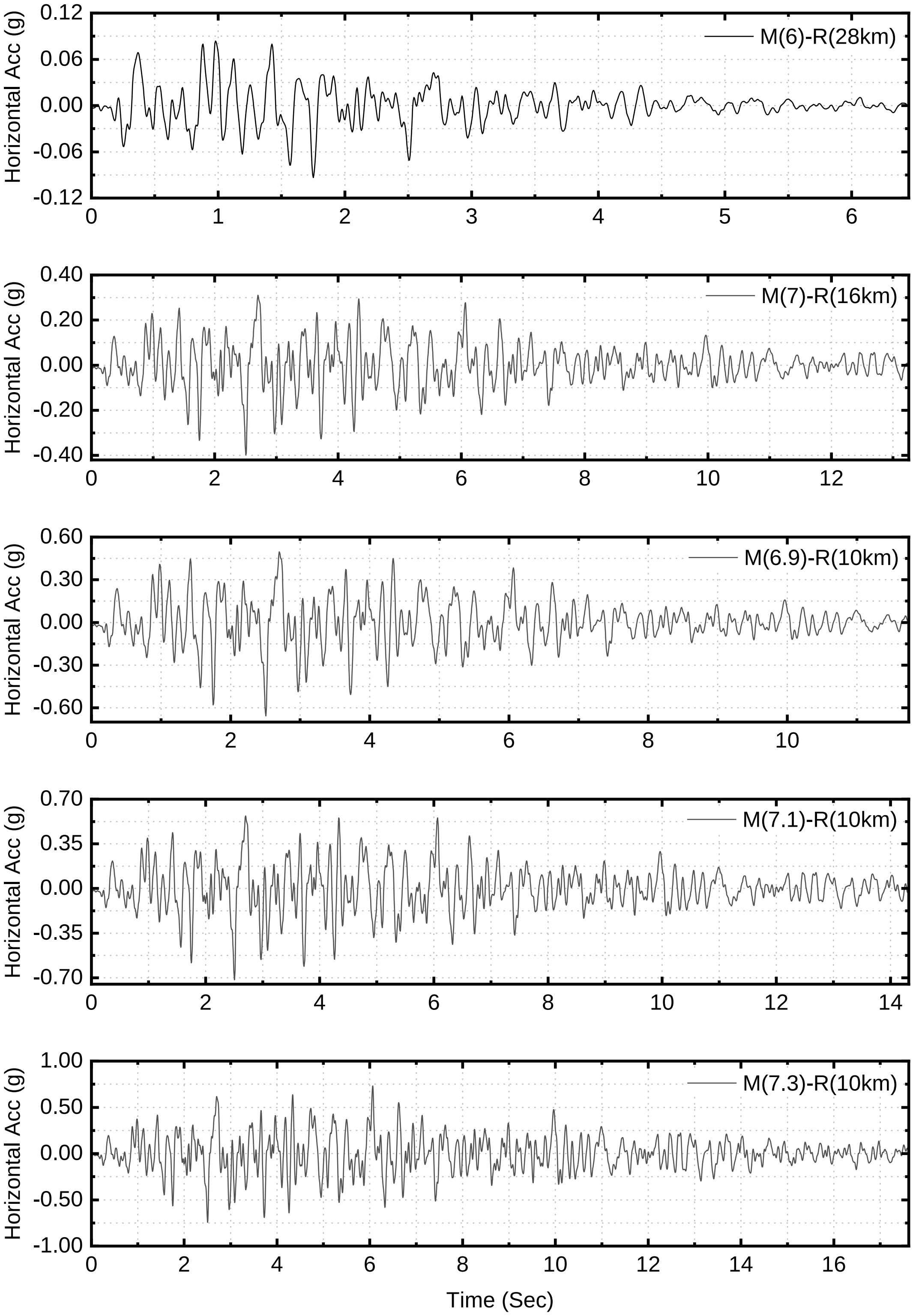

Figure 4-23 Acceleration time history of artificial accelerograms used for the shaking table experiment.

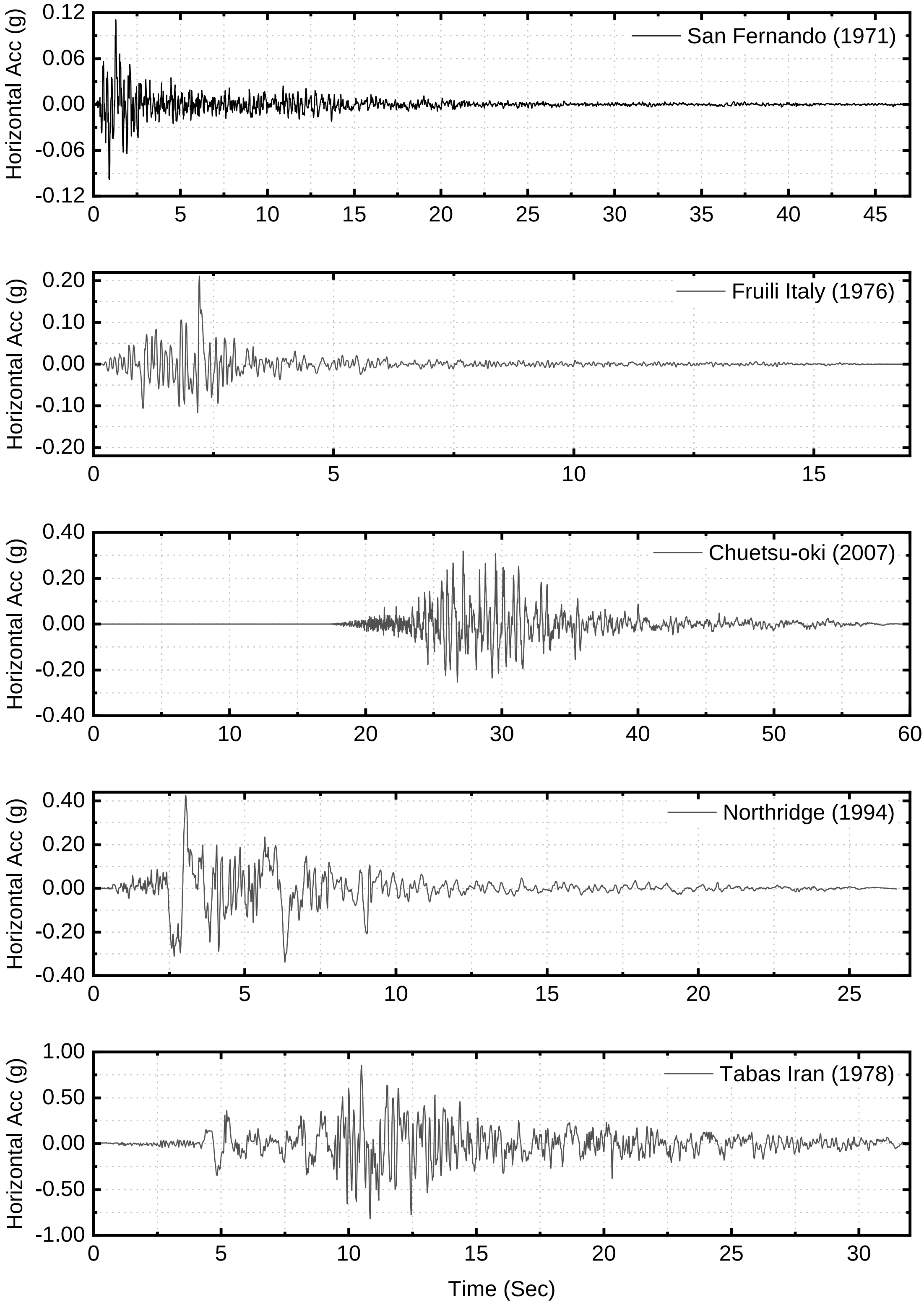

Figure 4-24 Acceleration time history of historical accelerograms used for the shaking table experiment.

4.5.2. Displacement response of the scaled down RW (base restrained) model against earthquake excitations

Figure 4-25 shows the displacement time history of the scaled down RW (base restrained) model when excited using the earthquake accelerograms (first set). Figure 4-25a and 4-25b show the displacement response of base restrained RW; at RW top and middle when excited using artificial accelerogram with PGA = 0.72g and 0.74g, respectively. Figure 4-25c and 4-25d show displacement response of base restrained RW at RW top and middle for historical accelerogram with PGA = 0.43g and 0.85g respectively. Relative displacements at RW top and middle have been normalized with respect to the height of the base restrained RW (400 mm). Less deflection of scaled down RW has been observed when analyzed using first set of earthquake excitations, which is due to high stiffness of miniature model. However, active state displacement of RW top has been observed against first set of earthquake base excitations.

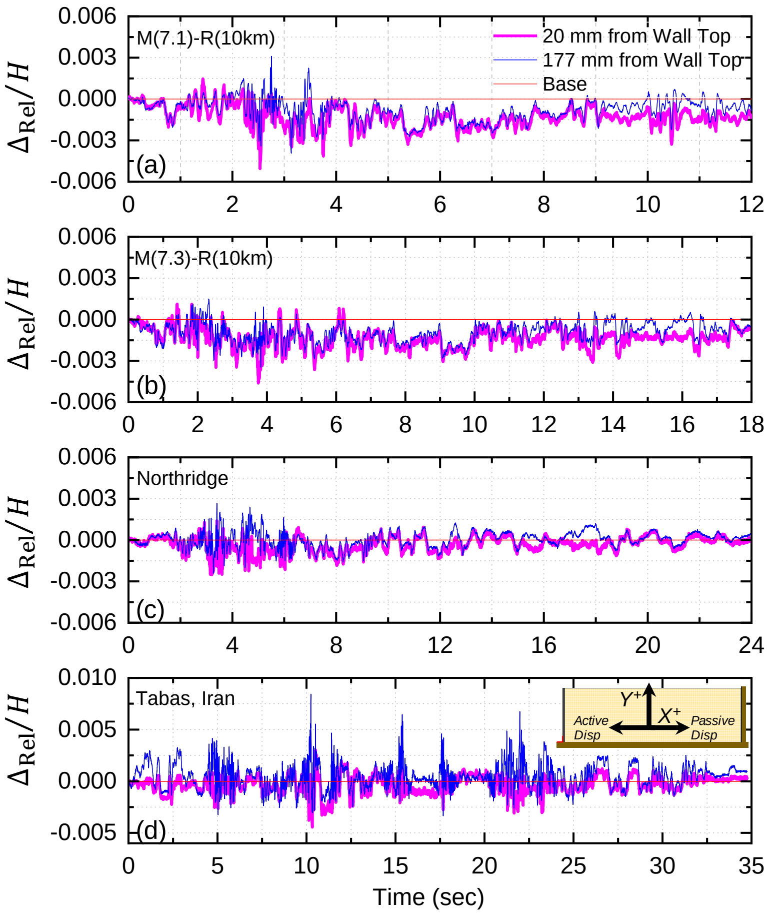

Figure 4-25 Displacement time history at scaled down RW (base restrained); top and middle, when subjected to earthquake base excitation during the shaking table test.

4.5.3. RSA of scaled down RW (base restrained) model against earthquake excitations

Figure 4-26 shows RSA for scaled down RW (base restrained) model when subjected to five artificial and five historical accelerograms (first set). Amplification of horizontal acceleration has been observed for all the cases. It has also been observed that the backfill responded more up to 0.08 sec time period.

Amplification of horizontal acceleration in backfill has also been investigated. Amplification factors (AF_{soil}) was obtained using the RSA at backfill top, middle and base. Figure 4-27 shows the method used for obtaining the AF_{soil} (Peak RSA at backfill top used as reference point for finding average of RSA at model base).

Figure 4-28 shows the bar chart of amplification factor of horizontal acceleration at top and middle of the backfill against different peak response spectral accelerations (increasing peak RSA of shaking table base has been shown). It was observed that the amplification of horizontal acceleration at the top of the backfill was not constant with the applied PGA. The average value of the amplification factor at the top and middle of the backfill was observed as 2.24 and 1.79, respectively.

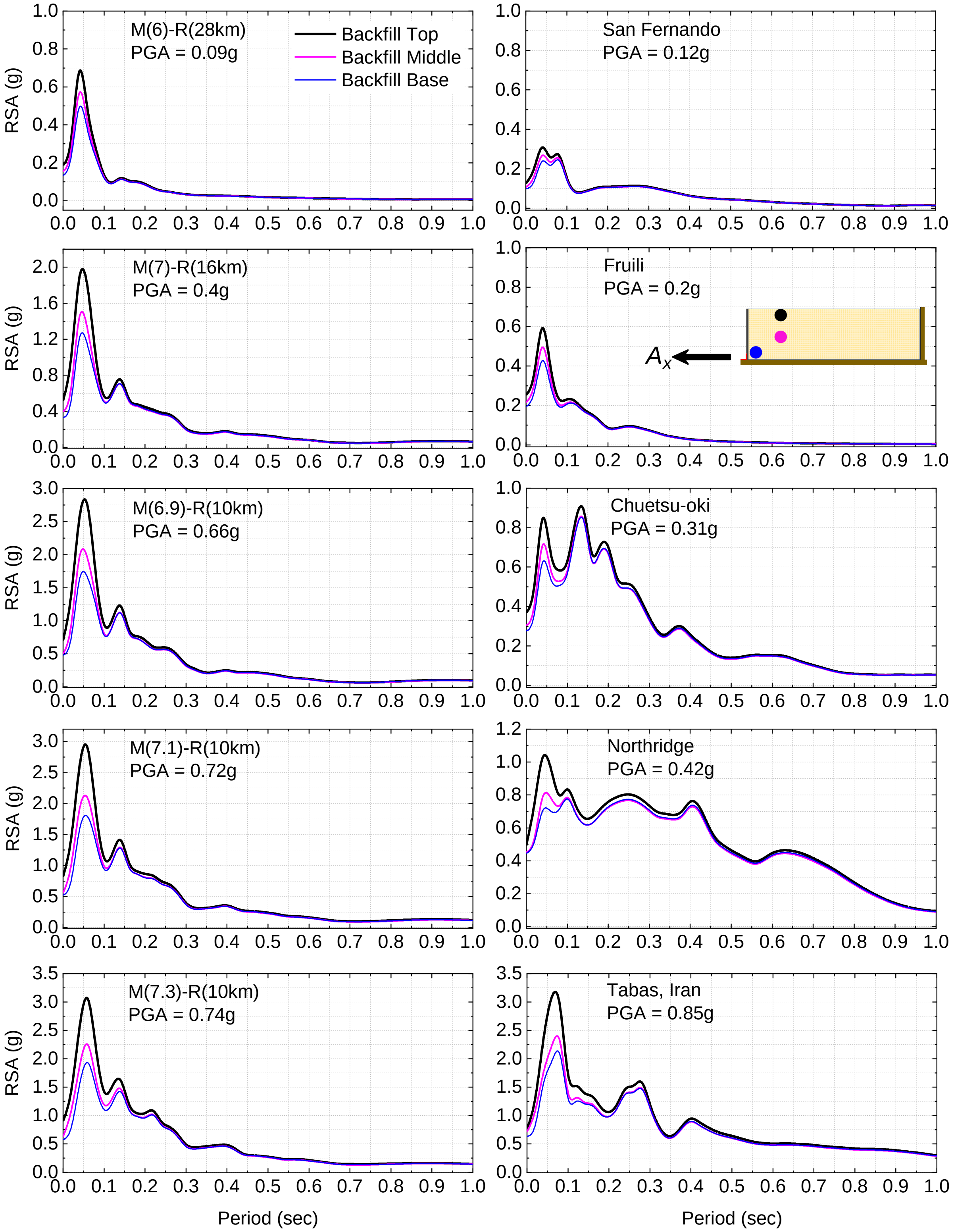

Figure 4-26 RSA for horizontal acceleration at backfill base, middle and top, when subjected to different earthquake excitations during the shaking table experiment.

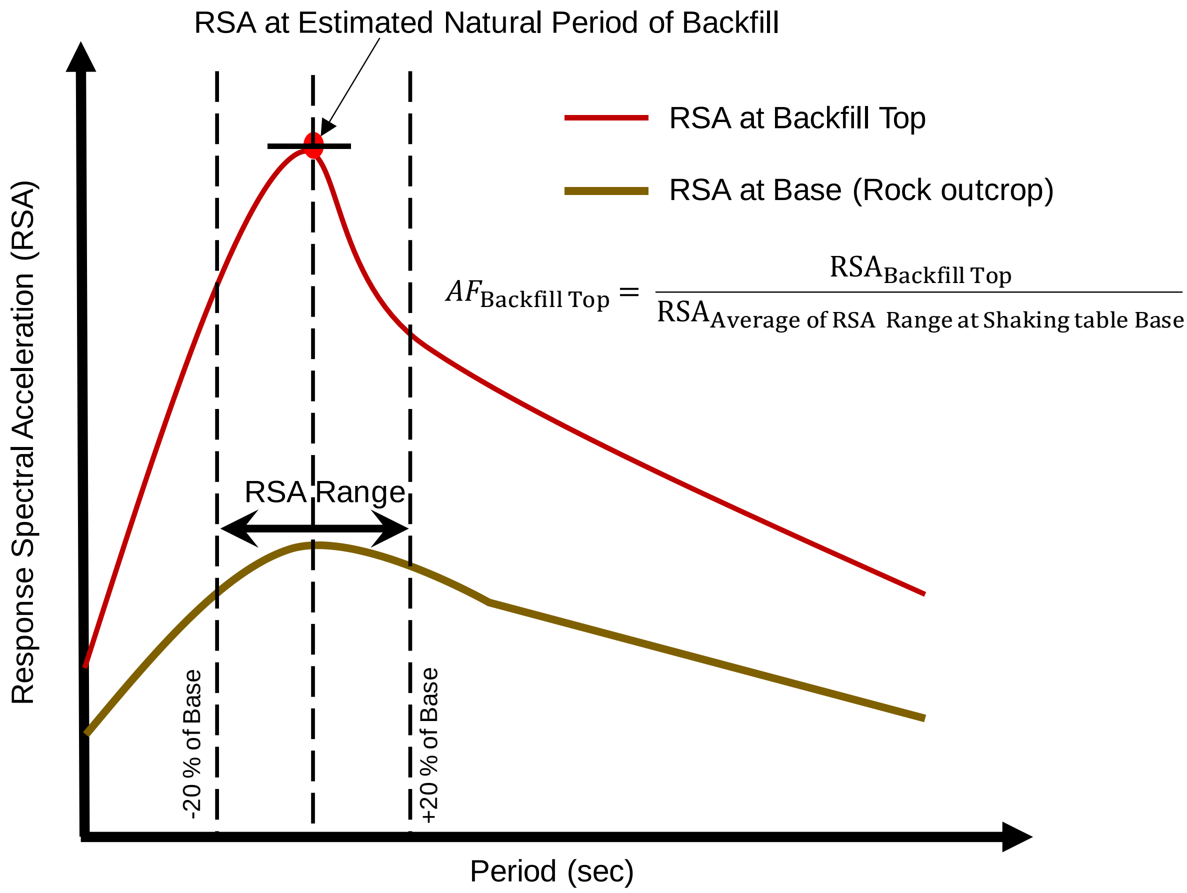

Figure 4-27 Estimation of AF_{Soil} during the shaking table experiment.

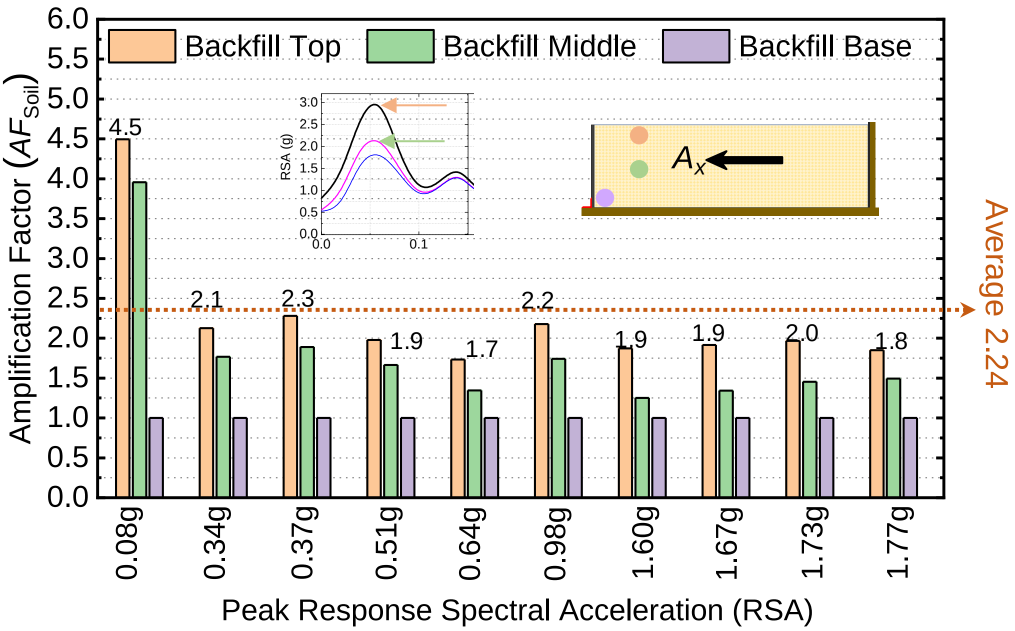

Figure 4-28 Maximum horizontal amplification at backfill middle and top (ratio of peaks accelerations), when subjected to different earthquake excitations during the shaking table experiment.

4.5.4. Displacement response of the scaled down RW (base restrained) model against earthquake excitations

Figure 4-29a and 4-29b show normalized displacement time history at scaled down RW (base restrained) top and middle height, when the model base was excited with Northridge and Tabas accelerogram, respectively (second set). The time step for both accelerograms has been reduced to twice of 10 scaled down accelerogram's time step. Higher displacement was observed at the top of the RW which was due to higher soil inertia acting that level. Moreover, it was observed that once the RW moves away from the soil (active state movement), the soil fell on it immediately following the gap formation. However, when the shaking table moves in the passive directions (i.e. positive *x*), the top of the RW was not able to push back the soil (because of high passive resistance of the backfill). Moreover, when the backfill moves in the passive direction the inertia of the soil at the top level further push it in the active direction. As a result only active state displacement of the base restrained RW was observed in the shaking table experiments.

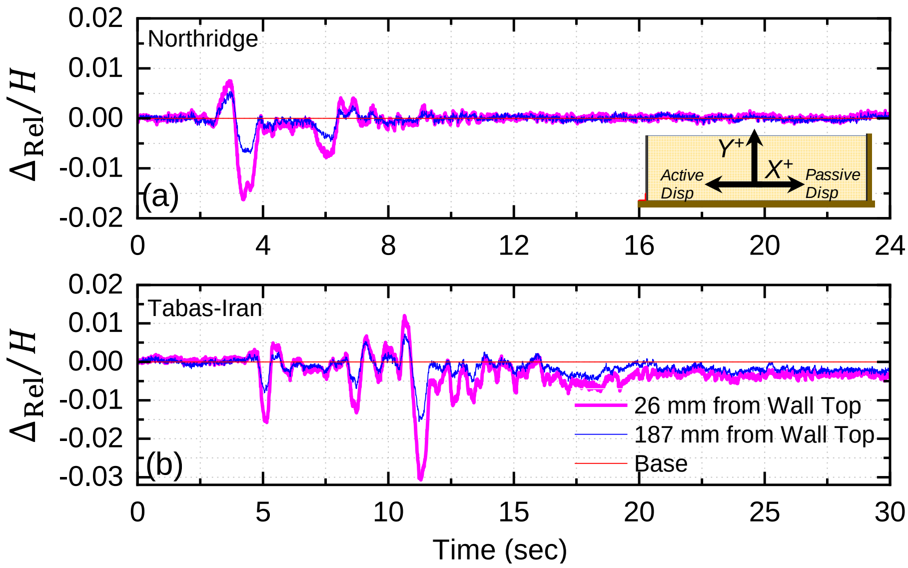

Figure 4-29 Displacement time history at scaled down RW (base restrained); top and middle, when subjected to 200% scaled ($\boldsymbol{\lambda_{\Delta t}} = \mathbf{2}\sqrt{\boldsymbol{\lambda_l}}$ & $\boldsymbol{\lambda_l} = \mathbf{10}$) earthquake base excitation during the shaking table test.

4.5.5. RSA of the scaled down RW (base restrained) model against earthquake excitations

Figure 4-30 shows the RSA for five historical accelerograms (2 x reduced time step). The boundary effects were observed for input base excitation for PGA ≥ 0.31g. The San Fernando and Fruili accelerograms shows 86% and 121% amplification in horizontal acceleration (relative to base), respectively.

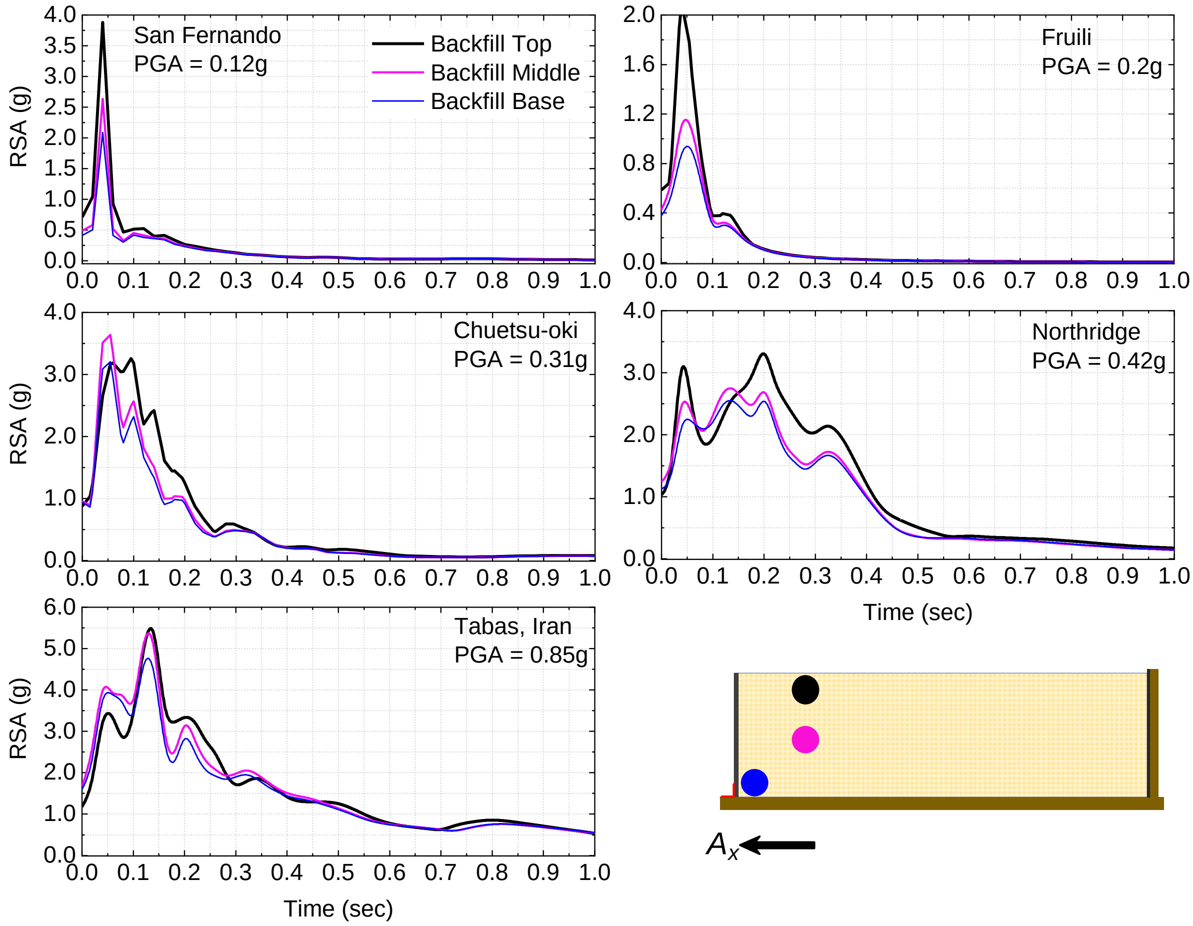

Figure 4-30 RSA for horizontal acceleration at backfill base, middle and top, when subjected to different earthquake excitations (200% scaled) during the shaking table experiment.

4.6. Estimation of the shear wave velocity in backfill

One of the prime objectives of the shaking table investigation was to estimate the shear wave velocity of the 0.4 m thick backfill. Unidirectional accelerometers had been inserted inside the backfill to capture accelerations developed in the backfill (figure 4-4). Accelerations at the base and top of the backfill could be used to estimate the shear wave travelling time. Figure 4-31 shows acceleration time history at backfill top and base when subjected to (a) multiple pulses and (b) half cycle sine pulse with 20 mm amplitude, respectively. The accelerations at the base and top of the backfill were identified during the initial phase of loading for avoiding distortions of results by wall soil separation and stress wave reflections. Identification of peaks has been shown in the inset diagram of figure 4-31(a and b). Once the acceleration peaks were identified, the time difference between two subsequent acceleration peaks was calculated. The shear wave velocity was then estimated using the following formulation:

$$V_{\mathrm{SH}} = \frac{Height\ of\ Soil\ Column\ (0.4m)}{Wave\ Travel\ Time\ from\ Backfill\ Base\ to\ Top} \tag{4.3}$$

Observations from synchronised recordings from the dynamic tests inferred an average shear wave velocity (VSH) of 27 m/s with the scaled down model inferring 85.4 m/s with the prototype ($\lambda_{\mathrm{V}} = \frac{V_{\mathrm{P}}}{V_{\mathrm{S}}} = \sqrt{\frac{\lambda_{\mathrm{E}}}{\lambda_{\rho}}} = \sqrt{\lambda_{\mathrm{l}}}$). It is acknowledged that the value of V_{SH} reported herein for a 4 m high prototype backfill is lower than the range of values used in site classification in codes of practices for defining the design seismic actions on structures (Anderson, 2008; Wair et al., 2012). This difference is because of the standard practice of averaging shear wave velocities over the upper 30 m of the soil layers, in comparison with 4m. Similarly low values of V_{SH} for backfill material has been reported in the experimental work of Yazdandoust (2017) and Wang et al. (2015). Similar results were obtained with other sets of shaking table experiments as shown in Table 4-1. It should be noted herein that with elastic soil column analysis, the shear wave velocity is estimated at 24 m/sec.

Table 4-1 Shear wave velocity in the backfill behind the base restrained RW (obtained from different base excitations).

Sr. No.	**Pulse Applied**	**Shear Wave Velocity (m/sec)**
1.	Half Cycle Sine – 20mm Amp	36.36
2.	Half Cycle Sine – 50mm Amp	28.57
3.	One Cycle Sine – 35mm Amp	20
4.	One Cycle Sine – 50mm Amp	33
5.	Multiple Pulses – 20 mm Amp	23
6.	Multiple Pulses – 25 mm Amp	21.1

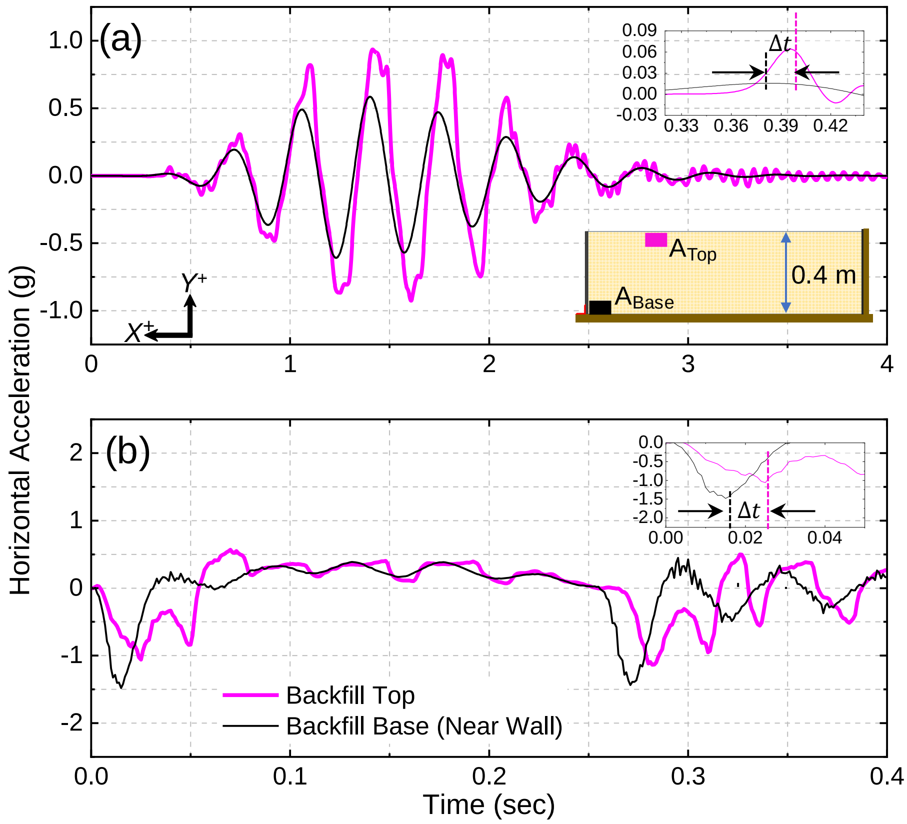

Figure 4-31 Estimation of shear wave velocity of backfill, from the shaking table experiment, when (a) excited using multiple pulses, (b) excited using half cycle sine pulse (20 mm amp and 0.25 sec duration).

4.7. Maximum ground acceleration and RW displacement

Figure 4-32 and 4-33 shows the displacement time history at RW top and acceleration time history at RW base and backfill top when excited using the multiple pulses and half cycle sine pulse, respectively. The applied base excitations have also been shown in the inset diagram of the figures. It should be noted herein, that no filtration of the output data has been performed for plotting figure 4-32 and 4-33 so that the time lag between the applied acceleration and displacement of the RW could be achieved.

A time lag was observed between the RW acceleration captured at the base and at the top which indicates that the maximum inertia of the applied excitation and maximum displacement of the RW did not occur at the same time.

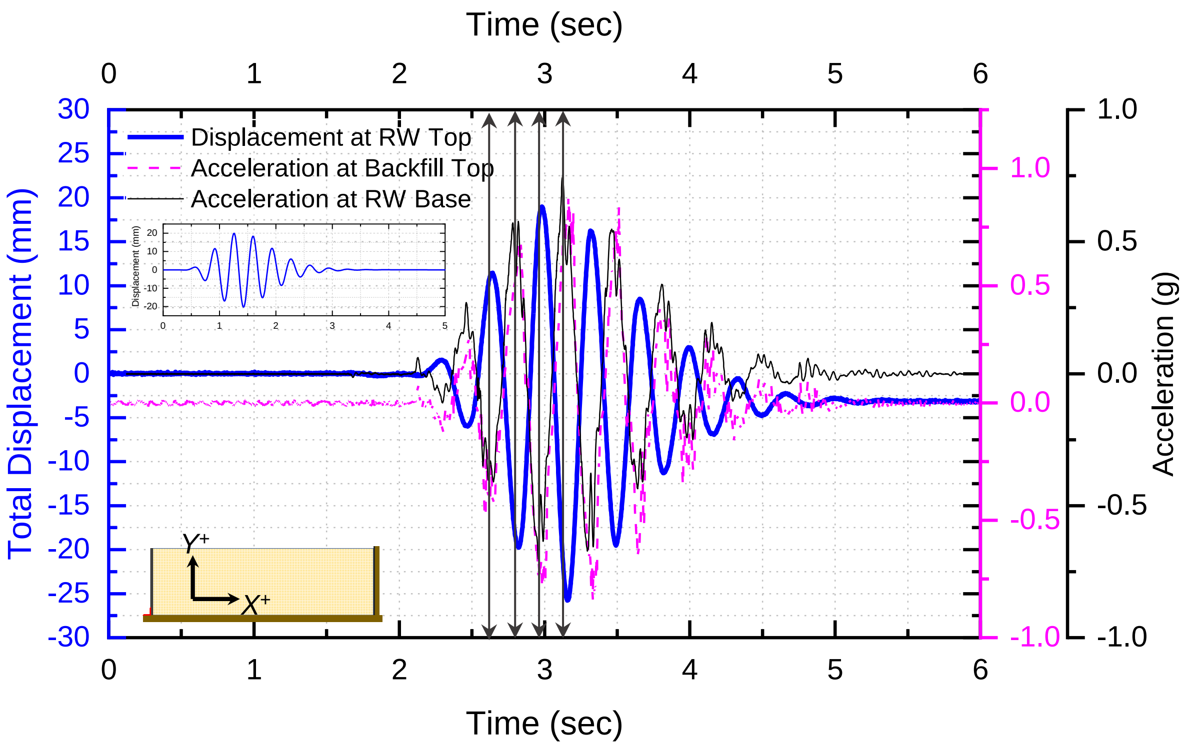

Figure 4-32 Total displacement at RW top and maximum acceleration at RW base, backfill top (multiple pulses as base excitation).

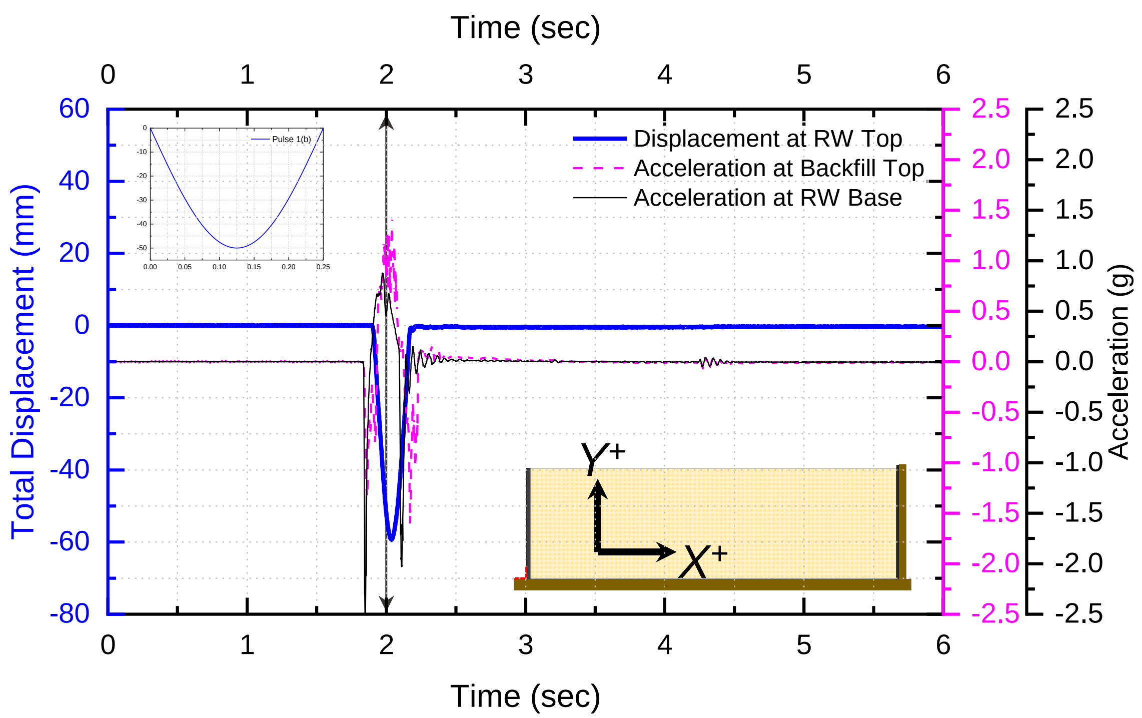

Figure 4-33 Total displacement at RW top and maximum acceleration at RW base, backfill top (half cycle sine pulse as base excitation).

4.8. The shaking table experiment with the scaled down RW (rotational base) model

4.8.1. Construction of the scaled down RW (rotational base) model

A detailed experimental investigation has been carried out for understanding the rotational behaviour of the RW supported by rock socketed pile foundations. Dynamic similitude analyses have been carried out for the selection of the RW material and estimation of the scaled rotational stiffness of pile foundation. Details of scaled down RW constructed with polycarbonate material, scaling of rotational stiffness of rock-socketed pile foundation, and selection of rotational springs to replicate rotational behaviour of rock-socketed pile foundation that has been presented in sections 3.4.3 and 3.4.4 of chapter 3.

Mild steel has been selected as the rotational spring material. Figure 4-34 and 4-35 shows details of the rotational springs used in the present study. Steel bars of 4.5 mm diameter has been used to fabricate the rotational springs. The internal diameter of the rotational spring coil was 22.5 mm. A total of 16 rotational springs were distributed uniformly on both sides of the C.G. (*y*-*y* axis) with higher c/c spacing at the "toe" side and lower c/c spacing at the "heel" side as shown in figure 4-36.

Steel rods of 19 mm diameter were used to mount rotational springs on them so that the desired location of the rotational spring could be achieved (as shown in figure 4-37a). Steel washers have been used on both sides of the rotational springs for preventing their movement along the steel rod. Free rotation of springs has been insured by providing a small spacing between the rotational springs and the steel washer, and between the rotational springs and the steel rod. Figure 4-37b shows rotational spring's distribution and position at the base of the RW (details in sections 3.4.3 and 3.4.4 of chapter 3).

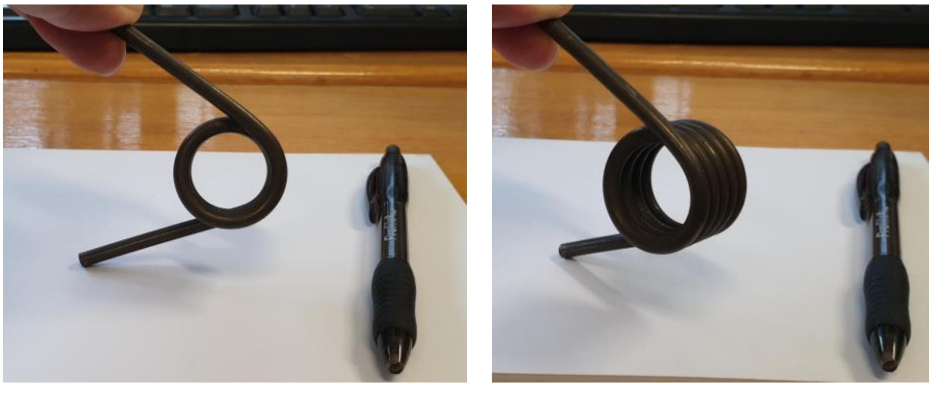

Figure 4-34 Fabricated mild spring rotational spring, with 171 N-mm/deg rotational stiffness.

Sandpaper has been applied at the base and back face of the scaled down RW for initiating friction between the backfill and RW. High-density foam has been applied at the base and backside of the wooden container, to simulate amplifications from the base soil and for minimizing boundary effects from the backside (figure 4-38a). A small gap was provided between the "heel" of the scaled down RW and the base foam to ensure free rotation of the scaled down RW (figure 4-37c). To prevent the falling of the backfill into the gap, high strength polymer band has also been used to cover the gap (no restriction in the RW rotation).

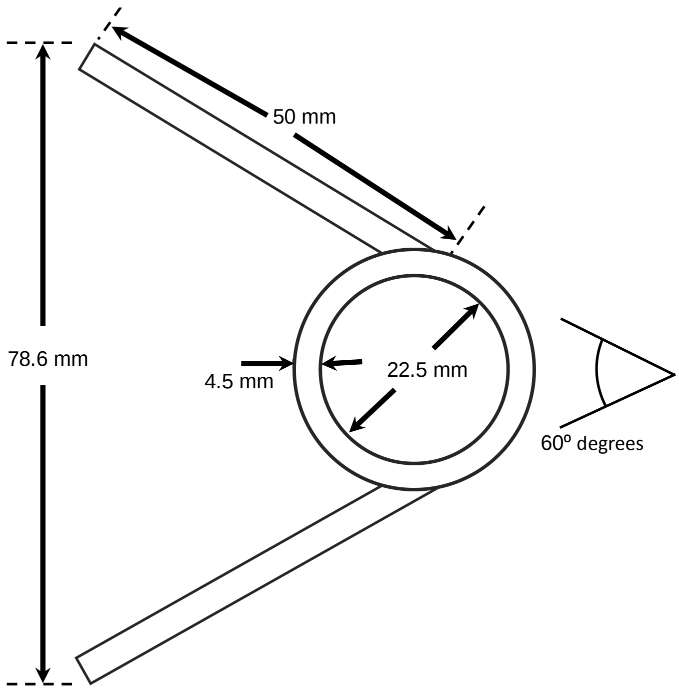

Figure 4-35 Details of rotational spring for 171 N-mm/degree rotational stiffness.

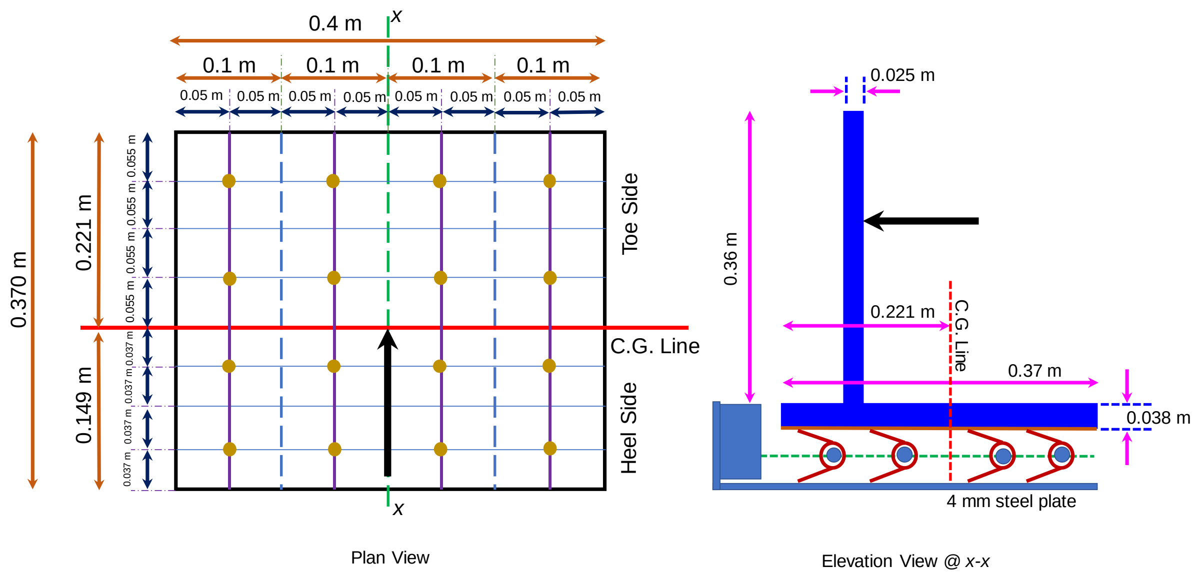

Figure 4-36 Distribution of rotational springs at the base of scaled down RW.

(a) Steel rods to accommodate rotational spring

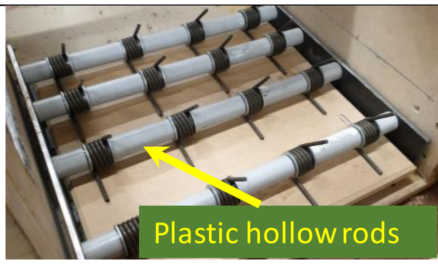

(b) Hollow plastic rods to maintain rotational spring position

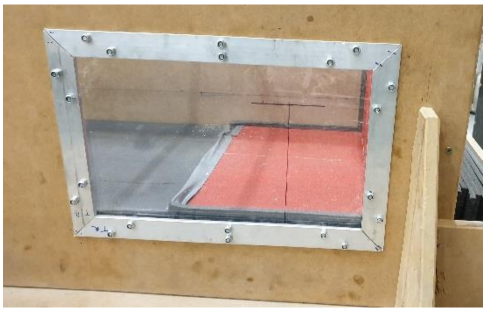

(c) Glass window to observe backfill behind scaled down RW

(d) Initial placement of scaled down RW on rotation spring foundation

Figure 4-37 Construction of rotational base for scaled down RW model, details of fabricated scaled down RW model.

4.8.2. Construction of backfill behind the scaled down RW (rotational base) model

Backfill behind the scaled down RW (rotational base) was constructed in four layers, the base layer was 75 mm high, and the top three layers are 100 mm high. Crushed rocks were used as the backfill material. The maximum dry density of crushed rocks was estimated as 1790 kg/m^3. The required weight of every layer of backfill was estimated against the maximum dry density of crushed rocks. The backfill was then compacted using the shaking table. Figure 4-38b shows the scaled down model of the RW with the rotational base after placing the backfill.

Figure 4-38 (a) High density foam applied at scaled down model base and backside (left), (b) constructed scaled down RW model supported by rotational springs.

4.8.3. Instrumentation setup for the shaking table experiment on the scaled down RW (rotational base)

As explained in sections 4.2.4 to 4.2.6, laser transducers and accelerometers were used for capturing the displacement and acceleration response of the scaled down RW (with rotational base). Figure 4-39 shows the instrument setup for the scaled down RW model (rotational base). Four laser transducers were used for capturing the displacement response of the scaled down RW (rotational base). Laser transducers were installed to capture the RW displacement at 13 mm, 189 mm, 313 mm below the scaled down RW (rotational base) top, and one laser transducer was installed to capture the movement of the shaking table.

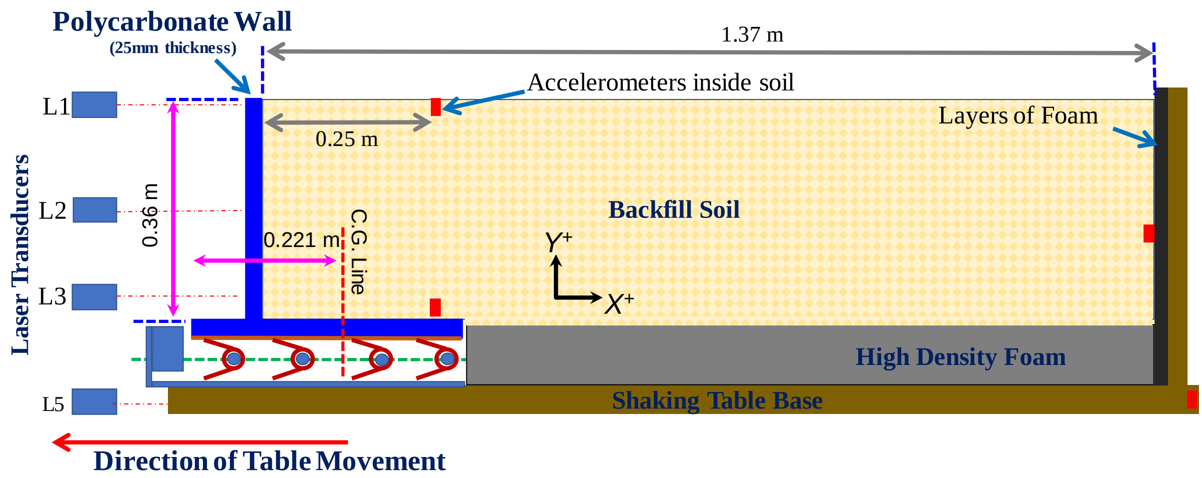

Figure 4-39 Instrument setup for the scaled down RW (with rotational base) model.

4.9. Seismic response of the scaled down RW (rotational base) model against multiple pulses

Seismic response of the scaled down RW (rotational base); has been analyzed against different pulses with peak acceleration ranging from 0.08g to 0.8g. Formulation shown in equation 4.2, has been used for generation of different types of pulses (Yazdandoust, 2017), program SeismoSignal 2016 (Seismosoft, 2016) has been used for generating displacement time history from the acceleration time history. Figure 4-40 shows the pulses that were used as input excitation in the shaking table experiment on the scaled down RW (rotational base). Every pulse had a peak frequency of 4hz, which is typical of an earthquake (Shumway, 2003).

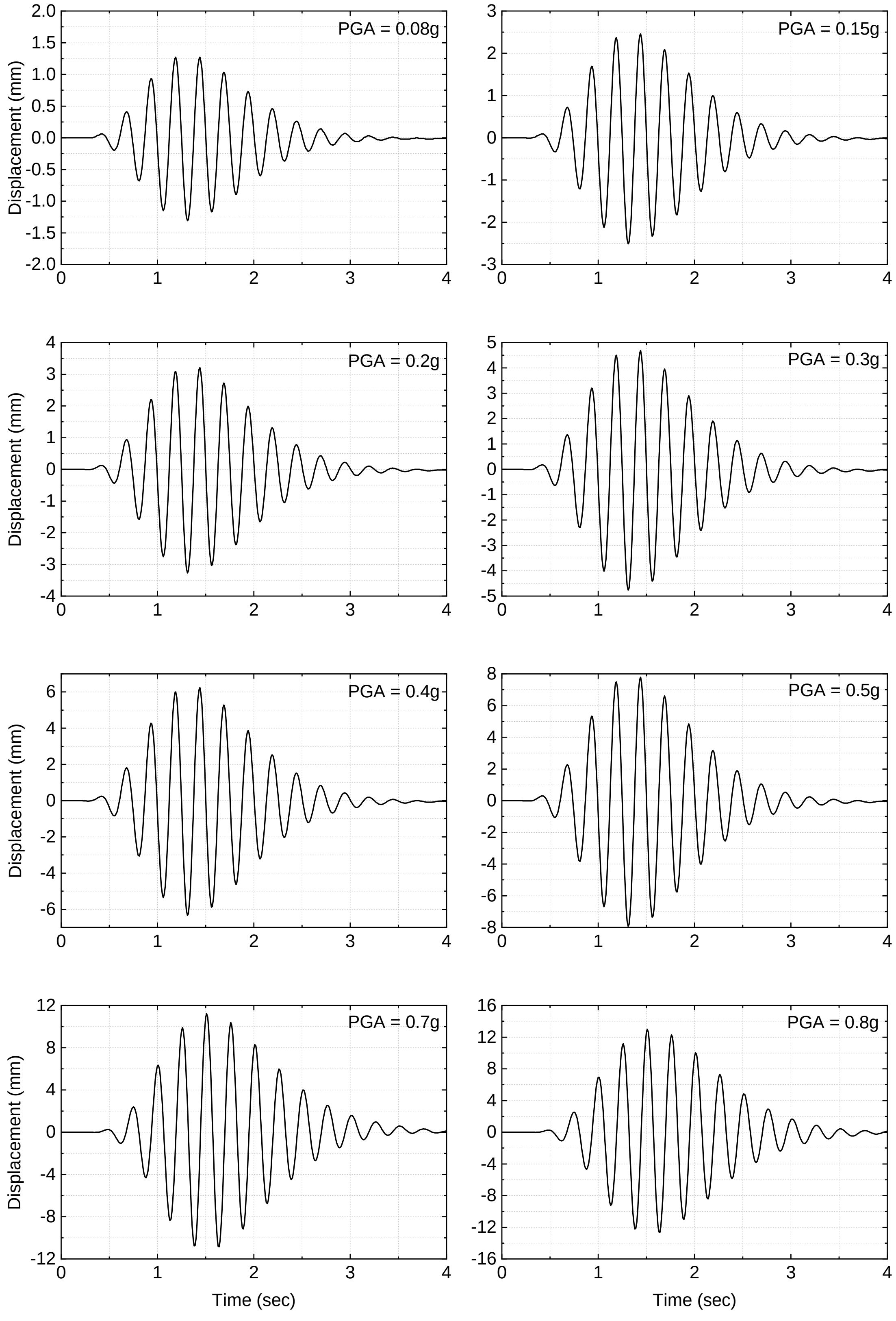

Figure 4-40 Applied multiple pulses on scaled down RW model (rotational base).

4.9.1. Displacement behaviour of the scaled down RW (rotational base) model against multiple pulses

Displacement behaviour of the scaled down RW (rotational base), against multiple pulses is shown in Figure 4-41. Relative displacement at the RW top (relative to base) has been calculated by the formulation shown in equation 4.1. Significant relative displacement at the top of the RW was observed for the multiple pulse excitations featuring PGA ≥ 0.4g. Higher relative displacements towards the top were observed in all cases. Table 4-2 show the percentage of relative displacement that has been normalized with respect to the height of the wall.

Table 4-2 Normalized displacement of the scaled down RW (rotational base).

Sr. No.	PGA	$\frac{\Delta_{\text{Rel at top}}}{H_{\text{stem}}}$ (%)
1.	0.4g	0.6
2.	0.5g	1.1
3.	0.7g	3.2
4.	0.8g	3.4

For a RW rotating about its base the formation of active failure wedge occurs when $\Delta_{\text{Rel at top}}$ > 0.002H (Clough and Duncan, 1971). Therefore, pulses with PGA ≥ 0.4g would generate active failure wedge in the backfill.

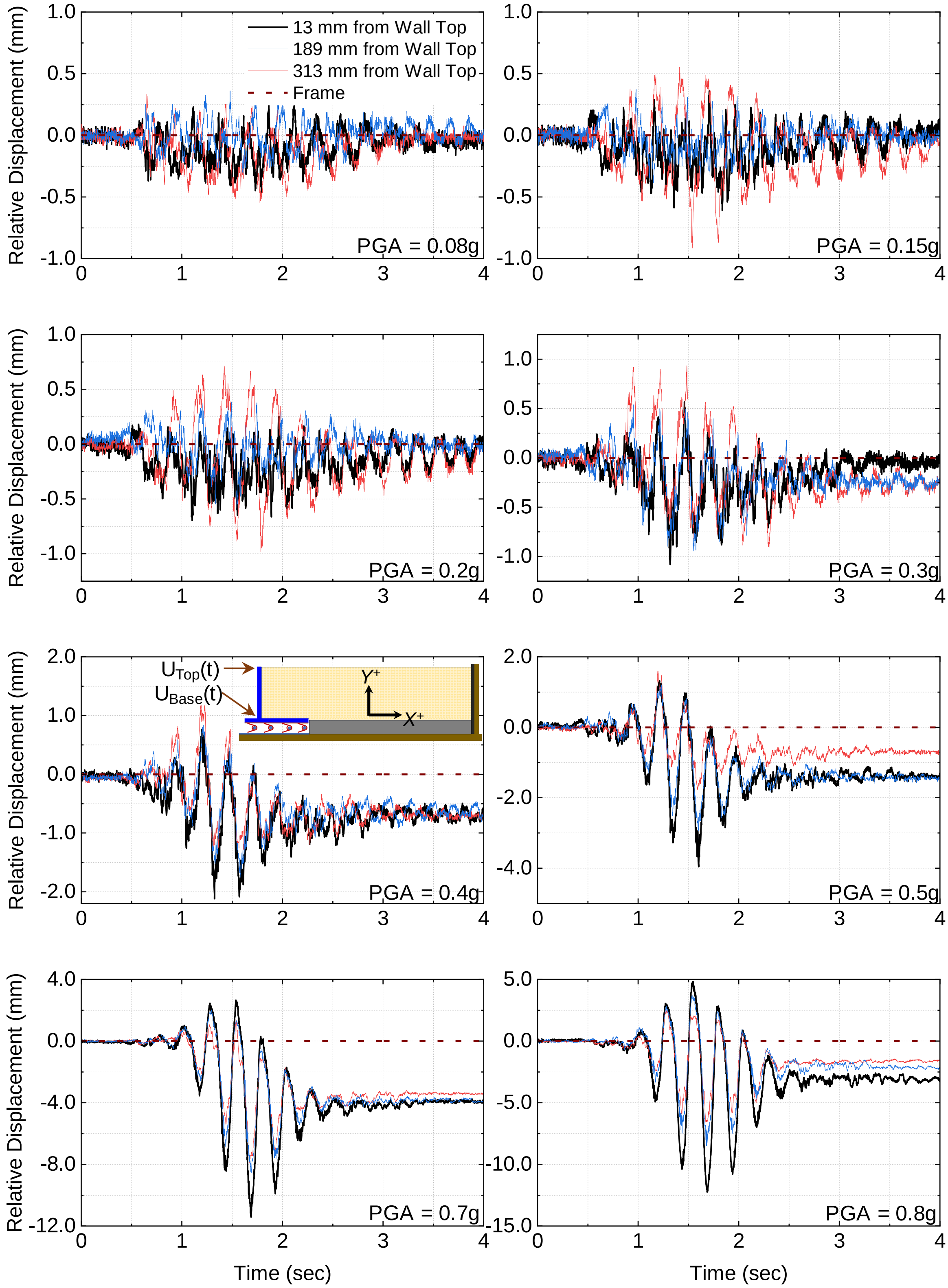

Figure 4-41 Displacement response of scaled down RW (rotational base) model; when subjected to multiple pulse base excitation.

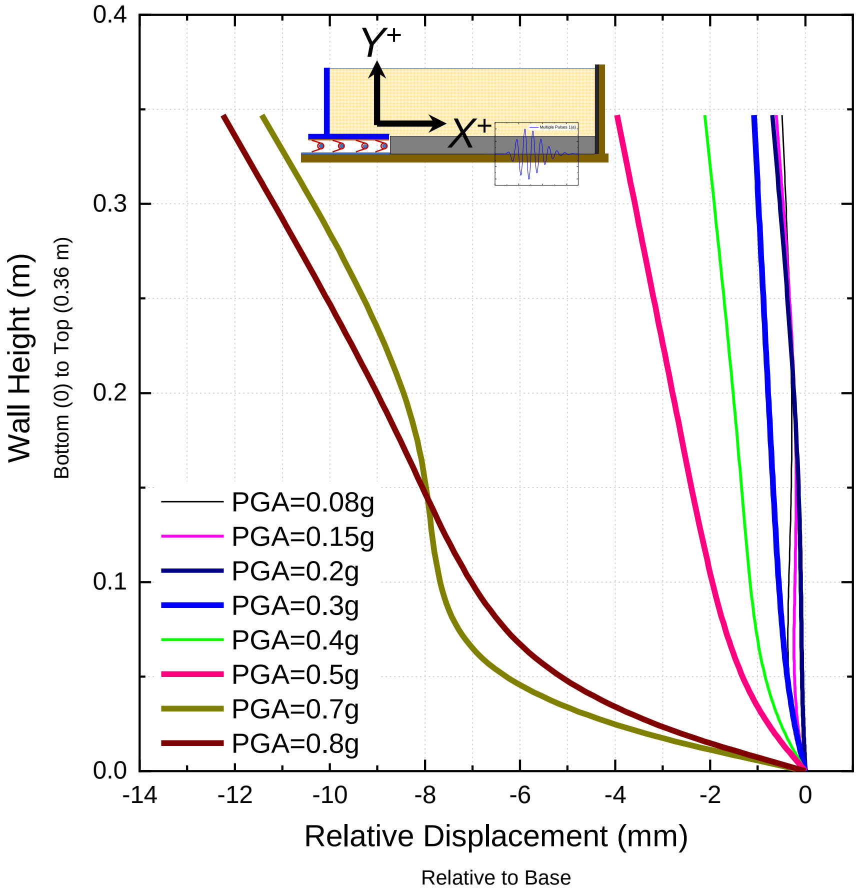

Figure 4-42 Maximum relative displacement along the RW (rotational base) height.

Figure 4-42 shows maximum relative displacement up the wall height when subjected to different pulse excitations. Higher displacement of the RW was observed with increasing PGA. For PGA ≥ 0.4g the uniform spacing of the lines representing displacement time-histories recorded at different positions up the height of the RW was also indicative of dominance by the fundamental mode of vibration (consistent with conditions observed under quasi-static actions and with base restrained scaled down RW). A nonlinear displacement behaviour of the RW was observed at the base and up to 100 mm height, above which a linear displacement pattern was observed in most cases. For a pulse with 0.7g PGA, a sinusoidal displacement pattern of the RW was observed. However, no signs of plastic deformation were observed in the scaled down RW (rotational base). Therefore, it could be concluded that higher modes/boundary reflections affected the shaking table experiment results for PGA ≥ 0.7g.

4.9.2. RSA for the scaled down RW (rotational base) model

Figure 4-43 shows amplification factor for the scaled down RW (rotational base) model when the RW base was excited using different pulses. The amplification factor (for A_x) relative to shaking table has been shown for the top of the backfill and at the heel. Method used for eastimating the AF_{Soil} is shown in figure 4-27. Significant amplification in the horizontal acceleration towards the top of the backfill was observed for all cases. It was observed that the RW respond more up to 0.15 sec time period (for PGA ≤ 0.66g). An average amplification factor of 1.89 (at RW top) was observed.

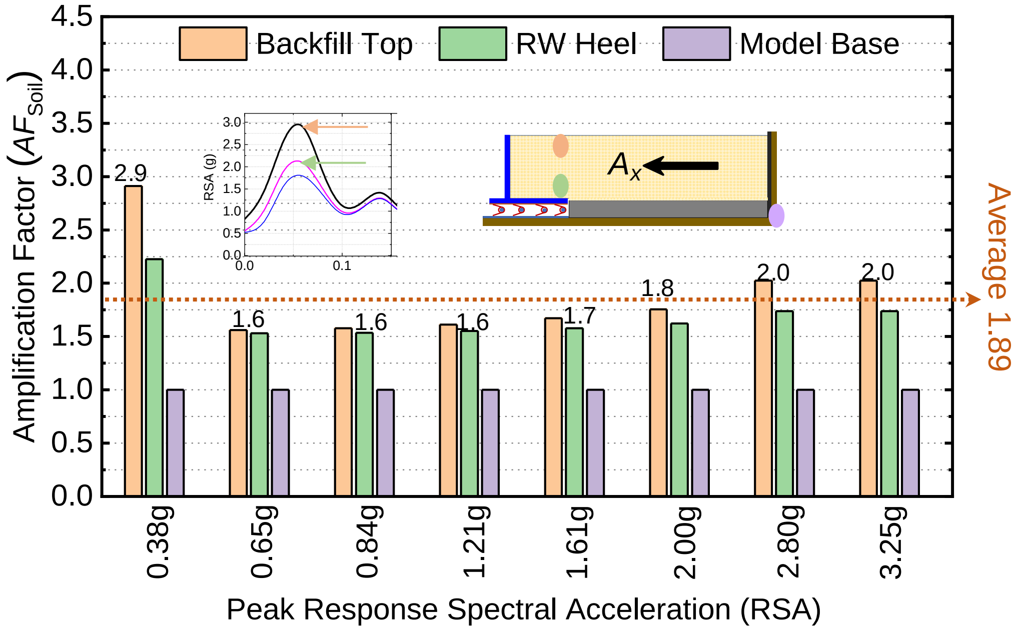

Figure 4-43 AF_{soil} of horizontal acceleration for scaled down RW (rotational base) model, at backfill top and RW heel; when subjected to different multiple pulses.

4.10. Shear wave velocity in the backfill of scaled down RW (rotational base) model

The shear wave velocity in the backfill behind the scaled down RW (rotational base) model was estimated based on acceleration time history captured by uniaxial accelerometers placed at shaking table and at the top of the backfill. Procedure for finding shear wave velocity of the backfill has been explained in section 4.6. Table 4-3 shows the shear wave velocity observed for different base excitations. Based on which the average shear wave velocity for the backfill behind the scaled down RW (rotational springs) has been estimated as 23.68 m/sec, as explained in section 4-6. The shear wave velocity based on elastic soil column was estimated at 23 m/sec.

Table 4-3 Shear wave velocity in the backfill behind the rotational base RW (obtained from different base excitations).

Sr. No.	**Multiple Pulse PGA**	**Shear Wave Velocity (m/sec)**
1.	0.08g	28.6
2.	0.15g	30.8
3.	0.2g	30.8
4.	0.3g	21.05
5.	0.4g	18.2
6.	0.5g	16
7.	0.7g	15.4
8.	0.8g	28.6

4.11. Chapter Summary and the critical observations from the shaking table experiment

A rigorous and detailed shaking table experiment has been performed on the scaled down RW models. The prime objective of the shaking table experiments was to understand the seismic response of earth retaining structures with different support conditions. Results of the shaking table experiments have been analyzed for understanding the effects of earthquake actions on the earth retaining structures.

The first set of shaking table experiments has been performed on the scaled down RW (base restrained) model (4mm thick Aluminum wall). Results of the shaking table experiments have been analyzed for understanding the earthquake induced displacement and rotation of base restrained RW. The following observations from the shaking table experiment on the base restrained RW model have been made:

1. The uniform spacing of the lines observed during pluck and pulse tests representing displacement time-histories recorded at different positions up the height of the RW was also indicative of dominance by the fundamental mode of vibration (consistent with conditions observed under quasi-static actions).
2. Displacement and rotation of the scaled down RW (base restrained) mainly depends on the nature and type of base excitations. Higher mode effects can also influence the displacement behaviour of the earth retaining structure.
3. Backfill inertia plays a vital role in seismic displacement and rotation of the base restrained RW model. Active state displacement of the base restrained RW model has also been observed for all cases.
4. Free vibration response of the scaled down RW (base restrained) has also been studied through different pluck tests. Constant modal properties have been obtained for the base restrained RW model.
5. Amplification of the horizontal acceleration towards the top of the backfill was also observed during different shaking table experiments. It was observed that increase in the amount of amplification (horizontal acceleration) was not constant with the applied peak ground acceleration. Higher AF_{soil} has been observed in based restrained RW than the RW with rotational base.

6. Separation of RW and backfill was observed in many cases, which leads to decrement in backfill pressure on the RW.
7. Shear wave velocity in the backfill was also estimated during the shaking table experiments.
8. The maximum ground acceleration at RW base and maximum RW displacement do not occur at the same time.

The second set of shaking table experiments has been conducted on the scaled down RW model fabricated using polycarbonate sheets, supported on mild steel rotational springs. Rotational springs were used to replicate the rotational behaviour of rock-socketed pile foundation. Following observations have been made based on the shaking table experiment on the scaled down RW (rotational base) model:

1. Displacement behaviour of the scaled down RW (rotational base) mainly depends on the severity of applied base excitation. Linear displacement behaviour of the RW and rotation of RW and backfill (above the RW heel) was observed during the shaking table experiment.
2. Similar to based restrained scaled down RW the RW with rotational base shown dominance by the fundamental mode of vibration (consistent with conditions observed under quasi-static actions).
3. The RW rotation (active state direction) was observed during the shaking table experiments. The rotation of RW and base springs highlights the importance of rock-socketed pile foundation on the seismic performance of the earth retaining structures.
4. Amplification of horizontal acceleration was observed in all cases. However, increment in amplification (horizontal acceleration) was not constant with applied peak ground acceleration.
5. Separation of the RW and backfill was observed for high PGA pulses, which leads to decrement in the backfill pressure on the RW. The RW and backfill separation also highlights the time-dependent nature of the dynamic backfill pressure and its importance on the seismic response of the earth retaining structures.
6. Minor deviations in the shear wave velocity were observed during different shaking table experiments on the RW (rotational base). This could be due to rotation of the RW, and the backfill above the RW heel slab.

Chapter 5. CHARACTERIZATION OF BACKFILL AND FINITE ELEMENT MODELLING OF SEISMIC ACTIONS ON EARTH RETAINING STRUCTURES

5.1. Introduction

Earth retaining structures are the key elements of a modern infrastructure system. Satisfactory performance of the earth retaining structures during an earthquake could be ensured by an accurate and realistic assessment of earthquake actions on them. Earthquake actions on the earth retaining structures could be simulated using finite element (FE) modelling techniques. However, outcomes of the FE analyses should be validated with experimental results, for ensuring the accuracy of the FE analyses results. The present chapter deals with the FE modelling of seismic actions on earth retaining structures. Results from FE analyses have been compared with shaking table experimental results. Details of the shaking table experiments have been presented in chapter 4. It should be noted herein that the presence of the backfill highly influences the earthquake response of earth retaining structures. Therefore, it is essential to understand the constitutive behaviour of the backfill materials. Consolidated drained (CD) triaxial test and one-dimensional compression tests have been performed on the soils which make up the backfill to understand its constitutive behaviour. Damping in the backfill is modelled using Rayleigh damping parameters. Observations from shaking table experiments and results from geotechnical testing of the backfill materials have been used for developing FE model of the retaining wall (RW), which was analyzed against shaking table base excitations. It was observed that the FE model can effectively replicate shaking table experimental results.

5.2. Characterization and constitutive behaviour of the backfill (crushed rock)

5.2.1 Particle size gradation of the backfill (crushed rock)

Crushed rocks have been used as the backfill materials for all the shaking table experiments. Sieve size analysis (Standards Australia: AS 1289.3.6.1- 2009; ASTM C136-2006) has been performed on the crushed rock samples for determining the particle size gradation curve. Figure 5-1 shows the particle size distribution curve obtained from sieve size analysis of crushed rocks.

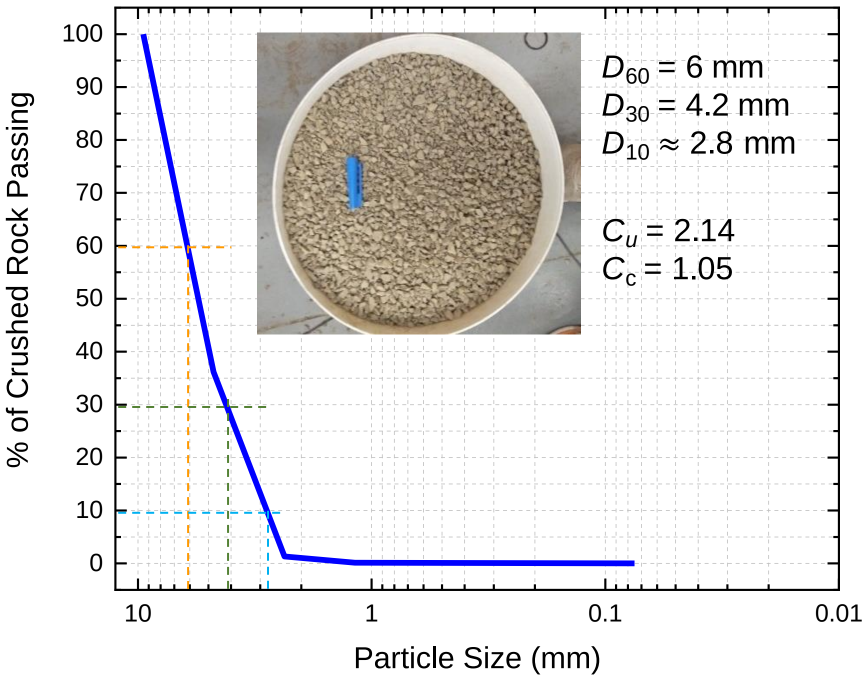

Figure 5-1 Particle size distribution curve for the crushed rock.

Based on the sieve size analysis results, the particle size of the crushed rock (backfill) at 60 %, 30 % and 10 % finer is estimated at 6 mm (D_{60}), 4.2 mm (D_{30}) and 2.8 mm (D_{10}) respectively. The coefficient of uniformity (C_u) is defined as the ratio of D_{60} and D_{10}, which indicates the range of different particle sizes in a given soil mass.

The soil mass with uniform particle size has C_u value close to 1 and the soil mass with narrow particle range has C_u value ranging from 2 to 3. Another important parameter is the coefficient of curvature (C_c), which is calculated using the following expression:

$$\text{Coefficient of curvature } (Cc) = (D_{30})^2/(D_{60} \times D_{10}) \tag{5.1}$$

Based on the particle size gradation, the coefficient of uniformity (C_u) for the crushed rock is estimated at 2.14, and the coefficient of curvature (C_c) is 1.05. These parameters classify the crushed rocks as a poorly graded soil with a narrow particle range.

5.2.2 One dimensional compression test for the backfill (crushed rock)

The modulus of the soil material depends on the level of confinement, level of strains and conditions of load applications. For earth retaining structures, the lateral movement of the backfill is normally well confined (i.e. no lateral strains). The soil modulus corresponds to such conditions is accordingly known as the constrained modulus which has been found to be a linear function of the vertical effective stress (Geoguide1 1993; Kim & Santamarina, 2008; Duncan & Bursey, 2013).

One dimensional (1-D) compression test has been performed on crushed rock samples for determining the relationship between vertical stress and vertical strain at different levels of confinement, based on which the constrained modulus (M_s) of the crushed rock is estimated by the use of the following expression.

$$M_s = \frac{\Delta\sigma_v}{\Delta\varepsilon_v} \tag{5.2}$$

where, σ_v is the vertical stress, and ε_v is the vertical strain.

Inset of figure 5-2 shows the laboratory setup for the 1-D compression test. A circular metal mould of 150 mm internal diameter and 119 mm height was used for the 1-D compression test. The crushed rock then placed inside the mould; using the under compaction method (Ladd, 1978), so that over compaction of the base soil layers could be avoided. A total of 78 % relative density (D_r) has been achieved for the 1-D compression test. The top surface of the crushed rock samples was covered with a steel plate of 150 mm in diameter so that a uniform surface load could be applied on the crushed rocks. The vertical load was then applied at the top plate with increasing loading steps. The vertical displacement of the top plate against the applied load has also been captured for determining the strain values against the corresponding loading step. Once the vertical stresses and strains have been obtained for different loading steps, equation 5.2 could be used to calculate the constrained modulus at different levels of confinement.

Figure 5-2 shows the variation of the constrained modulus with increasing level of confinement. A linear relationship was observed between the constrained modulus and increasing confining pressure, similar to what have been reported in Kim and Santamarina (2008).

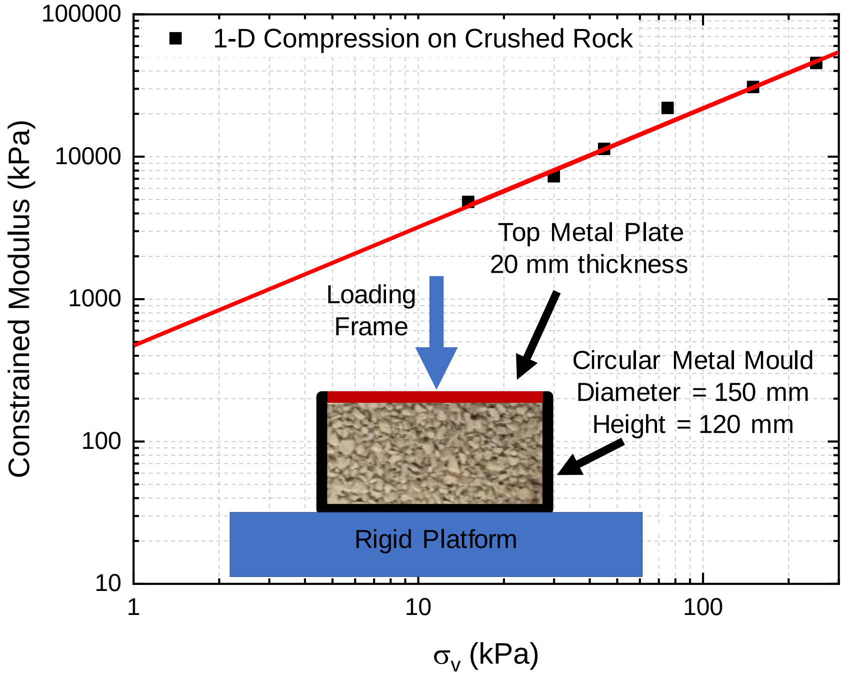

Figure 5-2 Variation of constrained modulus with vertical stress, observed during 1-D compression test.

5.2.3 Consolidated Drained (CD) Triaxial Test for the backfill (crushed rock)

Understanding the constitutive behaviour of the soil is an essential task based on which important engineering properties of the soils could be estimated. Triaxial tests have been used extensively for studying the constitutive behaviour of the undisturbed and reconstituted soil samples. The triaxial tests can be performed for understanding the short/long term response of the soil. Results obtained from the testing have been used to estimate the peak friction angle, cohesion, Poisson’s ratio, shear strength, dilation angle and elastic modulus for a given soil sample (Daheur et al., 2019; Omar and Sadrekarimi, 2015).

Triaxial tests can be classified into the following three major categories.

(i) Consolidated drained test (CD)
(ii) Consolidated undrained test (CU)

(iii)Unconsolidated undrained test (UU)

Suitability of these categories is decided based on the site conditions/application. The triaxial test procedure can be explained by its two major phases, namely consolidation and shearing. The consolidation of the soil sample occurs when the drainage valve of the triaxial apparatus is open during the consolidation phase. This allows a decrease in the sample pore water pressure. If the drainage valve is open during the shearing phase as well, then this condition is known as a drained test. In dealing with earth retaining structures it is noted that the backfill has been subjected to long term loading conditions where effective stress parameters control its behaviour. This long term loading condition could be replicated by the CD test. Therefore, it was decided to perform CD triaxial tests on the crushed rock samples.

Figure 5-3 Triaxial test set up for the CD test on the crushed rock.

Figure 5-3 shows the triaxial test apparatus at The University of Melbourne. CD triaxial tests were carried out for confinement pressures (σ_c) of 7, 34, 68, and 136 kPa as this range of values was considered to be representative of the scaled down, and the prototype, RW. The first step of the CD triaxial test was to prepare a soil sample using the under compaction method for minimizing over compaction of the base soil layers (Ladd, 1978). It should be noted that a polymeric membrane was used for all the triaxial tests. However, a piece of crushed rock is angular in shape. To prevent membrane breakage 80% of the D_r was targeted. Suction has also been applied to the crushed rock to support it during sample preparation. Figure 5-4a shows the polymeric membrane with the suctioned crushed rock inside. Different stages of CD triaxial test is also shown in Figure 5-4.

(a) Crushed rock sample with the polymeric membrane

(b) Crushed rock sample placed inside the pressure cell

(c) Sample during the CD test

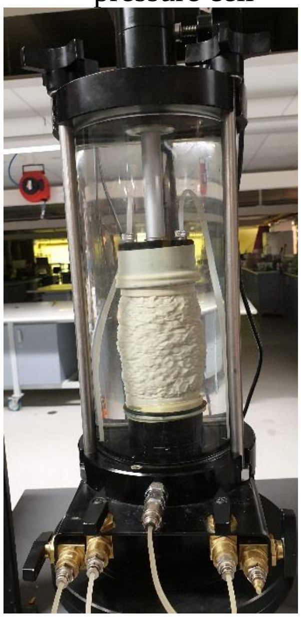

(d) Lateral bulging failure in the crushed rock sample

Figure 5-4 CD triaxial test on the crushed rock sample.

The CD triaxial test on the crushed rock sample was performed in the following steps (D7181 – 11).

(i) Initialization:

Initialization has been performed at the beginning of the triaxial test with a small pressure difference between the triaxial cell and the crushed rock sample. Initialization of the crushed rock sample was performed before each step, to match the cell and sample pressure observed from the previous step.

(ii) Saturation:

During the saturation phase, the sample was allowed to saturate so that all the air pores inside the soil sample can be removed by the pore fluid. During saturation the sample was allowed to swell by introducing an elevated pore pressure in it. The saturation was then performed by increasing the cell pressure in steps. However, effective stress in the soil sample should not exceed the shearing stress at any point in the saturation phase. Skempton coefficient (*B*) was set to 0.95 for saturation of crushed rocks.

(iii) Consolidation:

Consolidation phase was applied to the soil sample by introducing a desired effective vertical and horizontal stresses in the sample. The consolidation was performed for 24 hours. However, the specimen volume change was monitored continuously during the consolidation phase to decide if consolidation had been completed before the expiry of the 24 hours period.

(iv) Shearing:

Shearing of the crushed rock was performed by applying a vertical strain with constant strain rate (0.033/ min, %) at the top of the sample. The maximum strain limit was kept at 15%. Drainage was allowed during the shearing phase.

Figure 5-5 and 5-6 show deviatoric stress (σ_d) vs axial strain and volumetric strain vs axial strain obtained from the CD triaxial tests for three different confinement pressures of 34, 68 and 136 kPa.

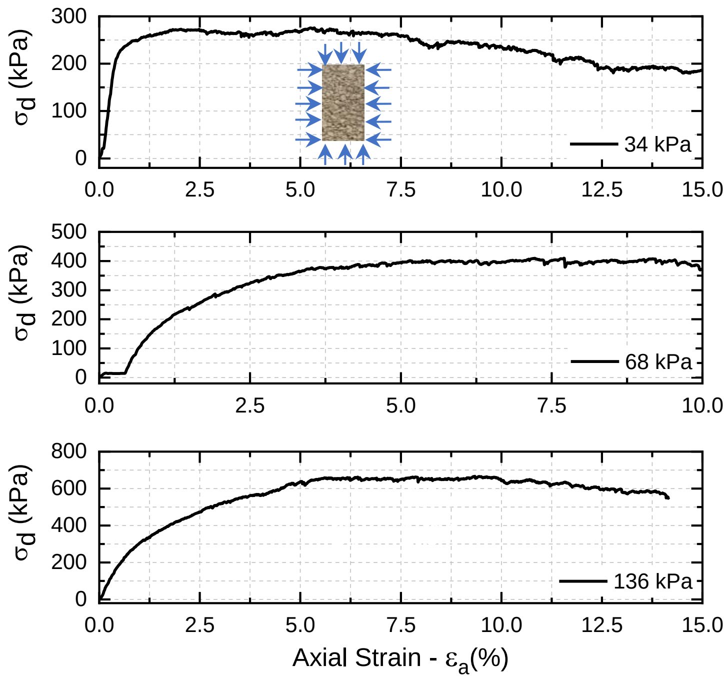

Figure 5-5 Deviatoric stress vs axial strain obtained from the CD triaxial test on the crushed rock.

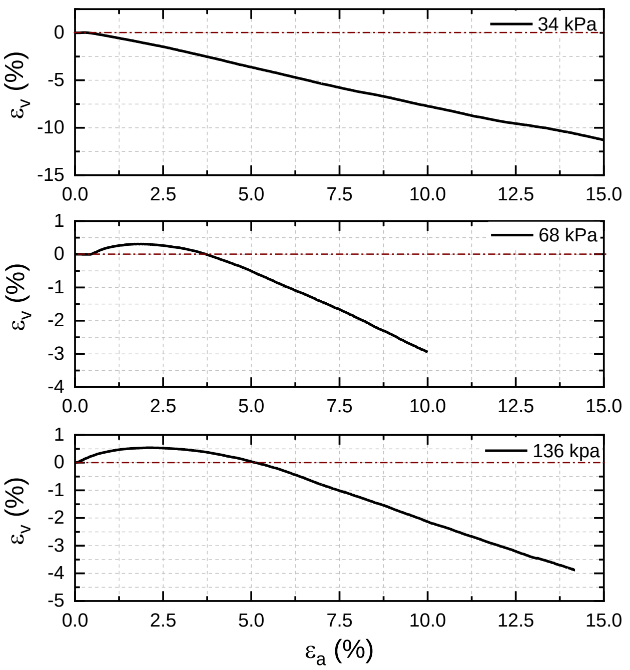

Figure 5-6 Volumetric strain vs axial strain obtained from the CD triaxial test on the crushed rock.

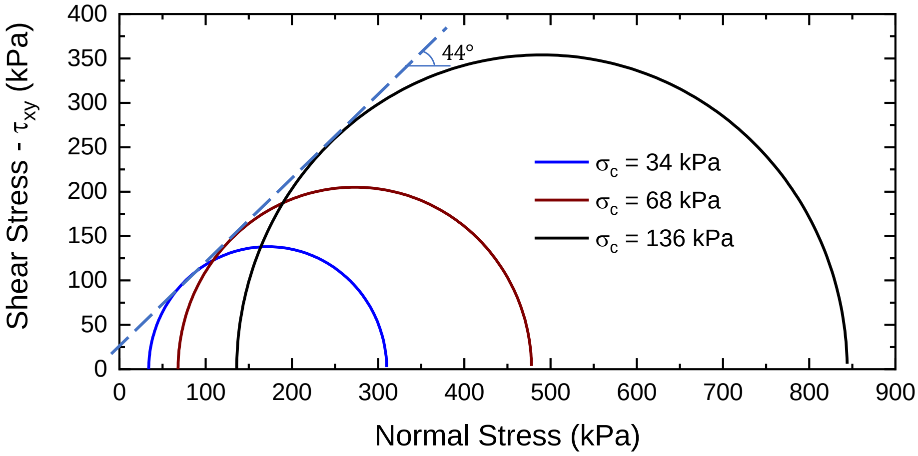

Figure 5-7 Mohr circle for the CD test on the crushed rock.

Figure 5-7 shows the Mohr circle diagram for the CD triaxial test on the crushed rocks. Based on the Mohr circle the angle of internal friction for the crushed rock was estimated at 44°. It should be noted herein that a small cohesion (25 kPa) was also observed for the crushed rock sample. A similar observation was reported by Arulrajah et al. (2012). The value of the Young's modulus as estimated from the CD test was 2.9 MPa approximately (for σ_c = 7 kPa) and was close to the value of the constrained modulus as observed from the 1-D compression test (2.5 MPa for σ_v = 7 kPa). Thus, the Young's modulus value recorded from the CD test was used as the input parameter for numerical modelling. Table 5-1 summarizes the properties obtained for the crushed rocks based on various geotechnical experimentations.

Table 5-1 Material properties for the crushed rock.

Sr. No.	Crushed rock property	Value (Unit)
1.	Maximum dry density	1790 kg/m^3
2.	D_{60} size	6 mm
3.	D_{30} size	4.2 mm
4.	Constrained modulus	2.5 MPa (for σ_v = 7 kPa)
5	Young's modulus	2.9 MPa (for σ_c = 7 kPa)
6.	The angle of internal friction	44°
7.	Poisson's ratio	0.45
8.	Dilation angle	19°.

5.3. Finite element (FE) modelling of seismic actions on the earth retaining structures

FE modelling of the seismic actions on the earth retaining structures was performed using FE software Abaqus. It was decided to evaluate the capability of the FE software for replicating the shaking table experiment results. The following steps were followed to develop a FE model for the scaled down base restrained RW.

5.3.1 Geometrical modelling of the scaled down RW (base restrained) model

Two-dimensional (2D) geometry of the scaled down base restrained RW model was developed using FE simulation software Abaqus (Abaqus User's Manual, 2013). Geometrical details of the two-dimensional (2D) FE model is shown in figure 5-8. It should be noted here that the RW is a plane strain problem (Aggour and Brown, 1973; Wood, 1973; Nadim and Whitman, 1983; Siddarthan and Maragakis, 1987). Therefore, the FE model of the RW was developed for plane strain conditions. Different parts such as the Aluminum wall, backfill, foam layer, shaking table base and back wall were modelled and meshed separately, and later assembled in the assembly section of Abaqus. An Aluminium wall of 0.4 m height and 4 mm thickness was modelled in front of the 1.72 m long and 0.4 m high backfill. A 10 mm thick high-density foam layer was also modelled at the back face of the backfill. The Aluminum RW was constrained with the shaking table base with the help of steel angle sections (40mm x 40 mm x 4mm). For simplicity and a better mesh quality only the outside angle section is modelled for constraining the RW with the model base. The cartesian directions "*x*" and "*y*" are also shown in figure 5-8 for the 2-D plane strain FE model. The stresses and displacements are positive in increasing "*x*" and "*y*" directions.

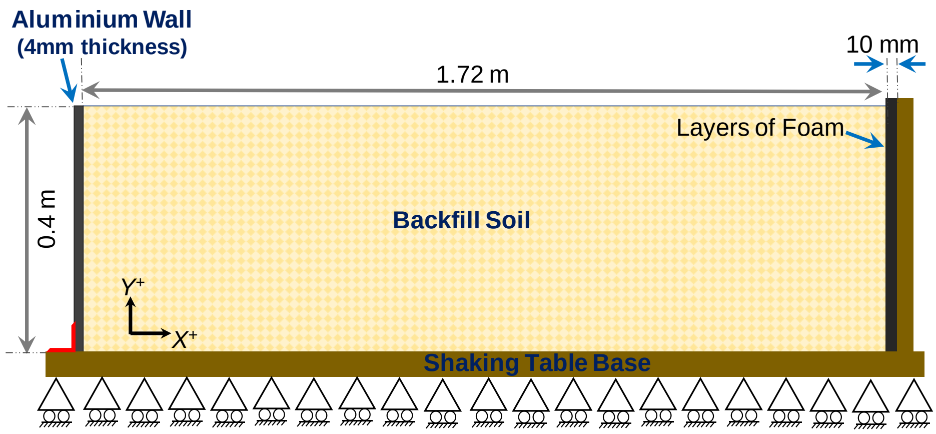

Figure 5-8 Details of scaled down RW (base restrained) FE model.

5.3.2. Material modelling

The Aluminum RW, high-density foam and the shaking table base were modelled using elastic material properties. Table 5-2 shows the material properties for all the materials considered in the FE modelling.

Table 5-2 Material properties for the FE model.

Sr. No.	Material	Density (Kg/m^3)	Elastic Modulus (Gpa)	Poisson's Ratio
1.	Retaining Wall	2700	69	0.33
2.	Backfill	1790	0.00290	0.45
3.	Angle, Base	7800	200	0.3
4.	Base Wood	1000	100	0.3
5.	Foam	2000	0.1	0.4

5.3.3. Constitutive modelling of the backfill "Mohr Coulomb material model"

Realistic and accurate constitutive modelling of the soil is an important aspect of FE modelling. Various constitutive models are available in several FE software packages. However, the validity of the constitutive models should be checked against experimental results for ensuring the capability of the constitutive models in replicating realistic and accurate seismic response behaviour of the backfill. The Mohr Coulomb model is a popular material model for numerical modelling of the soil in the post yield phase. Several researchers employed the Mohr Coulomb material model for numerical modelling of the soil with stipulated loading conditions (Yimsiri, et al., 2004; Song, 2012; Ghandil and Behnamfar, 2015). FE software Abaqus has inbuilt Mohr Coulomb model to simulate yielding of the soil. The hardening/softening of soil (crushed rock) could be simulated by calibrating the Mohr Coulomb material model against triaxial test results (Song, 2012).

Figure 5-9 shows the Mohr Coulomb yield surface on the deviatoric and meridional stress plane. The slope of the Mohr Coulomb yield surface on the meridional stress plane is the angle of internal friction (ϕ) of the soil. The intercept in the shear stress plane is the cohesion (c) parameter.

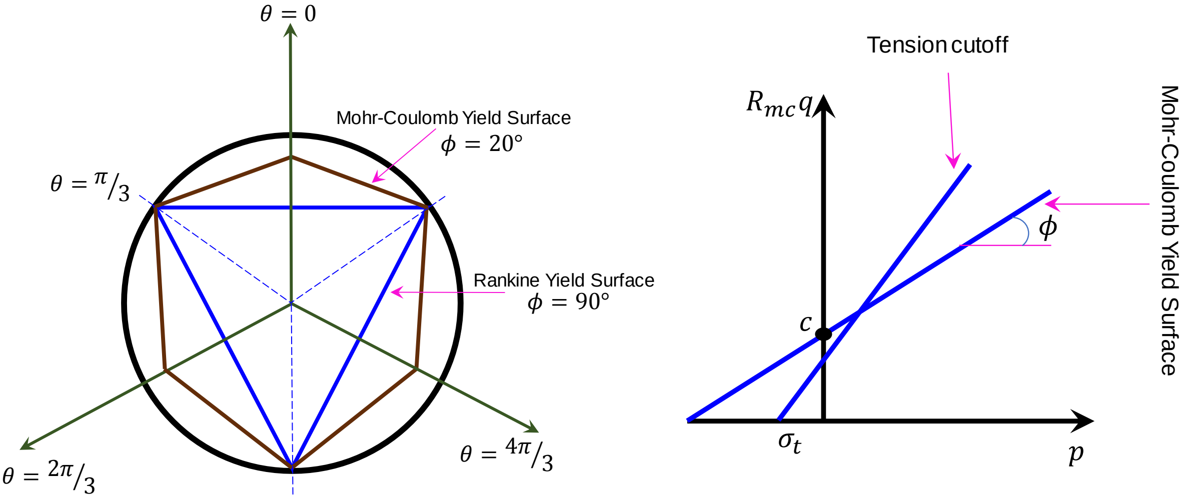

(a) Mohr Coulomb yield surface at the deviatoric stress plane

(b) Mohr Coulomb yield surface at the meridional plane

Figure 5-9 Mohr Coulomb yield surface at the deviatoric and meridional place (Abaqus User's Manual, 2013).

The angle of internal friction (ϕ) and cohesion (*c*) can be used for identifying the stress state, as explained by equation (5.3):

$$F = R_{\mathrm{mc}}q - p\tan\phi - c = 0 \tag{5.3}$$

In the above expression; the value of R_{mc}, depends on the deviatoric polar angle (θ_p) and the angle of internal friction (ϕ). R_{mc} is defined by equation (5.4),

$$R_{\mathrm{mc}}(\theta_{\mathrm{p}}, \phi) = \frac{1}{\sqrt{3}\cos\phi}\sin\left(\theta_{\mathrm{p}} + \frac{\pi}{3}\right) + \frac{1}{3}\cos\left(\theta_{\mathrm{p}} + \frac{\pi}{3}\right)\tan\phi \tag{5.4}$$

where, the deviatoric polar angle (θ_p) is defined as:

$$\cos(3\theta_{\mathrm{p}}) = \left(\frac{r}{q}\right)^3 \tag{5.5}$$

where, "*q*" is the mises equivalent stress or deviatoric stress:

$$q = \sqrt{\frac{3}{2}(s:s)} \tag{5.6}$$

and "r" depends on the deviatoric stress (third invariant).

$$\mathrm{r} = \left(\frac{9}{2}s.s:s\right)^{1/3} \tag{5.7}$$

The Mohr Coulomb model in Abaqus uses an elliptical function for smoothening the yield surface at the corners of the hexagon (figure 5-9a) as proposed by Menetrey and Willam (1995).

Flow rule (shown in equation 5.9) for the Mohr Coulomb plasticity can be used to simulate the hardening and softening behaviour of the soil,

$$d\varepsilon^{p} = \lambda\frac{\partial G}{\partial \sigma} \tag{5.8}$$

$$G = \sqrt{(\varepsilon c|_0 \tan\psi)^2 + (R_{\mathrm{mw}}q)^2} - p\tan\psi \tag{5.9}$$

where, G is the flow potential and ψ is the dilation angle of soil at "$p - R_{\mathrm{mw}}q$" plane, $\mathbf{c|_0}$ is the yield stress in cohesion. $\boldsymbol{\varepsilon}$ refers to the eccentricity on the meridional stress plane.

$$R_{\mathrm{mw}}(\theta, e) = \frac{4(1-\mathrm{e}^2)\cos^2\theta + (2\mathrm{e}-1)^2}{2(1-\mathrm{e}^2)\cos\theta + (2\mathrm{e}-1)\sqrt{4(1-\mathrm{e}^2)\cos^2\theta + 5\mathrm{e}^2 - 4\mathrm{e}}} R_{\mathrm{mc}}\left(\frac{\pi}{3}, \phi\right) \tag{5.10}$$

$$R_{\mathrm{mc}}\left(\frac{\pi}{3}, \phi\right) = \frac{3-\sin\phi}{6\cos\phi} \quad \text{(triaxial compression condition)} \tag{5.11}$$

$$e = \frac{3-\sin\phi}{3+\sin\phi} \tag{5.12}$$

where, e is the deviatoric eccentricity, which is the ratio of the shear stress along extension and compression meridian, and define out of roundness of the deviatoric section.

The deviatoric eccentricity (e) becomes a function of the friction angle when the lodge angle

$(\theta = \frac{\pi}{3})$

$$R_{\mathrm{mw}}\left(\frac{\pi}{3}, e\right) = R_{\mathrm{mc}}\left(\frac{\pi}{3}, \phi\right) = \frac{3-\sin\phi}{6\cos\phi} \tag{5.13}$$

It should be noted that the hardening and softening of the backfill material can be controlled by the cohesion and plastic strain options available in Abaqus. Calibration of the triaxial experimental data can be performed for the generation of hardening/softening rules for any given soil. The detailed process for calibration of the Mohr Coulomb model with the hardening/softening behaviour of the soil is explained by Potts and Zdravkovic (1999) and Song (2012).

The hardening and softening behaviour of the backfill material can be specified by the use of cohesive yield stress (c) and equivalent plastic strain ($\bar{\boldsymbol{\varepsilon}}^{\boldsymbol{pl}}$) options available in the MC model of FE software Abaqus. Detailed explanations of the process of calibrating the MC model with respect to the hardening/softening behaviour of the soil can be found in Potts & Zdravkovic (1999) and Song (2012). Relationship between the cohesive yield stress (c) and equivalent plastic strain ($\bar{\boldsymbol{\varepsilon}}^{\boldsymbol{pl}}$) can be simulated using five points for controlling the hardening/softening behaviour of the backfill. These five control points representing the elastic state, peak, softening, plastic and final state can be inferred from triaxial test results for a given level of confinement (Figure 5-10).

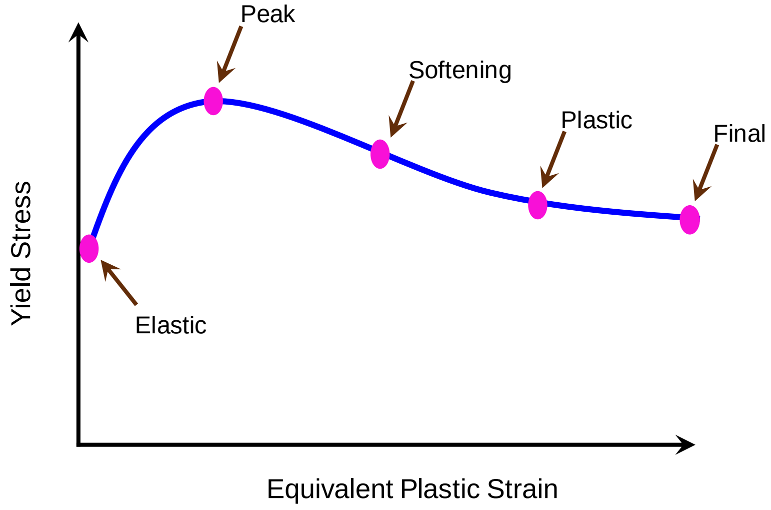

Figure 5-10 Generation of the hardening/softening curve for the backfill, using five control points (Song, 2012).

The triaxial test data can be used to define the elastic state, peak stress, softening stress, and plastic stress. The following formulations can be used to calculate the control points (Song, 2012).

$$E = \frac{\sigma_{\mathrm{d,el}}}{\varepsilon_{\mathrm{el}}} \tag{5.14}$$

$$\upsilon = -\frac{1}{2}\left(1 - \frac{\varepsilon_{\mathrm{v,el}}}{\varepsilon_{\mathrm{el}}}\right) \tag{5.15}$$

$$\phi = \tan^{-1}\left(\sqrt{\left(\frac{\left[\left(\sigma_{\mathrm{d,el}}/2\right) + \sigma_{\mathrm{c}}\right]^2}{\left[\left(\sigma_{\mathrm{d,el}}/2\right) + \sigma_{\mathrm{c}}\right]^2 - \left(\sigma_{\mathrm{d,el}}/2\right)^2}\right) - 1}\right) \tag{5.16}$$

$$\psi = \sin^{-1}\left(\frac{\varepsilon_{\mathrm{v,el}} - \varepsilon_{\mathrm{v,pl}}}{2\left(\varepsilon_{\mathrm{pl}} - \varepsilon_{\mathrm{el}}\right) + \left(\varepsilon_{\mathrm{v,el}} - \varepsilon_{\mathrm{v,pl}}\right)}\right) \tag{5.17}$$

$$c = \frac{(\sigma_{11} - \sigma_{22}) - (\sigma_{11} + \sigma_{22})sin\phi}{2cos\phi} \tag{5.18}$$

$$\bar{\varepsilon}^{pl} = \frac{\sigma_{11} \times \varepsilon_{11}^{p} + 2\left(\sigma_{22} \times \varepsilon_{22}^{p}\right)}{c} \tag{5.19}$$

The Mohr Coulomb yield function ($R_{mc}q$-ptanϕ-c=0) can be used to calculate the cohesive yield stress. The relationship between the strain work and yield stress can be used to calculate the equivalent plastic strain (Song, 2012). Figure 5-11 is a flow chart summarizing the procedure for obtaining the five control points (of Figure 5-10) using triaxial test data.

5.3.4. Calibration of the Mohr Coulomb model with the CD triaxial test data

Calibrations have been performed on the Mohr Coulomb model available in the FE software Abaqus for replicating the constitutive behaviour of crushed rocks (the backfill material) as obtained from the CD triaxial tests conducted by the author. One element test has been carried out in the FE software Abaqus, using an axisymmetric geometry. The FE simulations of the CD triaxial test on the crushed rock have been performed for four confinement pressures: 7, 34, 68 and 136 kPa respectively. Material properties of the crushed rock are shown in table 4-1. The hardening and the softening control points have been calculated based on the deviatoric stress and the axial strain data as obtained from the CD triaxial test. Figure 5-12 shows the cohesion yield stress vs equivalent plastic strain curve as obtained from the five-point calculations as mentioned in section 5.3.3 and explained by Potts and Zdravkovic (1999) and Song (2012).

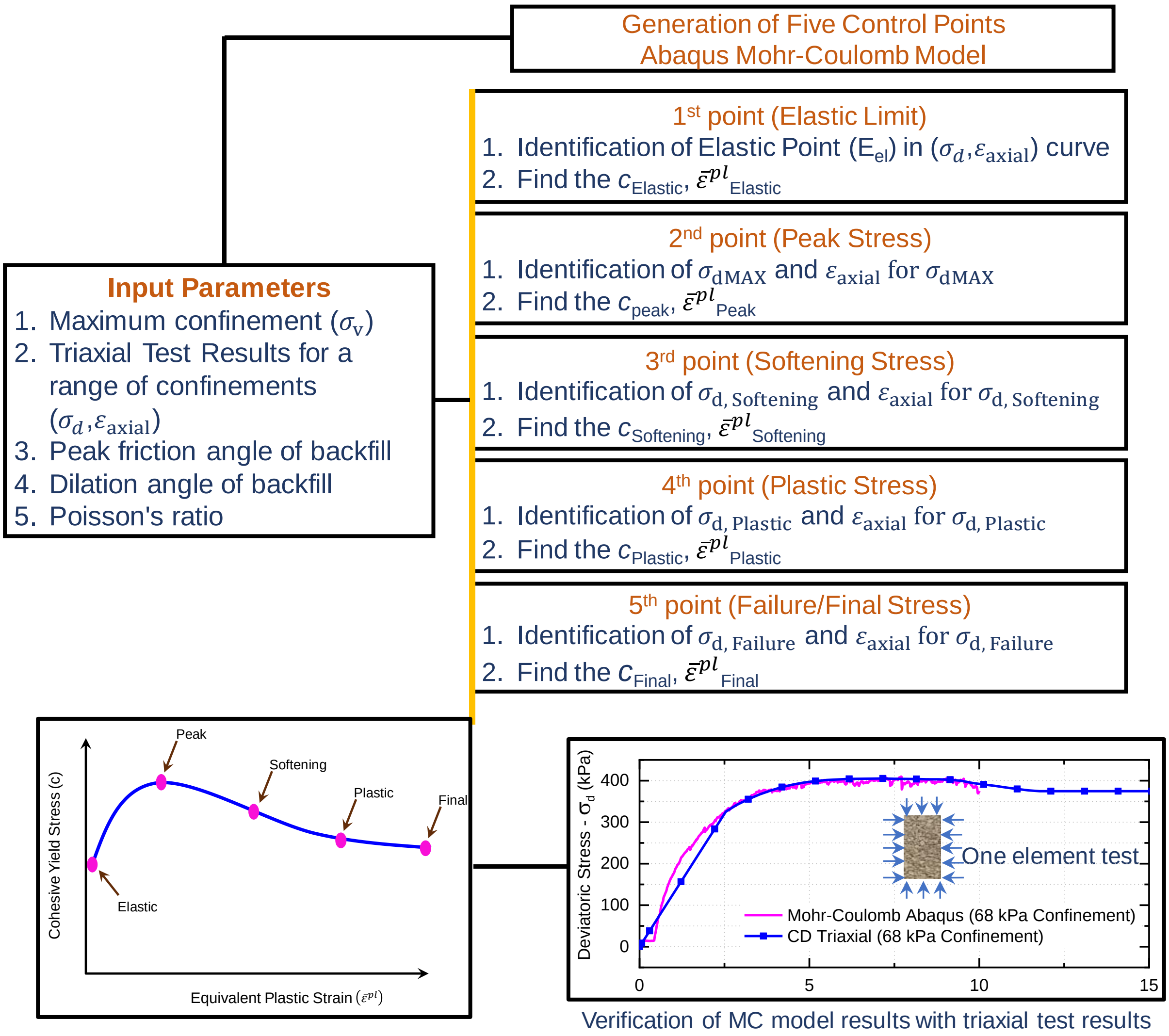

Figure 5-11 Procedure to obtain five control points of the hardening/softening curve of backfill, (based on Song, 2012).

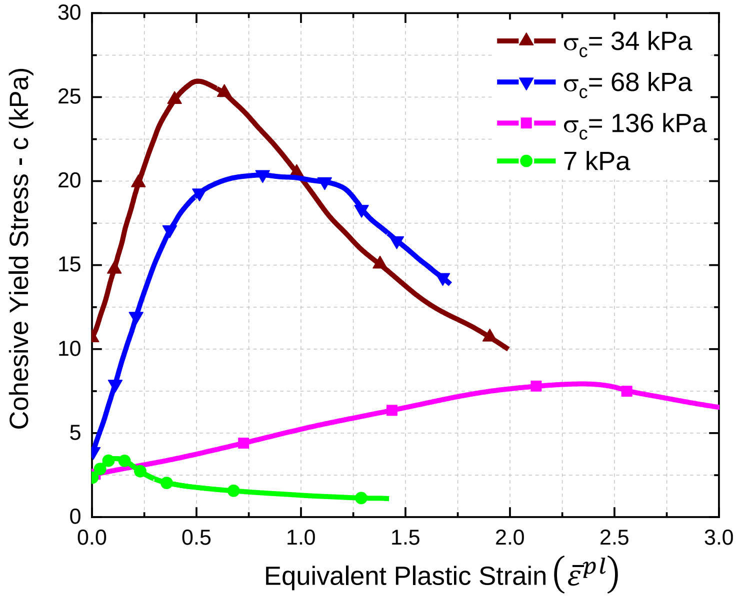

Figure 5-12 Curves for controlling the hardening and softening of the crushed rock for CD triaxial test performed at The University of Melbourne.

The static analyses in the FE software Abaqus have been performed in two steps. The first step was a geostatic step; for maintaining the equilibrium conditions following the initial application of the stresses (confinement). The second step was a soils step, in which the consolidation and the shearing of the crushed rock have been performed. The confinement has been applied at the specimen boundaries. A total 10 hours of consolidation was performed (enough for the crushed rock as observed during CD triaxial tests). Zero pore pressure has also been defined at the top of the FE model to simulate the drained conditions of the CD test. The shearing of the soil specimen then performed by applying a very slow strain rate of 0.033/min (%) at the sample top, while the sample base was restrained in the "*y*" direction in translation. Axisymmetric boundary condition was used at the plane of symmetry. Figure 5-13 shows the comparison of constitutive response obtained from the CD triaxial test and the FE simulations. Good agreement has been observed between the CD triaxial test and the FE results. Lateral shaking could initiate an additional thrust in the backfill resulting in an increase in the (vertical and lateral) confinement pressures (Siddharthan et al., 1994). The amount of such increase depends on the intensity of the applied excitations. As observed from numerical simulations of CD triaxial tests the MC model (which has been calibrated against a given level of confinement σ_c) is nonetheless able to give accurate simulations of the constitutive behaviour of the backfill when subject to a two-fold increase in the level of confinement.

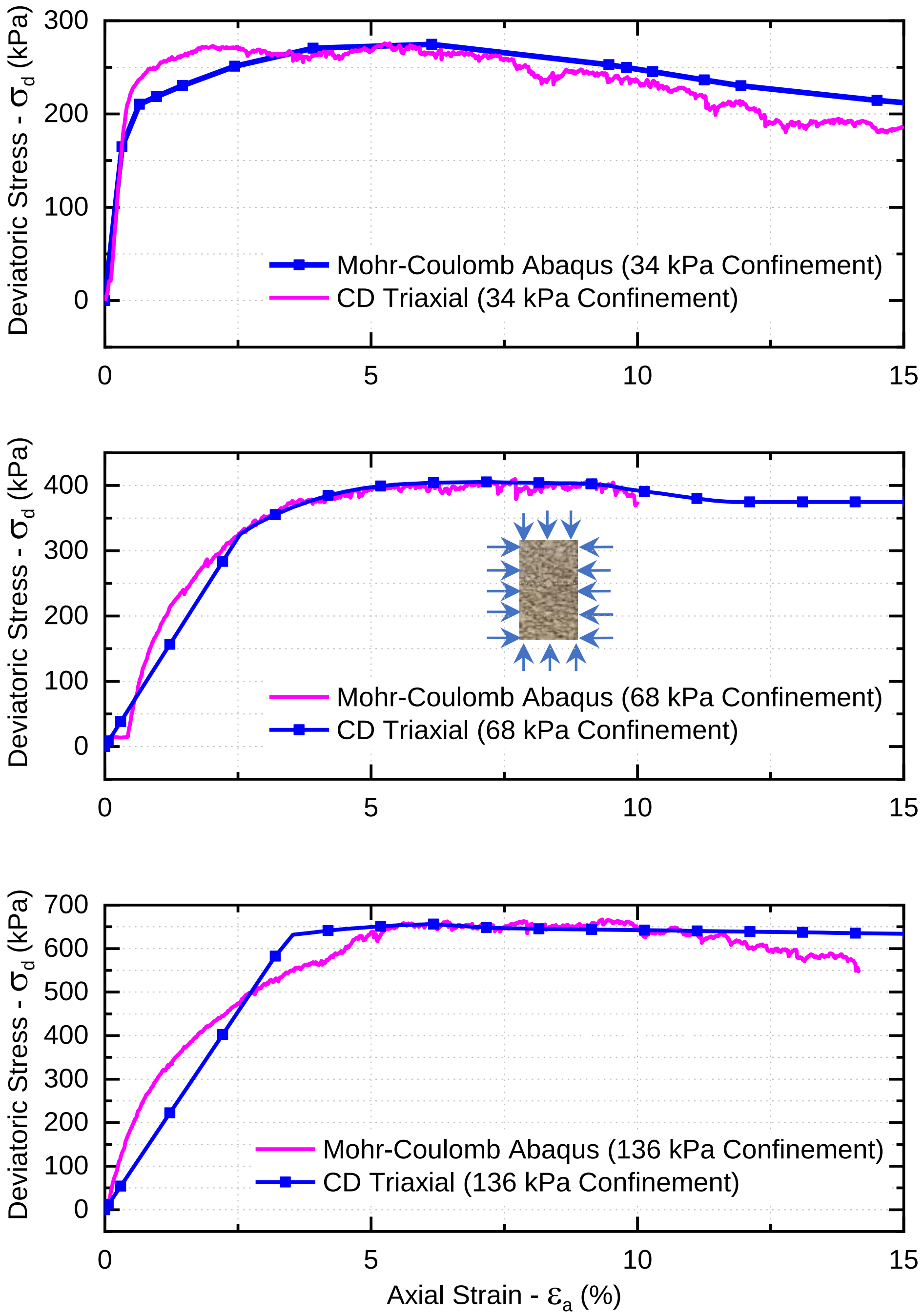

Figure 5-13 Calibration of the Mohr Coulomb material model to simulate the hardening/softening of the backfill (crushed rock).

5.3.5. Modelling of damping in the backfill

Damping is an important property of the backfill, especially when backfill is analyzed for the earthquake loading. It is not easy to model the accurate damping of the soil. However, the realistic modelling of soil damping could be achieved with the Rayleigh damping values (Ju and Ni, 2007). Therefore, in the present study the damping in the backfill has been modelled using the Rayleigh damping parameters.

The standard equation for the Rayleigh damping is shown in equation (5.20).

$$[C] = \alpha(M) + \beta(K) \tag{5.20}$$

where, $[C]$ is the damping, $[M]$ is the mass, and $[K]$ is the stiffness matrix. The first parameter α is a mass dependent parameter and second parameter β is a stiffness dependent parameter (Chopra, 2007).

Damping ratio (D) of the backfill is shown in equation (5.21).

$$D = \frac{1}{2}\left(\beta\omega + \frac{\alpha}{\omega}\right) \tag{5.21}$$

In the present study, values of α and β were estimated based on the natural frequency of the first two modes of vibration of the elastic soil column (backfill height, *H*) using the formulations given by equation (5.22) and (5.23). Both α and β are proportional to critical damping *D*1 and *D*2. In the present study *D*1 and *D*2 are both kept at 2.5%.

$$\alpha = 2\omega_1\omega_2(D_1\omega_2 - D_2\omega_1)/(\omega_2^2 - \omega_1^2) \tag{5.22}$$

$$\beta = 2(D_2\omega_2 - D_1\omega_1)/\pi[\omega_2^2 - \omega_1^2] \tag{5.23}$$

As explained in chapter 3, the shear wave velocity (V_{SH}) observed during the shaking table experiments on the scaled down RW model was close to the shear wave velocity estimated based on the use of the empirical relationship $V_{\mathrm{SH}} = \sqrt{\frac{G}{\rho}}$, = 24 m/sec where, *G* is the shear modulus ($G = \frac{E}{2(1+\upsilon)}$ = 1 MPa) and ρ is the density of the soil in assumed soil column behind the RW. The natural frequency of the soil column at the first and second mode is estimated using the following formulations:

$$f_1 = \frac{V_{SH}}{4H} \text{ or } T_1 = \frac{4H}{V_{SH}} \tag{5.24}$$

$$f_2 = \frac{3V_{SH}}{4H} \text{ or } T_1 = \frac{4H}{3V_{SH}} \text{(Eddine et al. 2017)} \tag{5.25}$$

Table 5-3 shows a comparison of the natural periods of scaled down backfill estimated during shaking table experiment and using the empirical relationship.

Table 5-3 Comparison of natural periods of backfill.

Method of estimation	**Natural period of fundamental vibration mode (second)**	**Natural period of second vibration mode (second)**
Measured on the shaking table	0.05	0.03
Estimated using the elastic soil column	0.07	0.02
Modelled in Abaqus	0.04	0.03

The capability of the proposed damping modelling approach has been verified with the results reported by Vucetic and Dobry (1991). Vucetic and Dobry (1991) studied the cyclic behaviour of the soils with different plasticity index (PI). Sandy soil with PI = 0 has been selected for comparison with the present damping model. The reference shear strain (γ_{ref}) was selected as 0.025 %, the initial viscous damping ratio (ξ_i) was selected to be 1.5 % and the maximum viscous damping ratio (ξ_{max}) was selected to be 16 %, as reported by Hardin and Drnevich model (Hardin and Drnevich, 1972). The following formulation was used to calculate the value of the equivalent viscous damping ratio ξ (as obtained from Rayleigh damping parameters) for a given shear strain (γ).

$$\xi = \xi_i + \xi_{max} \frac{\left(\frac{\gamma}{\gamma_{ref}}\right)}{\left(1 + \frac{\gamma}{\gamma_{ref}}\right)} \tag{5.26}$$

Figure 5-14 shows the comparison of the soil damping as obtained from the current modelling approach and reported by Vucetic and Dobry (1991). Good agreement has been observed between the proposed damping model and the results reported by Vucetic and Dobry (1991).

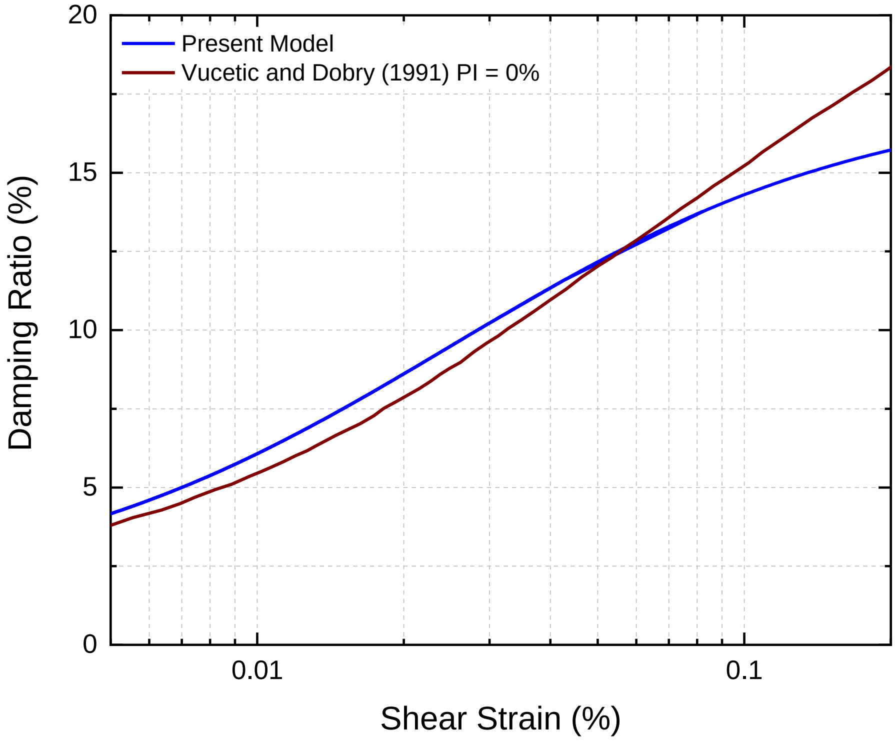

Figure 5-14 Comparison of the soil damping curve obtained from the proposed modelling approach and reported by Vucetic and Dobry (1991).

5.4. FE meshing, solution scheme and boundary conditions

Four node continuum plane strain element (CPE4R) with reduced integration, hourglass and distortion control scheme has been used for meshing the FE model. Figure 5-15 shows the FE mesh of the scaled down RW (base restrained) model. Free meshing style has been adopted to mesh the backfill. The structured mesh has been adopted to mesh other FE members. For increasing mesh accuracy, a denser mesh has been adopted at the RW-backfill interface and the backfill-base interface.

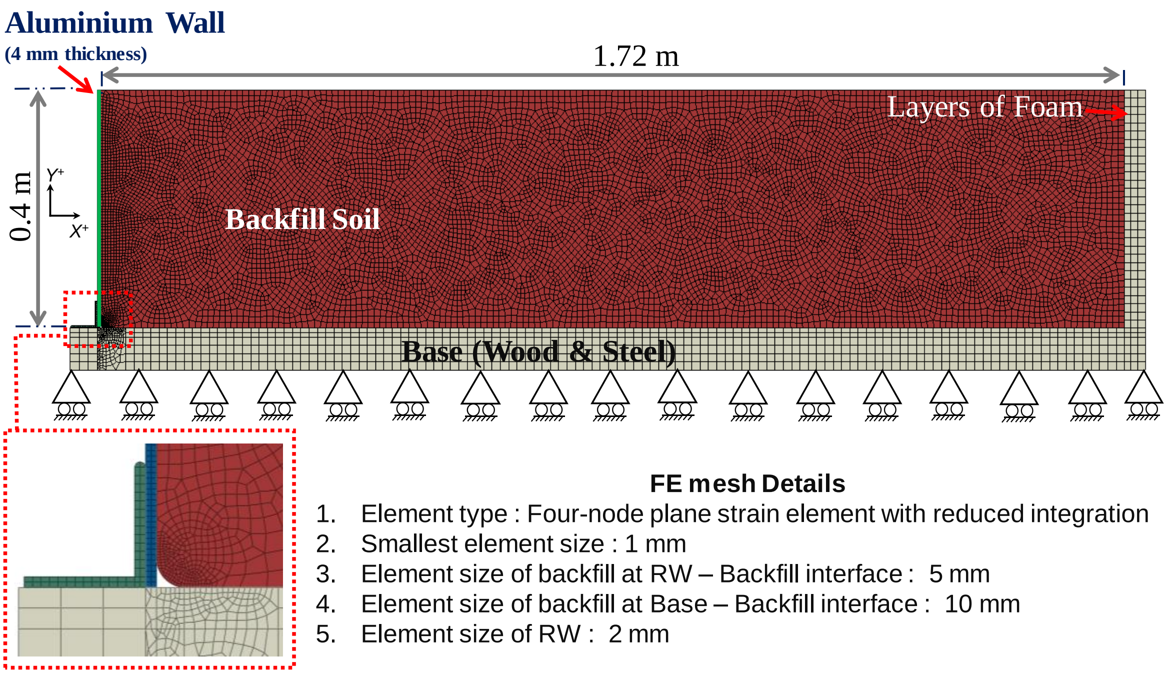

Figure 5-15 FE model of the scaled down RW (base restrained).

Nonlinear finite element analyses have been carried out using Abaqus explicit scheme, which is suitable for the large deformation problems (Abaqus/Explicit User's Manual, version 6.13. 2013). The interaction has been modelled as frictional contact in the tangential direction and "hard contact" in the normal direction. The coefficient of friction between the RW - backfill and foam - backfill is 0.64, and 0.1 respectively. It should be noted herein that during the high amplitude input pulses, the friction between the backfill and model base highly influence the overall displacement response of the RW (Hashemnia and Pourandi 2018). Therefore, all FE models have been calibrated for the coefficient of friction at interface of the backfill and the model base. Gravity loading was also applied on the scaled down FE RW model (base restrained), during the initial step.

Two types of boundary conditions have been adopted for the FE model. The first boundary condition was applied during the initial phase (no external loading) to satisfy equilibrium conditions, in which the vertical boundaries were restrained in lateral "*x*" direction, and the model base was restrained in vertical "*y*" direction. The geostatic stresses and void ratio have also been specified for the backfill during the initial phase. During the loading phase (dynamic explicit step), the base of the scaled down FE RW model was allowed to move in the "*x*" direction and restrained in the "*y*" direction. All pulses have been applied at the model base, during the dynamic explicit step. As mentioned earlier, the stresses are defined as positive for the increasing “*x*” and “*y*” direction.

5.5. Validation of the shaking table experiment results with FE simulations

An important stage of the shaking table experiments was to apply six excitation pulses with the purpose of validating the accuracies of the numerical model. Two half cycle sine pulse (shown in figure 4-16 of chapter 4), two one cycle sine pulse (shown in figure 4-17 of chapter 4) and two multiple pulses (shown in figure 4-20 of chapter 4) which were the targeted base excitations. Displacement of the shaking table base was captured during all the tests using laser sensors. The captured displacement time histories on the shaking table were used as input into the FE model as the base excitations (Figure A4 – 1). Figure 5-16 presents graphs showing a comparison of the relative displacement measured at the top of the RW with results from numerical simulations demonstrating good consistencies (when damping in the soil has been ignored in the simulations). Figure 5-17 shows further comparison when Rayleigh damping has been incorporated. Good agreement between the measured and simulated results is well demonstrated. Figure 5-18 shows the comparison of acceleration time histories at the top of the wall and the upper surface of the backfill also demonstrating good agreement. A few isolated anomalous acceleration spikes are featured in the measurements. Their influence on the behaviour of the RW was not noticeable because of their very short duration.

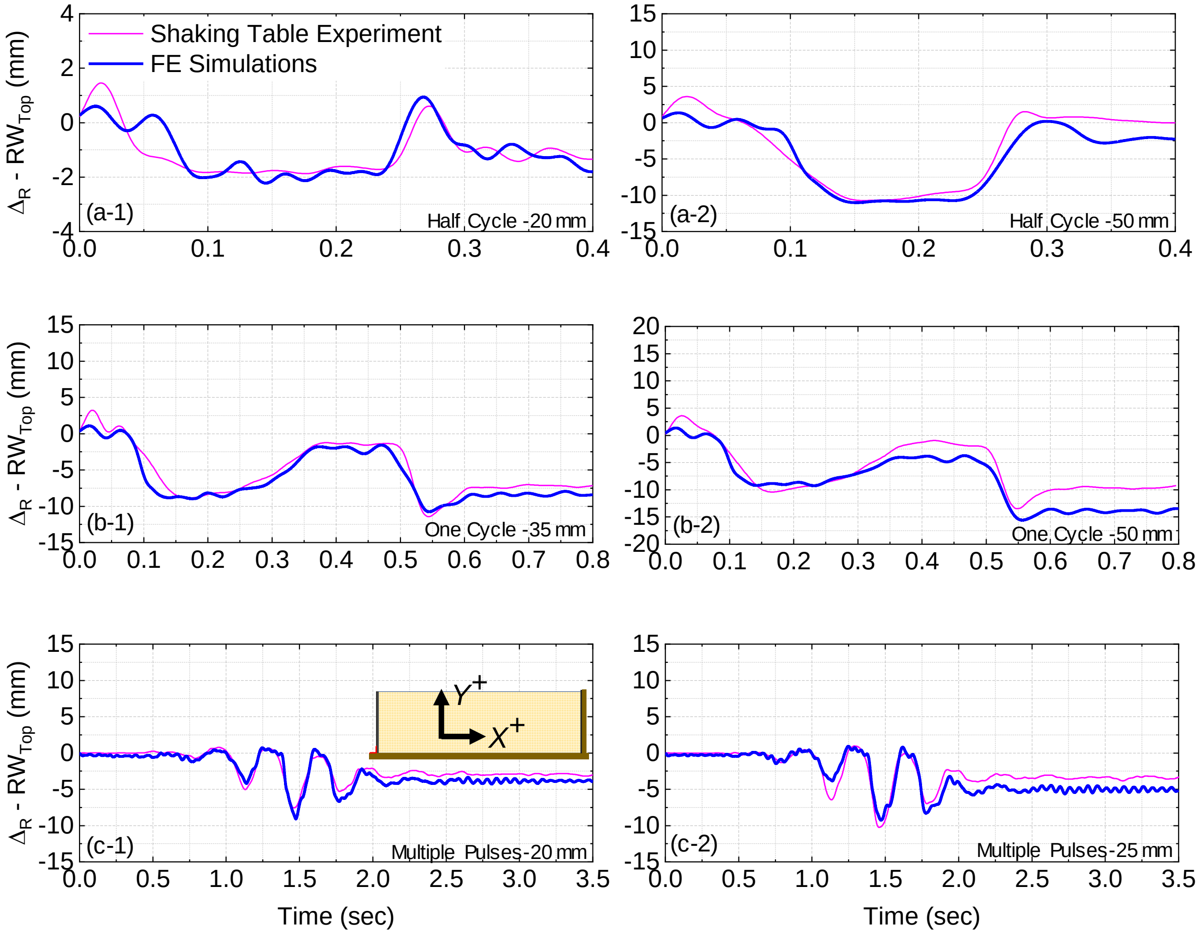

Figure 5-16 Comparison of measured and simulated relative displacement of RW.

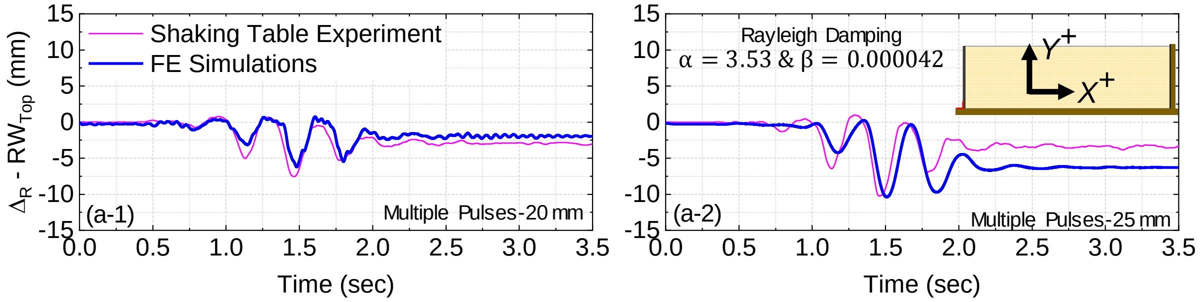

Figure 5-17 Comparison of measured and simulated relative displacement of RW (incorporating damping in the backfill).

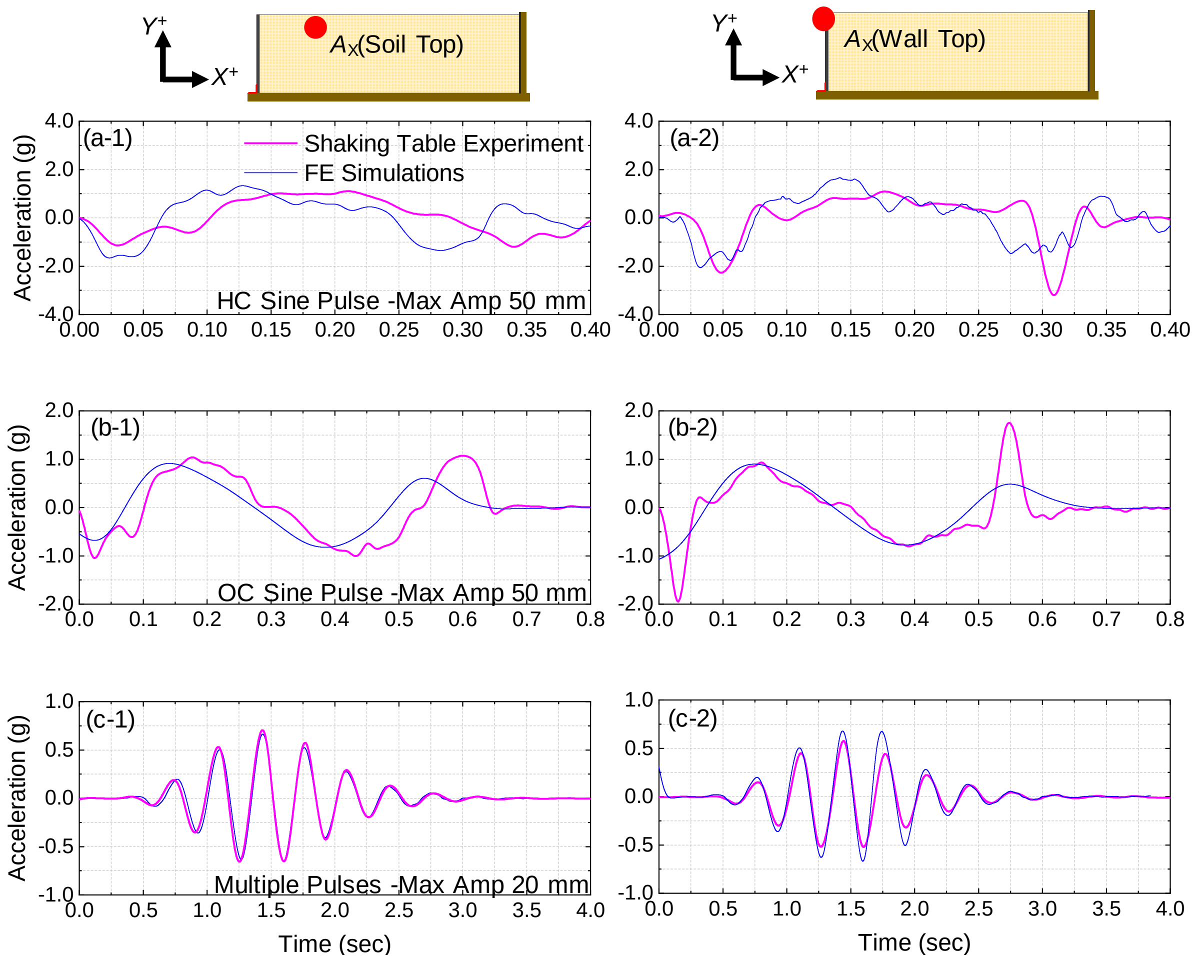

Figure 5-18 Comparison of measured and simulated accelerations on the RW base and backfill.

5.5.1 FE simulations on a base restrained prototype RW (with reflective boundary conditions)

FE modelling of a RW and backfill in seismic conditions based on a scale down factor (λ) of 10 has been presented in the earlier part of this chapter. This section presents the extension of the FE model simulations for the prototype RW (refer Figure 5-19). The procedure for applying FE simulations of the scaled down and prototype RW is basically the same. The prototype RW model was based excited by a string of pulses with a displacement amplitude which was 20 mm (as measured on the shaking table by displacement transducers during the scaled down experimentation) multiplied by a scaling factor ($\lambda_l = \frac{l_p}{l_s} = 10, \lambda_{\Delta t} = \frac{\Delta t_p}{\Delta t_s} = \sqrt{\lambda_l}$) as per the rule of dynamic similitude (Moncarz & Krawinkler, 1981). This same scaling factor is to be applied for making comparisons of the simulated results with measurements from the physical shaker table tests (of the scaled down model). Figure 5-20 presents such comparison for the relative displacement at the top of the RW when neglecting damping in the soil (Figure 5-20a), and when Rayleigh damping has been incorporated in the simulations (Figure 5-20b). Good agreement between the measured and simulated results is demonstrated in both cases.

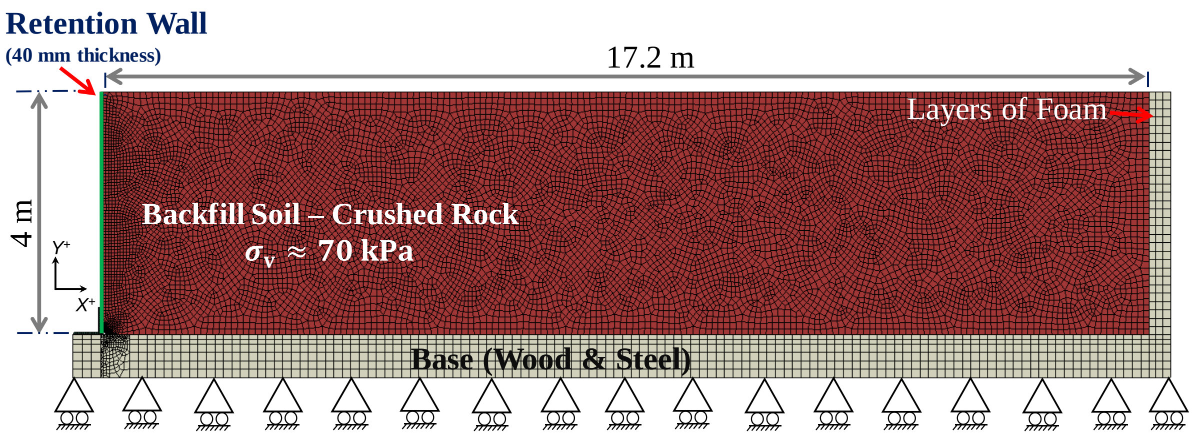

Figure 5-19 FE model of the prototype RW.

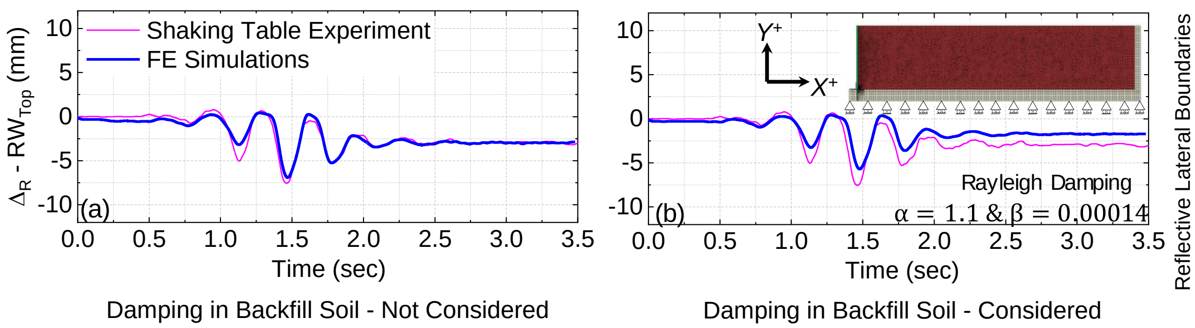

Figure 5-20 Comparison of measured (shaking table experiment) and simulated (prototype RW) relative displacement.

5.5.2 FE simulations on a base restrained prototype RW (with absorptive boundary conditions)

The backfill domain in the scaled down model should ideally be of sufficient length to emulate real conditions and to minimize wave reflections from boundaries which are purely artefacts of the experimental setup. However, modelling the geometry of the backfill as per real conditions can result in a very high demand on computer memory and computational time (Kuhlemeyer & Lysmer, 1973; Cakir, 2013). To circumvent around this issue a backfill of reduced dimension accompanied by an absorptive (viscous) boundary at the far end was incorporated into the modelling as shown in Figure 5-21 which presents the use of spring and dashpots at the designated boundary as per recommendations by (Cakir, 2013). Guidance on the stiffness and damping parameters of the springs and dashpots can be found in the Abaqus/Explicit User's Manual. This modified FE model of the prototype RW was subject to the same base excitations as applied to the model presented in the previous section. Figures 5-22a and 5-22b show comparisons of the simulated (scaled down) displacement time-histories for the top of the RW (without and with damping) against measurements from the shaking table tests in which absorption at the far end of the backfill was effected by the use of a layer of foam (Figure 4-2c of chapter 4). Good agreement between the measured and simulated results is once again demonstrated. Figure 5-23 shows a flow chart summarizing the procedure for obtaining a FE model of RW.

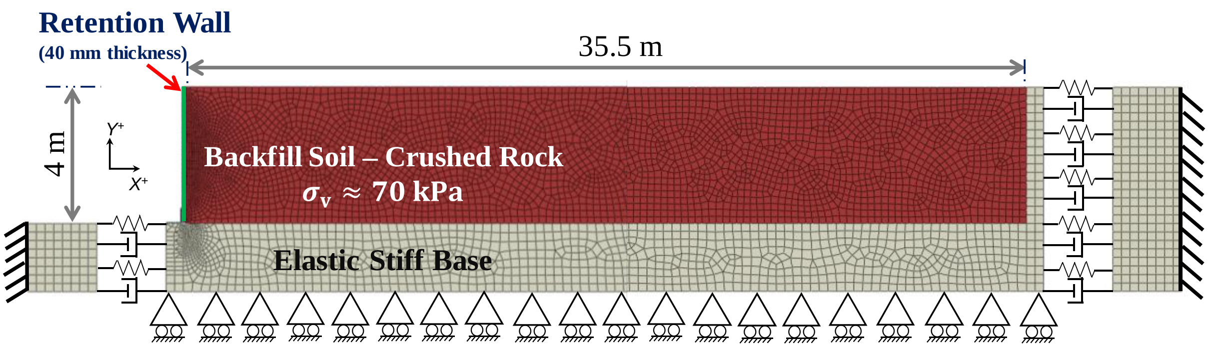

Figure 5-21 FE model of the prototype RW with spring and dashpot boundary conditions.

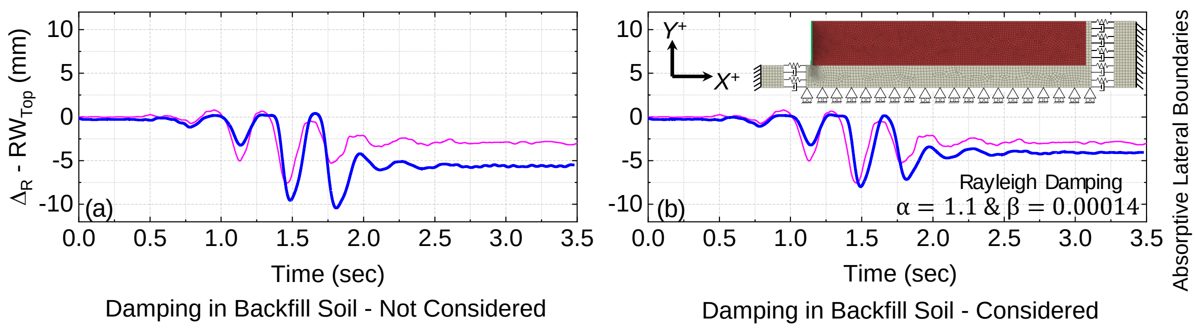

Figure 5-22 Comparison of measured (shaking table experiment) and simulated (prototype RW with spring and dashpot boundary) relative displacement.

Figure 5-23 Flow chart for FE modelling of seismic actions in earth retaining walls.

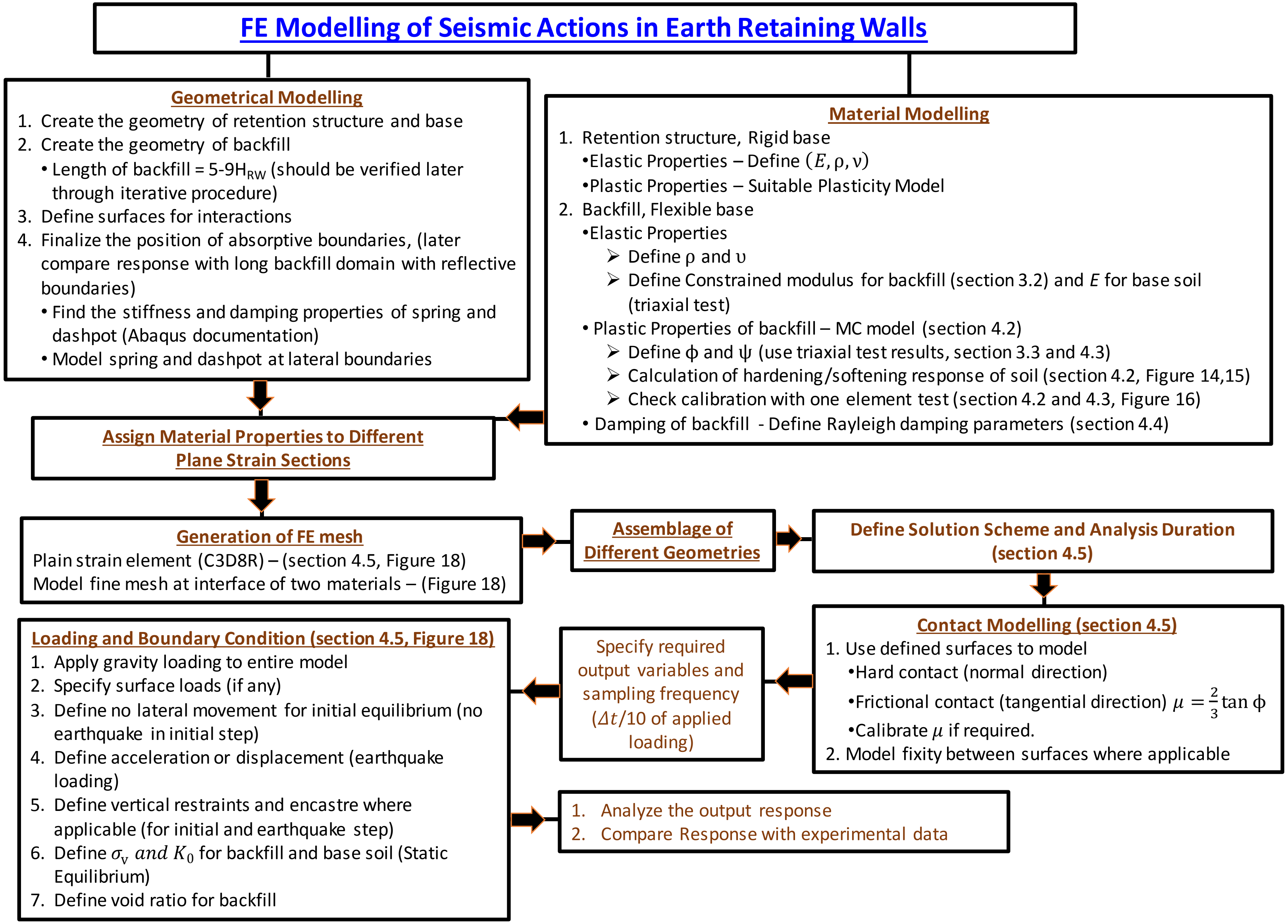

5.6. Chapter summary

Detailed geotechnical investigations have been carried out on the crushed rock samples, which were also used for the construction of the backfill behind the scaled down RW model. The engineering properties and constitutive behaviour of the backfill (crushed rock) have been used for developing a FE model of the backfill. Details of the Mohr Coulomb material model has also been presented. Calibration of the triaxial test data for simulation of the hardening and softening behaviour of the backfill has also been explained. The capability of the Mohr Coulomb material model has been evaluated for replication of the CD triaxial test results. Modelling of the Rayleigh damping for the backfill has also been explained. The geotechnical expertise and confidence gained from a detailed geotechnical investigation have been used to apply FE modelling of the seismic actions on the scaled down base restrained RW. Details of the FE modelling of seismic actions on the RW have been presented. The capability of FE models for replication of the shaking table experiment results has been well demonstrated as evidenced by good agreement between the shaking table experiments and FE simulations.

Chapter 6. SEISMIC BEHAVIOR OF BASE RESTRAINED EARTH RETAINING STRUCTURES

6.1. Introduction

The detailed shaking table experiments on base restrained retaining wall highlights the requirement of a detailed and rigorous investigation of seismic actions on the base restrained earth retaining structures. The present chapter outlines the seismic response behaviour of base restrained earth retaining structures. A detailed and rigorous finite element (FE) investigation has been performed on a base restrained retaining wall (RW) model. The knowledge gained from the shaking table experimental program has also been used for developing the FE model for the base restrained RW. The effects of earthquake actions on the base restrained RW have been investigated using different base excitations. Parametric investigations have also been performed for different backfill material types behind the RW. Reinforced concrete (RC) of the RW has been modelled using the concrete damaged plasticity (CDP) model, and the backfill behind the RW has been modelled using the Mohr Coulomb material model. The hardening and softening behaviour of the backfill have also been simulated by calibrating the Mohr Coulomb model parameters with triaxial test results. The optimum mesh and domain size for the FE model has also been investigated by performing a detailed mesh convergence and domain size study. The springs and dashpots have also been used at boundaries of the FE model for minimizing the boundary effects during the nonlinear time history analyses. The hand calculations were also proposed to estimate the earthquake induced displacement of the base restrained RW.

6.2. Two dimensional (2D) plane strain finite element (FE) modelling of the base restrained retaining wall (RW)

The two-dimensional (2D) plane strain FE model of the base restrained RW has been developed using FE software Abaqus (Abaqus User's Manual, 2013). It was assumed that the RW and backfill is founded over the rock outcrop. As discussed in chapter 5, the RW could be analyzed using the 2D (plane strain) or 3D (three-dimensional) stress state. However, similar results were obtained from nonlinear time history analyses of the 2D and 3D concrete wall models (A2.1.). Figure 6-1a shows the geometrical features of the base restrained RW model considered for the FE investigations. The RC RW, backfill and base rock have been modelled using 2D solid sections. The four node bilinear plane strain quadrilateral elements with reduced integration and hourglass control (CPE4R) have been used to generate the FE mesh. Structural elements have been used to mesh the RW, and free elements have been used to mesh the backfill and base rock.

The steel reinforcement (rebar) has been meshed using beam element (B31). Figure 6-1b shows the reinforcement details of the base restrained RW. The 25 mm diameter steel bar has been used as the primary rebar (backfill side) with 250 mm c/c spacing. The 16 mm diameter bar has been used as secondary rebar with 250 mm c/c spacing. The Base of the RW has also been reinforced using the 16 mm diameter rebars with 250 mm c/c spacing.

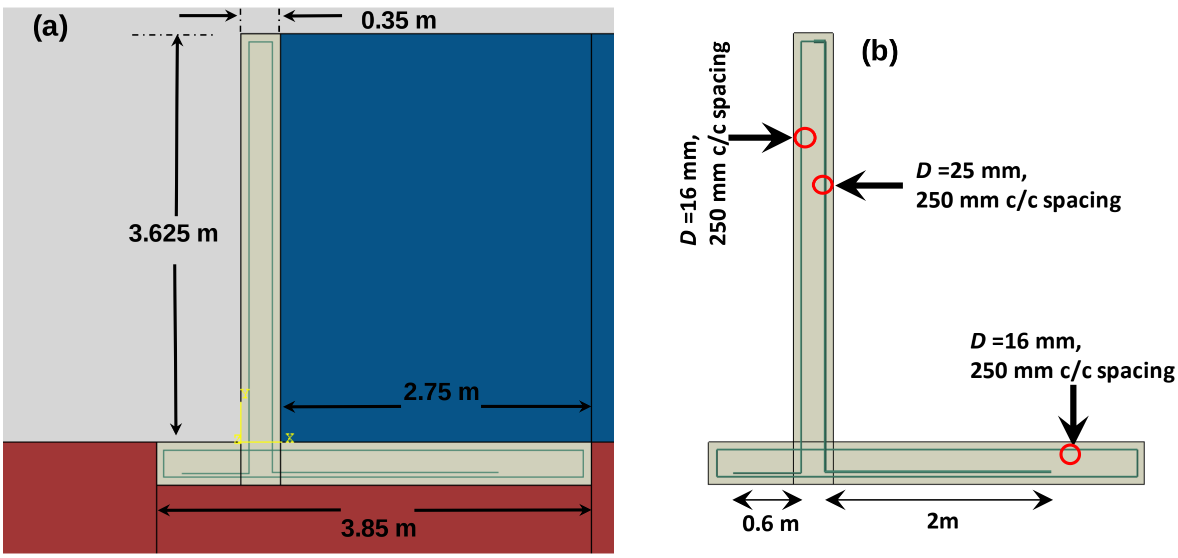

Figure 6-1 Geometrical details of the base restrained RW.

The rebar frame has been embedded inside the RW using the embedded region option available in Abaqus. Figure 6-2 shows the 2D plane strain FE model of the base restrained RW; founded on a stiff rock outcrop (base rock). The FE mesh of 2D RW model has also been shown in figure 6-2. The base of the RW has been restrained with the base rock by modelling fixity between the base of the RW and the top surface of the base rock. Contact elements have been used to model the following interfaces:

(i) the backfill and the base rock,

(ii) the RW stem and the backfill,

(iii) the RW heel slab and the backfill.

The surface to surface contact was modelled using frictional contact in the tangential direction. A frictional coefficient of $\frac{2}{3}\tan\phi$ has been specified for modelling the frictional contact, where ϕ is the angle of internal friction of the backfill. To prevent mesh penetration and pressure overclosure a hard contact has also been modelled in the normal direction for the above mentioned surfaces. Master and slave surfaces have also been specified for every contact definition.

The acceleration and displacement controlled type boundary conditions have been used for the FE model. The base of the FE model is free to translate in "*x*" direction (lateral direction) and restrained in "*y*" direction (vertical direction). The spring and dashpot system has also been adopted to model the vertical boundaries of the FE model. The observing/viscous boundaries have proven effective for reducing the boundary effects and the computational time (Kuhlemeyer and Lysmer, 1973; Cakir, 2013). The domain size analyses and details of the viscous boundaries have been present in section 6-3.

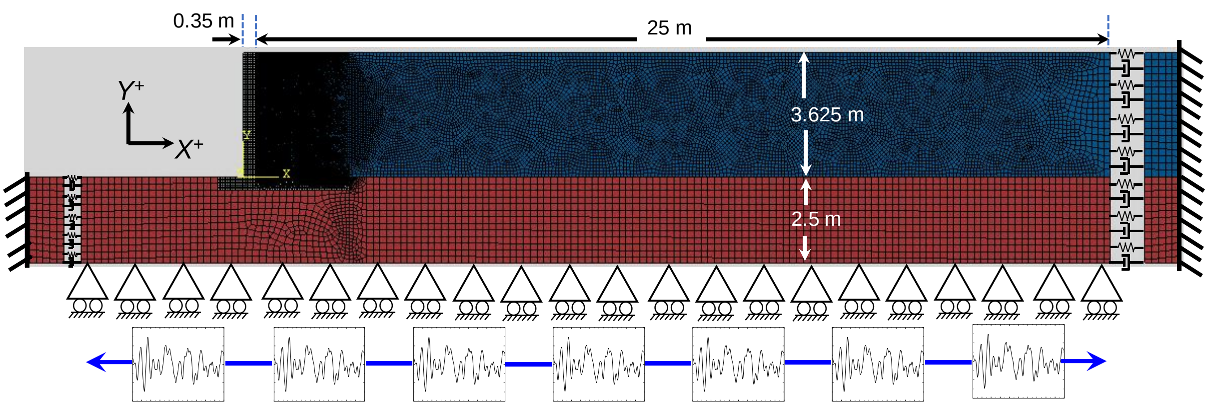

Figure 6-2 Two-dimensional plane strain FE model of base restrained RW.

Geostatic stresses have been defined for the backfill and the base rock domain. The prime objective to define the geostatic stresses was to ensure equilibrium of forces and accuracy of the FE results. Gravitational loading has also been applied to the entire FE model. The earthquake loading has been applied at the base of the FE model; using acceleration time history.

Nonlinear time history FE analyses have been carried out in the dynamic explicit module of Abaqus. The dynamic explicit solution scheme of the FE software Abaqus is popular for the large deformation numerical analysis (Abaqus/Explicit User's Manual, version 6.13. 2013). An explicit central difference integration rule has been used by Abaqus along with several small time increments. The computational efficiency has been achieved by using a diagonal element lumped mass matrix. The smallest stable time interval (Δt) for the explicit scheme of Abaqus depends on the smallest element dimension (L_{min}) and the stress wave velocity (V_{SV}). Equation 6.1 shows the relation between Δt, L_{min} and V_{SV}.

$$\Delta t = {}^{L_{\mathrm{min}}}/_{V_{\mathrm{SV}}} \tag{6.1}$$

Low sampling frequency has been chosen to read the FE result; in order to reduce data noise and to ensure accuracy of the FE results.

6.3. Constitutive modelling of the materials

6.3.1 Constitutive modelling of the backfill

The backfill has been modelled using the Mohr Coulomb material model; which is available in FE software Abaqus. The hardening and the softening behaviour of the backfill has been simulated by calibrating the Mohr Coulomb model with triaxial test data. Details of the Mohr Coulomb material model and calibrations with the triaxial test data has been presented in chapter 5. Parametric investigations have been performed for three different backfill types, (i) dune sand (Daheur et al. 2019), (ii) Fontainebleau sand (Dano et al. 2004) and (iii) crushed rocks (characterized at The University of Melbourne) respectively. Triaxial test results for the dune sand and the Fontainebleau sand are shown in Figure 6-3a and 6-3b, respectively. The calibration of the Mohr Coulomb material model (hardening and softening) with the triaxial test results of the dune and Fontainebleau sand have also been shown in figure 6-3. The damping for the backfill has been modelled using Rayleigh damping parameters. Details for finding the mass and the stiffness dependent damping values have also been explained in chapter 5. Figure 6-10 shows the engineering properties considered for different backfill type.

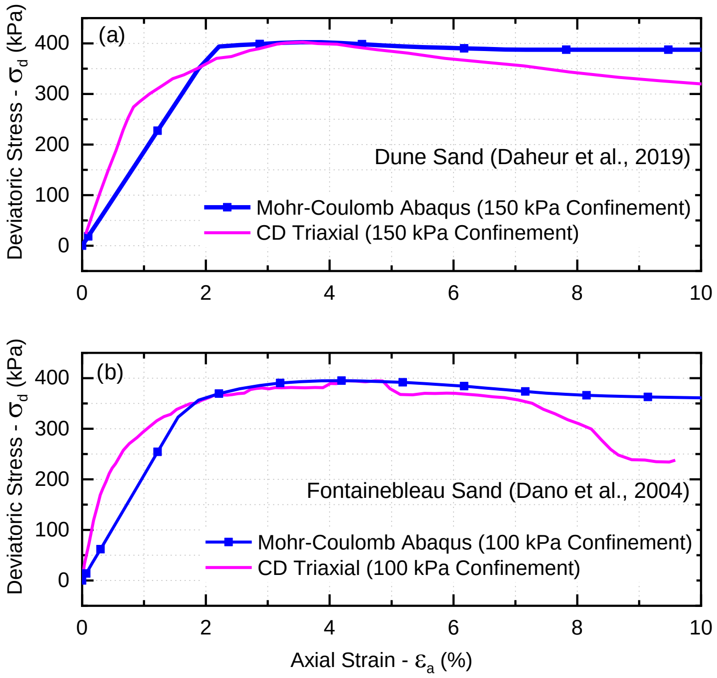

Figure 6-3 Constitutive behaviour of the dune sand and the Fontainebleau sand, calibration of the Mohr Coulomb model with the CD triaxial test results.

6.3.2. Constitutive modelling of the concrete

The concrete of RC RW has been modelled using the concrete damaged plasticity (CDP) model which is built into the FE software Abaqus. The CDP model is popular in modelling the contitutive behaviour of concrete (Lima, et al., 2016). The CDP model simulates the constitutive behaviour of concrete in compression and tension using the following formulation:

$$\sigma_t = (1 - d_t)E_0^{el}:\left(\varepsilon - \varepsilon_t^{pl}\right) \tag{6.2}$$

$$\sigma_c = (1 - d_c) E_0^{el} : \left(\varepsilon - \varepsilon_c^{pl} \right) \tag{6.3}$$

where, σ_t and σ_c represents the stress vectors for the compressive and tensile stresses, respectively. The ε_t^{pl} and ε_c^{pl} represents the equivalent plastic strains in tension and compression, respectively. The initial undamaged elastic modulus $\left(E_0^{el}\right)$ has been calculated from the stress-strain response of uniaxial compressive strength test of concrete (as shown in figure 6-4a). Damage variables d_t and d_c are functions of the plastic strains (Abaqus/Explicit User's Manual, version 6.13. 2013).

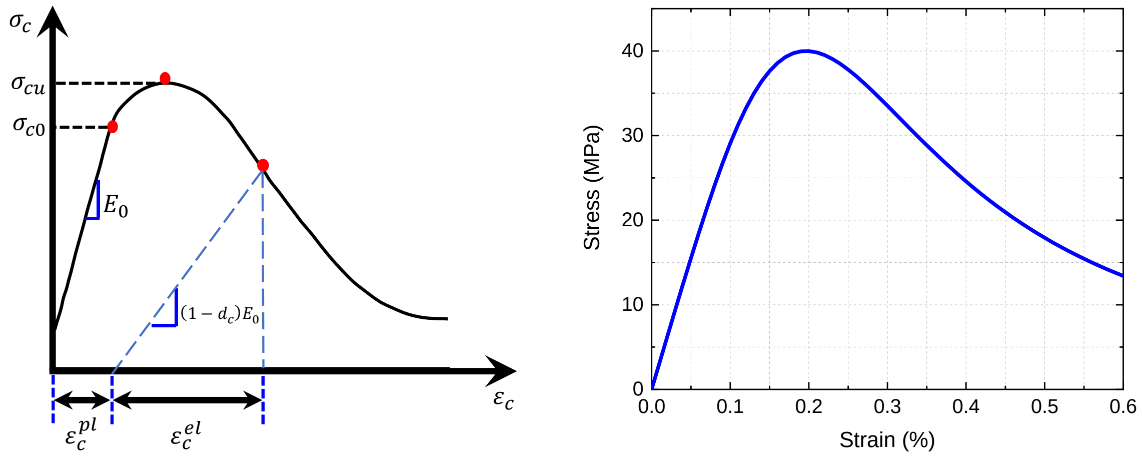

(a) Uniaxial compression for the CDP

(b) Stress-strain behaviour for the concrete

Figure 6-4 Response of the plain concrete in uniaxial compression (Abaqus/Explicit User's Manual, version 6.13. 2013).

The yield function of the CDP model initially developed by Lubliner et al. (1989) and later modified by Lee and Fenves (1998). Details of CDP yield function could be found in Abaqus/Explicit User's Manual, version 6.13. The CDP model follows a non associative flow rule. The plastic potential function is controlled by the dilation angle (at the deviatoric stress plane) and the eccentricity.

Table 6-1 shows the engineering properties considered for modelling the concrete using the CDP model. The concrete has a maximum compressive strength (f_{cu}) of 40 MPa; as considered in the structural design of the RW. The stress-strain response of the concrete in compression (f_{cu} =40 MPa) has been generated using procedure suggested by Carreira and Chu (1985). Figure 6-4b shows the stress-strain response of the concrete considered to model the base restrained RW. It was assumed that the inelastic behaviour of the concrete in compression starts when the stress in the concrete reaches 40% of f_{cu}.

The tensile behaviour of the concrete against the uniaxial tension has been modelled using the fracture energy approach. The tensile failure of concrete has been simulated by a linear softening model. Equations 6.3 and 6.4 were used to calculate the tensile strength of concrete (f_t) and the fracture energy (G_f).

The f_t and G_f have been calculated for the maximum compressive strength of concrete (f_{cu}) and the maximum aggregate size (d_a), (Lima, et al., 2016, Abaqus/Explicit User's Manual, version 6.13. 2013).

$$f_{\mathrm{t}} = 1.4\left(\frac{f_{\mathrm{cu}} - 8}{10}\right)^{\frac{2}{3}} \qquad (6.4)$$

$$G_{\mathrm{f}} = (0.0469d_a^2 - 0.5d_a + 26)\left(\frac{f_{\mathrm{cu}}}{10}\right)^{0.7} \qquad (6.5)$$

6.3.3. Constitutive modelling of the reinforcement steel

The bilinear stress-strain response of the steel has been used to simulate the constitutive behaviour of steel. The details of steel have been shown in table 6-1. Figure 6-5 shows the stress-strain response of the steel considered in the present study (EN 1992-1-2). The von-Mises plasticity model has been used to model the plastic behaviour of steel. In the von-Mises plasticity model, an isotropic hardening of the material has been defined with the help of the uniaxial yield stress and equivalent plastic strain. It should be noted herein that the size of the yield surface in the isotropic hardening changes uniformly in all directions (Abaqus/Explicit User's Manual, version 6.13. 2013).

Table 6-1 The engineering properties used to model concrete and steel.

Property – Unit	**Concrete**	**Steel**
Density (ρ) – kg/m^3	2400	7800
Young's modulus - GPa	31.62	200
Poisson's ratio (ν)	0.3	0.3
Maximum strength - MPa	40 (f_{cu})	415 (f_{st})
Plasticity model	Concrete damaged plasticity	von-Mises plasticity

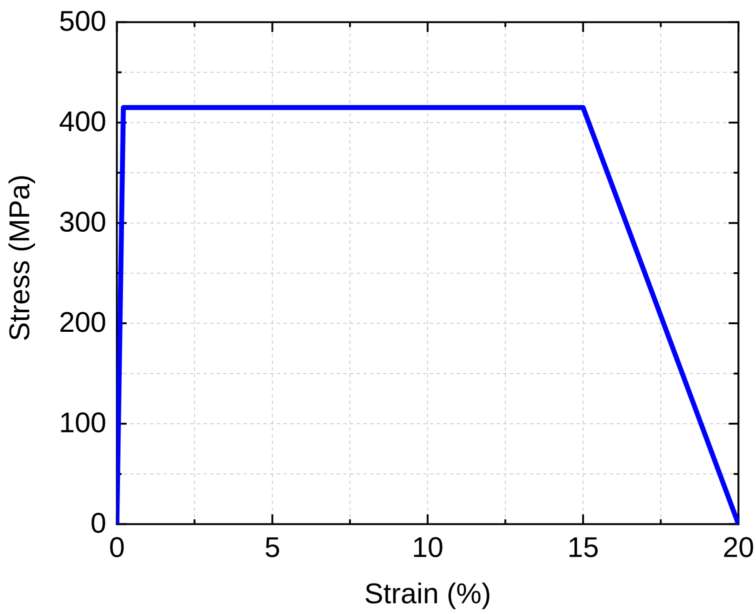

Figure 6-5 The stress-strain curve for steel.

6.4. Effect of the soil domain size on the seismic behaviour of the base restrained RW

The boundary effects may significantly affect the FE model results (Ling et al., 2005; Bakr and Ahmad, 2018). Therefore, a detailed parametric investigation has been performed for the different backfill domain lengths behind plain concrete RW. Three RW models with 25 m, 50 m and 100 m backfill domain length have been considered for domain size study. Crushed rock has been used as the backfill type for all three RW models. The Mohr Coulomb material model has been used to model the backfill. Details of the Mohr Coulomb material model and crushed rock have been presented in chapter 5. The Northridge accelerogram (090 CDMG Station 24278) has been used as base excitations for the FE simulations. Figure 6-6 shows the base restrained RW with different backfill domain lengths.

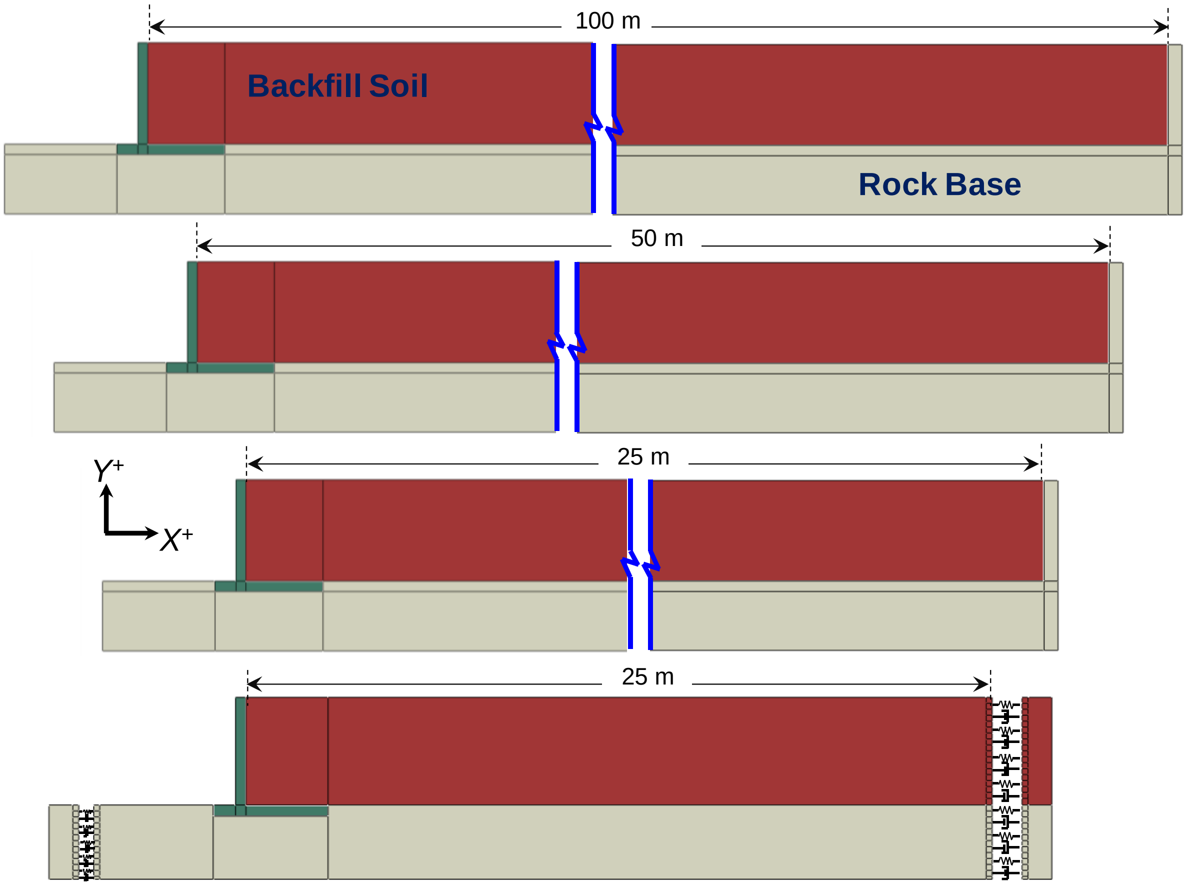

Figure 6-6 Base restrained RW with the different backfill domain lengths.

Figure 6-7 shows the relative displacement time history at the top of the RW; observed from different backfill domain lengths. It was observed that the RW with 100 m long backfill domain shows lesser relative displacement than the 50 m and 25 m long backfill domain. However, the computational time for the RW with 100 m long backfill domain was significantly higher than the other two domains. Therefore, it was decided to model the vertical boundaries of the FE model using viscous boundaries. The spring and dashpot system has been selected to model the verticle boundaries of the FE model (Abaqus/Explicit User's Manual, version 6.13. 2013).

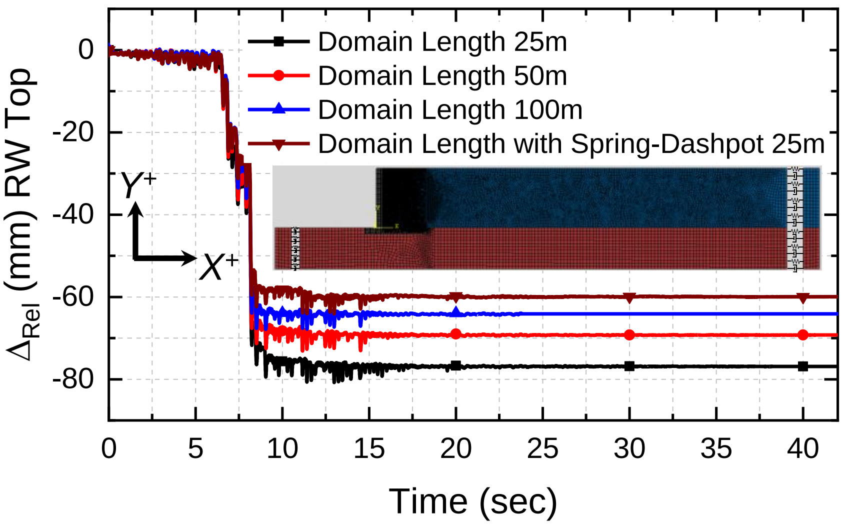

Figure 6-7 Domain size sensitivity study for the base restrained prototype RW.

Figure 6-8 shows the typical spring and dashpot system available in the FE software Abaqus. The stiffness and damping for the spring and dashpot system have been calculated for 80 m long backfill/base rock domain. The vertical spacing between two spring and dashpot sets has been kept at 200 mm. It is assumed that every spring and dashpot set is connected with the high stiffness rock at the left and righthand sides of the FE model. Figure 6-6d shows the base restrained plain concrete RW (25 m long backfill domain) with the spring and dashpot boundaries. The Northridge accelerogram (090 CDMG Station 24278) has been used as the base excitations. Figure 6-7 also shows the relative displacement at the top of the RW (RW with spring and dashpot system). It was observed that the RW with the spring and dashpot boundary type shows lesser displacement than other considered cases. The relative displacement of the RW with spring and dashpot boundary was close to the relative displacement obtained for the RW with 100 m long backfill domain. Moreover, the computational time for the RW with spring and dashpot boundary was significantly lesser than the computational time for RW with 50 and 100 m long backfill domains.

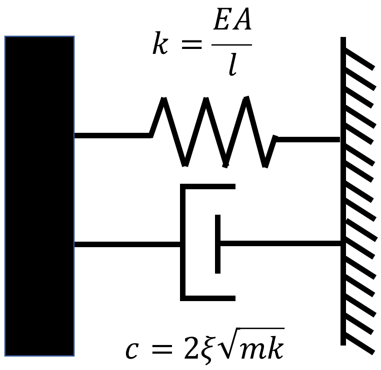

Figure 6-8 Typical spring and dashpot system in Abaqus (Abaqus/Explicit User's Manual, version 6.13. 2013).

6.5. Mesh sensitivity analysis for the base restrained RW

The mesh sensitivity analyses have been carried out for finding the optimum mesh size to ensure good accuracy of the FE results with reasonable computation time. Many researchers have studied the effects of the mesh size on the structural response, and observed that the FE analyses results were sensitive to mesh size. Moreover, a optimum mesh size could provide accurate FE results with lesser computational time (Kuhlemeyer and Lysmer, 1973; Cakir, 2013).

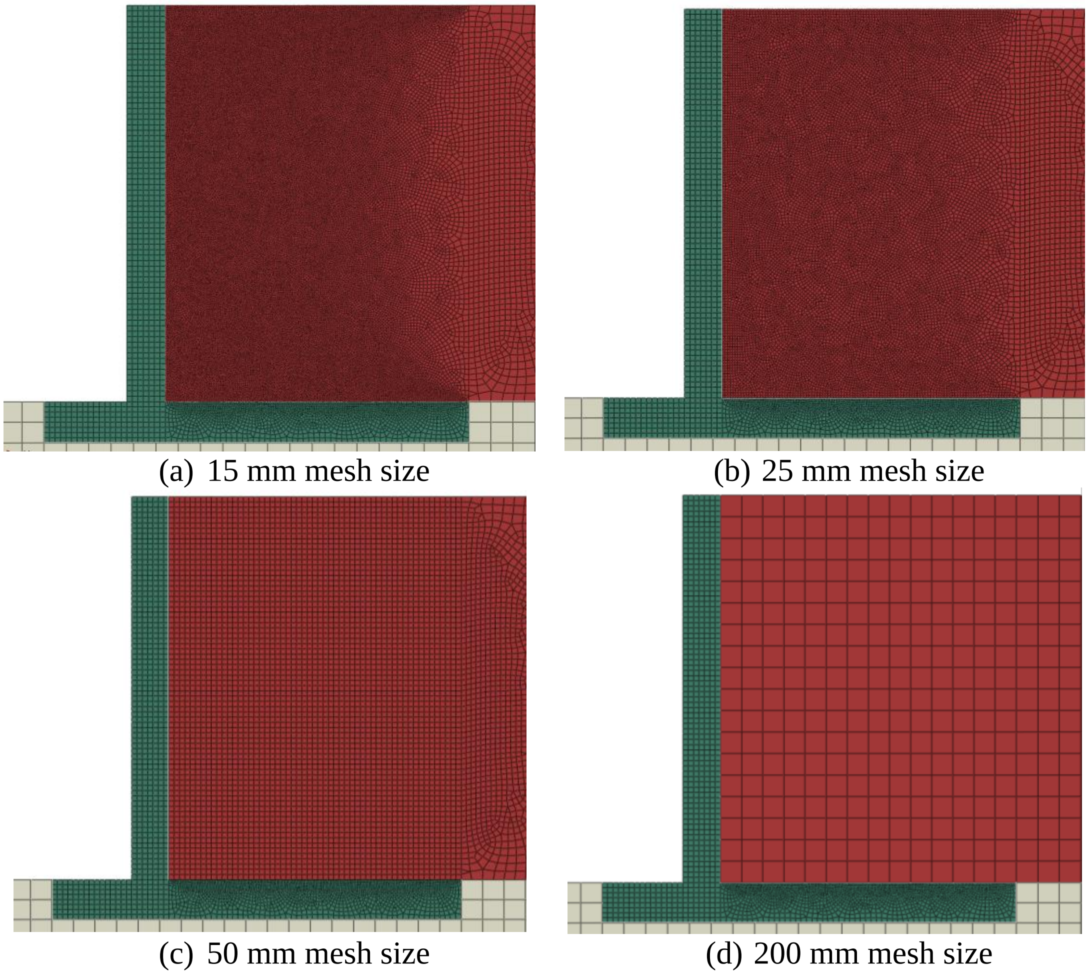

Figure 6-9 Different backfill mesh sizes considered for the mesh sensitivity analyses.

It was observed from shaking table experiments and the initial FE simulations of the base restrained RW that the backfill near the RW stem and the heel slab highly influence seismic response of the base restrained RW. Therefore, the focus of mesh sensitivity analysis was kept at the contact between the RW and the backfill

Mesh sensitivity study was performed by varying the mesh sizes of the backfill near the base restrained RW. The medium dense mesh was used for the RW and the base rock for avoiding shear locking effects. The four different backfill mesh sizes (15 mm, 25 mm, 50 mm and 200 mm) have been used for the mesh sensitivity analyses. Figure 6-9 shows the different backfill mesh sizes considered for mesh sensitivity analyses. FE modelling of the base restrained RW for mesh sensitivity analyses is similar to the domain size FE modelling (as explained in section 6.4).

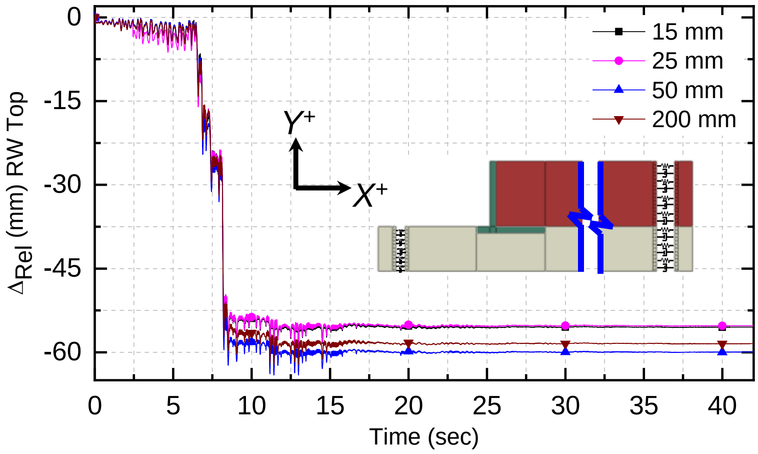

Figure 6-10 Mesh sensitivity analyses for backfill.

Figure 6-10 shows the relative displacement at the top of the RW observed for the different backfill mesh sizes. A minor difference has observed between the different backfill mesh sizes. Based on the mesh sensitivity analyses, 25 mm mesh size of the backfill has been selected for the FE investigations of seismic actions on the base restrained RW.

6.6. Parametric investigation on the base restrained RC RW

A detailed and rigorous parametric investigation has been performed for understanding the effects of earthquake actions on the base restrained earth retaining structures. Three different types of backfill have been considered for parametric investigations. Figure 6-11 shows the layout for the parametric investigation program along with details of different backfill material types. Nonlinear FE time history analyses have been performed for three backfill types. Base excitations were generated using five synthetic and five historical accelerograms. Details of the accelerogram selection and the acceleration time histories of the artificial and historical recorded accelerograms have been presented in chapter 4. Details of the earthquake records have also been presented in the appendix.

Results of the FE analyses have been analysed to study the displacement response behaviour of the base restrained RW, distribution of the backfill pressure up the RW, and amplification of the horizontal acceleration.

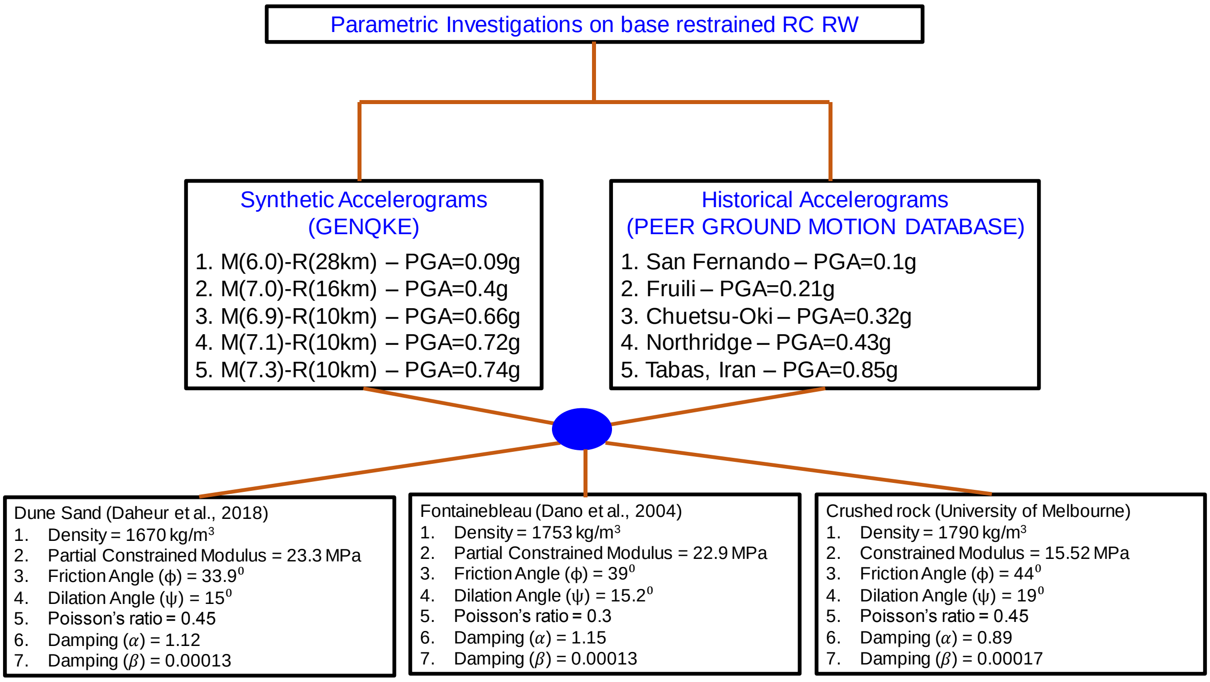

Figure 6-11 Layout of the parametric investigation on the base restrained RC RW.

6.6.1 Displacement response of the base restrained RC RW with different backfill soil type

6.6.1.a. Backfill type - Dune sand

Displacement response of the base restrained RW (dune sand as backfill) has been studied by means of the FE analyses results. Figure 6-12 shows the relative displacement time histories at the top of the RW for different base exciations. Higher relative displacement at the top of the RW can be seen with increasing peak ground acceleration (PGA). Permanent deformation of the RW has also been observed for all cases. Nonlinear displacement pattern of the RW stem has been observed, for PGA ≤ 0.2g. The plastic strains have been observed at RW stem base when PGA $>$ 0.2g, due to which a linear displacement up the stem wall was observed. Table 6-2 shows the maximum relative displacement at the top of the RW ($\Delta_{\text{Rel at top}}$) normalized with respect to the wall height (H_{stem}). It should be noted herein that for the RW rotating about their base, the formation of the active failure wedge occurs when $\frac{\Delta_{\text{Rel at top}}}{H_{\text{stem}}} > 0.002$ (Sherif et al., 1984; Clough and Duncan, 1991). As shown in table 6-2 an active failure wedge in the backfill was formed when PGA ≥ 0.32g.

It can also be seen from the FE analyses results that because of the high inertial forces from the backfill; relative displacement of the RW occurs only in the active "x^-" direction (i.e. in the direction away from the backfill). Similar active displacement of the base restrained RW was observed during the shaking table experiments.

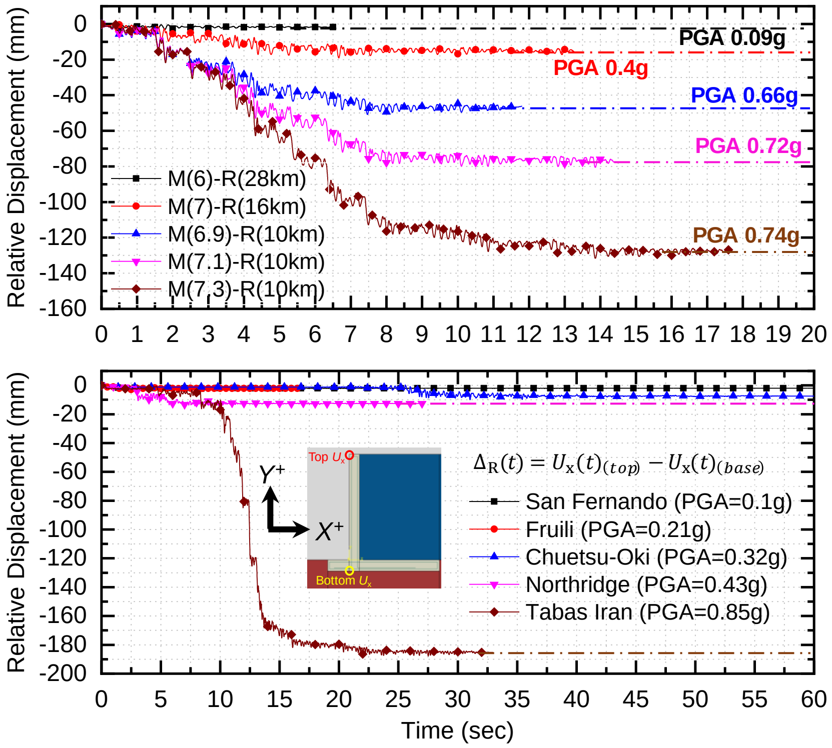

Figure 6-12 Relative displacement at the top of the RW when subjected to different accelerograms, Dune sand as the backfill.

Table 6-2 Normalized displacement of the base restrained RC RW, when subjected to different ground excitations, Dune sand as the backfill.

Sr. No.	PGA	$\frac{\Delta_{\text{Rel at top}}}{H_{\text{stem}}}$ (%)	Ground Motion Description
1.	0.09g	0.085	M(6)-R(28km)
2.	0.12g	0.092	San Fernando
3.	0.21g	0.093	Fruilli
4.	0.32g	0.274	Chuetsu-Oki
5.	0.4g	0.526	M(7)-R(16km)
6.	0.42g	0.394	Northridge
7.	0.66g	1.402	M(6.9)-R(10km)
8.	0.72g	2.221	M(7.1)-R(10km)
9.	0.74g	3.629	M(7.3)-R(10km)
10.	0.85g	5.179	Tabas, Iran

Figure 6-13 shows the maximum dynamic soil pressure up the wall height for different base excitations (dune sand backfill type). The backfill pressure for “at rest” and “Coulomb’s active state” conditions are also shown for comparison. The pseudo-static backfill pressure (shown in figure 6-13) has also been calculated up the wall height using the Mononobe-Okabe (MO) equation (Mononobe and Matsuo; 1929), for 100% PGA or maximum possible K_h (EN1998-5)

FE simulations have been used to generate "x" direction backfill pressure (lateral) time history at the top, middle and base of the RW. The time corresponds to the maximum backfill pressure was identified to find the backfill pressure distribution up the wall height. Nonlinear profiles of the backfill pressure up the wall height was observed for all cases. In some cases, high stress concentrations can be seen from the FE simulations of the backfill response near the base (3.55 m from the top). This is indicative of a high backfill pressure at the base of the RW.

It was observed that for various base excitations, the MO method underestimates the maximum dynamic soil pressure behind the base restrained RW. A higher backfill pressure was observed near the mid height of the RW when PGA ≤ 0.43g. For PGA ≥ 0.66g higher backfill pressure was observed near the base. Figure 6-13 also shows the residual backfill pressure distribution at the end of FE analysis. The observed residual backfill pressure is shown to be significantly higher than the Coulomb's active state pressure. This confirms the formation of active failure wedge in the backfill (PGA > 0.32g). The residual backfill pressure has a nonlinear pressure profile along the RW stem height.

It should be noted herein that with the dune sand as backfill, the soil pressure at the end of the analysis has been found to be similar, or slightly higher than the at rest backfill pressure but with exception similar observations have also been reported by the Mikola and Sitar (2013) for the centrifuge shaking of basement walls. This observation raised the importance of considering the time dependent nature of the backfill pressure. It should be noted that no correlation can be seen between the value of the peak acceleration and that to the maximum dynamic backfill pressure.

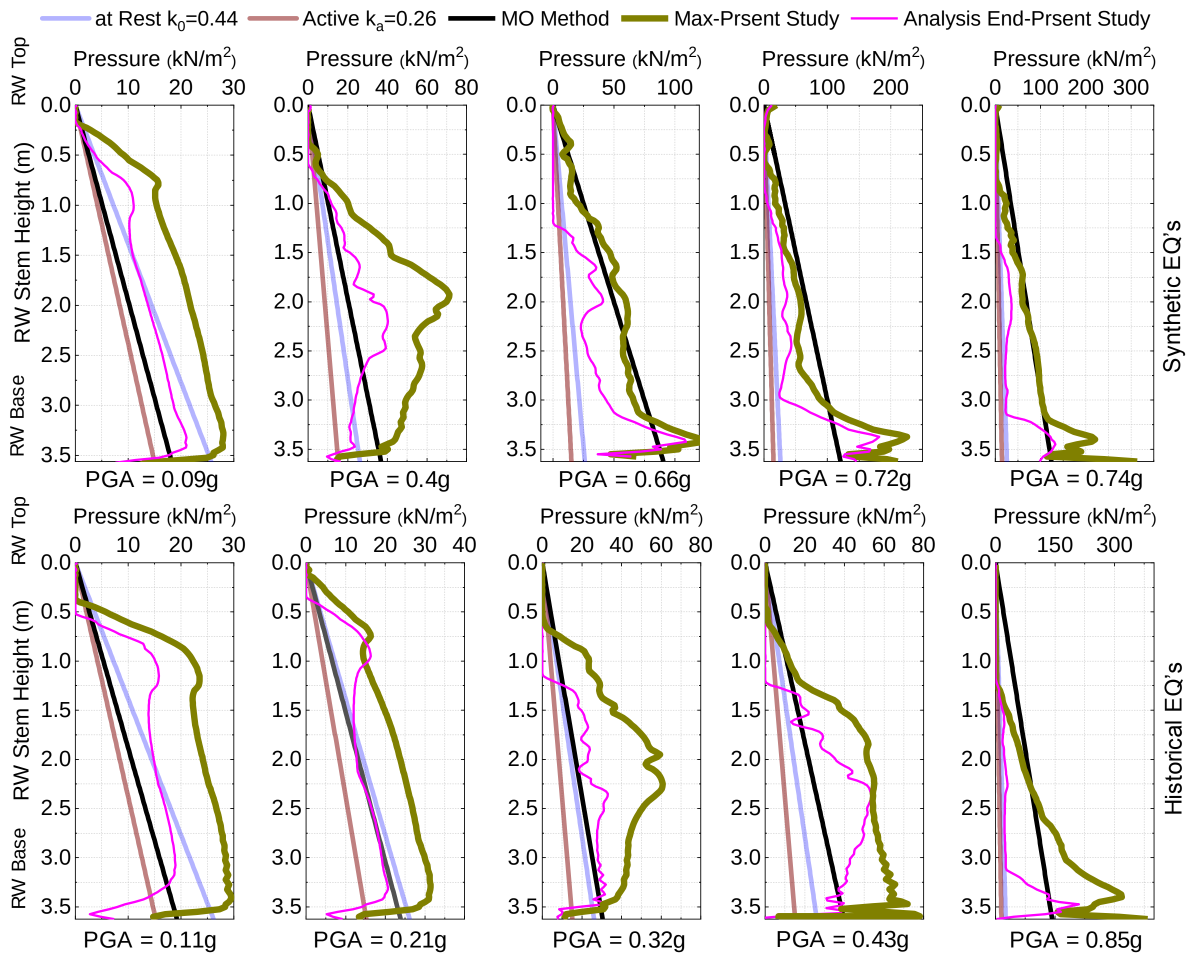

Figure 6-13 Backfill pressure up the RW height, calculated for different stress states (at rest, active state), dynamic soil pressure calculated using the MO equation and from FE analysis, Dune sand as backfill type for the ten base excitations (refer table 6-2).

Amplification of the horizontal acceleration in the backfill (dune sand) has also been investigated. Figure 6-14 shows the response spectrum acceleration (RSA) for the base restrained RW, when subjected to the different base excitations. The RSA has been shown at the base, middle, and top of the backfill. Significant amplification of the horizontal acceleration towards the backfill top has been observed for all cases. It has also been observed that the backfill responding until 0.2 sec time period. Due to interaction with the RW; the free field acceleration response of the backfill has been altered. For all cases, amplification of the horizontal acceleration has been observed up to 0.5 sec period.

Figure 6-15a shows a typical RSA obtained at backfill base and top. The peak value of RSA at backfill top was the natural period of backfill. The peak value of RSA at the base was then estimated as the average value of RSA of applied accelerogram for the period equals to $\pm$ 20 % of the period of maximum RSA at top.

Figure 6-15b shows the bar chart of the amplification factor (horizontal acceleration) for increasing RSA values. No direct correlation has been observed between the peak RSA and amplification factor (AF). However, for peak RSA $>$ 1.1g, a decrement in AF_{soil} at backfill top was observed. Moreover, an average AF of 3.1 and 1.9 was observed at the top and middle level. It should be noted herein that a higher backfill pressure was observed at RW mid height, which results in higher amplification of the horizontal acceleration.

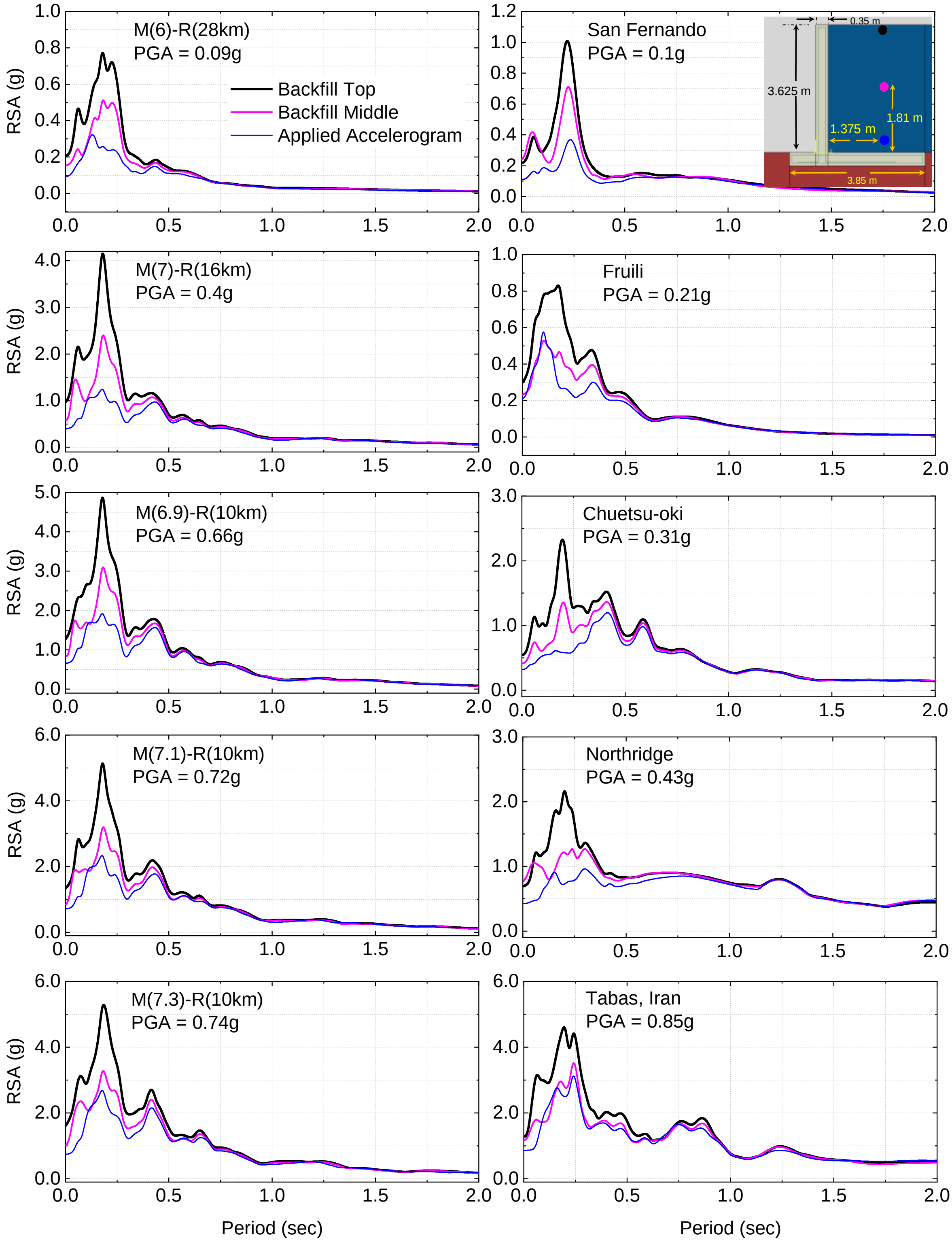

Figure 6-14 RSA for base restrained RW, when subjected to different ground motions, backfill type Dune sand.

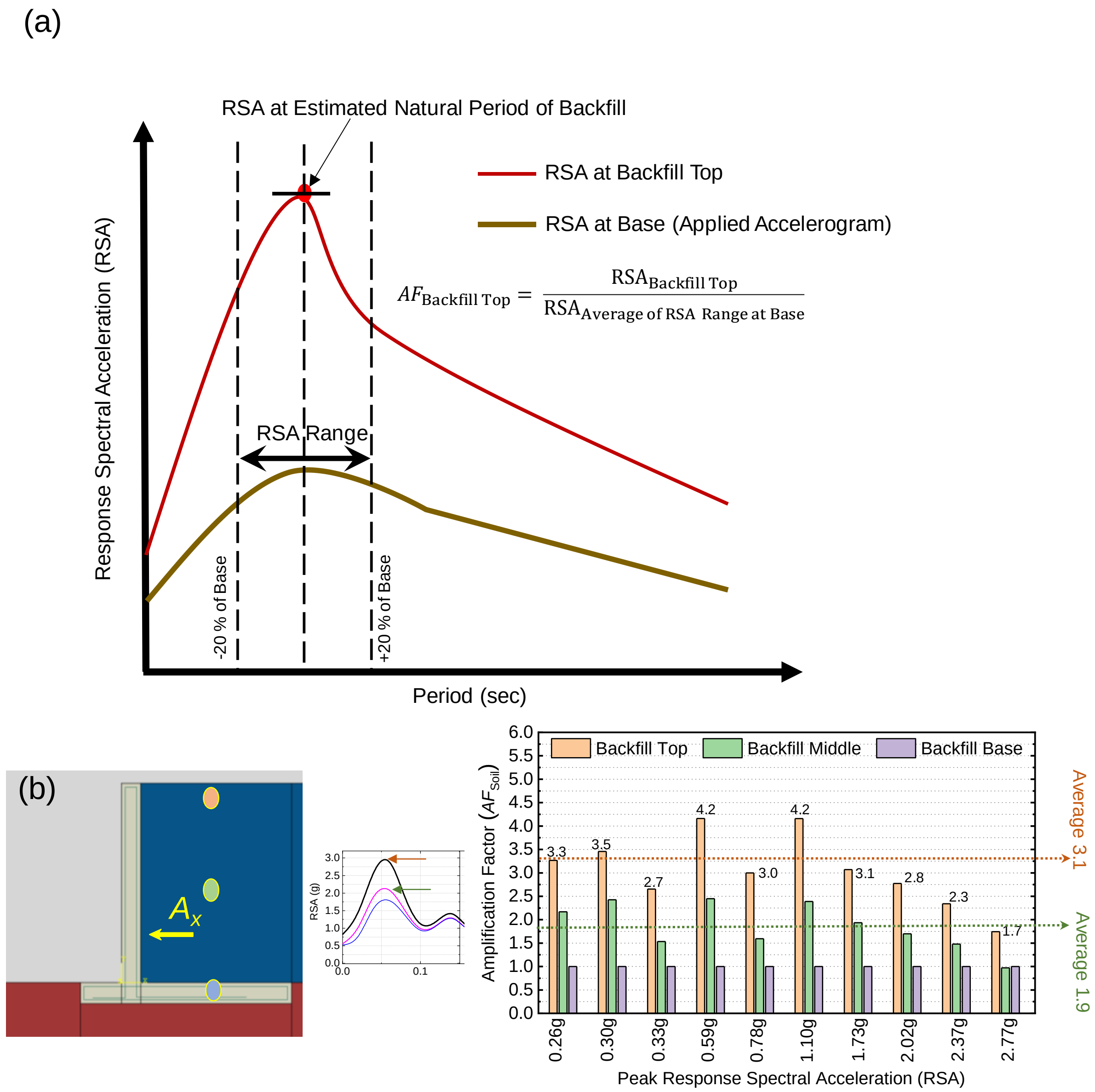

Figure 6-15 Amplification factor (horizontal acceleration) for base restrained RW, when subjected to different ground motions, backfill type Dune sand.

6.6.1.b. Backfill type - Fontainebleau sand

The seismic response of the base restrained RW with Fontainebleau sand (backfill) has been studied against ten different base excitations. Figure 6-16 shows the relative displacement time history at the top of the RW for Fontainebleau sand to be used as backfill. A RW with Fontainebleau sand as backfill shows slightly higher displacement than a RW with dune sand as backfill type. It has been observed that relative displacement at the top of the RW depends on the applied excitations and its value increases with increasing value of PGA.

The formation of active failure wedge in the backfill has also been observed for PGA ≥ 0.32g (Clough and Duncan; 1991). Table 6-3 shows the maximum relative displacement at the top of the RW ($\Delta_{\text{Rel at top}}$) normalized with respect to the wall height (H_{stem}). The RW with Fontainebleau sand backfill shows higher values of $\Delta_{\text{Rel}}/\text{H}_{\text{Stem}}$ than RW with dune sand as backfill.

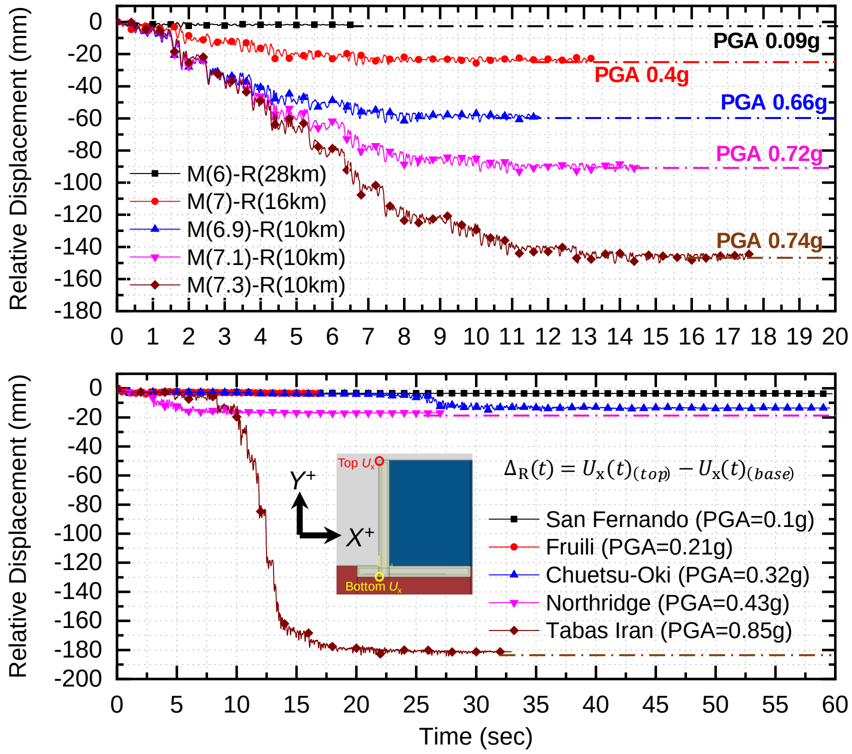

Figure 6-16 Relative displacement at the top of the RW when subjected to different accelerograms, Fontainebleau sand as the backfill.

Table 6-3 Normalized displacement of the base restrained RC RW when subjected to different ground excitations, Fontainebleau sand as backfill.

Sr. No.	PGA	$\frac{\Delta_{\text{Rel at top}}}{H_{\text{stem}}}$ (%)	Ground Motion Description
1.	0.09g	0.085	M(6)-R(28km)
2.	0.12g	0.103	San Fernando
3.	0.21g	0.109	Fruilli
4.	0.32g	0.442	Chuetsu-Oki
5.	0.4g	0.739	M(7)-R(16km)
6.	0.42g	0.497	Northridge
7.	0.66g	1.728	M(6.9)-R(10km)
8.	0.72g	2.594	M(7.1)-R(10km)
9.	0.74g	4.142	M(7.3)-R(10km)
10.	0.85g	5.098	Tabas, Iran

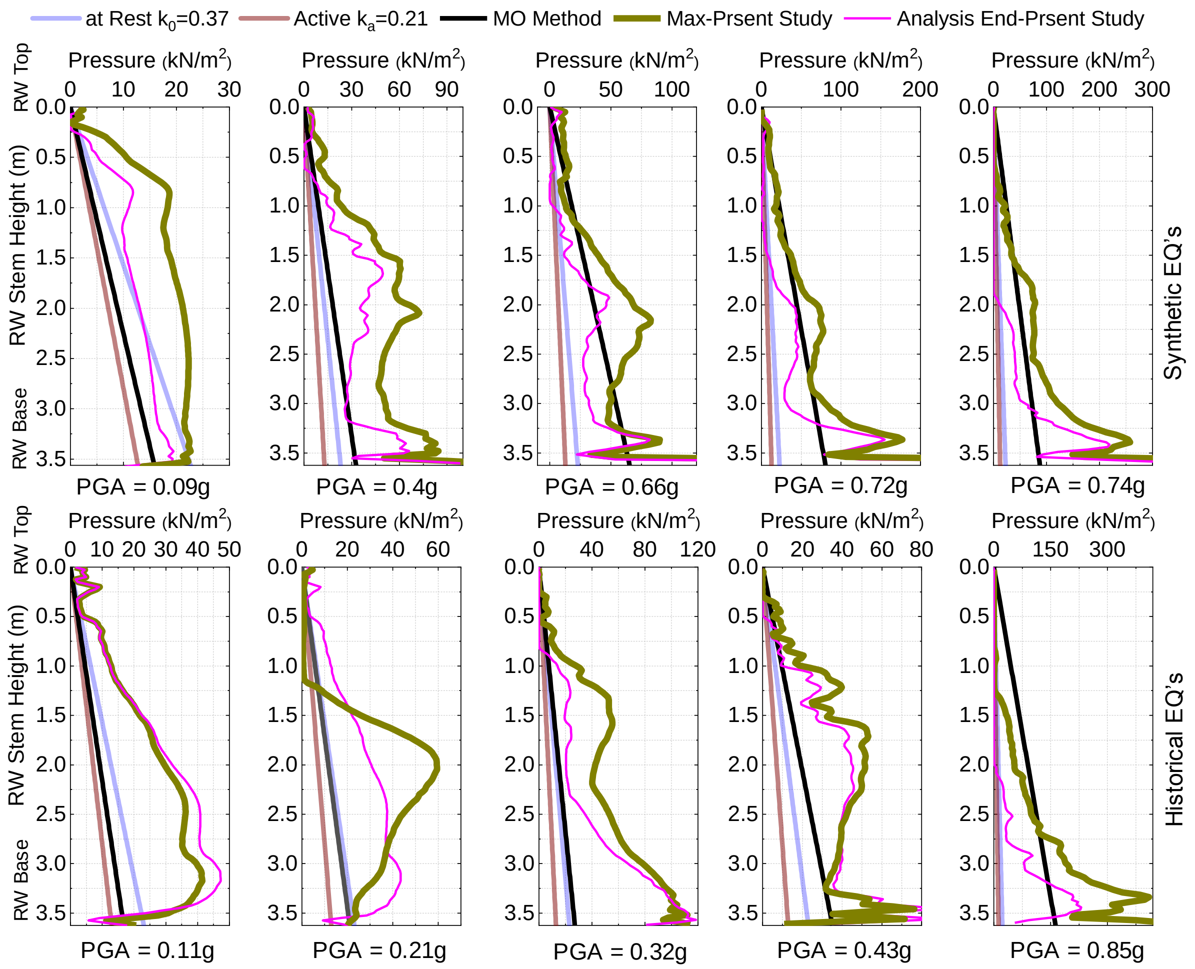

Figure 6-17 Backfill pressure up the RW height, calculated for different stress states (at rest, active state), dynamic soil pressure calculated using the MO equation and from present FE analysis, Fontainebleau sand as backfill type for the ten base excitation

Figure 6-17 shows the distribution of the backfill pressure along the RW stem height based on present FE analyses; for Fontainbleau sand backfill. The backfill pressure for “at rest” and “Coulomb’s active state” conditions have also been shown up the wall height. The pseudo-static backfill pressure calculated using the MO equation and the static backfill pressure at the end of FE analysis are shown in figure 6-17. It can be seen that MO equation underestimates the backfill pressure behind the RW significantly. A nonlinear dynamic pressure profile has been observed up the wall height in the case of Fontainebleau sand being used as the backfill material.

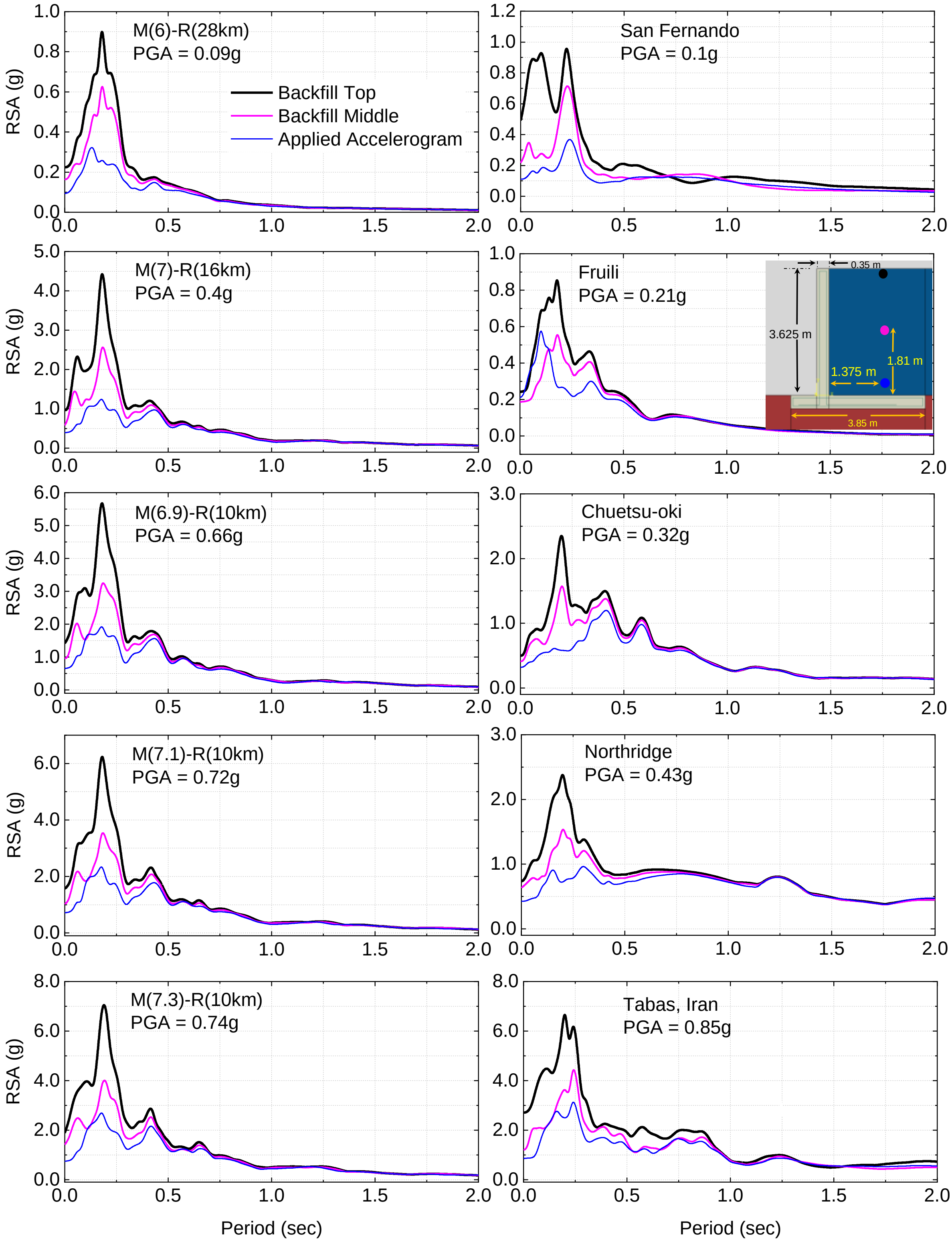

Figure 6-18 RSA for the base restrained RW, when subjected to different ground motions, backfill type Fontainebleau sand.

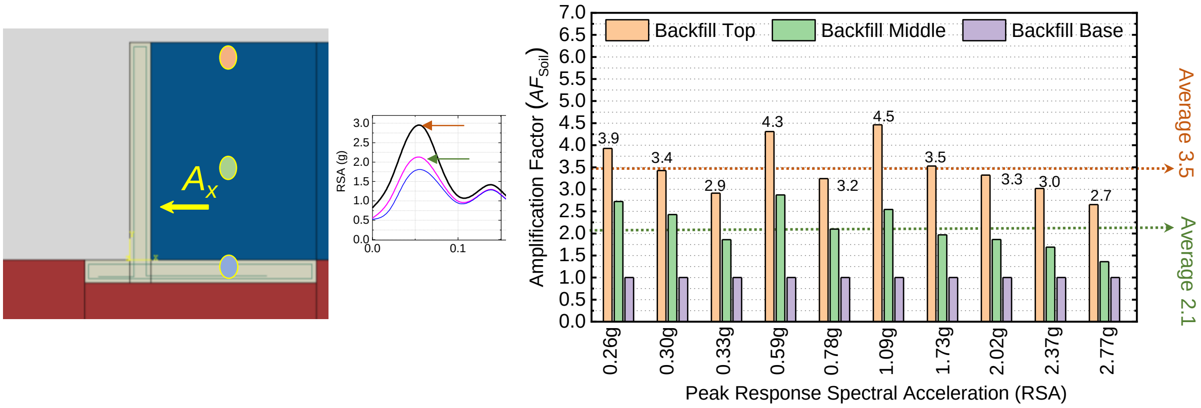

Figure 6-19 Amplification factor (horizontal acceleration) for the base restrained RW, when subjected to different ground motions, backfill type Fontainebleau sand.

Figure 6-18 and 6-19 shows amplification of the horizontal acceleration in the Fontainebleau sand backfill against different excitations. Amplification of the horizontal acceleration towards the top of the backfill was observed for all cases and is shown to be higher than the case of using dune sand as backfill. Thus, RW with Fontainebleau sand as backfill shows higher relative displacement at the top. No significant amplification of the horizontal acceleration was observed at natural periods exceeding 0.5 sec.

6.6.1.c. Backfill type – crushed rock

Figure 6-20 shows the relative displacement time history at the top of the RW which used crushed rocks as backfill. Higher relative displacement at the top of the RW was observed. Table 6-4 shows the maximum relative displacement at the top of the RW ($\Delta_{\text{Rel at top}}$) normalized with respect to the wall height (H_{stem}). The ratio $\Delta_{\text{Rel}}/H_{\text{Stem}}$ of the RW with crushed rocks as backfill is also higher. The active failure wedge formation in the crushed rock backfill has been observed for PGA ≥ 0.32g (Clough and Duncan; 1991).

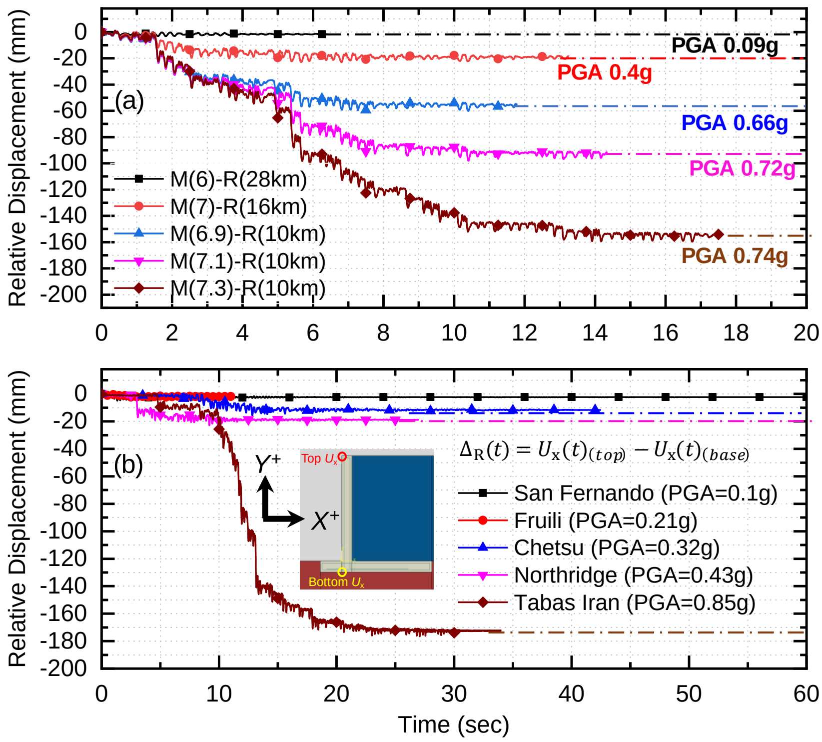

Figure 6-20 Relative displacement at the top of the RW when subjected to different accelerograms, backfill type crushed rock.

Table 6-4 Normalized displacement of base restrained RC RW, when subjected to different ground excitations, crushed rock as backfill.

Sr. No.	PGA	$\frac{\Delta_{\mathbf{Rel\ at\ top}}}{\boldsymbol{H}_{\mathbf{stem}}}$ (%)	Ground Motion Description
1.	0.09g	0.087	M(6)-R(28km)
2.	0.12g	0.134	San Fernando
3.	0.21g	0.103	Fruilli
4.	0.32g	0.429	Chuetsu-Oki
5.	0.4g	0.633	M(7)-R(16km)
6.	0.42g	0.631	Northridge
7.	0.66g	1.659	M(6.9)-R(10km)
8.	0.72g	2.700	M(7.1)-R(10km)
9.	0.74g	4.403	M(7.3)-R(10km)
10.	0.85g	4.871	Tabas, Iran

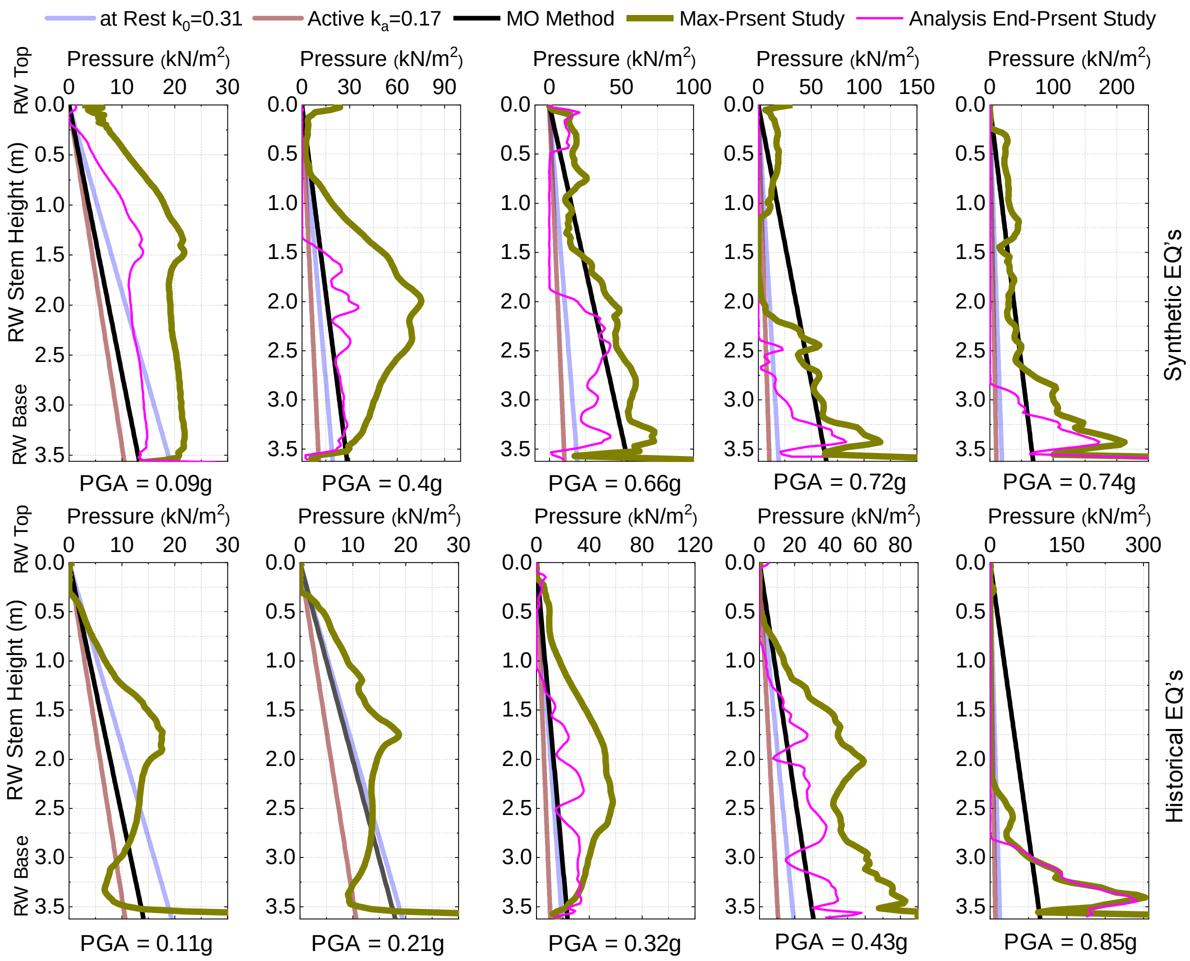

Figure 6-21 Backfill pressure up the RW height, calculated for different stress states (at rest, active state), dynamic soil pressure calculated using the MO equation and from present FE analysis, crushed rock as backfill type for the ten base excitation

Figure 6-21 shows the distribution of backfill pressure up the wall height for crushed rocks being used as backfill. The backfill pressure has been shown for different stress states (as mentioned in section 6.6.1.a). A RW using crushed rocks as backfill exhibit lower backfill pressure than a RW which uses Fontainebleau or dune sand as backfill. It was also observed that because of the higher inertial forces; a RW with crushed rocks as backfill exhibits higher wall displacement. For a RW with crushed rock as backfill, the pressure experienced at the end of FE analysis was found to be less than or equal to the dynamic pressure estimated using the MO equation.

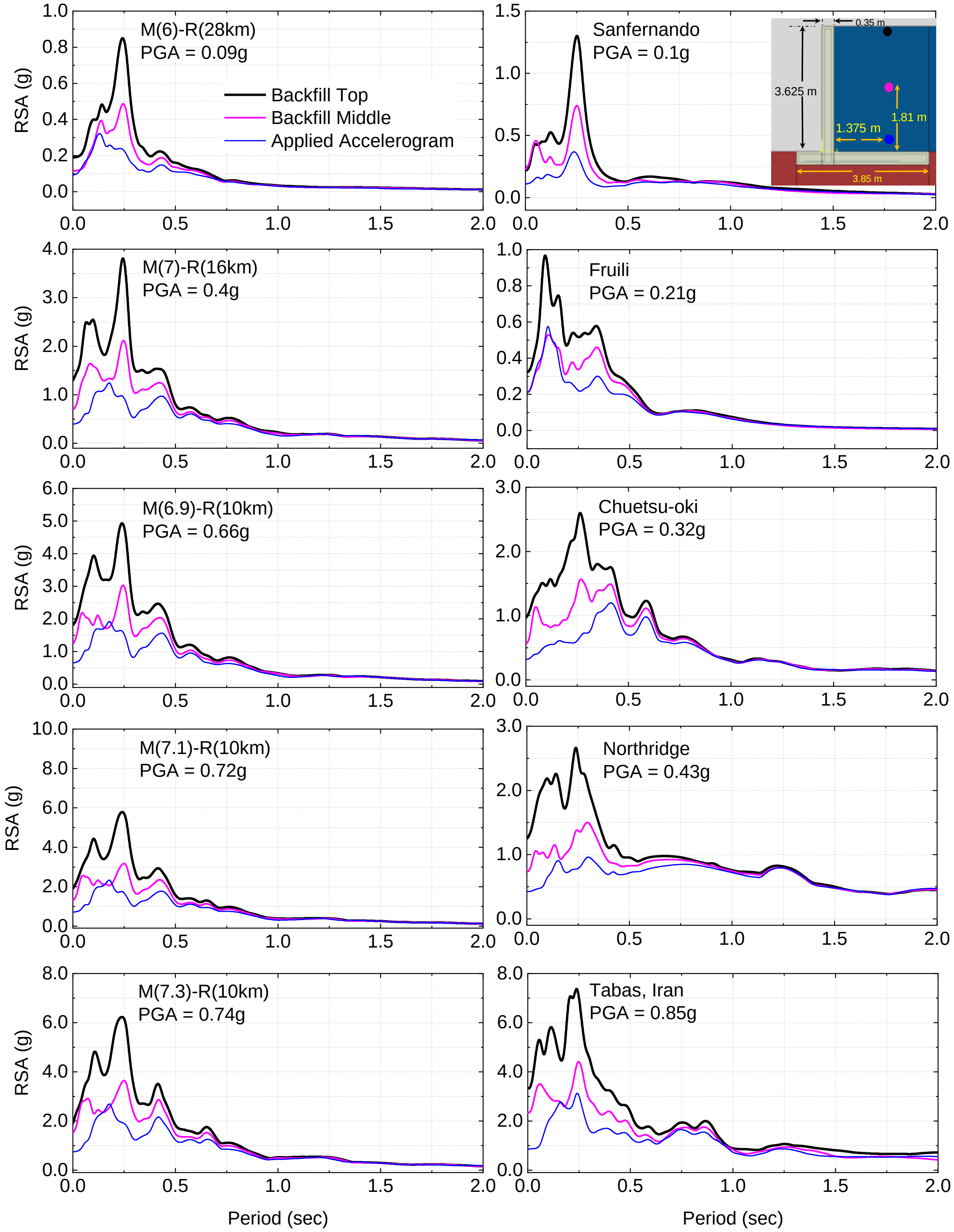

Figure 6-22 RSA for base restrained RW, when subjected to different ground motions, backfill type crushed rock.

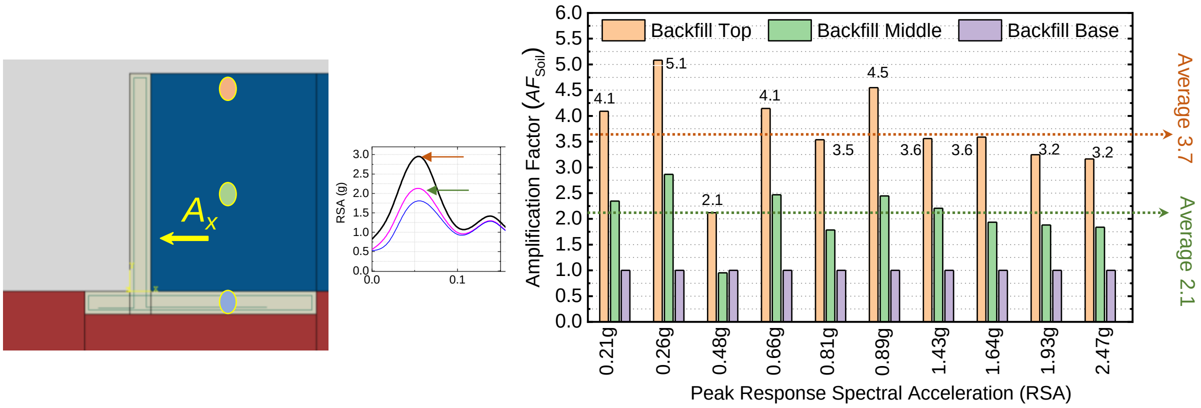

Figure 6-23 Amplification factor (horizontal acceleration) for base restrained RW, when subjected to different ground motions, backfill type crushed rock.

Figure 6-22 shows the RSA for the base restrained RW with crushed rocks as backfill materials. Significant amplification of the horizontal acceleration has been observed across all base excitations. Slightly higher amplification was observed with crushed rocks as backfill than with dune sand as backfill.

Figure 6-23 shows the values of the AF_{soil} with increasing peak RSA at backfill base. The AF_{soil} does not seem to be sensitive to the types of backfill materials given that figures 6-15, 6-19 and 6-23 present results that are not very different.

6.6.2. Summary for seismic response of the base restrained RW with different backfill types

The nonlinear time history analyses have been performed for the base restrained RW. Different backfill type and several base excitations have been considered for the parametric investigations. It was observed that the formation of the active failure wedge in the backfill primarily depends on the relative displacement of At the top of the RW (base restrained). In many cases, the active failure wedge in the backfill was formed for PGA $\geq$ 0.32g. Figure 6-24 shows the permanent displacement of the RW up its height for three different backfill materials against the different base excitations. The nonlinear displacement profile of the RW stem has been observed for PGA $\leq$ 0.4g, after which linear profile of the RW stem has been observed. It was also observed that for PGA $\leq$ 0.4g the RW with the Fontainebleau sand backfill shows slightly higher relative displacement than the other backfill types. For PGA $\geq$ 0.4g the RW with the crushed rock backfill type shows slightly higher or similar displacement than the Fontainebleau and dune sand backfill.

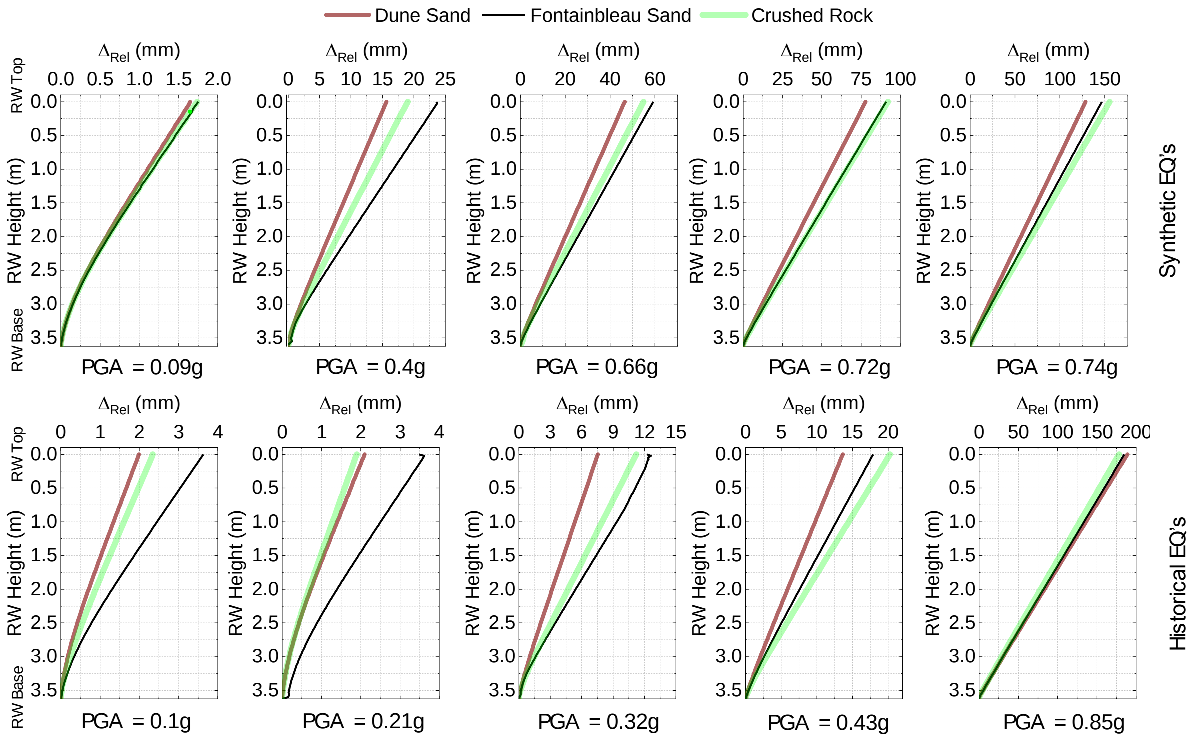

Figure 6-24 Residual deformation of the base restrained RW against different base excitations, for different backfill types.

Figure 6-25 shows the maximum relative displacement at the top of the RW for the ten synthetic and historical accelerograms. From figure 6-25a it was observed that for synthetic base excitations the RW with crushed rocks backfill shows higher relative displacement than the RW with the Fontainebleau and dune sand backfill. However, similar maximum relative displacements have been observed for different backfill types when excited using the historical accelerograms (figure 6-25b). Figure 6-26 shows plastic strain (PE) in different backfills at the end of FE analyses. Synthetic accelerograqm with PGA =0.66g has been used as base excitation. Slightly lower PE has been observed for RW with Dune sand backfill than the RW with the Fontainebleau and crushed rock backfill.

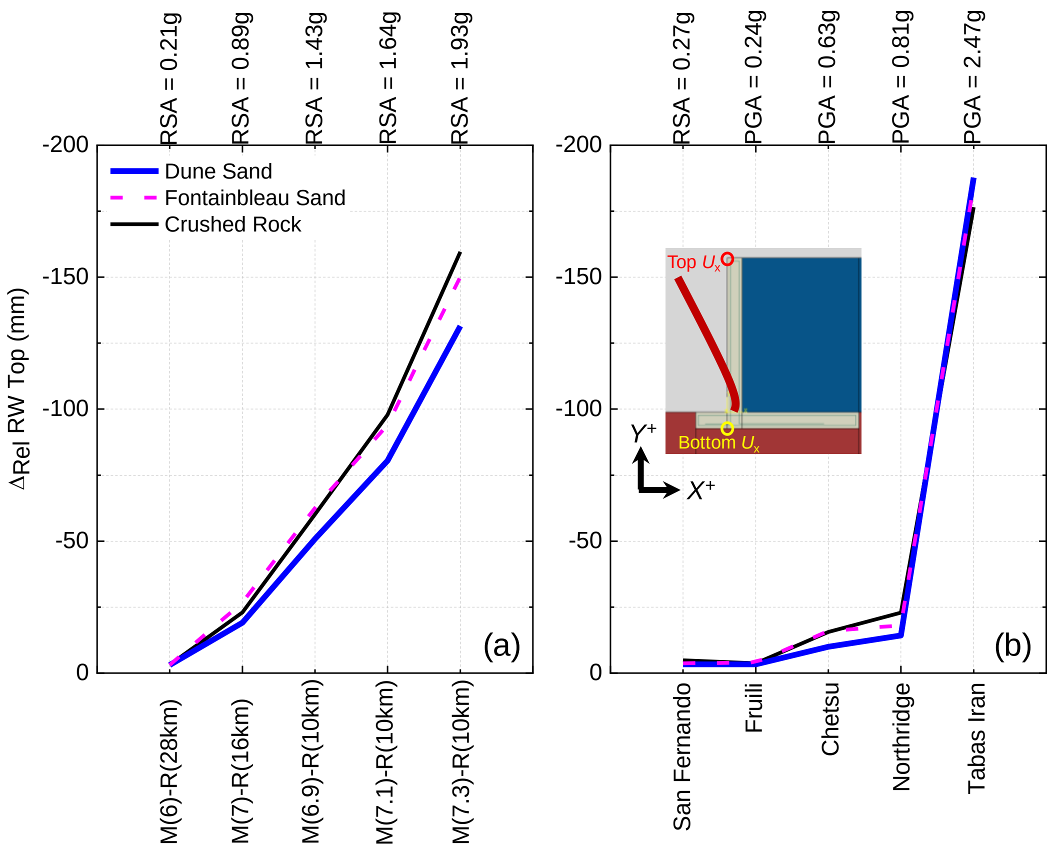

Figure 6-25 Summary of the maximum relative displacement at the top of the RW for different backfill type, against different base excitations.

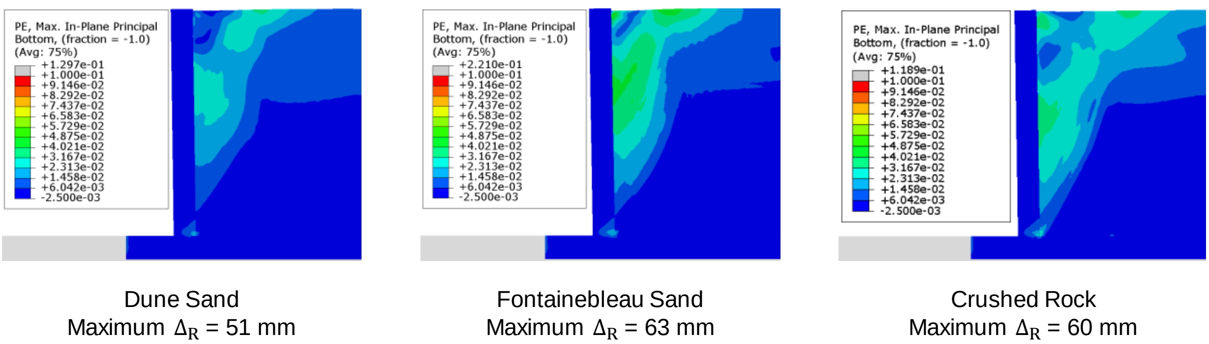

Figure 6-26 Comparison of plastic strain (PE) in backfill at the end of analysis when subjected to M(6.9)-R(10 km) earthquake, PGA = 0.66g.

6.7. Hand calculations to estimate the earthquake induced displacement of base restrained RW

Earthquake induced seismic displacement of the base restrained RW can be estimated by performing FE analysis on the RW models. However, performing FE analyses on the prototype RW models require experience in FE simulations and knowledge on constitutive modelling. Moreover, FE analyses have high computational cost. Therefore, a simple hand calculation procedure has been suggested for estimating the maximum earthquake induced elastic displacement (δ_{max}) of the base restrained RW. Figure 6-27a shows the base restrained RW model. The height and thickness of RW is "H" and "t_w" respectively. Figure 6-27b and 6-27c shows the seismic body force for the RW stem and the dynamic soil pressure (assuming triangular distribution along RW height) on the base restrained RW. The formulations used to estimate the peak seismic RW displacement have also been shown in figure 6-27.

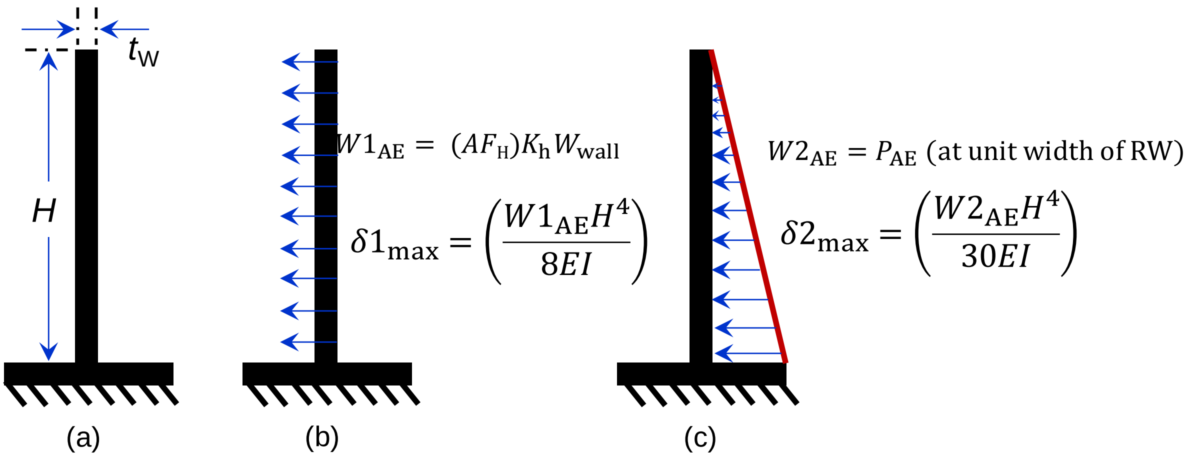

Figure 6-27 Estimation of peak elastic displacement of the base restrained RW.

It should be noted herein that the base restrained RW supports a uniform and horizontal cohesionless backfill behind it. The interface angle (δ) between the RW and the backfill has been considered as $\phi/2$. The seismic pressure behind the RW stem has been estimated using the MO equation (explained in section 2). The MO equation provides the pseudo-static pressure on the RW stem, which increases linearly along the RW depth. The pseudo-static lateral pressure coefficient (K_{AE}) has been estimated for 100 % K_h or maximum possible K_h (EN 1998-5). Seismic force due to the amplification of the horizontal acceleration in the backfill (AF_H) could also be estimated by the use of the following formulation:

$$P_{AE} = AF_H K_{AE} \gamma_{Backfill} H \quad (6.6)$$

The maximum displacement due to the RW inertia forces has been calculated using the following formulation (derivation shown in A. 1.3.):

$$\delta 1_{max} = \left(\frac{W1_{\mathrm{AE}} H^4}{8EI}\right) \tag{6.7}$$

where, $W1_{AE}$ = body force at unit height of RW = $(AF_{\mathrm{H}} \times k_{\mathrm{h}} \times W_{\mathrm{Wall}})$.

E = Young's modulus of the RW, I = Moment of Inertia of the RW

The maximum displacement due to the seismic active pressure has been calculated using the following formulation (derivation shown in A. 1.3.):

$$\delta 2_{max} = \left(\frac{W2_{\mathrm{AE}} H^4}{30EI}\right) \tag{6.8}$$

where, $W2_{AE}$ = P_{AE} = Seismic force per unit width of the RW

E = Young's modulus of the RW, I = Moment of Inertia of the RW

Once $\delta 1_{\mathrm{max}}$ and $\delta 2_{\mathrm{max}}$ are calculated the maximum displacement at the top of the RW can be calculated by submission of the $\delta 1_{\mathrm{max}}$ and $\delta 2_{\mathrm{max}}$. The derivations for finding the maximum displacements of base resrained cantilever with uniformly distributed and varying load have been presented in section A3.1. Figure 6-28 shows the detailed process for finding the earthquake induced elastic displacement of base restrained RW.

Input Parameters

1. RW height (H)
2. RW thickness (t_w)
3. RW Young's Modulus (E_{wall})
4. Moment of Inertia (I)
5. Unit weight of backfill ($\gamma_{Backfill}$)
6. Unit weight of RW material (γ_{Wall})
7. Backfill friction angle (ϕ)
8. RW backfill interface angle (δ)
9. Horizontal seismic coefficient (k_h)
10. Amplification factor (AF_H)

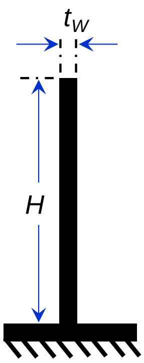

Calculations

1. Find body force at unit height of RW ($W1_{AE}$)

$$W1_{AE} = AF_H K_h W_{wall}$$

2. MO dynamic pressure coefficient (K_{AE})

$$K_{AE} = \frac{\text{Cos}^2(\phi - \theta - \psi)}{\cos\psi \, \text{Cos}^2\theta \cos(\delta + \theta + \psi)\left[1 + \sqrt{\frac{\sin(\delta + \phi)\sin(\phi - \beta - \psi)}{\cos(\delta + \theta + \psi)\cos(\beta - \theta)}}\right]^2}$$

3. Dynamic soil pressure at RW base (P_{AE})

$$P_{AE} = AF_H \, K_{AE} \gamma_{Backfill} H_{wall}$$

4. Use P_{AE} as triangular load per unit width of RW ($W2_{AE}$)

5. Find maximum displacement due to RW body force ($\delta 1_{max}$)

$$\delta 1_{max} = \left(\frac{W1_{AE} H^4}{8EI}\right)$$

6. Find maximum displacement due to dynamic soil pressure ($\delta 2_{max}$)

$$\delta 2_{max} = \left(\frac{W2_{AE} H^4}{30EI}\right)$$

7. Find maximum elastic displacement of base restrained RW:

$$\delta_{max} = \delta 1_{max} + \delta 2_{max}$$

Figure 6-28 Steps to estimate the maximum elastic seismic displacement of the base restrained RW.

6.7.1. Validation of the hand calculation results with the shaking table experiment and FE simulation results.

The validity of the proposed hand calculations has been examined by comparing the maximum RW displacements obtained from the hand calculations with the shaking table experiment results. It should be noted herein that the maximum acceleration obtained at the shaking table base has been used as PGA for the hand calculation.

During the shaking table experiments, a gap formulation has been observed between the Aluminum RW and the backfill. Due to the gap formulation, the backfill pressure behind the RW has dropped (Anderson, 2008; Ertugrul and Trandafir, 2014). However, in the hand calculations, the lateral coefficient for seismic earth pressure (K_{AE}) has been estimated using the MO method for 100 % PGA or maximum possible PGA (EN 1998-5). Because of this, the amplification of the horizontal acceleration for the scaled down RW model is neglected (AF_H = 1); Considering the amplification of the horizontal acceleration in the backfill with $K_{AE\text{ -100 \% PGA}}$ will overestimate the seismic pressure on the scaled down RW model. Table 6-5 shows details of the scaled down base restrained RW.

Table 6-5 Details of the scaled down base restrained RW for hand calculations.

Sr. No.	Description	Value (Units)
1.	RW height (above supports)	0.36 (m)
2.	RW thickness	0.004 (m)
3.	Density of RW material	2700 kg/m^3
4.	Young’s modulus	69 (GPa)
5.	Inertia of RW (*I*)	5.33E-9 m^4/m
6.	Density of backfill	1790 kg/m^3
7.	Friction angle backfill	44°

Table 6-6 shows the details of the base excitations and recorded PGA at the shaking table base. The maximum elastic displacements at the top of the RW obtained from the hand calculations and shaking table experiments have also been shown in table 6-6. Figure 6-29 also shows the maximum elastic displacement of the scaled down RW model estimated from the hand calculations and obtained from the shaking table experiment. Good agreement is shown between results from hand calculations and shaking table experimental results.

Table 6-6 Comparison of the maximum seismic displacement of the scaled down RW, obtained from the proposed hand calculations and shaking table experiments.

Sr. No.	Details of base excitation	PGA of base excitation (g)	PGA recorded at shaking table base (g)	Maximum displacement recorded by laser sensor (mm)	Maximum displacement by hand calculations (mm)
1.	Chuetsu-Oki ($\lambda_{\Delta t} = 4\sqrt{\lambda_l}$ & $\lambda_l = 10$) (figure 4-24)	0.32	0.32	3.3	3.41
2.	Northridge ($\lambda_{\Delta t} = 2\sqrt{\lambda_l}$ & $\lambda_l = 10$) (figure 4-24)	0.43	0.41	6.51	4.25
3.	Multiple pulses (3 Hz/20 mm max dis) (figure 4-20)	0.73	0.62	7.55	7.05
4.	Multiple pulses (3 Hz/25 mm max dis) (figure 4-20)	0.9	0.76	10.24	10.35
5.	Tabas, Iran ($\lambda_{\Delta t} = 2\sqrt{\lambda_l}$ & $\lambda_l = 10$) (figure 4-24)	0.85	0.8	12.29	11.73
7.	Multiple pulses (4 Hz/ 20 mm max disp) (figure A4-1)	1	0.82	11.87	12.82
8.	Multiple pulses (4 Hz/ 25 mm max disp) (figure A4-1) – K_{AE} reduced to 50 % as high separation of RW-Backfill Observed	1.55	1.145	20.03	21.25

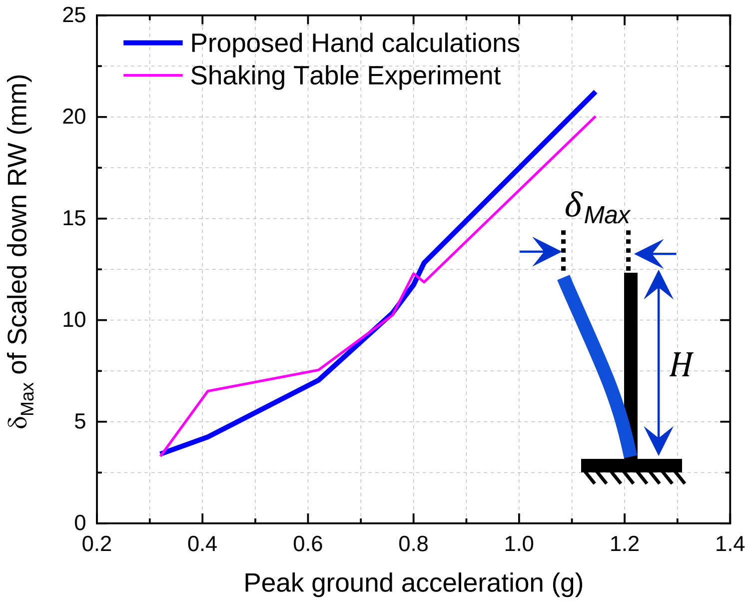

Figure 6-29 Comparison of the maximum elastic displacement of the base restrained RW, obtained from the hand calculations and shaking table experiments.

The validity of the proposed hand calculations has also been examined for estimation of the δ_{max} for the prototype base restrained RW. A detailed parametric investigation has been performed for flexible and rigid RW's with different backfill. Table 6-7 shows geometrical and material details of the prototype base restrained RW's. Steps shown in figure 6-28 were used for finding the δ_{max} for the prototype RW.

Table 6-7 Geometrical and material details of the prototype base restrained RW.

Sr. No.	Description	Flexible RW 1	Flexible RW 2	Stiff RW
1.	RW stem height	3.625 (m)	9.0 (m)	3.625 (m)
2.	RW thickness	0.15 (m)	0.5 (m)	0.65 (m)
3.	Density of RW material	2400 (kg/m^3)		
4.	Young's modulus	25.0 (GPa)	25 (GPa)	65 (GPa)
5.	Inertia of RW (I)	0.000281 (m^4/m)	0.0104 (m^4/m)	0.0229 (m^4/m)
6.	Density of backfill	Dune Sand: 1670 (kg/m^3) Fontainebleau Sand: 1753 (kg/m^3) Crushed Rock: 1790 (kg/m^3)		
7.	Friction angle backfill	Dune Sand: 34^o Fontainebleau Sand: 39^o Crushed Rock: 44^o		

Details of the FE modelling of seismic actions on the base restrained RW have been presented in section 6.2 of the present chapter. Nonlinear FE analyses have been performed for different base excitations (PGA range from 0.093g to 0.74g). Synthetic accelerograms (section 4.5.1, figure 4-24 of chapter 4) were used as input ground motion.

In the case of prototype RW a range of AF_H has been considered based on the type of RW and backfill. During the shaking table experiment on scaled down flexible RW ($\lambda_l = 10$ & $H_{RW} = 0.4\ m$) an AF_H of 2.24 was observed (figure 4-28 of chapter 4). Therefore, for flexible RW 1 (crushed rock backfill), $AF_H = 2$ has been considered. It was observed during several investigations that amplification of horizontal acceleration reduces with decrement in friction angle of backfill (Ghosh, 2008; Bhattacharjee & Krishna, 2015). Therefore, $AF_H = 1.5$ and 1.25 has been considered for RW with Fontainebleau sand ($\phi = 39^0$) and Dune sand ($\phi = 34^0$)

backfill respectively. The amplification of horizontal acceleration in soil layers resting over bed rock decreases with increasing height of soil layer (Roesset, J. M. 1970). Therefore, in the case of Flexible RW 2, AF_{H} = 1.5 , 1.35 and 1.00 has been considered for RW with crushed rock ($\phi = 44^{0}$), Fontainebleau sand ($\phi = 39^{0}$) and Dune sand ($\phi = 34^{0}$) backfill respectively. In the case of stiff RW higher accelerations at RW stem (increasing towards the RW top) has been observed due to high stiffness and less movement. Therefore, AF_{H} = 5 , 4.5 and 4.0 has been considered for RW with crushed rock ($\phi = 44^{0}$), Fontainebleau sand ($\phi = 39^{0}$) and Dune sand ($\phi = 34^{0}$) backfill respectively.

Figure 6-30 to 6-32 shows the comparison of $\delta_{\max}$ ($\Delta_{\mathrm{R-RW\,Top}}$) for the base restrained RW; obtained from the FE simulations with the proposed hand calculations. Good agreement has been observed between the hand calculations and the FE analysis results.

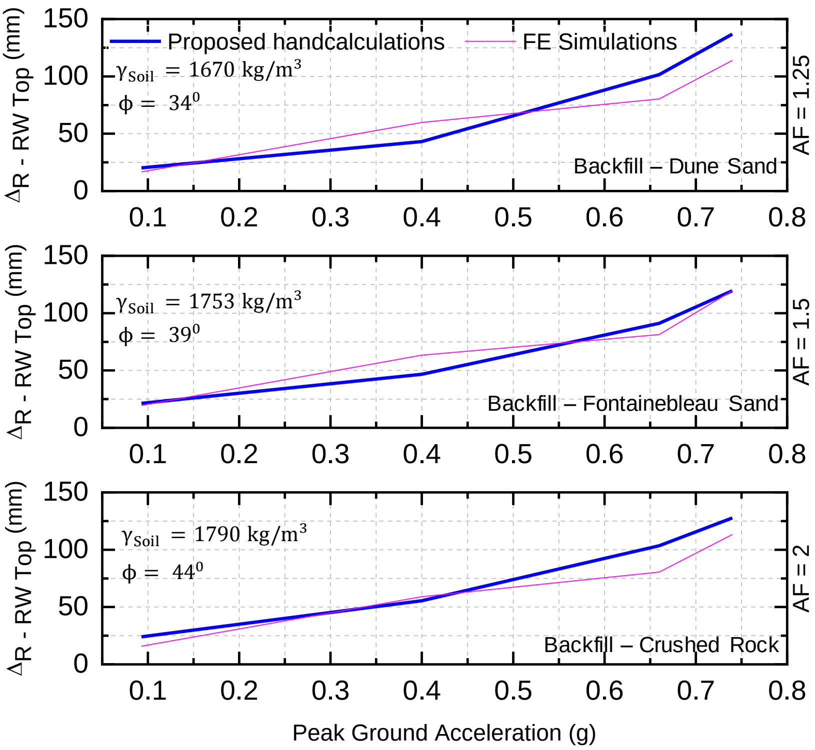

Figure 6-30 Comparison of the maximum elastic displacement of the base restrained flexible RW 1, obtained from the hand calculations and FE simulations.

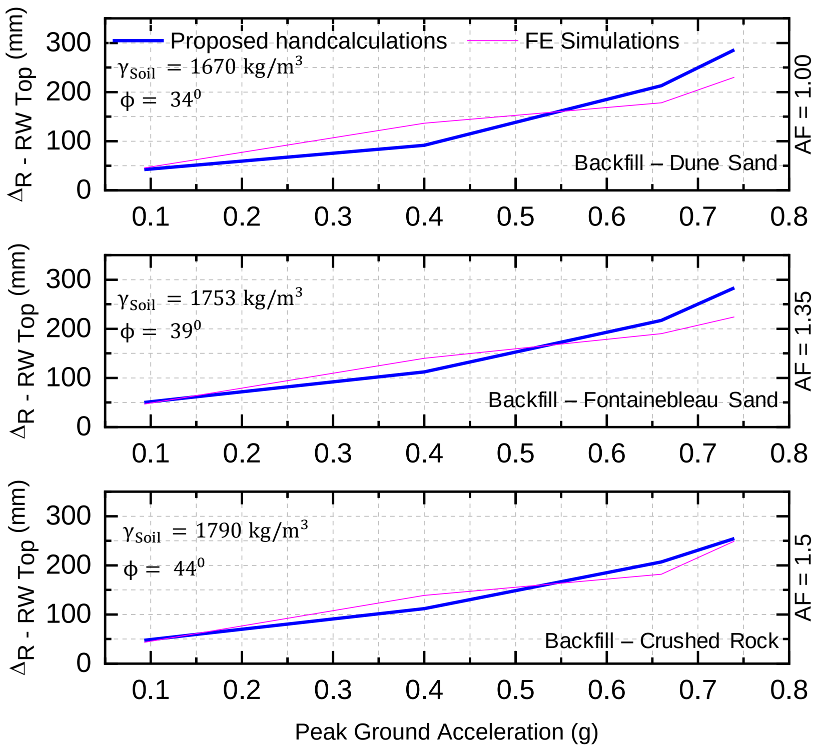

Figure 6-31 Comparison of the maximum elastic displacement of the base restrained flexible RW 2, obtained from the hand calculations and FE simulations.

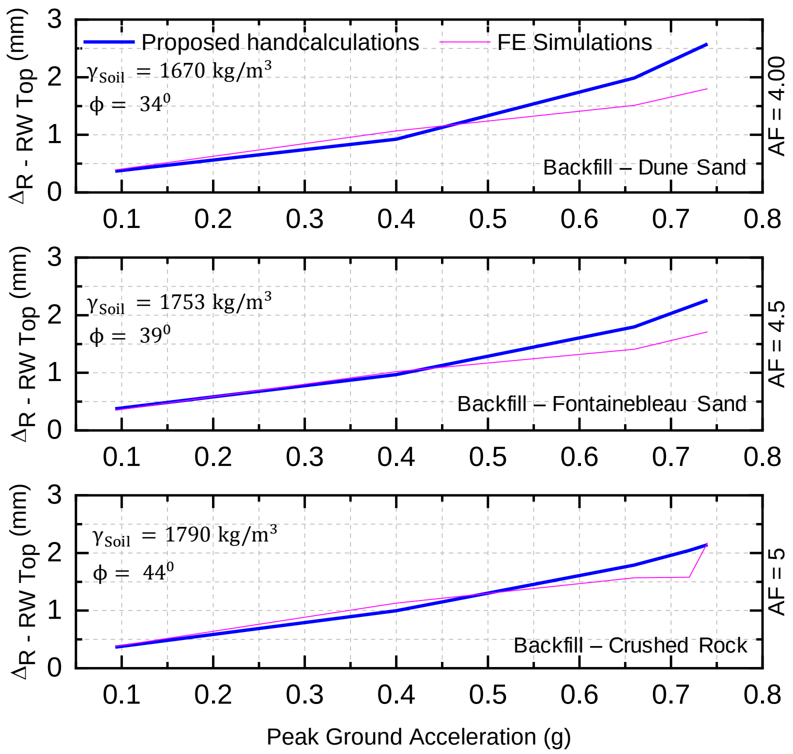

Figure 6-32 Comparison of the maximum elastic displacement of the base restrained stiff RW, obtained from the hand calculations and FE simulations.

6.8. Chapter summary

Nonlinear FE analyses have been carried out for understanding the earthquake induced displacement behavior of the base restrained RC RW. The FE analyses have been performed on the 2D plane strain prototype RW models. The parametric investigations have also been performed for the three different cohesionless backfill materials, (i) Dune sand, (ii) Fontainebleau sand, and (iii) crushed rocks. Each of the backfill material has been modelled using the Mohr Coulomb material model along with the hardening and softening behaviour. The earthquake response behaviour of the FE models have been investigated against ten synthetic and historical recorded accelerograms. Backfill pressure of a nonlinear profile behind the RW stem has been observed for all the cases. It was also observed that the maximum inertial force from backfill is not related to applied PGA. The dynamic backfill pressure obtained from FE analyses has been compared with the backfill pressure as estimated using the MO equation. It was found that the MO method mostly underestimates the backfill pressure on the RW. The residual backfill pressure has also been recorded at the end of the FE simulations. Similar average amplification factors of the horizontal acceleration have been observed for all the three types of backfill from the FE simulations. It was also observed that the deflection profile of the RW stem wall, depends highly on the intensity of the applied PGA. From parametric investigations for different backfill types, it was observed that the type of backfill does not significantly influence the seismic displacement demand of the base restrained RW. Simple hand calculations have also been proposed for estimation of the earthquake induced maximum elastic displacement of the base restrained RW.

Chapter 7. SEISMIC BEHAVIOR OF FREE-STANDING EARTH RETAINING STRUCTURES

7.1. Introduction

Satisfactory performance of free-standing earth retaining structures during a design level seismic event could be ensured by an accurate and realistic assessment of seismic actions on them. In the present chapter, a free-standing cantilever retaining wall (CRW) has been analyzed against earthquake loading. Detailed and rigorous parametric investigations have been performed for different base excitations and types of backfill. The non-linear time history analyses have been performed using finite element (FE) software Abaqus. Backfill materials the free-standing CRW has been modelled using the Mohr Coulomb material model. Hardening and softening behaviour of the soil material also been simulated. Mesh sensitivity study has been performed for the FE model of free-standing CRW. Spring and dashpot system have been used to model vertical boundaries of the FE model so that the boundary effects could be minimized.

Results of FE analyses have been studied for the earthquake induced displacement demand of free-standing CRW. Earthquake induced backfill pressure and its role on the seismic displacement behaviour of earth retaining structures has also been studied. Significant amplification of horizontal acceleration in the backfill has been observed. The softening of the backfill materials and mobilization of angle of friction in the soil can profoundly influence the seismic response behaviour of a free-standing retaining wall.

7.2. Two dimensional (2D) plane strain finite element (FE) modelling of free-standing cantilever retaining wall (CRW)

The FE model of a free-standing CRW has been developed using the FE software Abaqus. Figure 7-1 shows the geometrical details of two dimensional (2D) plane strain FE model of a free-standing CRW. The CRW and the backfill behaviour behind it was modelled above a firm rock stratum. It was assumed that free-standing CRW's are generally constructed above rock outcrops or high bearing capacity soil strata. The stem wall and base slab of a free-standing CRW was modelled as a high stiffness concrete material. Height and thickness of the stem wall were kept at 5 m and 0.6 m respectively. A 30 m long and 5.6 m high backfill domain was modelled behind the CRW. The depth of firm rock below the CRW was kept at 6.5m. Four nodes bilinear plane strain quadrilateral elements with reduced integration and hourglass control (CPE4R) were used to generate the FE mesh. Freestyle meshing technique was adopted for generating the mesh for all parts. Figure 7-2 shows the FE mesh of 2D free-standing CRW model. Contact was modelled at the interface of the stem wall with the backfill, heel slab with the backfill, CRW slab with the firm rock, and firm rock with the backfill. Frictional contact was modelled in the tangential direction for interfaces mentioned earlier. The coefficient of friction was kept at $\tan(\frac{2}{3}\phi)$, where ϕ is the angle of internal friction of the backfill. The coefficient of friction at the interface of the CRW base slab and frim rock was kept at 0.6 (Armstrong, R. C.; 1992). Hard contact was also modelled for all interfaces, for minimizing mesh penetrations. Master and slave surfaces have been defined for all contacts. Gravity loading was applied to the entire FE model during the non-linear time history FE analyses. Geostatic stresses have also been defined for the backfill and firm rock, for ensuring equilibrium of forces. The non-linear time history FE analyses have been performed in the dynamic explicit scheme of the FE software Abaqus. The dynamic explicit scheme is suitable for simulation of large deformation FE analyses (Abaqus/Explicit User's Manual, version 6.13. 2013). Details of the explicit solution scheme of Abaqus have been discussed in chapter 6 (section 6.2). Spring and dashpot type lateral boundaries were used for minimizing the boundary effects, and for avoiding large backfill domain. Domain size study for the backfill domain length is presented in chapter 6. Figure 7-1 also shows the boundary conditions used in the non-linear time history FE analysis of the free-standing CRW. During the initial step, vertical boundaries of the FE model were restrained from moving in the lateral direction ("*x*" direction). During the dynamic explicit step, the FE domain between spring and dashpot boundaries was free to translate in the lateral (“*x*”) direction. The bottom of the rock domain between the spring and dashpot boundaries was restrained in vertical (“*y*”) direction. Acceleration time history has been applied at the base of the rock domain during the dynamic explicit step. Low sampling frequency was kept for output results for ensuring good accuracy of the FE simulations. The sign convention is also shown in figure 7-1: stress and displacement are positive in the increasing “*x”* and “*y”* directions.

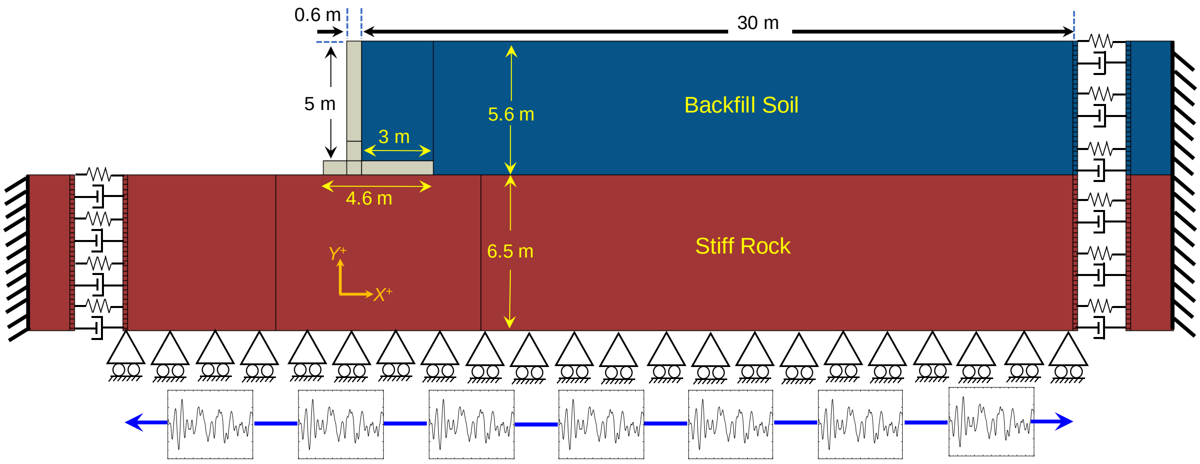

Figure 7-1 Geometrical details and boundary conditions of free-standing CRW model.

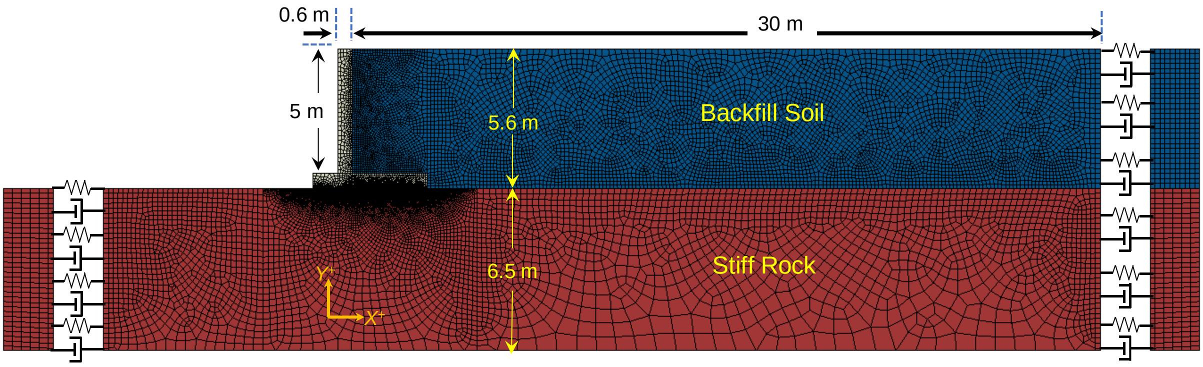

Figure 7-2 Two-dimensional plane strain FE model of free-standing CRW.

7.3. Constitutive modelling of materials

7.3.1. Constitutive modelling of the backfill

The backfill was modelled using the Mohr Coulomb material model. Details of the Mohr Coulomb material model has been presented in chapter 5. As explained in chapter 6, detailed parametric investigations have been performed for three different backfill types: (i) Dune sand (Daheur et al. 2019), (ii) Fontainebleau sand (Dano et al. 2004) and (iii) crushed rocks (characterized at The University of Melbourne) respectively. Mohr Coulomb material model has been calibrated for simulating the hardening and softening behaviour of the backfills. Details of the Mohr Coulomb model and calibration with the constitutive behaviour of the backfill have been presented in chapter 5 (section 5.3.4) and 6 (section 6.3.1). Damping in the backfill was modelled using Rayleigh damping parameters. Details of the modelling have been presented in chapter 5 (section 5.3.5). Figure 7-5 shows engineering properties considered for different backfill types. It should be noted herein that for crushed rocks backfill, the constrained modulus was obtained based on 1D compression test performed by the author. However, in the case of Dune sand (Daheur et al. 2019) and Fontainebleau sand (Dano et al. 2004) the partial constrained modulus was estimated from triaxial test results. This is because triaxial test results generally overestimate the constrained modulus of the soil (Geoguide I, 1993; Angelim et al.; 2016).

7.3.2. Constitutive modelling of the Concrete and firm rock

The stem and base slab of the CRW were modelled as a concrete material based on elastic properties. The density of concrete was kept at 2400 kg/m^3. The Young's modulus and Poisson's ratio of concrete were kept at 70 GPa (to avoid concrete deformation) and 0.3. The firm rock below the CRW was modelled as elastic materials with 2800 kg/m^3 density and 200 GPa young's modulus (for avoiding base deformation).

7.4. Mesh sensitivity study for free-standing CRW domain

Mesh sensitivity studies were performed for free-standing CRW domain. It should be noted herein that in the case of a free-standing CRW, the mesh size at the interface of different materials can also influence results from FE simulations. Therefore, a detailed parametric investigation has been performed by varying the mesh size at contact points at different parts of the model.

Table 7-1 to 7-4 shows different mesh sizes considered for the free-standing CRW domain. An optimum mesh size of a free-standing CRW domain was desired so that high accuracy of results could be ensured with optimum computational time. The crushed rocks were used as the backfill material for mesh sensitivity analyses. Details of the modelling of crushed rocks have been presented in chapter 7. All FE models of varying mesh size have been analyzed against multiple pulses (refer figure 7-3). Non-linear time history analyses have been performed in the dynamic explicit scheme of the FE software Abaqus. Figure 7-4 shows the displacement time-histories of a free-standing CRW for different mesh sizes. Mesh type 4 was selected for use in the more detailed FE study of a free-standing CRW in view of the trend of convergence observed.

Table 7-1 Mesh type 1 for free-standing CRW domain.

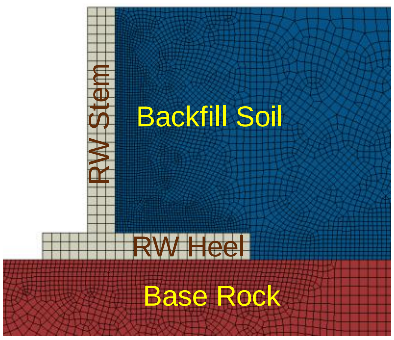

Part Name	Location	Mesh Size (mm)
Backfill	Soil - CRW Stem interface	60
Backfill	Soil - CRW Heel interface	60
Backfill	Soil - base rock interface	100
Retaining Wall	CRW stem - soil interface	200
Retaining Wall	CRW heel – soil interface	200
Retaining Wall	CRW – base rock interface	200
Base	Base rock - CRW interface	100
Base	Base rock – soil interface	200

Table 7-2 Mesh type 2 for free-standing CRW domain.

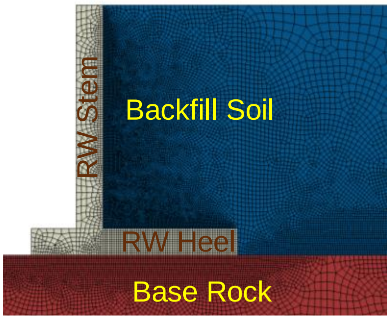

Part Name	Location	Mesh Size (mm)
Backfill	Soil - CRW Stem interface	30
Backfill	Soil - CRW Heel interface	30
Backfill	Soil - base rock interface	50
Retaining Wall	CRW stem - soil interface	50
Retaining Wall	CRW heel – soil interface	50
Retaining Wall	CRW – base rock interface	50
Base	Base rock - CRW interface	25
Base	Base rock – soil interface	100

Table 7-3 Mesh type 3 for free-standing CRW domain.

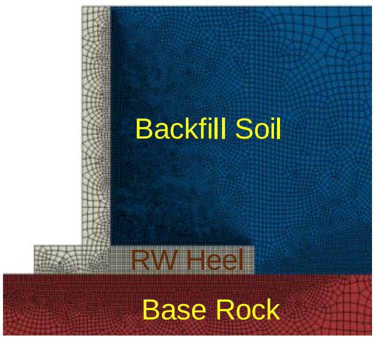

Part Name	Location	Mesh Size (mm)
Backfill	Soil - CRW Stem interface	30
Backfill	Soil - CRW Heel interface	15
Backfill	Soil - base rock interface	50
Retaining Wall	CRW stem - soil interface	25
Retaining Wall	CRW heel – soil interface	50
Retaining Wall	CRW – base rock interface	10
Base	Base rock - CRW interface	20
Base	Base rock – soil interface	100

Table 7-4 Mesh type 4 for free-standing CRW domain.

Part Name	Location	Mesh Size (mm)
Backfill	Soil - CRW Stem interface	80
Backfill	Soil - CRW Heel interface	80
Backfill	Soil - base rock interface	150
Retaining Wall	CRW stem - soil interface	60
Retaining Wall	CRW heel – soil interface	50
Retaining Wall	CRW – base rock interface	25
Base	Base rock - CRW interface	40
Base	Base rock – soil interface	250

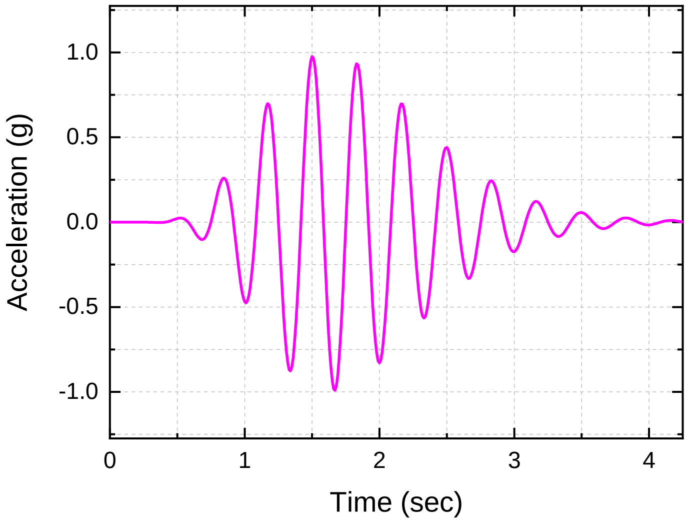

Figure 7-3 Applied acceleration time history for mesh sensitivity study on free-standing CRW.

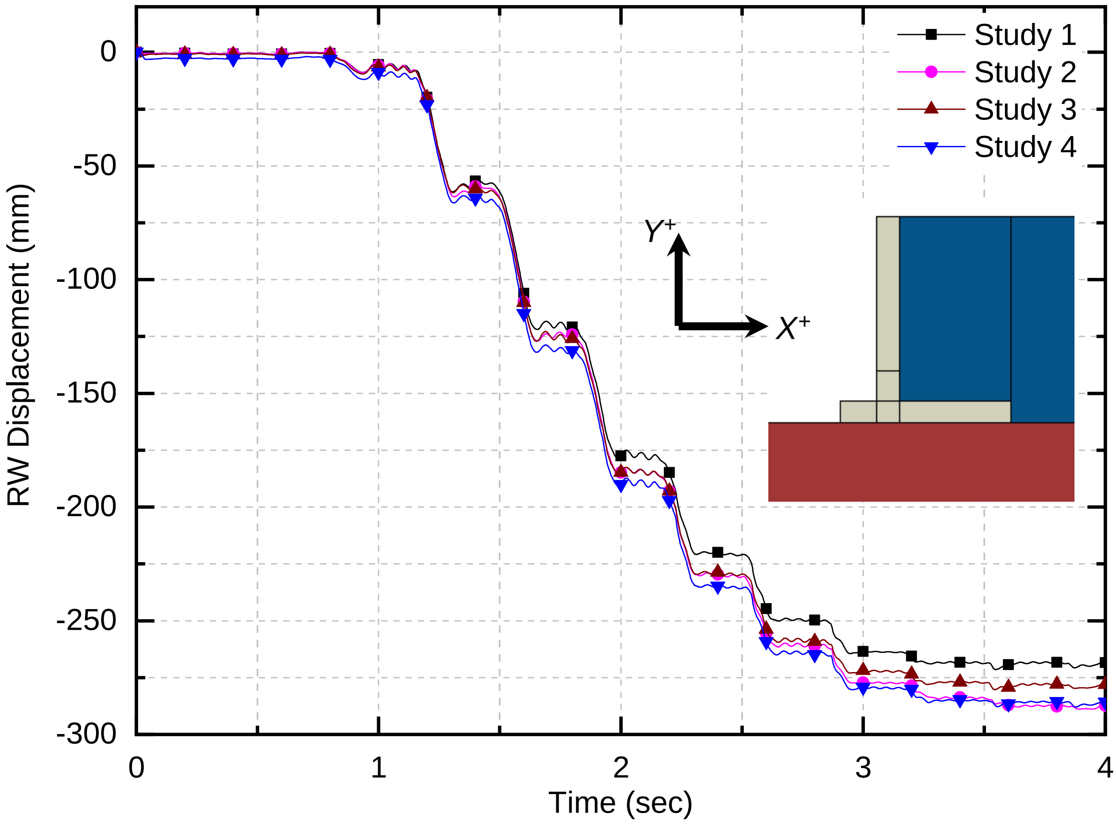

Figure 7-4 Displacement of free-standing CRW for different mesh types.

7.5. Parametric investigation on Free-standing CRW

A detailed and rigorous parametric investigation has been performed for studying the effects of earthquake actions on a free-standing CRW. The parametric investigations have been performed for three different backfill types. Figure 7-5 shows the plan for the parametric investigation. Material details of different backfills considered for parametric investigations is shown in figure 7-5. Non-linear FE time history analyses were performed for ten base excitations (acceleration time histories) which were simulated using ten synthetic and historical recorded accelerograms. Details of the accelerogram selection have been presented in chapter 4. The acceleration time histories of all ten accelerograms have been shown in figures 4-23 and 4-24 (chapter 4). Results of the FE analyses have been analyzed for studying the displacement response behaviour of the free-standing CRW, the backfill pressure up the wall height, and amplification of the horizontal acceleration in the backfill.

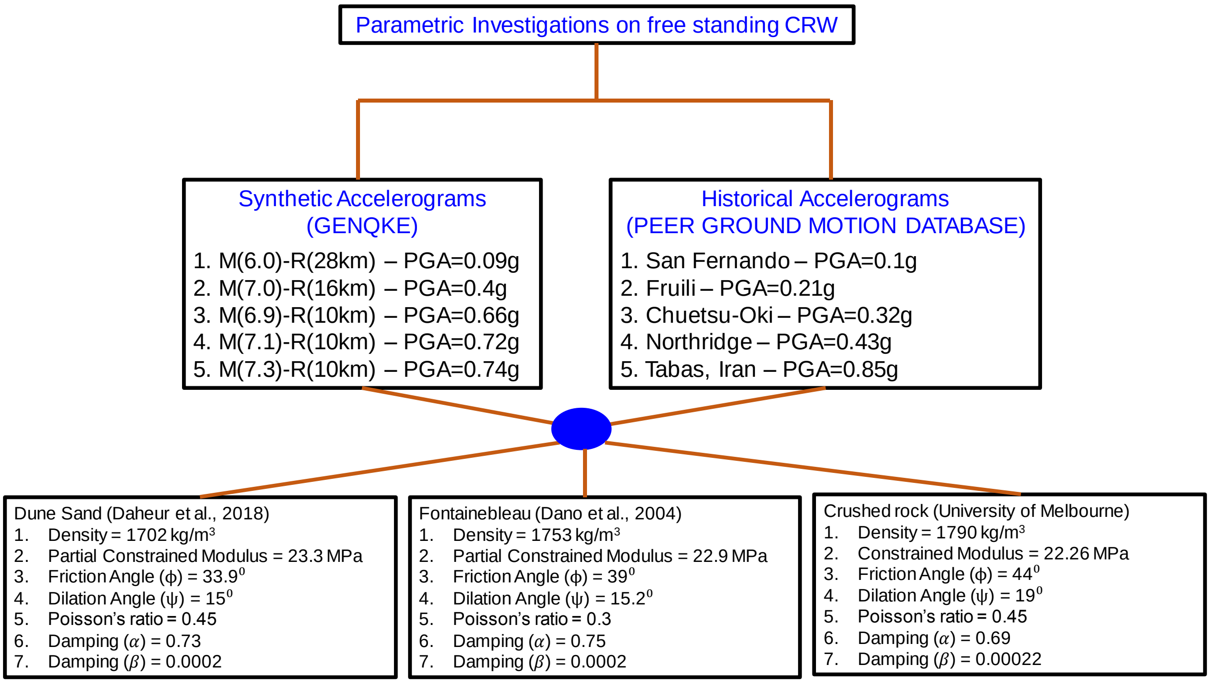

Figure 7-5 Parametric investigations on CRW.

7.6 Seismic performance of free-standing CRW with Dune sand backfill type

7.6.1. Displacement response of CRW, Backfill type - Dune sand

The displacement response of a free-standing CRW with dune sand as backfill has been studied against different base excitations. Figure 7-6 shows the displacement (sliding) of a CRW when subjected to ten synthetic and historical recorded earthquakes. The CRW with dune sand as backfill shows higher active state displacement than the CRW with Fontainebleau sand or crushed rocks as backfill type. It should be noted herein that in order to improve the seismic performance of CRW with Dune sand backfill the density of Dune sand has been slightly increased to 1702 kg/m^3 (whereas 1670 kg/m^3 has been used in Chapter 6 and 8). It was observed that the softening of Dune sand (natural sand) occurs at a low strain level, and this resulted in increasing seismic thrust on the CRW. As a result, higher permanent displacement of the CRW with Dune sand as backfill was observed. Other researchers reported similar observations for gravity type retaining walls (Huang et al.; 2009, McManus et al. 2017). In the case of a free-standing CRW, the permanent wall displacement can be profoundly influenced by the nature of the base excitations (Anderson, 2008). The Chuetsu accelerogram (PGA = 0.32g) shows a sinusoidal ground movement, and the CRW displaced in the "active direction" whenever the direction of the acceleration changed towards the backfill. Therefore, the CRW when excited by the Chuetsu accelerogram shows higher displacement than the CRW that was excited by the Northridge accelerogram. Similar behaviour of the CRW was observed for all three backfill types when analyzed against the Chuetsu accelerogram.

Table 7-5 and 7-6 shows the summary of permanent displacements of the CRW with Dune sand as backfill. Damage to the CRW for different base excitations has also been presented, by relating the displacement of the CRW at different levels of damage. Formation of active failure wedge has been considered when $\frac{\Delta}{\mathrm{H}} > 0.6$-0.8% (Potts & Fourie, 1986). The permissible and failure displacements for free-standing retaining walls have also been shown, as suggested by Huang et al. (2009). Formation of active failure wedge was observed for CRW with dune sand as backfill when PGA $\geq$ 0.3g. Significant damage to the CRW was observed at PGA $\geq$ 0.6g, and failure of the CRW was observed at PGA $\geq$ 0.7g.

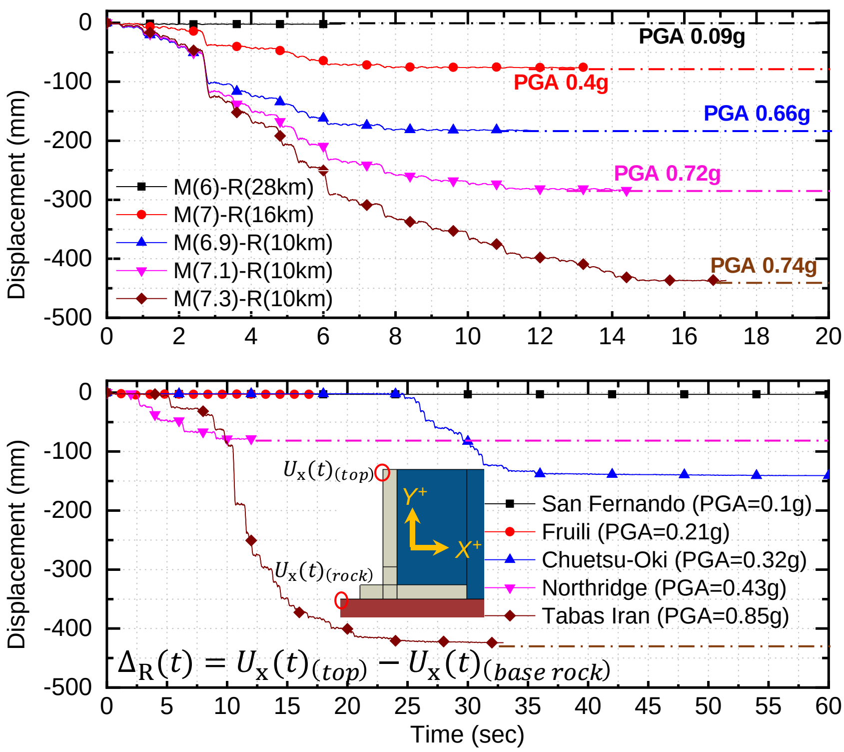

Figure 7-6 Displacement of free-standing CRW when subjected to different accelerograms, backfill type Dune sand.

Table 7-5 Damage quantification for CRW - Dune sand backfill type, when subjected to different synthetic accelerograms.

Sr. No.	M-R Combination	PGA (g)	Permissible Displacement (Huang et al.; 2009)	Failure Displacement (Huang et al.; 2009)	Displacement (mm) Present Study	Damage Level
1	M(6)-R28(Km)	0.08	0.02H = 112 mm	0.05H = 280 mm	2.48	**No Damage**
2	M(7)-R16(Km)	0.4			75.89	**No Damage (Active wedge formation)**
3	M(6.9)-R10(Km)	0.66			182.44	**Significant Damage**
4	M(7.1)-R10(Km)	0.72			284.09	**Failure**
5	M(7.3)-R10(Km)	0.74			436.87	**Failure**

Table 7-6 Damage quantification for CRW - Dune sand backfill type, when subjected to different historical accelerograms.

Sr. No.	M-R Combination	PGA (g)	Permissible Displacement (Huang et al.; 2009)	Failure Displacement (Huang et al.; 2009)	Observed Displacement (mm)	Damage
1	San fernando	0.1	0.02H = 112 mm	0.05H = 280 mm	3.01	No Damage
2	Fruili	0.21			2.93	No Damage
3	Chuetsu	0.32			140.59	Significant Damage (Active wedge formation)
4	Northridge	0.43			78.74	No Damage (Active wedge formation)
5	Tabas	0.85			423.97	Failure

7.6.2. Backfill pressure on CRW, Backfill type - Dune sand

Figure 7-7 shows pressure of the backfill up the wall height of a CRW, for different base excitations. The Dynamic backfill pressure as observed from present FE analyses and estimated using the conventional Mononobe-Okabe (MO) equation has also been shown. Lateral pressure up the wall height of the CRW for "at rest" and "Coulomb's active state" condition has also been shown in figure 7-7. FE analyses show a non-linear backfill pressure up the wall height. Similar observations were reported by Ishibashi and Fang (1987) for rigid retaining walls. It was observed that the conventional MO equation underestimate the backfill pressure for PGA ≤ 0.4g. In the case of PGA > 0.4 g, FE simulations show maximum dynamic pressure at mid height of the CRW. However, the MO equation underestimates the backfill pressure at mid height and overestimates the backfill pressure at the top and the base. Non-linear residual pressure, exceeding the Coulomb's active pressure up the wall height was also observed for all cases.

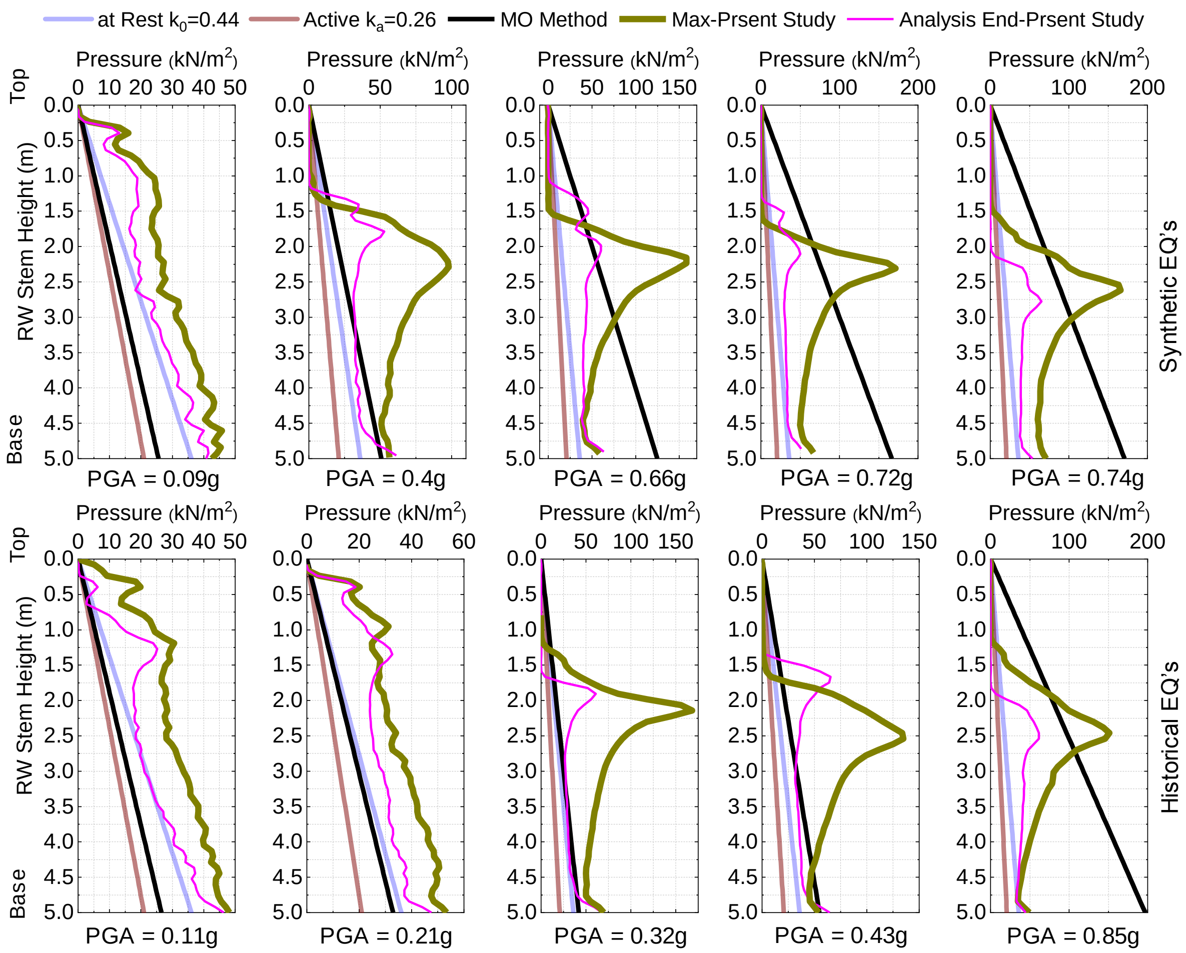

Figure 7-7 Backfill pressure up the CRW height, calculated for different stress states (at rest, Coulomb's active state), dynamic soil pressure calculated using MO equation and present FE analysis, Dune sand as backfill type.

7.6.3. Amplification of horizontal acceleration for CRW, Backfill type - Dune sand

Amplification of the horizontal acceleration in the backfill above the CRW's heel slab has also been studied. Figure 7-8 shows the response spectrum acceleration (RSA) of the horizontal acceleration of the backfill (which was made of Dune sand) at the base, middle and top for different base excitations. Amplification of the horizontal acceleration was observed for all cases. As mentioned earlier, the displacement response behaviour of a free-standing CRW mainly depends on the ground displacement. Therefore, the CRW shows higher amplification and displacement when excited by the Chuetsu accelerogram. The RSA of the backfill is shown to have diminished to a low level at natural periods exceeding 0.75 sec or so.

Figure 7-9a shows the procedure for obtaining the amplification factor in backfill (AF_{Soil}). Figure 7-9b shows the bar chart of AF_{Soil} of horizontal acceleration above the CRW heel slab at the base, middle and top of the backfill. No correlation has been observed between the applied base excitations and amplification factors. However, for the high values of RSA a decrement in AF_{Soil} was observed. The average value of the AF_{Soil} was found to be 2.1 and 1.39 at the top and at mid-height, respectively.

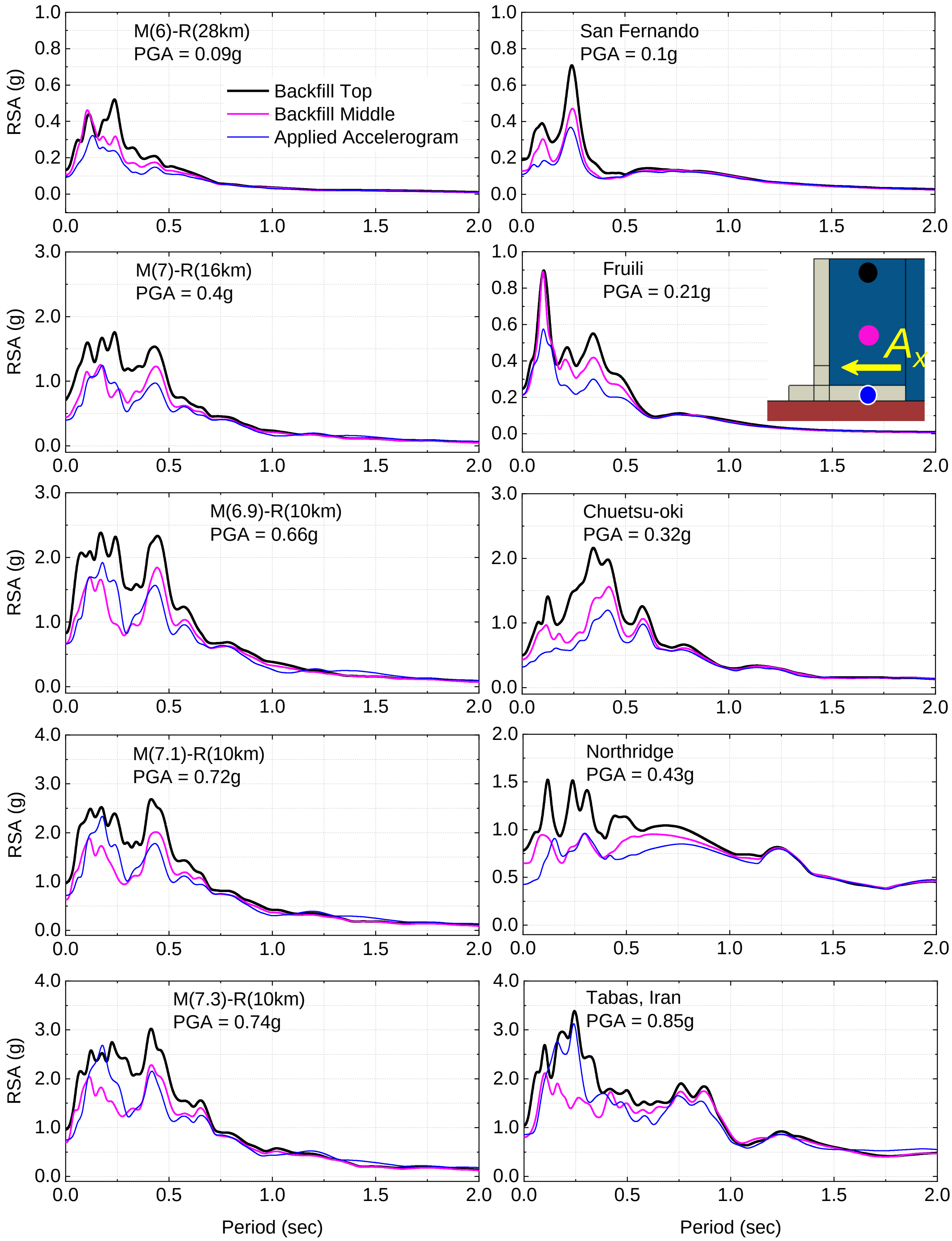

Figure 7-8 RSA for free-standing CRW, when subjected to different ground motions, backfill type Dune sand.

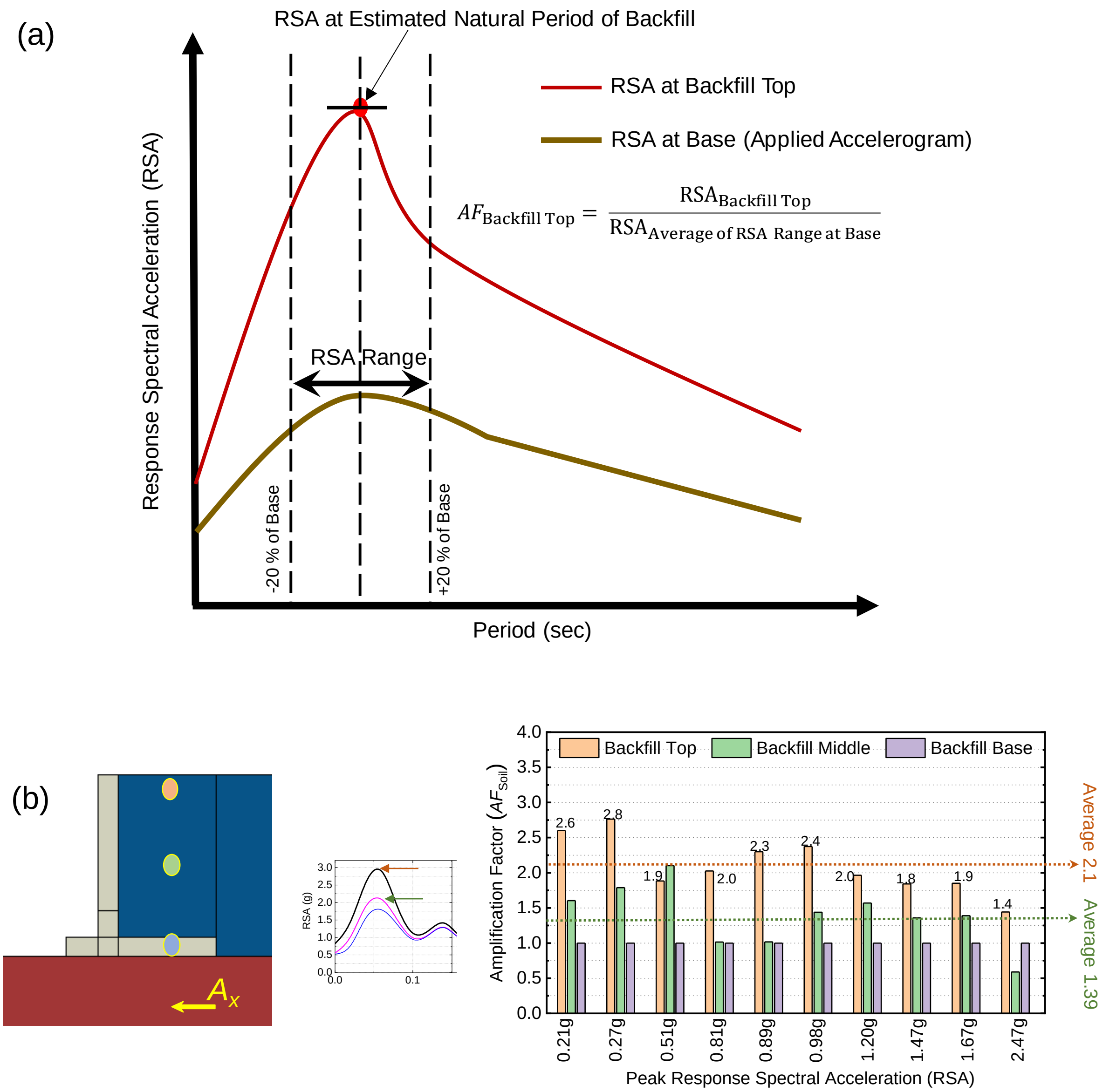

Figure 7-9 Amplification factor (horizontal acceleration) for free-standing CRW, when subjected to different ground motions, backfill type Dune sand.

7.7 Seismic performance of free-standing CRW with Fontainebleau sand backfill type

7.7.1. Displacement response of CRW, Backfill type - Fontainebleau sand

Figure 7-10 shows the displacement of a free-standing CRW with Fontainebleau sand backfill when excited using different accelerograms. Higher active state sliding of CRW was observed with increasing PGA for all cases, except for the Chuetsu accelerogram (justified in section 7.6.1). Formation of active failure wedge in backfill was observed when PGA > 0.3g. No damage or minor damage to the CRW was observed for PGA <0.66g, after which significant damage (and failure) to the CRW was observed. Table 7-7 and 7-8 shows quantification of damage observed for a free-standing CRW against different base excitations.

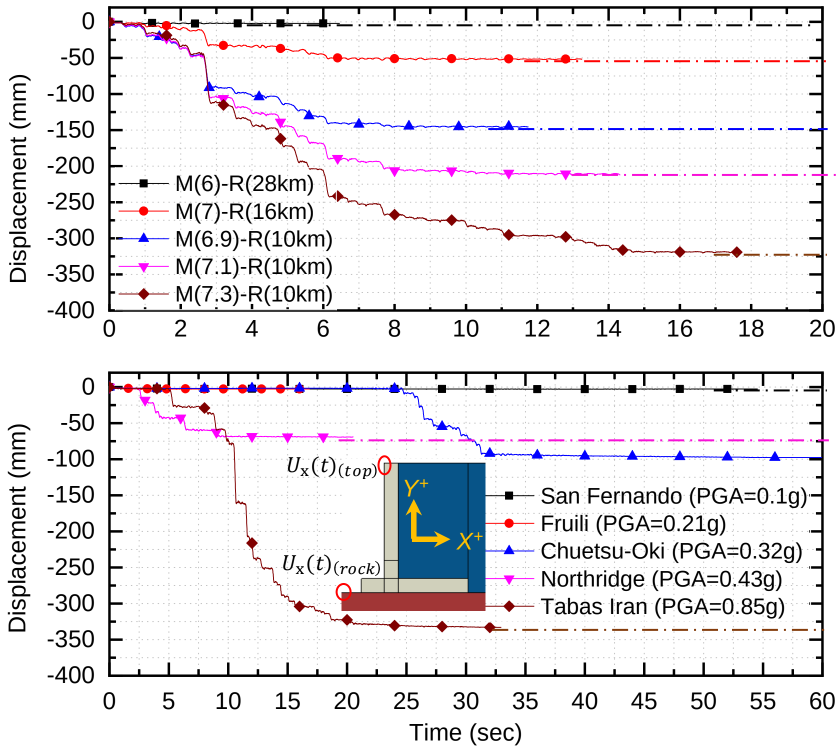

Figure 7-10 Displacement of free-standing CRW when subjected to different accelerograms, backfill type Fontainebleau sand.

Table 7-7 Damage quantification for CRW - Fontainebleau sand backfill type, when subjected to different synthetic accelerograms.

Sr. No.	M-R Combination	PGA (g)	Permissible Displacement (Huang et al.; 2009)	Failure Displacement (Huang et al.; 2009)	Displacement (mm) Present Study	Damage Level
1	M(6)-R28(Km)	0.08	0.02H = 112 mm	0.05H = 280 mm	2.1	**No Damage**
2	M(7)-R16(Km)	0.4			51.9	**No Damage (Active wedge formation)**
3	M(6.9)-R10(Km)	0.66			145.62	**Minor Damage**
4	M(7.1)-R10(Km)	0.72			211.8	**Significant Damage**
5	M(7.3)-R10(Km)	0.74			319.1	**Failure**

Table 7-8 Damage quantification for CRW - Fontainebleau sand backfill type, when subjected to different historical accelerograms.

Sr. No.	M-R Combination	PGA (g)	Permissible Displacement (Huang et al.; 2009)	Failure Displacement (Huang et al.; 2009)	Observed Displacement (mm)	Damage
1	San fernando	0.1	0.02H = 112 mm	0.05H = 280 mm	2.72	No Damage
2	Fruili	0.21			2.53	No Damage
3	Chuetsu	0.32			97.59	No Damage (Active wedge formation)
4	Northridge	0.43			69.25	No Damage (Active wedge formation)
5	Tabas	0.85			333.04	Failure

7.7.2. Backfill pressure on CRW, Backfill type - Fontainebleau sand

Figure 7-11 shows the backfill pressure up the stem height of a free-standing CRW. A non-linear dynamic soil pressure has been observed from present FE analyses, for PGA > 0.3g. A higher backfill pressure was observed at mid height of the CRW. In most cases the MO equation underestimates the backfill pressure at mid height. Residual backfill pressure exceeding the Coulomb's active state pressure was also observed in all cases. It was observed that the softening of the Fontainebleau sand occurs at higher strain levels than Dune sand. Therefore, the CRW with Fontainebleau sand as backfill shows a limited displacement demand and slightly higher residual backfill pressure (for PGA > 0.4g) in comparison with a CRW in which Dune sand was used as backfill.

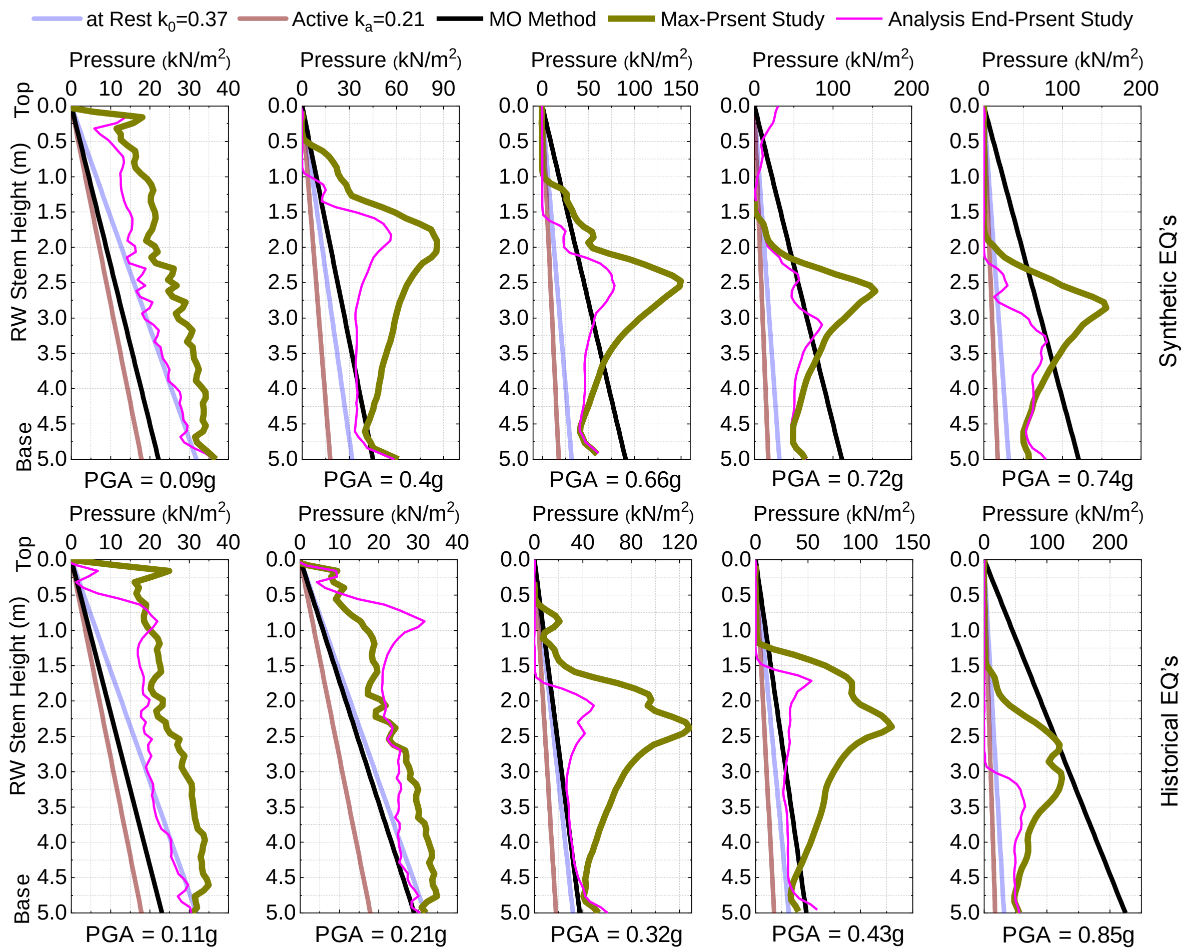

Figure 7-11 Backfill pressure up the CRW height, calculated for different stress states (at rest, Coulomb's active state), dynamic soil pressure calculated using MO equation and present FE analysis, Fontainebleau sand as backfill type.

7.7.3. Amplification of horizontal acceleration for CRW, Backfill type – Fontainebleau sand

Figure 7-12 shows the RSA for a free-standing CRW with Fontainebleau sand as backfill when subjected to different base excitations. For PGA > 0.43g; higher RSA of horizontal acceleration was observed than a CRW which used Dune sand as backfill. It was observed that when Fontainebleau sand was used as backfill, the complete mobilization of the soil's shear strength did not occur. Because of this, lesser softening of the Fontainebleau sand occurred and also lesser amount of sliding of the CRW (Fontainebleau sand backfill) and higher RSA of the horizontal acceleration at high PGA. This observation raises the importance of the choice of backfill material in terms of its potential influence on the seismic response behaviour of a free-standing earth retaining structure.

Figure 7-13 shows AF_{Soil} for horizontal acceleration for Fontainbleau sand backfill type. Average AF_{Soil} of 2.06 and 1.32 was observed at the top and at the middle, which is similar to Dune sand type backfill. Similar to Dune sand backfill, no co-relation has been observed between the applied PGA and AF_{Soil}.

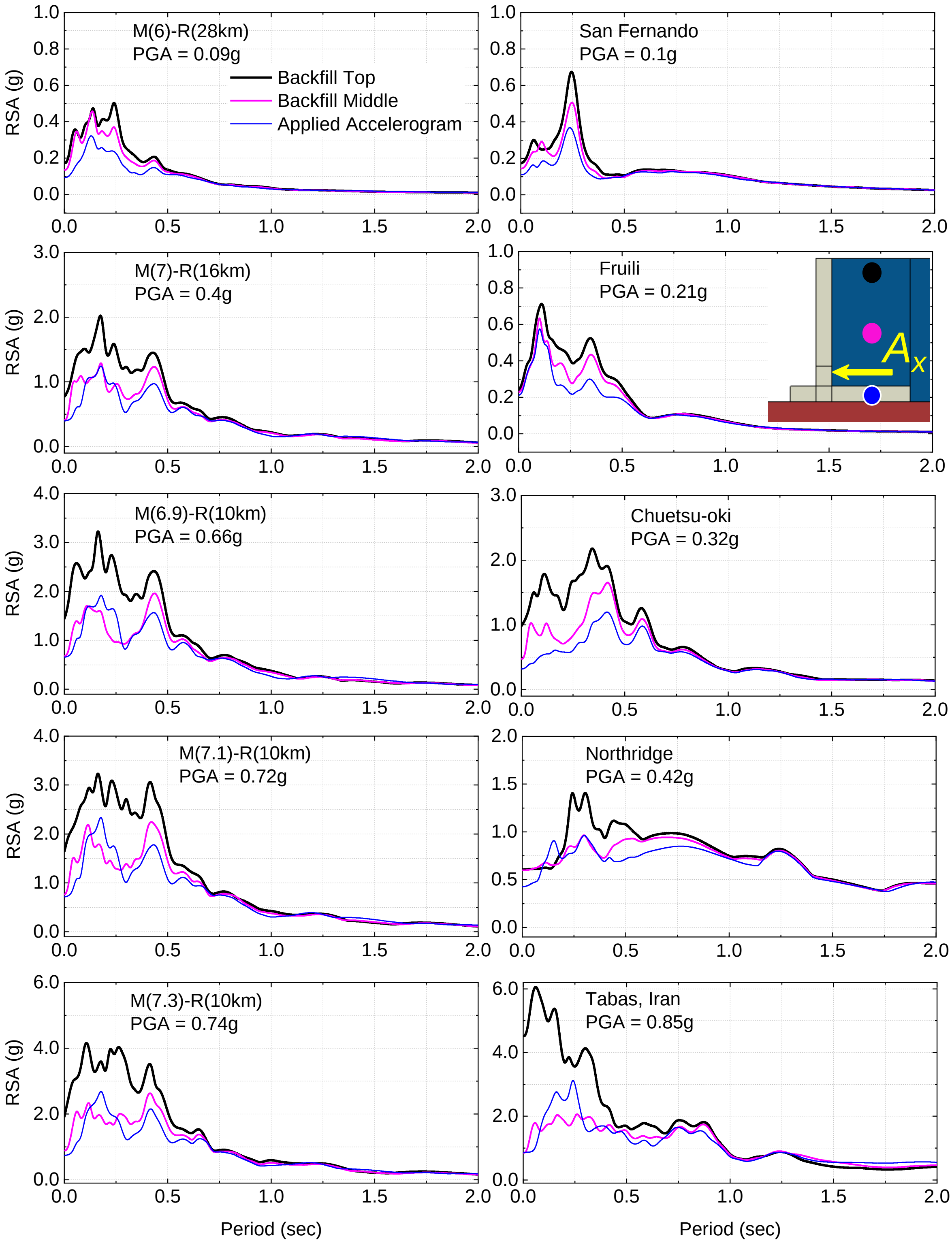

Figure 7-12 RSA for free-standing CRW, when subjected to different ground motions, backfill type Fontainebleau sand.

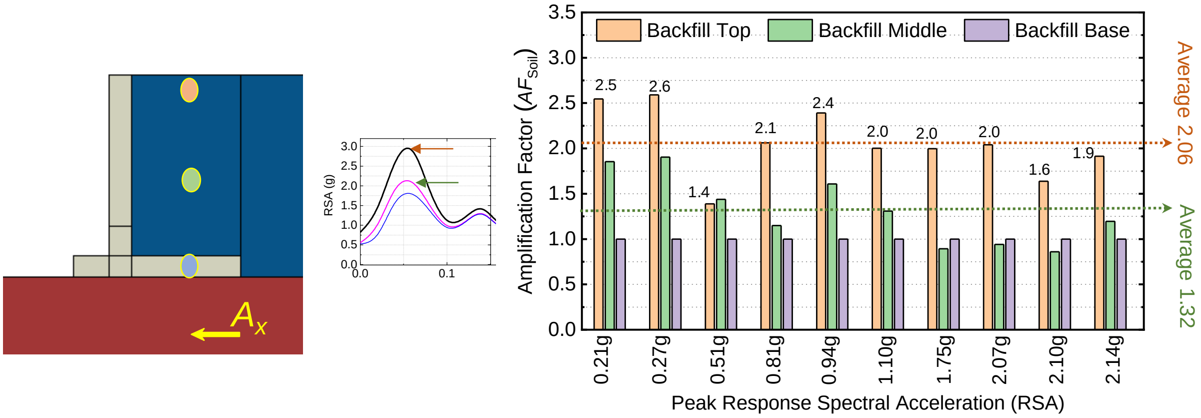

Figure 7-13 Amplification factor (horizontal acceleration) for free-standing CRW, when subjected to different ground motions, backfill type Fontainebleau sand.

7.8 Seismic performance of free-standing CRW with crushed rock backfill type

7.8.1. Displacement response of CRW, Backfill type - crushed rock

Figure 7-14 shows the displacement time history of a free-standing CRW with crushed rocks as backfill when subjected to different base excitations. Formation of active failure wedge was observed at PGA > 0.3g. It should be noted herein that the softening of crushed rock occurs at a high axial strain. As a result, lesser displacement demand of the CRW was observed in comparison with CRW, which made use of sand as backfill. Table 7-9 and 7-10 shows the damage of CRW with crushed rock backfill type. Failure of the CRW was observed for PGA > 0.74g, which indicates better performance of the CRW with crushed rocks as backfill as opposed to the use of sand as backfill.

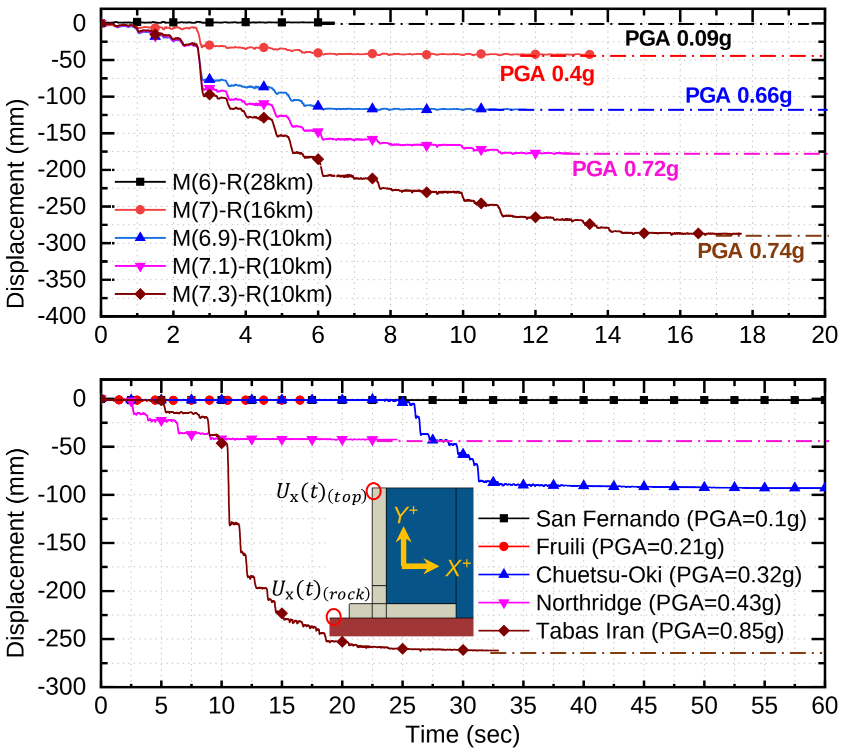

Figure 7-14 Displacement of free-standing CRW when subjected to different accelerograms, backfill type crushed rock.

Table 7-9 Damage quantification for CRW - crushed rock backfill type, when subjected to different synthetic accelerograms.

Sr. No.	M-R Combination	PGA (g)	Permissible Displacement (Huang et al.; 2009)	Failure Displacement (Huang et al.; 2009)	Displacement (mm) Present Study	Damage Level
1	M(6)-R28(Km)	0.08	0.02H = 112 mm	0.05H = 280 mm	1.37	**No Damage**
2	M(7)-R16(Km)	0.4			42.4	**No Damage (Active wedge formation)**
3	M(6.9)-R10(Km)	0.66			117.34	**Minor Damage**
4	M(7.1)-R10(Km)	0.72			177.52	**Significant Damage**
5	M(7.3)-R10(Km)	0.74			287.48	**Failure**

Table 7-10 Damage quantification for CRW - crushed rock backfill type, when subjected to different historical accelerograms.

Sr. No.	M-R Combination	PGA (g)	Permissible Displacement (Huang et al.; 2009)	Failure Displacement (Huang et al.; 2009)	Observed Displacement (mm)	Damage
1	San fernando	0.1	0.02H = 112 mm	0.05H = 280 mm	1.00	No Damage
2	Fruili	0.21			2.00	No Damage
3	Chuetsu	0.32			93	No Damage (Active wedge formation)
4	Northridge	0.43			42	No Damage (Active wedge formation)
5	Tabas	0.85			262	**Significant Damage**

7.8.2. Backfill pressure on CRW, Backfill type – crushed rock

Figure 7-15 shows the backfill pressure up the wall height of a free-standing CRW with crushed rocks as backfill. Backfill pressure with a non-linear profile was observed up the wall height similar to observations made on CRW which made use of sand as backfill. The MO equation underestimates backfill pressure for most cases. Residual backfill pressure has also been observed for all cases, which was more than the residual backfill pressure observed from other two backfill types. It was also observed that due to lesser movement of the CRW with crushed rocks as backfill high residual stresses accumulated at the wall – backfill interface. This observation also highlights the influence of the choice of materials for the backfill on the seismic performance of the earth retaining structures.

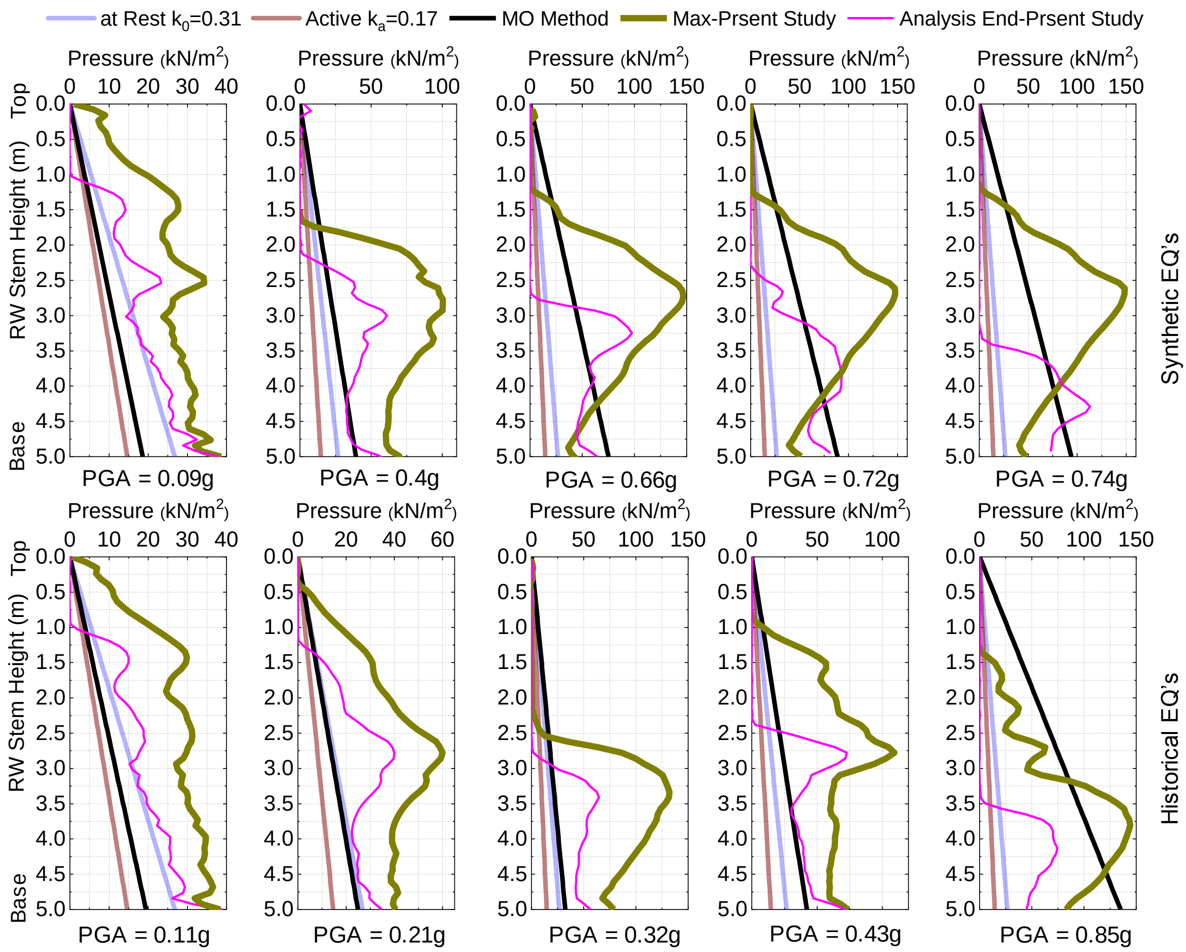

Figure 7-15 Backfill pressure up the CRW height, calculated for different stress states (at rest, Coulomb's active state), dynamic soil pressure calculated using MO equation and present FE analysis, crushed rock as backfill type.

7.8.3. Amplification of horizontal acceleration for CRW, Backfill type – crushed rock

Figure 7-16 shows the RSA of the horizontal acceleration at different heights up the wall above the heel slab of the CRW with crushed rocks as backfill material. Higher amplification has been observed for all cases than a CRW with sand as backfill. As mentioned before, due to the lesser movement, the CRW with crushed rock backfill shows slightly higher amplification than other two backfill types.

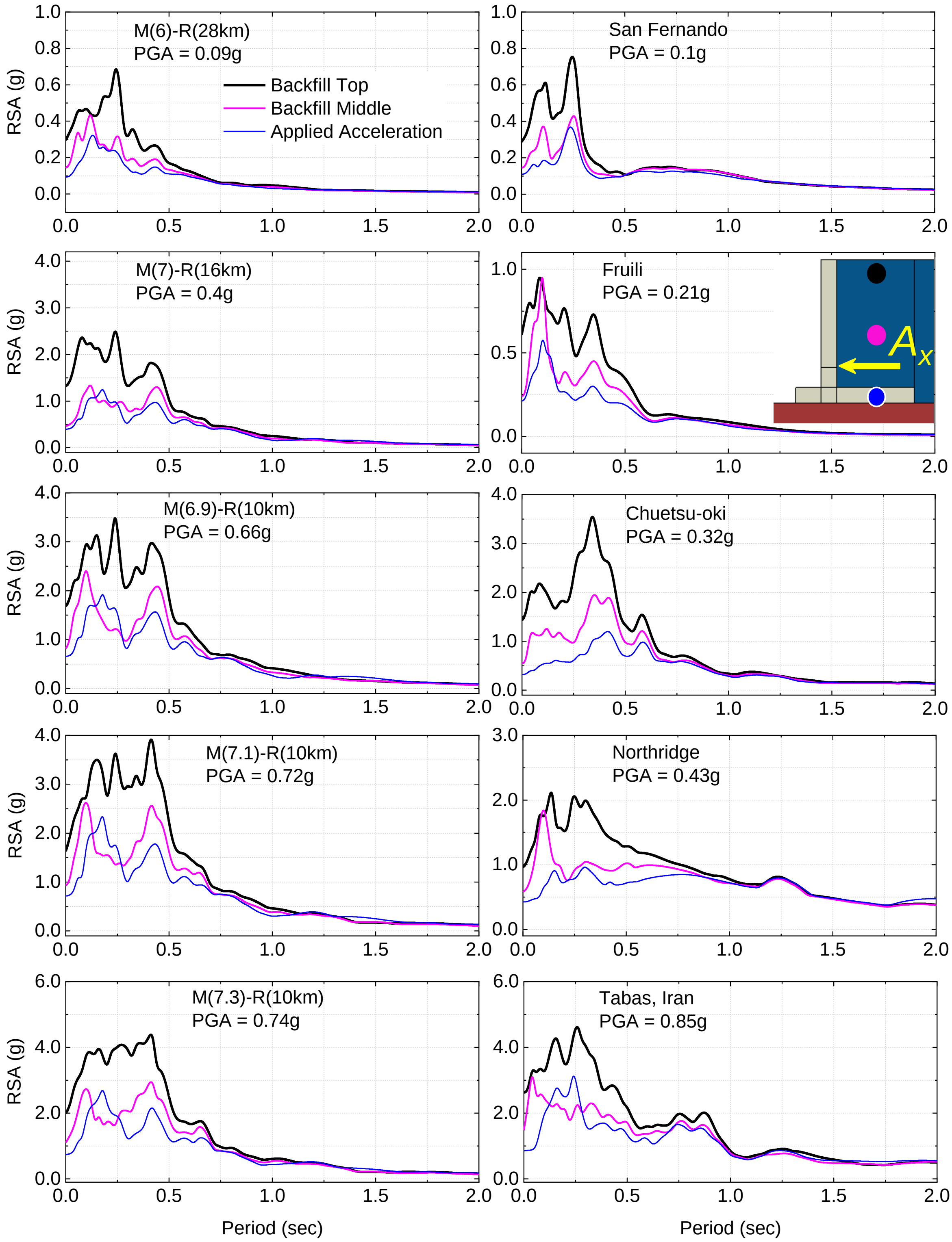

Figure 7-16 RSA for free-standing CRW, when subjected to different ground motions, backfill type crushed rock.

Figure 7-17 shows the AF_{Soil} for horizontal acceleration in the backfill made of crushed rocks at the base, middle and top, above the heel slab when subjected to different base excitations.

Because of the higher amplification, the average AF_{Soil} was 2.83 and 1.43 at the top, and middle respectively. These amplification factors are slightly higher than those observed in CRW, which made use of sand as backfill, which could be due to the higher residual backfill pressure in CRW with crushed rock backfill.

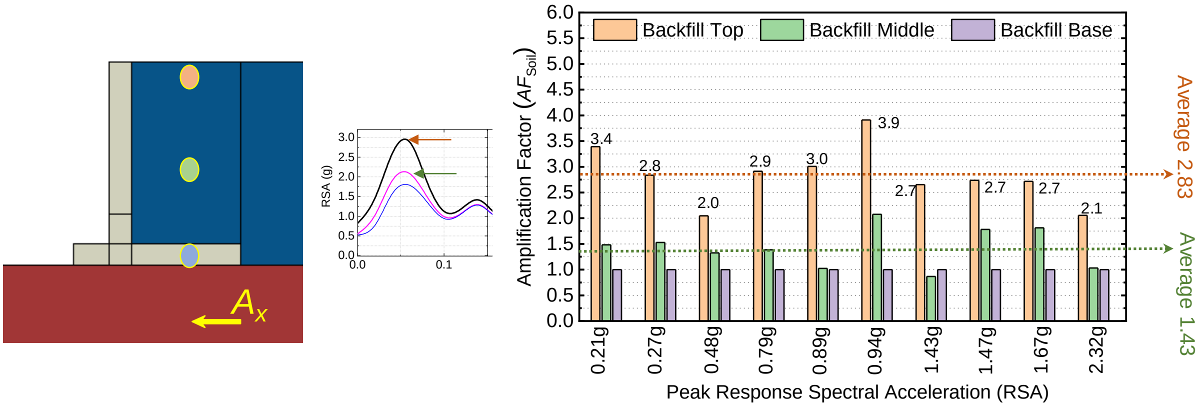

Figure 7-17 Amplification factor (horizontal acceleration) for free-standing CRW, when subjected to different ground motions, backfill type crushed rock.

7.9. Summary for seismic response of free-standing CRW with different backfill types

Figure 7-18 shows the residual displacement of a free-standing CRW for different types of backfill materials, against different base excitations. It was observed that CRW with Dune sand backfill type shows maximum displacement for all cases. It was also observed that softening of Dune sand occurs at lower axial strain, due to this mobilization of soils friction angle starts at the lower strain level, which results in a higher displacement of free-standing CRW. Justification of higher residual displacement for Chuetsu accelerogram case was discussed in section 7.6.1. The crushed rock backfill type showed lesser displacement amongst all three backfills, due to the softening of the crushed rocks at high strain levels. Hardening and softening of backfill could be understood by the levels of stresses in backfill which are primly responsible for mobilization of soil’s strength. In the case of crushed rock, the mobilization of soil’s strength occurs at higher stress levels compare to sands which results in lesser sliding of RW (Yang et al., 2012). Figure 7-19 shows the backfill plastic strain (PE) observed at the end of FE analyses when analyzed against the synthetic accelerogram with PGA = 0.66. Dune sand as backfill shown maximum PE at the end of FE analysis than Fontainebleau sand and crushed rock. On the other side crushed rock as backfill shown the lesser plastic strain at backfill top and middle. This proves the suitability of granular soils for backfill construction for free-standing earth retaining structures.

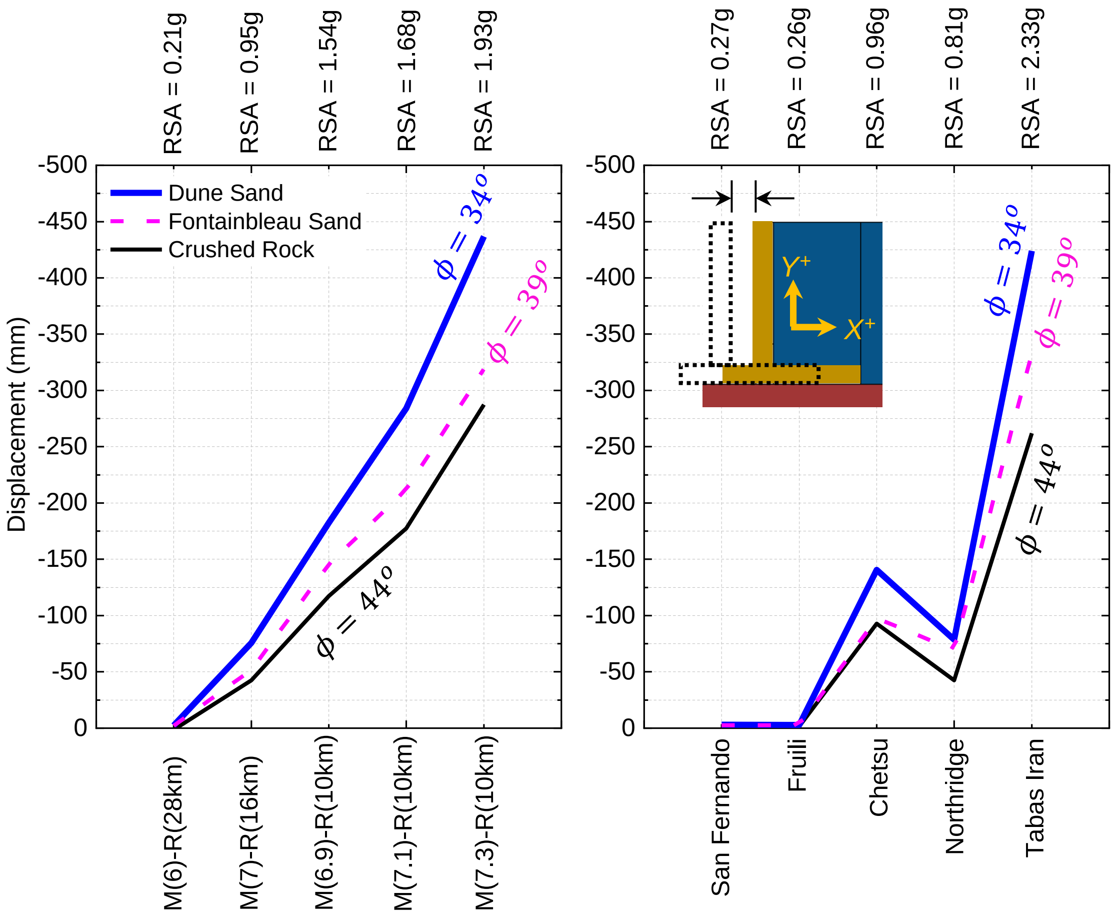

Figure 7-18 Summary of maximum residual displacement of free-standing CRW for different backfill type, against different base excitations.

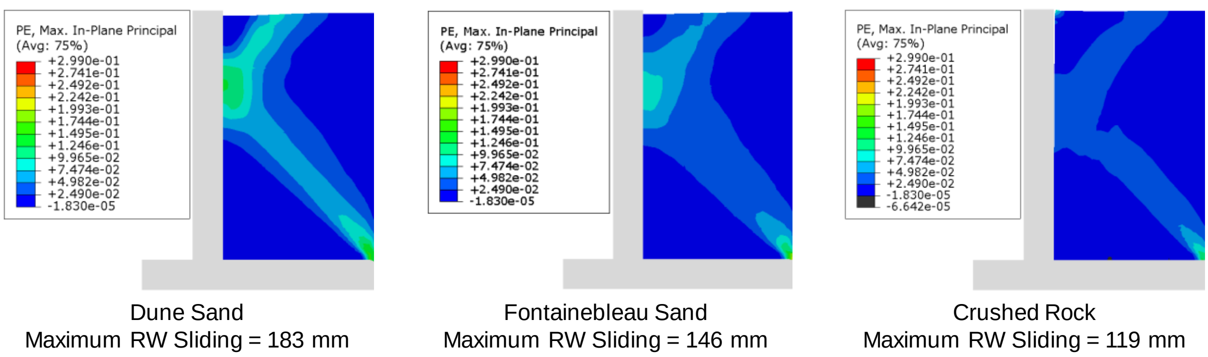

Figure 7-19 Comparison of plastic strain (PE) in backfill at the end of analysis when subjected to M(6.9)-R(10 km) earthquake, PGA = 0.66g.

7.10. Chapter closure

A detailed and rigorous FE investigation has been performed on FE models of free-standing CRW. The non-linear dynamic FE analyses have been performed on 2D plane strain FE models of free-standing CRW. The parametric investigations have also been performed for three different backfill types and ten base excitations. It was observed that the hardening and softening behaviour of the backfill can profoundly influence the earthquake induced displacement demand on the free-standing CRW. The CRW with granular backfill showed better seismic performance than CRW with natural sand backfills.

Chapter 8. SEISMIC BEHAVIOR OF RETAINING WALL FOUNDED ON ROCK-SOCKETED PILED FOUNDATION

8.1. Introduction

The present chapter deals with the seismic performance of a retaining wall (RW) which is founded on a Rock-Socketed (R-S) piled foundation. Finite element (FE) analyses have been carried out on two-dimensional (2D) models of this type of RW. Detailed and rigorous parametric investigations have been performed for different types of backfill. Non-linear time history analyses have been performed using software Abaqus. The backfill behind the RW has also been modelled using the Mohr Coulomb material model. The hardening and softening behaviour of backfill has been analysed. For minimizing boundary effects, springs and dashpots have been used to model the vertical boundaries of the FE model.

Results of the FE analyses have been analyzed for studying the earthquake induced rotation of the RW and its piled foundation. It was observed that the backfill can influence the seismic performance of the RW and the R-S piles. Higher rotation of the RW was observed for natural sand as backfill. Formation of the active failure wedge was observed in all the cases. Non-linear dynamic pressure was observed up the wall height. The conventional Mononobe-Okabe (MO) equation was found to have underestimated the backfill pressure at PGA $\leq$ 0.4g, and have also overestimated the backfill pressure at PGA > 0.4g. Higher displacement of the R-S piles in the vicinity of the pile cap was also observed for all the cases. The RW with the crushed rocks (granular) as backfill shows better seismic performance than RW with natural sand as backfills.

8.2. Two-dimensional (2D) plane strain finite element (FE) modelling of retaining wall (RW) founded on R-S piled foundation

FE model of RW founded on R-S piled foundation has been developed using FE software Abaqus. Geometrical details of 2D plane strain FE model of RW founded on R-S piled foundation is shown in figure 8-1. It was assumed that the RW construction site has a weak soil stratum of 24 m thickness, below which firm rock was located. Therefore, four R-S piles of 25 m length and 0.75 m diameter have been selected to support the RW. The socket length for R-S piles was kept at 1.125 m (1.5 times of pile diameter - IRC 78:2014). Pile cap and piles have been modelled using the elastic concrete material. The height and thickness of RW stem have been kept at 7.5 m and 0.8 m, respectively. The length and height of the backfill domain behind the RW were kept at 30 m and 9.05 m, respectively. A layer of firm rock with a total depth of 6.5 m was modelled below the weak base soil. Figure 8-1 shows the dimension of the FE model. The piled foundation was not a plane strain problem. However, plane strain behaviour could be simulated by altering the rigidity of the piles. Seismic response behaviour of the 3D and 2D RW models (founded on piled foundation) has been compared in chapter 3. It was observed that the 2D plane strain model of the R-S piled foundation (rigidity altered) could effectively replicate the 3D response behaviour of the R-S piled foundations. Figure 8-2 shows the FE mesh of the 2D RW, which was founded on R-S piled foundation. The FE mesh of the 2D model was generated using the four node bilinear plane strain quadrilateral elements with reduced integration and hourglass control (CPE4R). Free-style meshing technique was adopted to generate the mesh for all parts of the model. Contact was also modelled at different interfaces. Frictional contact was modelled at the interface of the stem with backfill, heel slab with backfill, and base with backfill. The coefficient of friction has been kept at $\tan(\frac{2}{3}\phi)$, where ϕ is the angle of internal friction of the backfill. Frictionless contact has been modelled between the vertical surfaces of the piles and base soil. The coefficient of friction between the piles and the rock socket was at 0.6 (Armstrong, R. C.; 1992, IRC 78:2014). To minimize mesh penetrations, hard contact was specified for all the interfaces. The master and slave surfaces were defined for all the contacts. Gravity loading was applied to the entire FE model in the non-linear time history FE analysis. The geostatic stresses have also been defined for the backfill, base soil and firm rock, for ensuring the equilibrium of forces. Non-linear time history FE analyses have been performed in dynamic explicit scheme of the FE software Abaqus (Abaqus/Explicit User’s Manual, version 6.13. 2013). Explicit solution scheme of Abaqus has been presented in chapter 5. Spring and dashpot type lateral boundaries were used for minimizing boundary effects, and for avoiding a large backfill domain. Domain size study for the backfill has been presented in chapter 6. Figure 8-2 also shows boundary conditions in non-linear time history analysis of the RW which was founded on R-S piles. Details of the boundary and loading conditions have also been presented in chapter 6. The sign convention used in the present study is presented in figure 8-2. The stresses and displacements are positive in the increasing "*x*" and "*y*" direction.

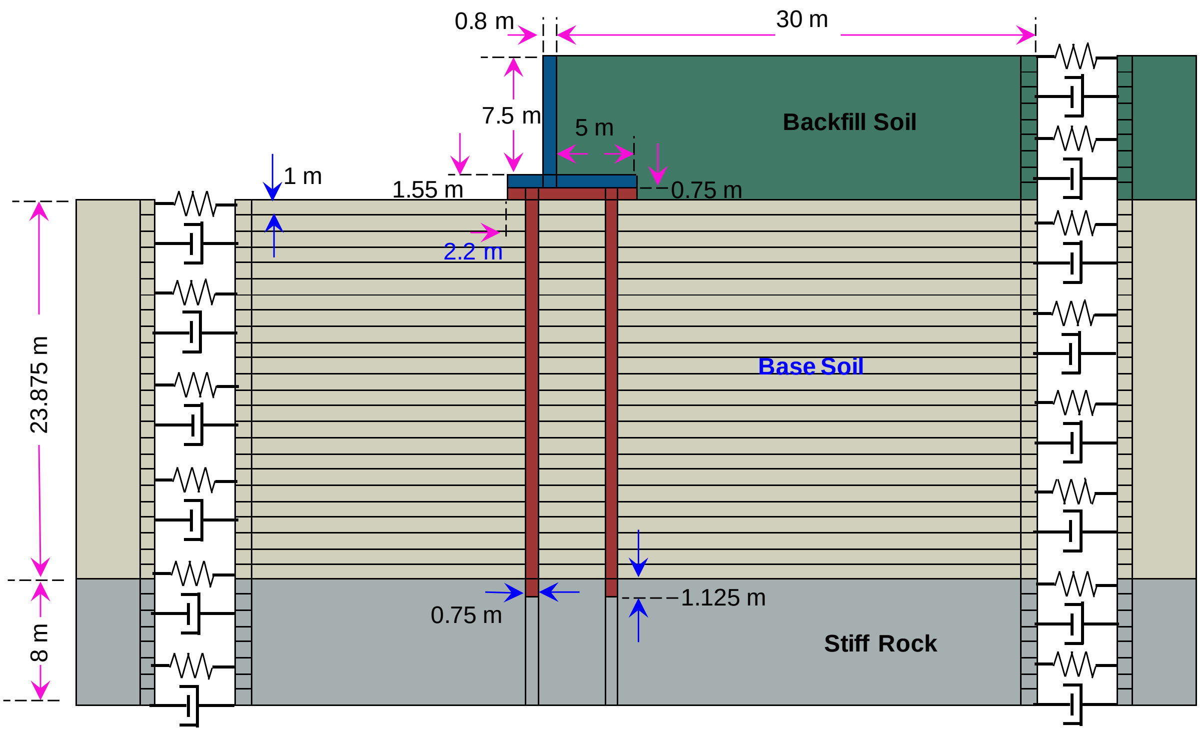

Figure 8-1 Geometrical details of RW founded on R-S piled foundation.

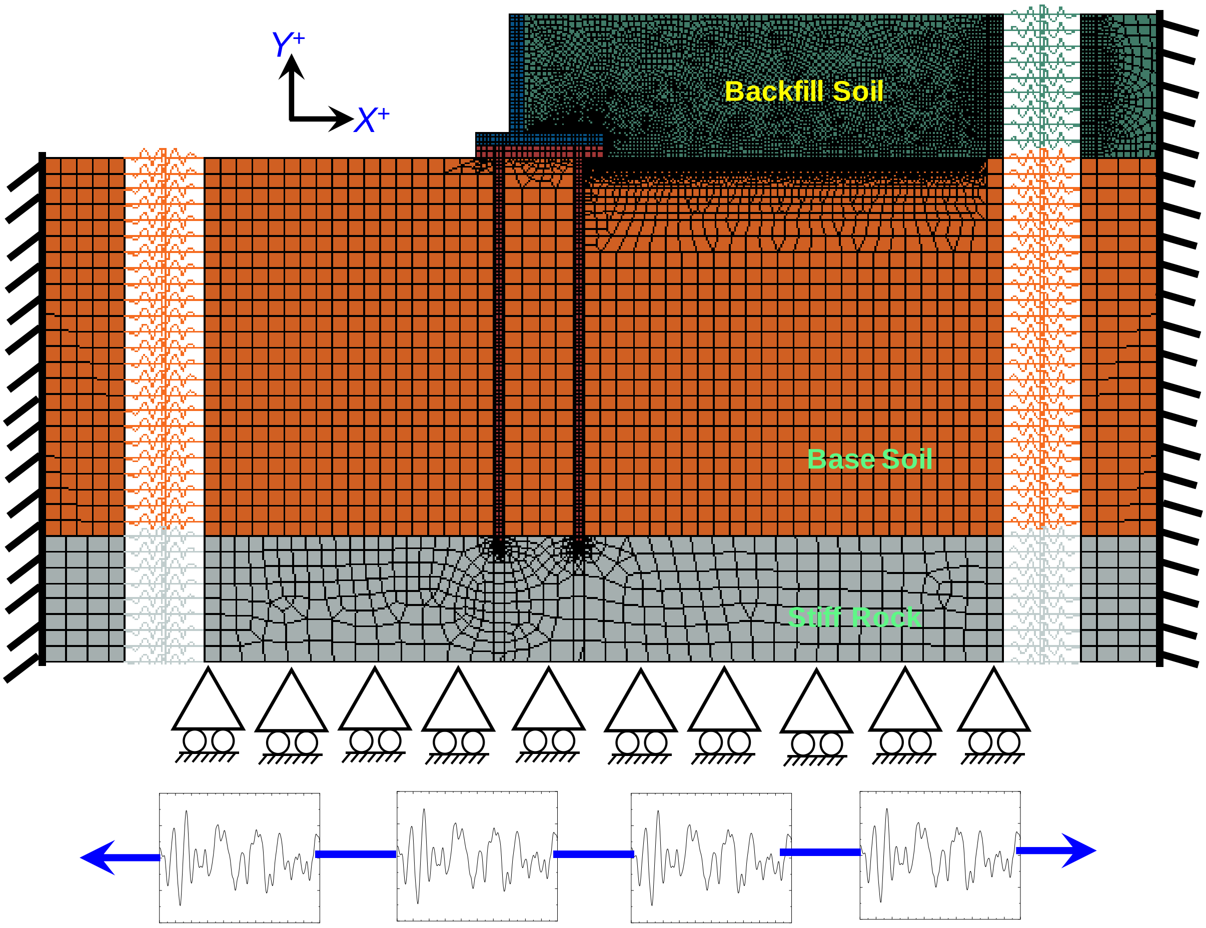

Figure 8-2 “2D” plane strain FE model of RW founded on R-S piled foundation.

8.3. Constitutive modelling of materials

8.3.1. Constitutive modelling of the backfill

Mohr Coulomb material model was used for modelling the backfill behind the RW. Details of constitutive modelling of the backfill have been presented in chapter 5 and 6. Parametric investigations have been performed for three different backfill types: (i) Dune sand (Daheur et al. 2019), (ii) Fontainebleau sand (Dano et al. 2004), and (iii) crushed rocks (which was characterized by the author at The University of Melbourne) respectively. As explained in chapter 5 and 6, the calibrated Mohr Coulomb model could simulate the hardening and softening behaviour of backfill. Thus, the Mohr Coulomb model has been calibrated against the triaxial test results for all backfills types considered in the parametric investigations. Calibration details of the Mohr Coulomb model have been presented in chapter 5 and 6. Rayleigh damping parameters were used for modelling damping in the backfill. Details for determining the Rayleigh damping parameters have been presented in chapter 5. The constrained modulus obtained from 1D compression test has been used for modelling the crushed rocks as backfill. It was observed that the triaxial test results generally overestimated the constrained modulus of the soils (Geoguide I, 1993; Angelim et al., 2016). Therefore, the partial constrained modulus has been used for modelling the two types of natural sand. Figure 8-4 shows details of material properties considered for modelling the backfill.

8.3.2. Constitutive modelling of the base soil

The Ariake clay (Tanaka et al. 2001) has been considered for modelling the base soil material. The modulus of the soil increases with increasing depth and confinement (Tanaka et al. 2001). Figure 8-3 shows the variation of Ariake clay's shear modulus with increasing depth. In the present study, the total depth of the base soil was taken to be 23.875 m. Therefore, the base soil was modelled in 24 layers with layer thickness of 1 m for the upper 23 layers. The depth-dependent Young's modulus of the base soil has also been modelled. Damping in the base soil was modelled using Rayleigh damping. The average value of the Young's modulus was used for finding the mass and stiffness dependent damping parameters of the base soil. Engineering properties of Ariake clay is shown in figure 8-4.

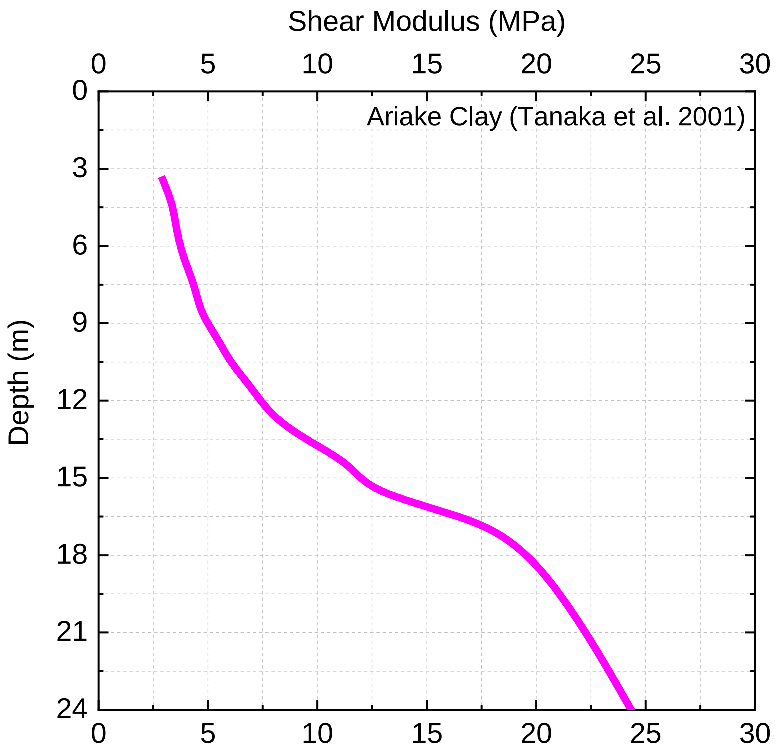

Figure 8-3 Variation of shear modulus for Ariake clay (Tanaka et al. 2001).

8.4. Parametric investigations for RW founded on R-S piled foundation

Seismic response behaviour of a RW founded on R-S piles was studied by performing a detailed parametric investigation. The 2D plane strain FE model of the RW which was founded on R-S piles was analyzed for different backfill types. The base of the FE model was excited using five synthetic accelerograms; generated at the rock outcrop. Acceleration time histories and details of the accelerogram selection have been presented in chapter 4. The outcomes of FE analyses have been studied for (i) displacement and rotational response of the RW and the R-S piles, (ii) amplification of the horizontal acceleration in the backfill, and (iii) dynamic pressure behind the RW. Figure 8-4 shows the plan for parametric investigations of the RW founded on R-S piles.

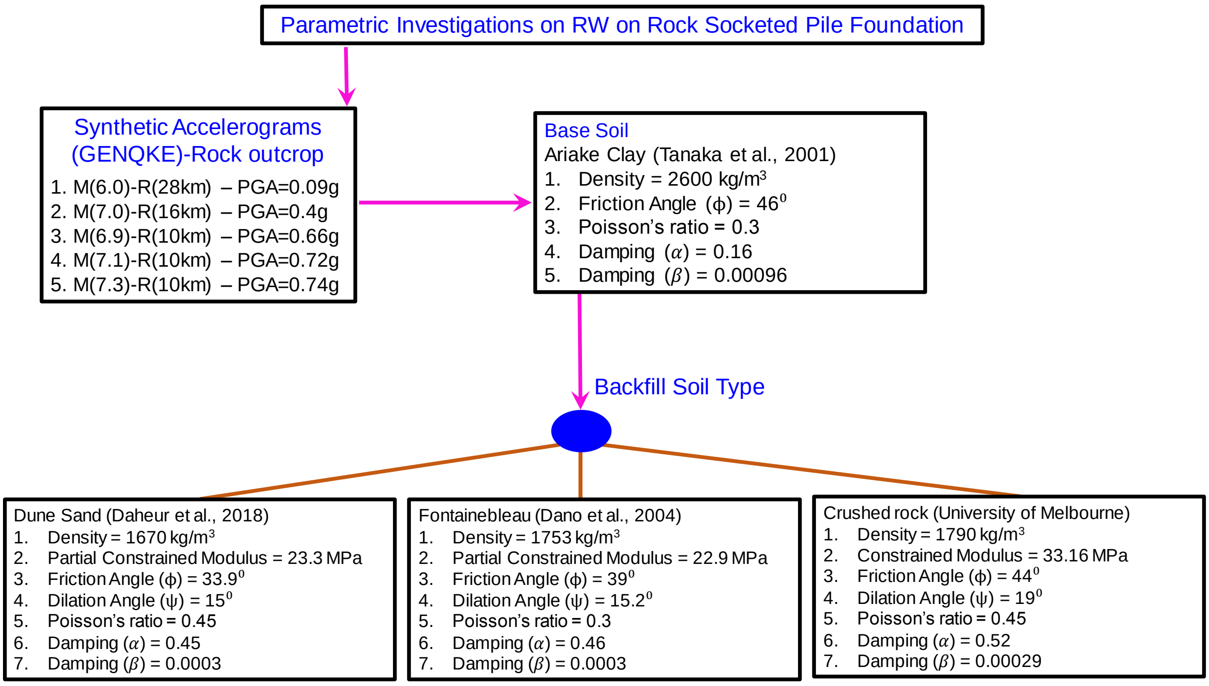

Figure 8-4 Details of parametric investigations on RW founded on R-S piled foundation.

8.5 Seismic performance of RW founded on R-S piled foundation with Dune sand backfill type

8.5.1. The rotational response of RW, Backfill type - Dune sand

The rotational response of the RW founded on R-S piles has been studied against different base excitations. Figure 8-5 shows the rotation of the stem wall against different base excitations. The formulation used to calculate the RW rotation is also shown in the inset diagram of figure 8-5. Increase in the rotation of the RW was observed with increasing intensity of motion. Formation of an active failure wedge was also observed for all cases. Table 8-1 shows displacement quantification for the RW founded on R-S piles. Table 8-1 shows the maximum relative displacement of piles (at pile cap, relative to base of the piles) and maximum relative displacement at the top of the RW (relative to the base). The static serviceability limit for lateral displacement of fixed head piles has been suggested at 1 % of the pile diameter (7.5 mm, IRC 78:2014). The maximum elastic limit of the lateral displacement of the pile has been suggested at 2 % to 4 % of the pile diameter, beyond which plastic deformation of piles may occur resulting in excessive settlement of the RW in a weak soil stratum (Shirato et al., 2009). It should be noted herein that plastic hinges could be formed in the R-S piles. However, locating plastic hinges in the piles and its repair could be a difficult task. Therefore, the serviceability of piles should be checked for the seismic performance (Callisto and Rampello, 2013).

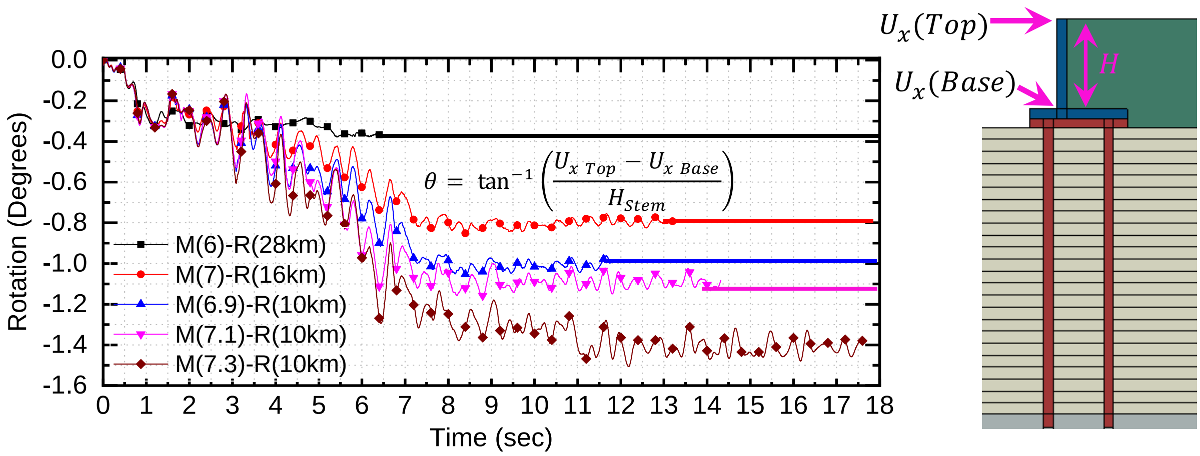

Figure 8-5 Rotation of RW founded on R-S piled foundation against different base excitations, backfill type Dune sand.

Table 8-1 Displacement quantification for RW (founded on R-S piled foundation) for different base excitations, backfill type Dune sand.

Sr. No.	M-R Combination	PGA (g)	Serviceable displacement at pile top (IRC 78:2014)	Maximum elastic displacement at pile top (Shirato et al., 2009)	Displacement of pile Present Study (mm) $Ux_{\text{Pile Top}}-Ux_{\text{Pile base}}$	Relative Displacement of RW (mm) $Ux_{\text{Stem Top}}-Ux_{\text{Stem base}}$
1	M(6)-R28(Km)	0.08	1% Pile Dia = 7.5 mm	≥ 4% Pile Dia = 30 mm	159	50
2	M(7)-R16(Km)	0.4			215	112
3	M(6.9)-R10(Km)	0.66			257	138
4	M(8.1)-R10(Km)	0.72			320	152
5	M(8.3)-R10(Km)	0.74			376	197

8.5.2. Backfill pressure on RW, Backfill type - Dune sand

Figure 8-6 shows dynamic pressure obtained up the wall height. A non-linear dynamic pressure was observed for all cases. For base excitation with PGA = 0.09g and 0.4 g, conventional MO equation was shown to underestimate the backfill pressure, especially near the heel slab. However, for PGA > 0.4g, the MO equation overestimates dynamic pressure up the wall height. Residual backfill pressure exceeding the Coulomb's active state pressure was also observed for all cases. This confirms the formation of an active failure wedge in the backfill behind the RW founded on R-S piles.

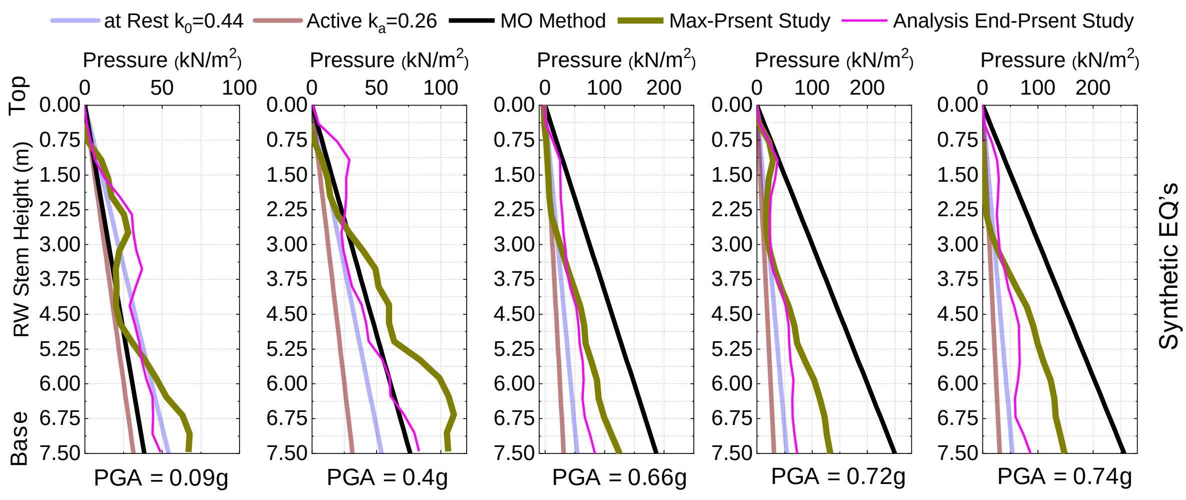

Figure 8-6 Backfill pressure up the RW height, calculated for different stress states (at rest, Coulomb active state), dynamic soil pressure from MO equation and present FE analysis, Dune sand as backfill type.

8.5.3. Amplification of horizontal acceleration for RW, Backfill type - Dune sand

Figure 8-7 shows the RSA of horizontal accelerations for the RW, which was founded on R-S piles when subjected to different base excitations. RSA was obtained from the horizontal acceleration which was captured at the base, middle, and top of the backfill. Amplification of the horizontal acceleration was observed for all cases, resulting in higher inertia forces and displacement of the RW. Figure 8-8b shows amplification factor (AF_{soil}) of the horizontal accelerations at the middle and top of the backfill, method used for finding the AF_{soil} is shown in figure 8-8a. The average amplification factor was estimated as 2.77 at backfill top. Decrement in AF_{soil} was observed with increasing RSA.

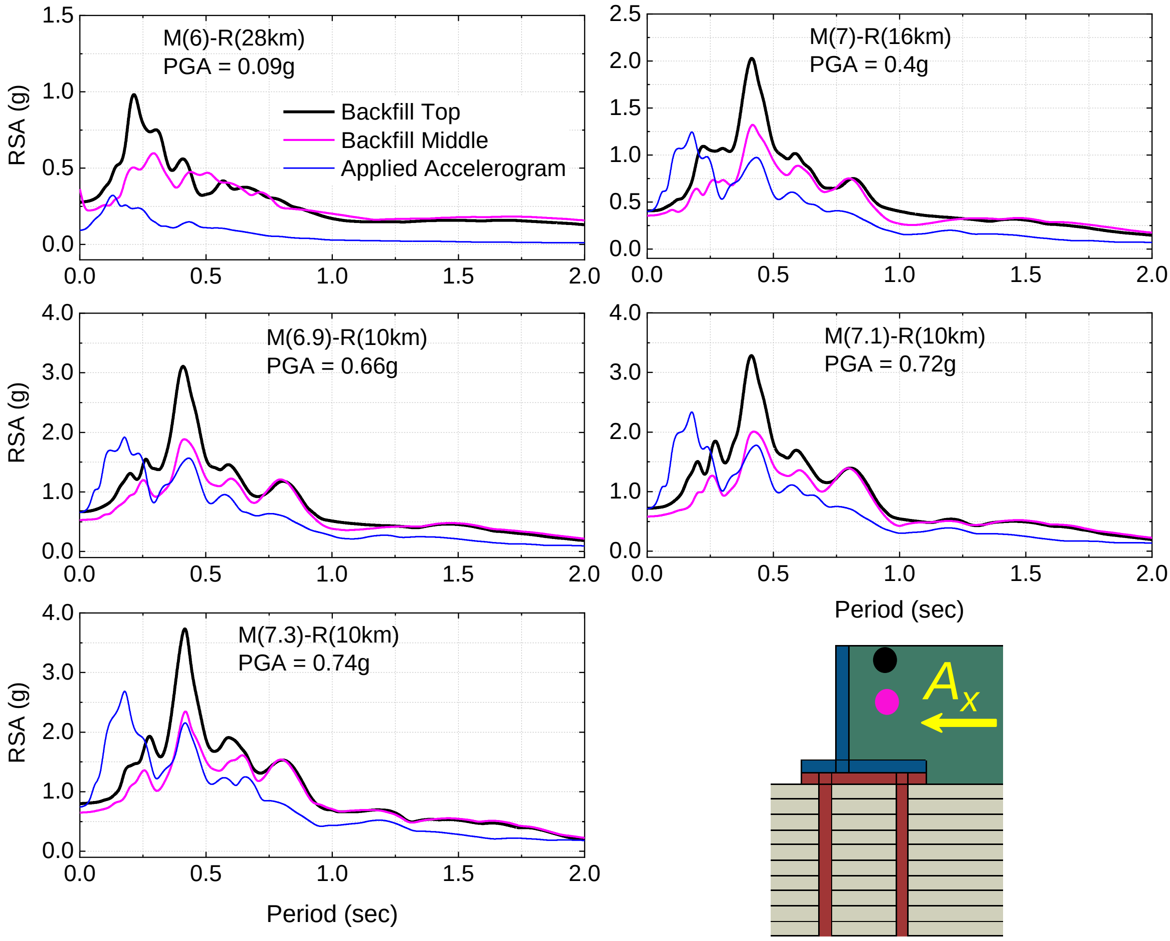

Figure 8-7 RSA for RW founded on R-S piled foundation against different base excitations, backfill type Dune sand.

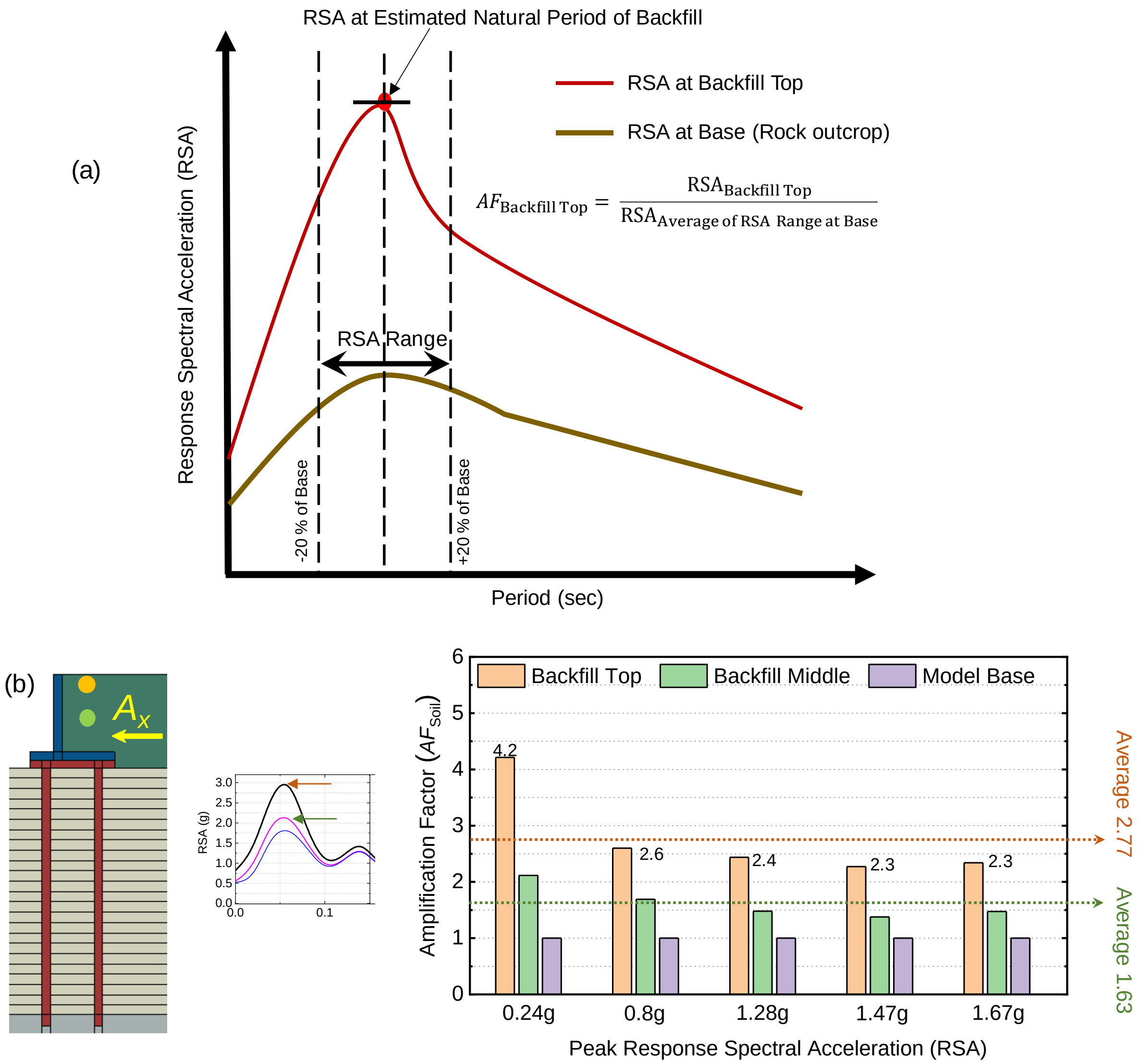

Figure 8-8 Amplification factor (horizontal acceleration) for RW founded on R-S piled foundation against different base excitations, backfill type Dune sand.

8.6 Seismic performance of RW founded on R-S piled foundation with Fontainebleau sand backfill type

8.6.1. The rotational response of RW, Backfill type - Fontainebleau sand

Figure 8-9 shows the rotational response of a RW with Fontainebleau sand as backfill when subjected to different base excitations. The RW shows lesser rotation than one which has Dune sand as backfill. Table 8-2 shows the quantification of the displacement demand for R-S piles and stem wall. For all cases, displacement of the R-S piles at their base was found to exceed the static serviceability and elastic limits (as mentioned in section 8.5.1).

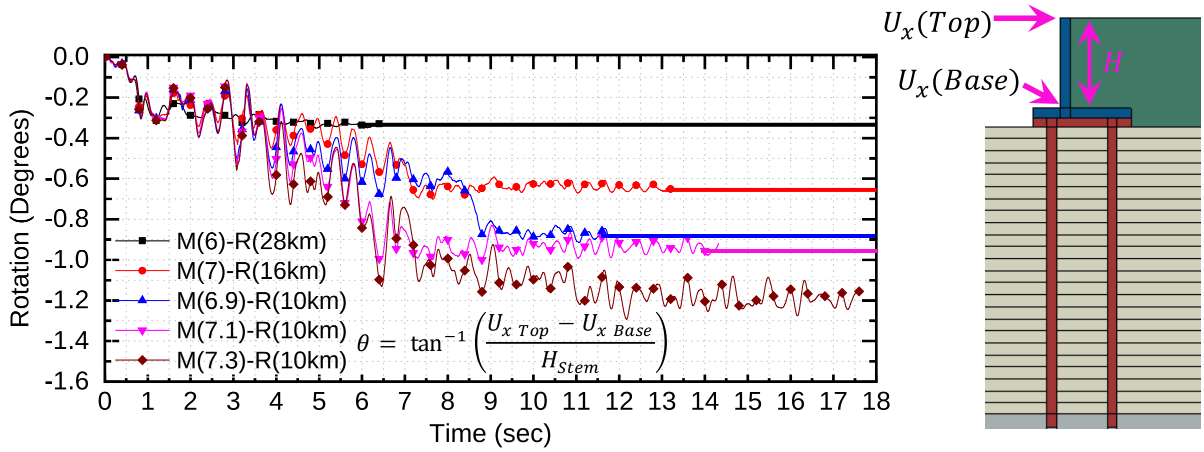

Figure 8-9 Rotation of RW founded on R-S piled foundation against different base excitations, backfill type Fontainebleau sand.

Table 8-2 Displacement quantification of RW founded on R-S piled foundation for different base excitations, backfill type Fontainebleau sand.

Sr. No.	M-R Combination	PGA (g)	Serviceable displacement at pile top (IRC 78:2014)	Maximum elastic displacement at pile top (Shirato et al., 2009)	Displacement of pile Present Study (mm) $Ux_{\text{Pile Top}}$-$Ux_{\text{Pile base}}$	Relative Displacement of RW (mm) $Ux_{\text{Stem Top}}$-$Ux_{\text{Stem base}}$
1	M(6)-R28(Km)	0.08	1% Pile Dia = 7.5 mm	≥ 4% Pile Dia = 30 mm	155	46
2	M(7)-R16(Km)	0.4			198	92
3	M(6.9)-R10(Km)	0.66			249	120
4	M(8.1)-R10(Km)	0.72			311	131
5	M(8.3)-R10(Km)	0.74			375	169

8.6.2. Backfill pressure on RW, Backfill type - Fontainebleau sand

Figure 8-10 shows backfill pressure behind the RW which has Fontainebleau sand as backfill. Non-linear dynamic pressure was observed behind the RW at PGA = 0.09g and 0.4g. At PGA ≥ 0.4g FE analyses show the linear distribution of backfill pressure up the wall height. The MO equation underestimates dynamic soil pressure at PGA ≤ 0.4g; however, the same equation overestimates dynamic soil pressure at PGA of 0.4g and above. The backfill pressure was found to be lower in comparison with a RW which used Dune sand as backfill.

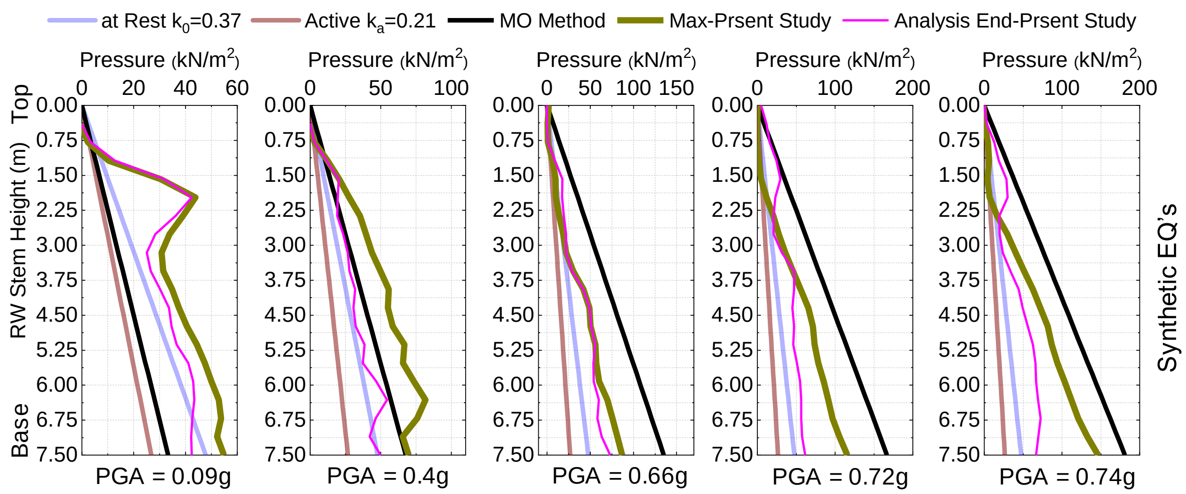

Figure 8-10 Backfill pressure up the RW height, calculated for different stress states (at rest, Coulomb active state), dynamic soil pressure from MO equation and present FE analysis, Fontainebleau sand as backfill type.

8.6.3. Amplification of horizontal acceleration for RW, Backfill type – Fontainebleau sand

Figure 8-11 shows the RSA of horizontal acceleration in the backfill. Amplification of horizontal acceleration was observed for all cases. Higher amplification was observed with increasing PGA. RSA in the backfill was slightly higher in comparison with a RW which used Dune sand as backfill. Figure 8-12 shows bar chart for AF_{Soil} at the top and middle (relative to base) for different base excitations. The average AF_{Soil} at the top and middle was 2.9 and 1.6, respectively. Decrement in AF_{Soil} was observed with increasing RSA.

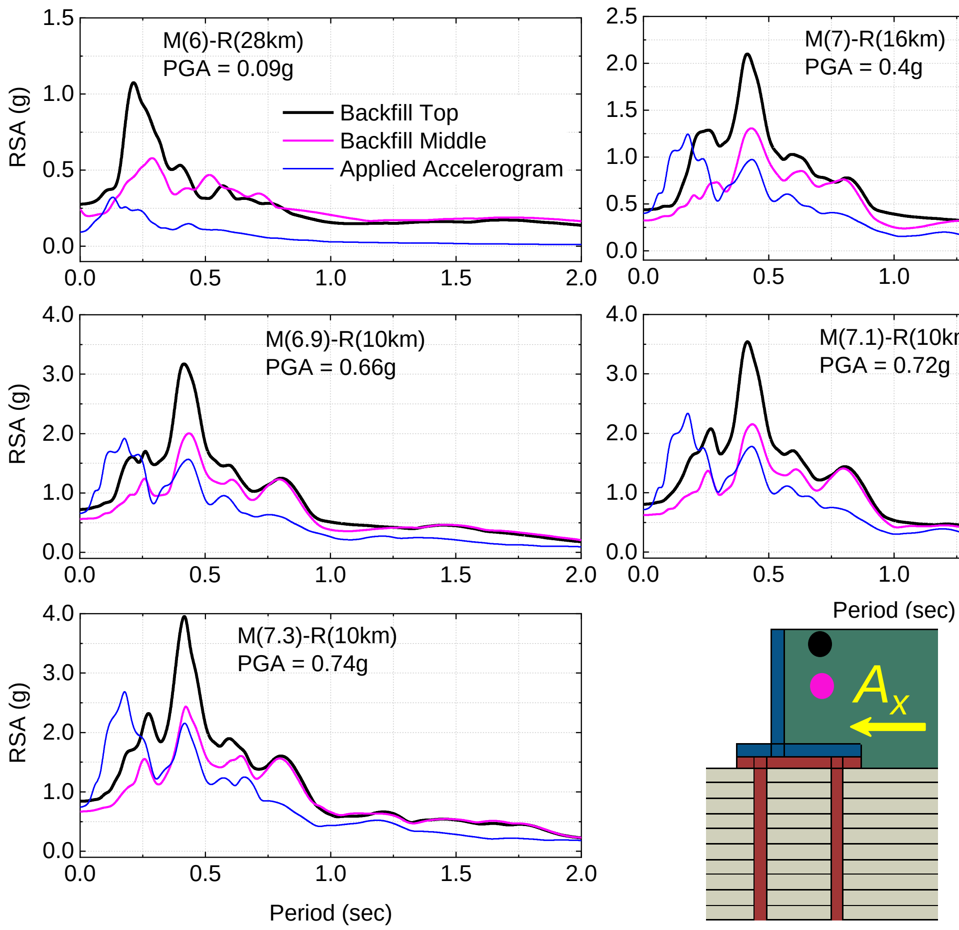

Figure 8-11 RSA for RW founded on R-S piled foundation against different base excitations, backfill type Fontainebleau sand.

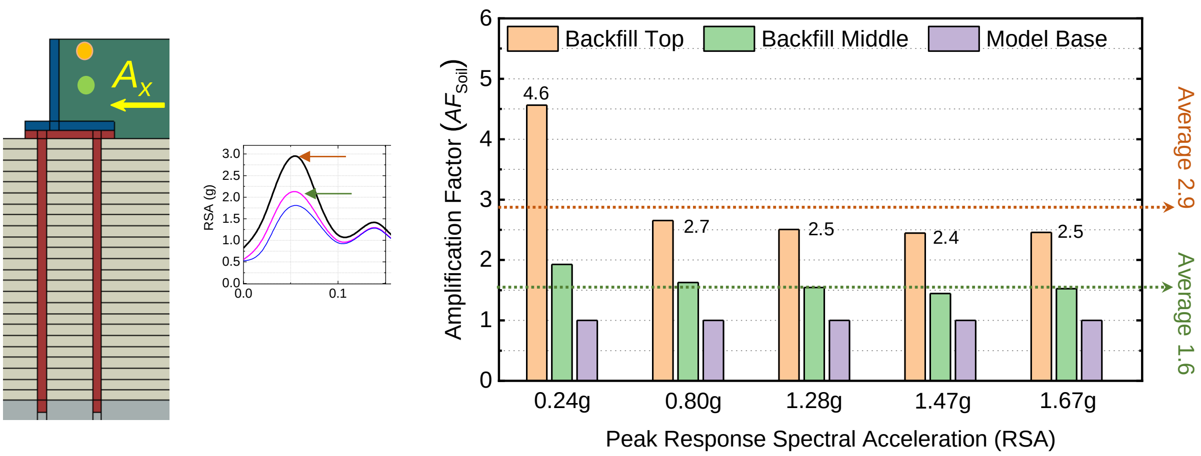

Figure 8-12 Amplification factor (horizontal acceleration) for RW founded on R-S piled foundation against different base excitations, backfill type Fontainebleau sand.

8.7 Seismic performance of RW founded on R-S piled foundation with crushed rock backfill type

8.7.1. The rotational response of RW, Backfill type - crushed rock

Figure 8-13 shows the rotation of the RW against different base excitations for a RW where crushed rocks were used as backfill. Significant reduction in the rotation was observed when compared with the rotation of a RW where sand backfills were used instead. Maximum rotation of the RW was observed at 1.26^o for M(7.3)-R10km base excitation (PGA = 0.74g), which was lower than the maximum rotation observed on a RW where sand backfill was used. Table 8-3 shows maximum relative displacement at (i) top of the RW, and (ii) top of the pile for different base excitations. Higher displacements of the R-S piles at the pile cap level was observed for all cases. The elastic serviceability limits were shown to be exceeded.

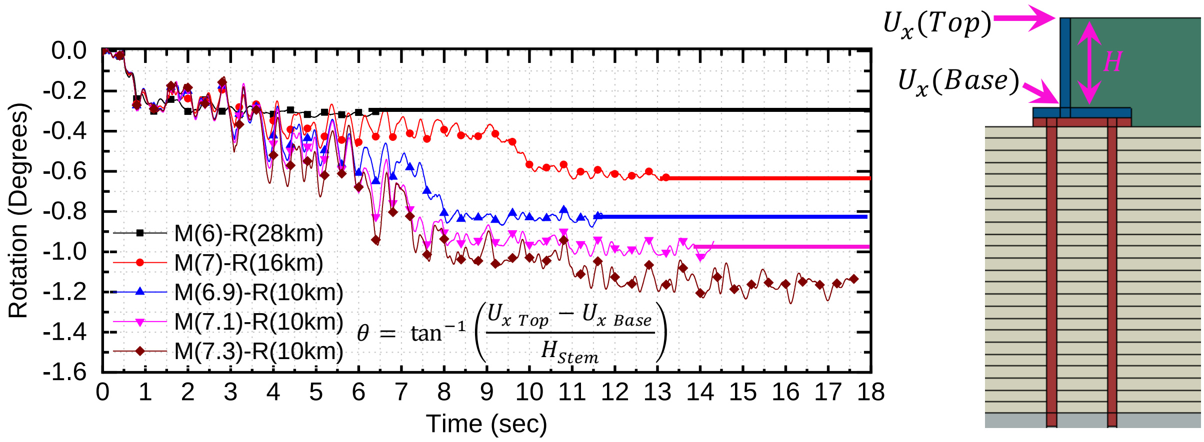

Figure 8-13 Rotation of RW founded on R-S piled foundation against different base excitations, backfill type crushed rock.

Table 8-3 Displacement quantification of RW founded on R-S piled foundation for different base excitations, backfill type crushed rock.

Sr. No.	M-R Combination	PGA (g)	Serviceable displacement at pile top (IRC 78:2014)	Maximum elastic displacement at pile top (Shirato et al., 2009)	Displacement of pile Present Study (mm) $Ux_{\text{Pile Top}}$-$Ux_{\text{Pile base}}$	Relative Displacement of RW (mm) $Ux_{\text{Stem Top}}$-$Ux_{\text{Stem base}}$
1	M(6)-R28(Km)	0.08	1% Pile Dia = 7.5 mm	≥ 4% Pile Dia = 30 mm	153	43
2	M(7)-R16(Km)	0.4			201	85
3	M(6.9)-R10(Km)	0.66			240	115
4	M(8.1)-R10(Km)	0.72			296	135
5	M(8.3)-R10(Km)	0.74			361	165

8.7.2. Backfill pressure on RW, Backfill type – crushed rock

Figure 8-14 shows the dynamic backfill pressure up the wall height as observed from the FE analyses. Static soil pressures and dynamic pressure from the MO equation have also been shown. Non-linear dynamic pressure profile behind the RW was observed for crushed rocks used as backfill. It was also observed that crushed rocks used as backfill shows higher backfill pressure in comparison with RW which used sand as backfill for PGA ≤ 0.66g. Residual soil pressure exceeding the Coulomb's active state pressure was observed for all cases.

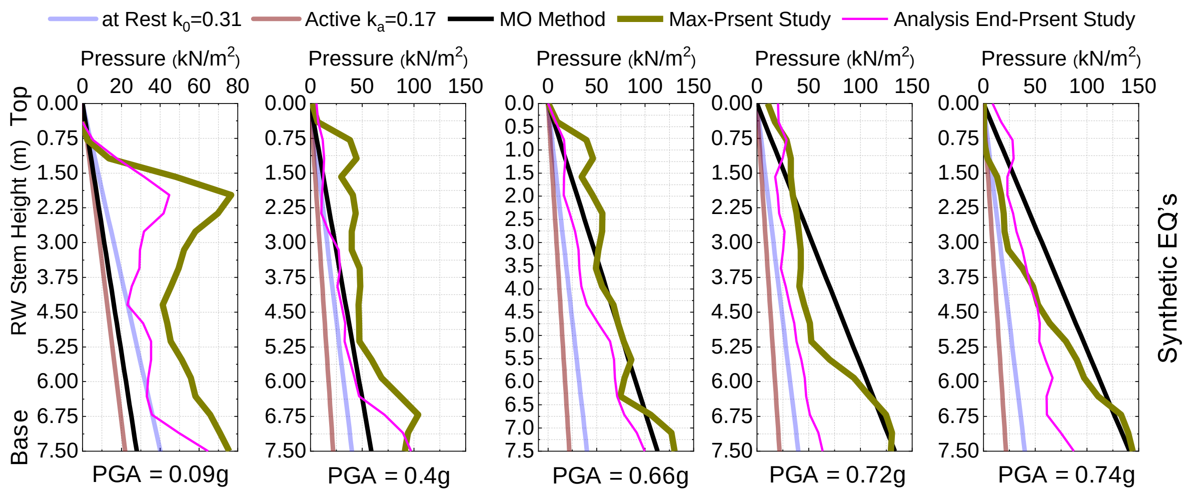

Figure 8-14 Backfill pressure up the RW height, calculated for different stress states (at rest, Coulomb's active state), dynamic soil pressure from MO equation and present FE analysis, crushed rock as backfill type.

8.7.3. Amplification of horizontal acceleration for RW, Backfill type – crushed rock

Figure 8-15 shows RSA of the horizontal acceleration at the base, middle and top of the RW above the heel slab when analyzed against different base excitations. Amplification of the horizontal acceleration was slightly lower than cases where Fontainebleau sand was used as backfill. The RSA in the backfill features diminished amplitudes beyond 0.75 sec period. Figure 8-16 shows the bar chart of the AF_{Soil} in the backfill at the base, middle and top of the RW above the heel slab. Average AF_{Soil} of 2.6 and 1.5 was observed at the top and middle respectively.

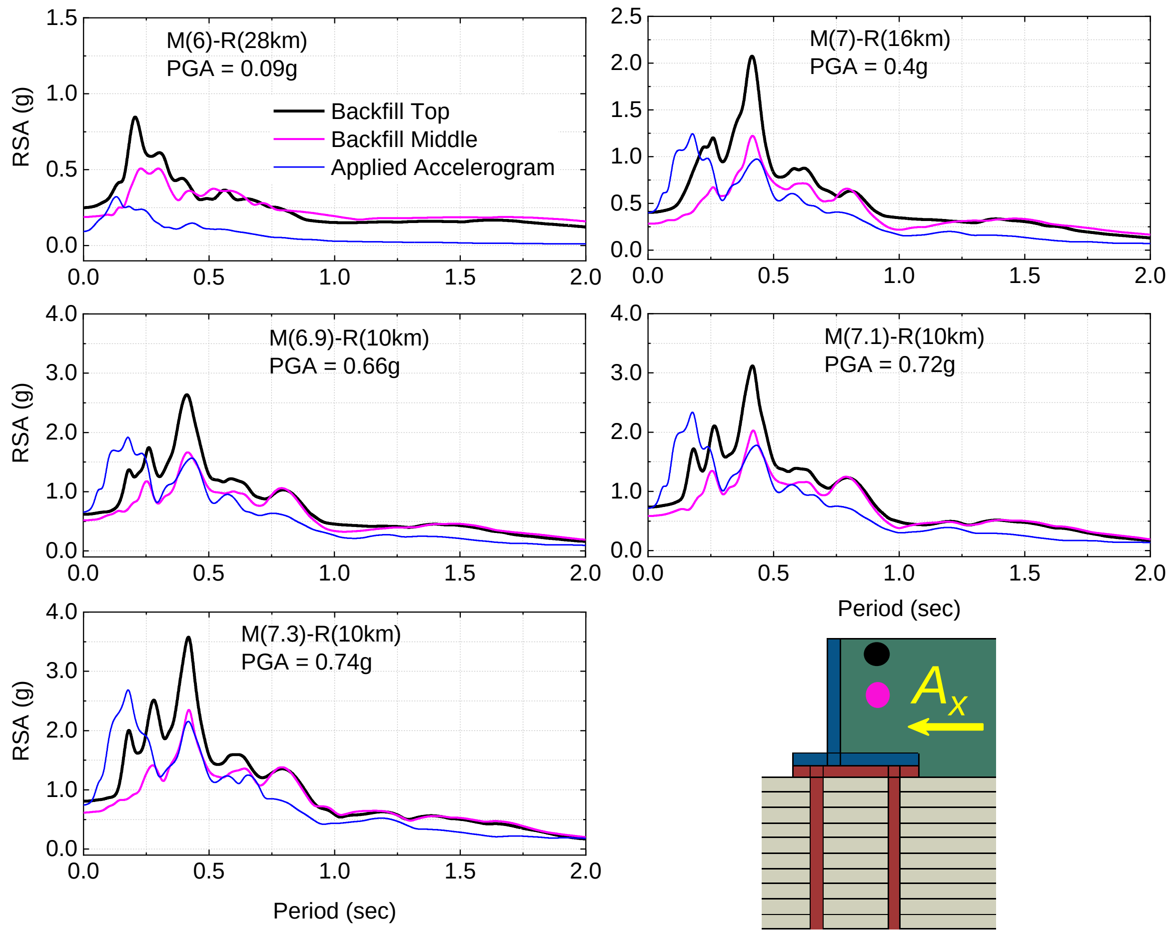

Figure 8-15 RSA for RW founded on R-S piled foundation against different base excitations, backfill type crushed rock.

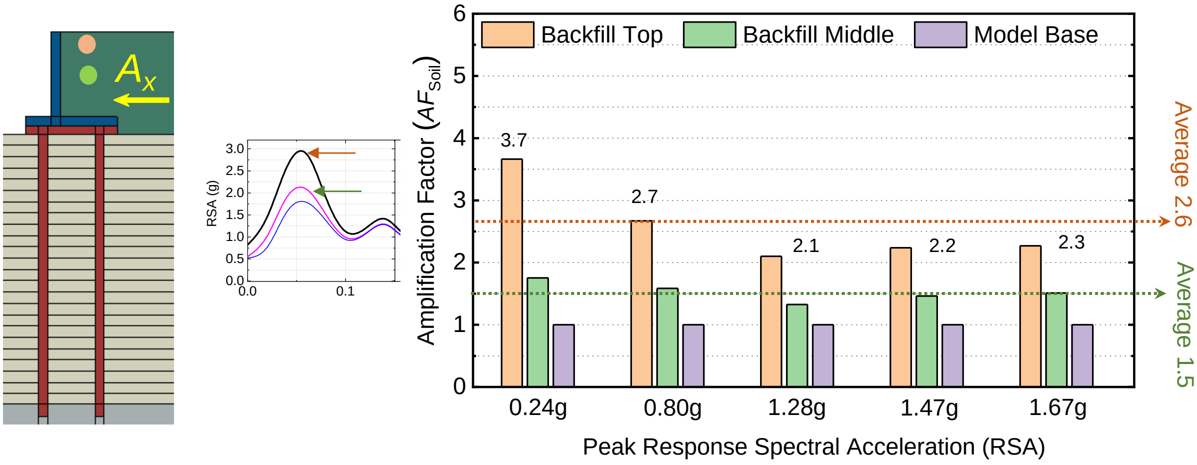

Figure 8-16 Amplification factor (horizontal acceleration) for RW founded on R-S piled foundation against different base excitations, backfill type crushed rock.

8.8. Summary for seismic response of RW founded on R-S piled foundation with different backfill types

Figure 8-17 shows the maximum AF_{soil} of the horizontal acceleration as observed at the top of the backfill for all three backfill types, against different base excitations. It was observed from figure 8-17 that the crushed rock backfill shows slightly lower AF_{soil} than other cases. Decrement in AF_{soil} with increasing RSA was observed for all backfill types. Figure 8-18 shows maximum relative displacement at the top of the RW (figure 8-18a) and at the pile heads (figure 8-18b) when analyzed against different base excitations. Higher displacement of the RW was observed with RW which used Dune sand as backfill. This observation shows the influence on the choice of the backfill on the seismic performance of the earth retaining structures; founded on R-S piled foundation. Displacement at the pile heads has also been shown in figure 8-18b. It is shown that the piles supporting the RW with Dune sand as backfill shows higher displacements than RW which employed the other backfill materials. A RW with crushed rocks as backfill shows lesser displacement in comparison with cases where sand was used as backfill. For all cases, the pile head displacements exceeded the stipulated elastic limits. Therefore, potential inelastic behaviour of the R-S piles has to be allowed for in the seismic design of the earth retaining structures.

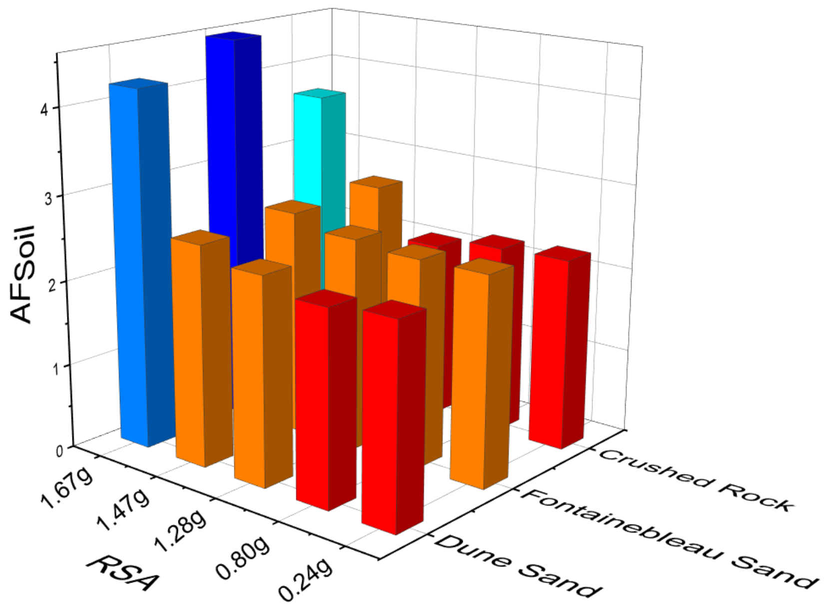

Figure 8-17 Summary of AF (horizontal acceleration) in backfill top for different backfill types, when subjected to different base excitations.

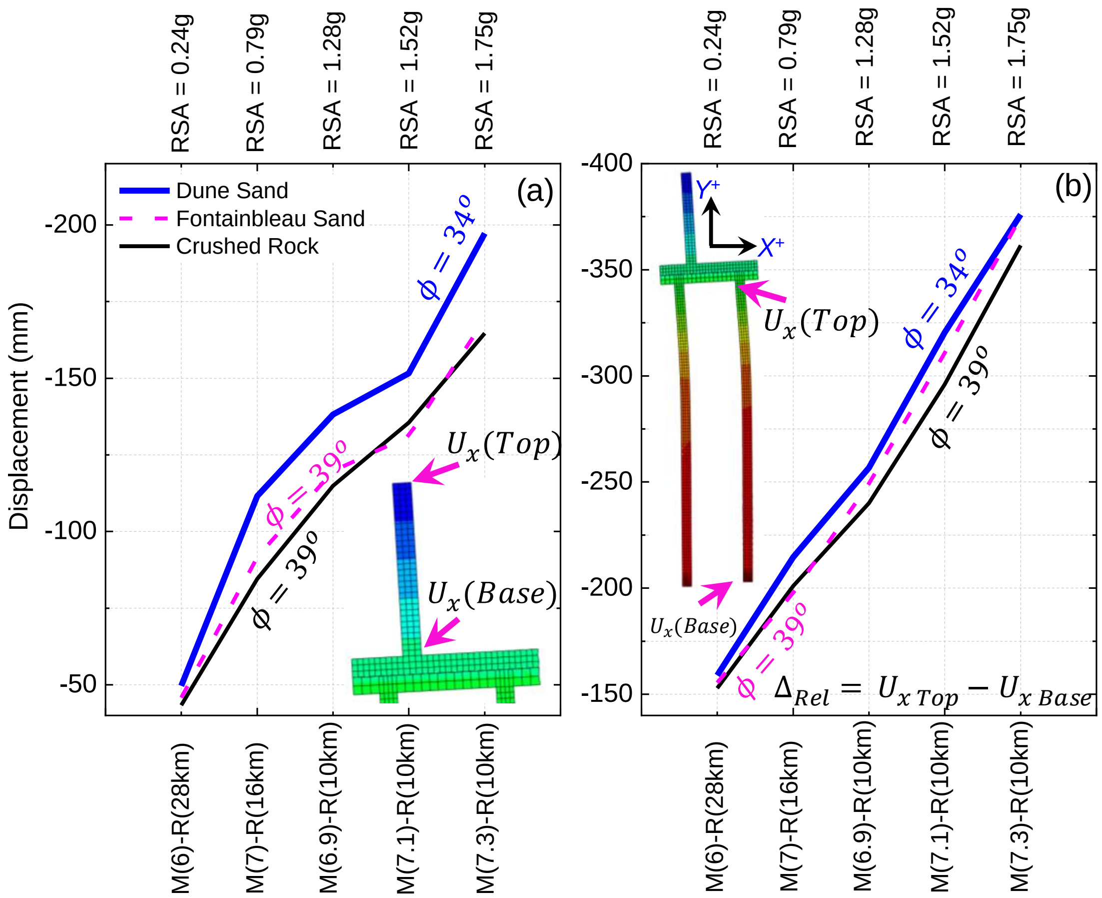

Figure 8-18 Summary of maximum displacement of RW founded on R-S piled foundation, for different backfill type, against different base excitations.

8.9. Chapter closure

Seismic performance of RW founded on R-S piled foundation has been studied. The earthquake response of RW has been analyzed against five different synthetic accelerograms. A detailed and rigorous parametric investigation has been performed for three different backfill types. It was observed that backfill softening behaviour can profoundly influence the earthquake induced displacement demand of the RW and the R-S piles. Granular (crushed rocks) backfill shows better seismic performance than natural sands. Non-linear backfill pressure profiles behind the RW was observed for all the backfill types. The influence of the backfill thrust on the seismic displacement of the R-S piles was also observed. Amplification of the horizontal acceleration in the backfill was observed for all cases. The high relative displacement of R-S piles at the pile heads was observed even at low PGA for all backfill types. The importance of allowing for post-elastic behaviour of the R-S piles supporting the earth retaining structures is highlighted.

Chapter 9. CONCLUSIONS

9.1. Summary of Ph. D. Research

Earthquake induced displacement and rotational behaviour is critical to the seismic performance of earth retaining structures. Past earthquakes highlight the importance of considering earthquake induced displacement as a major design parameter for this type of structures. This thesis deals with the assessment of earthquake induced displacement behaviour. The research was conducted in three phases. The first phase was about conducting a detailed shaking table experiment on two types of earth retaining structures. Results of shaking table experiments have been analysed for studying the dynamic response behaviour of scaled down retaining wall models. The amplification of horizontal acceleration in the backfill and the shear wave velocity of the backfill materials have also been studied. The second phase was about conducting a detailed geotechnical investigation for characterization the backfill materials, and the development of a finite element (FE) model for replicating the potential seismic response behaviour of the structure. The third phase was about FE simulations of the seismic actions. Parametric investigations have been performed on the FE models to study the effects of earthquake actions on different forms of retaining walls.

The major research outcomes are summarized in below:

Phase 1- The shaking table experiment on scaled down models of earth retaining structures.

(i) The inertia of the backfill played an important role in the seismic displacement and rotational behaviour of the retaining wall.
(ii) The maximum (input) acceleration and displacement at the base of the RW did not occur at the same time.
(iii) The earthquake response behaviour of the earth retaining structure profoundly depends on the severity of ground shaking. Wall-soil separation was observed for the base-restrained and rotational base retaining wall when subjected to severe ground shaking.
(iv) The shaking table experiments were used for estimating the dynamic properties of the scaled down retaining wall model, namely the natural period and shear wave velocity of the backfill.
(v) Amplification of horizontal acceleration in the backfill was not sensitive to the intensity of ground shaking.

Phase 2- Characterization of the backfill soil.

(i) Laboratory-based geotechnical investigations such as static tri-axial tests could adequately characterize the seismic response behaviour of the backfill materials.
(ii) The calibrated Mohr Coulomb material model can effectively replicate the hardening/softening behaviour of the backfill.
(iii) The developed FE models of earth retaining structure and the backfill can be used to predict their seismic responses with good accuracy.

Phase 3- Finite element investigations on the earth retaining structures.

(a) Base restrained retaining wall

(i) The type of backfill does not have a strong influence on the seismic displacement demand on a base restrained retaining wall.

(ii) Amplification of the horizontal acceleration was not sensitive to the intensity of ground shaking.

(iii) The proposed simplified hand calculations procedure is able to predict the earthquake induced displacement of a base restrained retaining wall with good accuracy.

(b) Free-standing retaining wall

(i) The hardening/softening behaviour of the backfill can profoundly influence the seismic displacement demand of a free-standing retaining wall.

(ii) Granular backfill (crushed rocks) shows better seismic performance than backfills constructed from natural sands.

(iii) Amplification of the horizontal acceleration was not sensitive to the intensity of ground shaking.

(c) Cantilever retaining wall founded on rock-socketed pile foundation

(i) The type of backfill can profoundly influence the seismic displacement demand of the cantilevered retaining wall and the rock-socketed piles. Granular backfill (crushed rocks) shows better seismic performance than backfills constructed using natural sands.

(ii) Displacement of the rock-socketed piles at pile cap should be checked against the stipulated elastic limits in a rare earthquake event.

(iii) The amplification of the horizontal acceleration was not sensitive to the intensity of ground shaking.

9.2. Limitations and scope for future research

(i) The shaking table experiments have only been performed on scaled down models of earth retaining structures. In conditions of intense base excitations reflections of stress waves from model boundaries were observed. The boundary effects could be minimized by constructing a laminar container or shear beam container.

(ii) The role of cohesionless backfill soil on seismic performance of earth retaining structures has been investigated. Therefore, a detailed experimental and numerical investigation could be performed for studying the seismic displacement behaviour of earth retaining structures with a $c - \phi$ backfill.

(iii) Seismic response behaviour of retaining walls with rock-socketed piled foundation has also been investigated. The displacements observed for the rock-socketed piles exceeded the stipulated elastic limits. Thus, a more detailed investigation should be performed for studying the seismic behaviour of earth retaining structures founded on rock-socketed piles taken into account post elastic behaviour of the piles.

(iv) Bridge abutments play a significant role in modern transportation system. Therefore, experimental and numerical investigations should be conducted for studying the earthquake induced displacement behaviour of bridge abutments and the connected superstructure of the bridge. Simple hand calculation procedures should be developed and validated for modelling the earthquake induced slip of the girders resting on the bridge abutments, and the risk of unseating from the bridge supports.

REFERENCES

Abaqus/Explicit User's Manual, version 6.13. (2013) Dassault Systèmes Simulia Corporation, Providence, Rhode Island, USA.

Aggour, M. S., & Brown, C. B. (1973). Retaining walls in seismic areas. Proceedings, 5th World Conference on Earthquake Engineering, Rome, Italy, 2624-2627.

Amirsardari, A., Goldsworthy, H. M., & Lumantarna, E. (2017). Seismic site response analysis leading to revised design response spectra for Australia. Journal of Earthquake Engineering, 21(6), 861-890.

Anderson, D. G. (2008). Seismic analysis and design of retaining walls, buried structures, slopes, & embankments (Vol. 611). Transportation Research Board.

Angelim, R. R., Da Cunha, R. P., & Sales, M. M. (2016). Determining the elastic deformation modulus from a compacted earth embankment via laboratory and ménard pressuremeter tests. Soils & Rocks, 39(3), 285-300.

Armstrong, R. C. (1992). Engineering and design: Revision of thrust block criteria in TM 5-813-5/AFM 88-10, Vol 5 Appendix C (No. ETL-1110-3-446). Corps of engineers Washington DC.

Arulrajah, A., Ali, M. M. Y., Piratheepan, J., & Bo, M. W. (2012). Geotechnical properties of waste excavation rock in pavement subbase applications. Journal of materials in civil engineering, 24(7), 924-932.

AS 1289.3.6.1 (2009). Australian Standard-Methods of testing soils for engineering purposes - Method 3.6.1: Soil classification tests - Determination of the particle size distribution of a soil - Standard method of analysis by sieving.

AS 4678 (2002). Australian Standard. Earth-Retaining Structures.

ASTM, C. (2006). Standard test method for sieve analysis of fine and coarse aggregates. ASTM C136-06.

Bakr, J. A. (2018). Displacement-based approach for seismic stability of retaining structures. Doctoral dissertation, The University of Manchester (United Kingdom).

Bakr, J., & Ahmad, S. M. (2018). A finite element performance-based approach to correlate movement of a rigid retaining wall with seismic earth pressure. Soil Dynamics and Earthquake Engineering, 114, 460-479.

Bhattacharjee, A., & Krishna, A. M. (2015). Strain behavior of backfill soil in rigid faced reinforced soil walls subjected to seismic excitation. International Journal of Geosynthetics and Ground Engineering, 1(2), 14.

Bolton, M. D., & Steedman, R. S. (1982). Centrifugal testing of microconcrete retaining walls subjected to base shaking. Soil Dynamics & Earthquake Engineering Conference, Southampton.

Bowles, J. E. (1982). Foundation Analysis & Design, McGraw–Hill Book Company.

Brown, A., & Gibson, G. (2004). A multi-tiered earthquake hazard model for Australia. Tectonophysics, 390(1-4), 25-43.

Buckingham, E. (1914). On physically similar systems; illustrations of the use of dimensional equations. Physical review, 4(4), 345.

Cakir, T. (2013). Evaluation of the effect of earthquake frequency content on seismic behavior of cantilever retaining wall including soil–structure interaction. Soil Dynamics and Earthquake Engineering, 45, 96-111.

Callisto, L., & Rampello, S. (2013). Capacity design of retaining structures and bridge abutments with deep foundations. Journal of geotechnical and geoenvironmental engineering, 139(7), 1086-1095.

Carreira, D. J., & Chu, K. H. (1985, November). Stress-strain relationship for plain concrete in compression. In Journal Proceedings (Vol. 82, No. 6, pp. 797-804).

Chang, M. F. (1997). Lateral earth pressures behind rotating walls. Canadian Geotechnical Journal, 34(4), 498-509.

Chen, L. (2014). Active earth pressure of retaining wall considering wall movement. European journal of environmental and civil engineering, 18(8), 910-926.

Chopra, A. K. (2007). Dynamics of structures theory and application to earthquake engineering. Pearson Education.

Choudhury, D., & Chatterjee, S. (2006). Displacement-based seismic active earth pressure on rigid retaining walls. Electronic Journal of Geotechnical Engineering, USA, 11, Bundle c, 2006, paper No 0660.

Choudhury, D., Nimbalkar, S. S., & Mandal, J. N. (2006). Comparison of pseudo-static and pseudo-dynamic methods for seismic earth pressures on retaining wall. Journal of Indian Geophysical Union, 10 (4), 263-271.

Clough, G. W., & Duncan, J. M. (1971). Finite element analyses of retaining wall behavior. Journal of Geotechnical Engineering (ASCE), 97(12), 1657–1673.

Clough, G. W., & Duncan, J. M. (1991). Earth pressures. In Foundation engineering handbook, Springer, Boston, MA, pp. 223-235.

Clough, G. W., & Fragaszy, R. F. (1977). A study of earth loadings on floodway retaining structures in the 1971 San Fernando Valley earthquake. In Proceedings of the sixth world conference on earthquake engineering, 3.

Crosariol, V. A. (2010). Scale model shake table testing of underground structures in soft clay. Master of Science thesis, California Polytechnic State University, USA.

Daheur, E. G., Goual, I., Taibi, S., & Mitiche-Kettab, R. (2019). Effect of dune sand incorporation on the physical & mechanical behaviour of tuff: (experimental investigation). Geotechnical & Geological Engineering, 37(3), 1687-1701.

Dano, C., Hicher, P. Y., & Tailliez, S. (2004). Engineering properties of grouted sands. Journal of Geotechnical and Geoenvironmental engineering, 130(3), 328-338.

Das, B. M., & Sivakugan, N. (2016). Fundamentals of geotechnical engineering. Cengage Learning.

Di Santolo, A. S., Penna, A., Evangelista, A., Kloukinas, P., Mylonakis, G. E., Simonelli, A. L., & Taylor, C. A. (2012). Experimental Investigation of Dynamic Behaviour of Cantilever Retaining Walls. In Proceedings of 15th World Conference on Earthquake Engineering, Lisbon.

Duncan, J. M., & Bursey, A. (2013). Soil modulus correlations. In Foundation Engineering in the Face of Uncertainty: Honoring Fred H. Kulhawy, pp. 321-336.

Earth Mechanics, I. N. C. (2005). Field investigation report for abutment backfill characterization. Rep. No. SSRP-05/02.

EN 1992-1-2. (2004). Eurocode 2: Design of concrete structures-Part 1-2: General rules-structural fire design. European Committee for Standardization.

EN 1998-5: 2004: Eurocode 8: Design of structures for earthquake resistance. Foundations, retaining structures and geotechnical aspects.

Ertugrul, O. L., & Trandafir, A. C. (2014). Seismic earth pressures on flexible cantilever retaining walls with deformable inclusions. Journal of Rock Mechanics & Geotechnical Engineering, 6(5), 417-427.

Eurocode 8 (2005): Design of structures for earthquake resistance. Part, 1, 1998-1.

Eurocode, C. E. N. (2004). 8: design of structures for earthquake resistance–Part 5: Foundations, retaining structures & geotechnical aspects EN 1998-5: 2004. Brussels: European Committee for Standardization.

Gamal, M. E., (1996). Seismic design issues relating to bridge abutments. Doctoral Dissertation, University of Nevada, Reno, USA.

Geoguide, I. (1993). Guide to retaining wall design. Geotechnical Engineering Office, Government of Hong Kong.

Ghandil, M., & Behnamfar, F. (2015). The near-field method for dynamic analysis of structures on soft soils including inelastic soil–structure interaction. Soil Dynamics and Earthquake Engineering, 75, 1-17.

Ghosh, P. (2008). Seismic active earth pressure behind a nonvertical retaining wall using pseudo-dynamic analysis. Canadian Geotechnical Journal, 45(1), 117-123.

Hardin, B. O., & Drnevich, V. P. (1972). Shear modulus and damping in soils: measurement and parameter effects. Journal of Soil Mechanics & Foundations Div, 98(sm6).

Hashemnia, K., & Pourandi, S. (2018). Study the effect of vibration frequency and amplitude on the quality of fluidization of a vibrated granular flow using discrete element method. Powder technology, 327, 335-345.

Huang, C. C., Wu, S. H., & Wu, H. J. (2009). Seismic displacement criterion for soil retaining walls based on soil strength mobilization. Journal of geotechnical and geoenvironmental engineering, 135(1), 74-83.

Iai, S., & Kameoka, T. (1993). Finite element analysis of earthquake induced damage to anchored sheet pile quay walls. Soils and foundations, 33(1), 71-91.

Ichihara, M., & Matsuzawa, H. (1973). Earth pressure during earthquake. Soils and Foundations, 13(4), 75-86.

IRC-78 (2014). Standard Specifications & Code of Practice for Road Bridges. Foundations and Substructure, Indian Roads Congress.

Ishibashi, I., & Fang, Y. S. (1987). Dynamic earth pressures with different wall movement modes. Soils and Foundations, 27(4), 11-22.

Jha, A. (2004). Dynamic testing of structures using scale models. Master Dissertation, Concordia University, Canada.

Ju, S. H., & Ni, S. H. (2007). Determining Rayleigh damping parameters of soils for finite element analysis. International journal for numerical and analytical methods in geomechanics, 31(10), 1239-1255.

Keykhosropour, L., & Lemnitzer, A. (2019). Experimental studies of seismic soil pressures on vertical flexible, underground structures and analytical comparisons. Soil Dynamics and Earthquake Engineering, 118, 166-178.

Kim, H.-K. & Santamarina, J. C. (2008). Sand-rubber mixtures (large rubber chips). Canadian Geotechnical Journal, 45, 1457-1466.

Kloukinas, P., di Santolo, A. S., Penna, A., Dietz, M., Evangelista, A., Simonelli, A. L., & Mylonakis, G. (2015). Investigation of seismic response of cantilever retaining walls: Limit analysis vs shaking table testing. Soil Dynamics and Earthquake Engineering, 77, 432-445.

Koseki, J. (2002). Seismic performance of retaining walls—case histories and model tests. In Proceedings of the Fourth Forum on Implications of Recent Earthquakes on Seismic Risk, Japan: Tokyo Institute of Technology, 95-107.

Koseki, J., Munaf, Y., Sato, T., Tatsuoka, F., Tateyama, M., & Kojima, K. (1998). Shaking and tilt table tests of geosynthetic-reinforced soil and conventional-type retaining walls. Geosynthetics International, 5(1-2), 73-96.

Koseki, J., Tateyama, M., Tatsuoka, F., & Horii, K. (1995). Back analyses of soil retaining walls for railway embankments damaged by the 1995 Hyogoken-nanbu earthquake. Joint Report on, 31-56.

Kuhlemeyer, R. L., & Lysmer, J. (1973). Finite element method accuracy for wave propagation problems. Journal of Soil Mechanics and Foundations Div, 99 (Tech Rpt).

Ladd, R. S. (1978). Preparing test specimens using undercompaction. Geotechnical Testing Journal, 1(1), 16-23.

Lam, N. T. K. (1999). Program 'GENQKE' User’s Guide. Department of Civil and Environmental Engineering. The University of Melbourne, Australia.

Latha, G. M. & Krishna, A. M. (2006). Shaking table studies on reinforced soil retaining walls. Indian Geotechnical Journal, Vol 36, pp 321-333.

Lee, J., & Fenves, G. L. (1998). Plastic-damage model for cyclic loading of concrete structures. Journal of engineering mechanics, 124(8), 892-900.

Li, X., & Aguilar, O. (2000). Elastic earth pressures on rigid walls under earthquake loading. Journal of earthquake engineering, 4(04), 415-435.

Lima, M. M., Doh, J. H., Hadi, M. N., & Miller, D. (2016). The effects of CFRP orientation on the strengthening of reinforced concrete structures. The Structural Design of Tall and Special Buildings, 25(15), 759-784.

Ling, H. I., Liu, H., & Mohri, Y. (2005). Parametric studies on the behavior of reinforced soil retaining walls under earthquake loading. Journal of engineering mechanics, 131(10), 1056-1065.

Ling, H. I., Mohri, Y., Leshchinsky, D., Burke, C., Matsushima, K., & Liu, H. (2005). Large-scale shaking table tests on modular-block reinforced soil retaining walls. Journal of Geotechnical & Geoenvironmental engineering, 131(4), 465-476.

Lubliner, J., Oliver, J., Oller, S., & Oñate, E. (1989). A plastic-damage model for concrete. Int. J. Solids and Structures.

Lumantarna, E., Lam, N., Wilson, J., & Griffith, M. (2010). Inelastic displacement demand of strength-degraded structures. Journal of Earthquake Engineering, 14(4), 487-511.

Madabhushi, S. P. G., & Haigh, S. K. (2005). The Bhuj, India earthquake of 26th January 2001: A field report by Earthquake Engineering Field Investigation Team (EEFIT).

Matasovic, N., Caldwell, J., & Guptill, P. (2004). The Role of Geotechnical Factors in Northridge Earthquake Residential Damage. In Proceedings of 5th International Conference on Case Histories in Geotechnical Engineering.

Matsuo, H., & Ohara, S. (1965). Dynamic pore water pressure acting on quay walls during earthquakes. In Proceedings of 3rd World Conference on Earthquake Engineering, 1, 130-140.

Matuo, H. & Ohara, S. (1960). Lateral earth pressure and stability of quay walls during earthquakes. In Proceedings of 2nd World Conference on Earthquake Engineering, Tokyo, Japan.

McManus, K., Traylen, N., Clayton, P. & Wood, J. (2017). Earthquake geotechnical engineering practice, Module 6: Earthquake resistant retaining wall design, New Zealand geotechnical society INC.

Mechanics, E. (2005). Field investigation report for abutment backfill characterization. SSRP, 5, 02.

Mei, G., Chen, Q., & Song, L. (2009). Model for predicting displacement-dependent lateral earth pressure. Canadian geotechnical journal, 46(8), 969-975.

Menetrey, P., & Willam, K. J. (1995). Triaxial failure criterion for concrete and its generalization. ACI Structural Journal, 92(3), 311-318.

Mikola, R. G. & Sitar, N. (2013). Seismic earth pressures on retaining structures in cohesionless soils, California Department of Transportation (Caltrans), Report No. UCB GT 13-01.

Monaco, P., & Marchetti, S. (2004). Evaluation of the coefficient of subgrade reaction for design of multi-propped diaphragm walls from DMT moduli. Proceedings International Site Characterization.

Moncarz, P. D., Krawinkler, H. (1981). Theory and application of experimental model analysis in earthquake engineering, The John A. Blume Earthquake Engineering Center, 1981, Stanford University, California, USA.

Mononobe, N. & Matsuo, H. (1929). On the determination of earth pressures during earthquakes. Proceedings, World Engineering Conference, 9(388).

Munoz, H., & Kiyota, T. (2020). Deformation and localisation behaviours of reinforced gravelly backfill using shaking table tests. Journal of Rock Mechanics and Geotechnical Engineering, 12(1), 102-111.

Murphy, G. (1950). Similitude in Engineering. Ronald Press, New York.

Nadim, F., & Whitman, R. V. (1983). Seismically induced movement of retaining walls. Journal of Geotechnical Engineering, 109(7), 915-931.

Newmark, N. M. (1965). Effects of earthquakes on dams and embankments. Geotechnique, 15(2), 139-160.

Okabe, S. (1926). General Theory of Earth Pressure. Journal of the Japanese Society of Civil Engineers, Tokyo, Japan, 12(1).

Oldecop, L. & Zabala, F. (1996). Shaking table test on small prototype of soil retaining wall. Instituto De Investigaciones Antisismicas, National University of San Juan, Argentina.

Omar, T., & Sadrekarimi, A. (2015). Effect of triaxial specimen size on engineering design & analysis. International Journal of Geo-Engineering, 6(1), 5.

Ortiz, L. A., Scott, R. F., & Lee, J. (1983). Dynamic centrifuge testing of a cantilever retaining wall. Earthquake Engineering and Structural Dynamics, 11(2), 251-268.

Potts, D. M., & Fourie, A. B. (1986). A numerical study of the effects of wall deformation on earth pressures. International journal for numerical and analytical methods in geomechanics, 10(4), 383-405.

Potts, D. M., & Zdravković, L. (1999). Finite element analysis in geotechnical engineering: theory. Thomas Telford.

Prasad, S. K., Towhata, I., Chandradhara, G. P., & Nanjundaswamy, P. (2004). Shaking Table Tests in Earthquake Geotechnical Engineering. Current Science, 87, 10: 1398-404.

Qiang, S. Q., Chunling, X. U., Bing, L., & Liqiang, T. (2009). Slope instabilities in the severest disaster areas of 512 Wenchuan earthquake,17(1), 39-49.

Richards Jr, R., & Elms, D. G. (1979). Seismic behavior of gravity retaining walls. Journal of Geotechnical and Geoenvironmental Engineering, 105(ASCE 14496).

Roesset, J. M. (1970). Fundamentals of Soil Amplification. In seismic design for nuclear power plants. Ed. R.J. Hansen. The MIT Press, Cambridge, MA, 183-244.

Sandri, D. (1997). A performance summary of reinforced soil structures in the greater Los Angeles area after the Northridge earthquake. Geotextiles and Geomembranes, 15(4-6), 235-253.

Seed, H. B., Whitman, R. V. (1970). Design of earth retaining structures for dynamic loads. Proceedings, ASCE Specialty Conference on Lateral Stresses in the Ground and Design of Earth Retaining Structures, New York, USA, 103-147.

Seismosoft. (2016). SeismoSignal 2016 – A computer program for signal processing of strong-motion data.

Shahi, R., Lam, N., Gad, E., Wilson, J., & Watson, K. (2017). Seismic assessment of cold-formed steel stud bracing wall panels using direct displacement based design approach. Bulletin of earthquake engineering, 15(3), 1261-1277.

Shakal, A. F. (1994). CSMIP strong-motion records from the Northridge, California earthquake of January 17 1994.

Shayo, T., & Cheng, U. C. (2009). Caltrans Seismic Design Analysis of Retaining Walls Project.

Sherif, M. A. & Fang, YS. (1984). Dynamic earth pressures on walls rotating about the top. Soils and Foundations, 24(4), 109-117.

Sherif, M. A., Yungshow, F., & Russell, I. (1984). K_a & K_0 behind rotating & non-yielding wall. Journal Geotechnical Engineering, 110(1), 113-121.

Shirato, M., Kohno, T., & Nakatani, S. (2009). Geotechnical criteria for serviceability limit state of horizontally loaded deep foundations. In Geotechnical Risk and Safety, CRC Press, 133-140.

Shumway, R. H. (2003). Time-frequency clustering and discriminant analysis. Statistics & probability letters, 63(3), 307-314.

Shumway, R. H. (2003). Time-frequency clustering and discriminant analysis. Statistics & probability letters, 63(3), 307-314.

Siddharthan, R., & Maragakis, E. (1987). Seismic performance of flexible retaining walls supporting dry cohesionless soils. In Developments in geotechnical engineering, Elsevier, 45, 151-165.

Siddharthan, R., El-Gamal, M., & Maragakis, E. A. (1994). Investigation of performance of bridge abutments in seismic regions. Journal of Structural Engineering, ASCE, Vol. 120(4), 1327-1346.

Simonelli, A. L., Carafa, P., Feola, A., Crewe, A. J., & Taylor, C. A. (2000). Retaining walls under seismic actions: Shaking table testing and numerical approaches. 12th World Conference on Earthquake Engineering, Auckland, New Zealand.

Song, A. (2012). Deformation analysis of sand specimens using 3 D digital image correlation for the calibration of an elasto-plastic model. Doctoral dissertation, Texas A & M University, (USA).

Stadler, A. T. (1996). Dynamic centrifuge testing of cantilever retaining walls. University of Colorado at Boulder: Boulder, CO, USA.

Standard, A. (2009). 1289.3. 6.1. Standard method of analysis by sieving in Methods of testing soils for engineering purposes—Soil classification tests—Determination of the particle size distribution of a soil.

Standard, A. S. T. M. D7181-11 (2011). Method for Consolidated Drained Triaxial Compression Test for Soils, 1, 1-11.

Steedman, R. S. (1998). Seismic design of retaining walls. Proceedings of the Institution of Civil Engineers-Geotechnical Engineering, 131(1), 12-22.

Tanaka, H., Locat, J., Shibuya, S., Soon, T. T., & Shiwakoti, D. R. (2001). Characterization of Singapore, Bangkok, and Ariake clays. Canadian Geotechnical Journal, 38(2), 378-400.

Tatsuoka, F., Tateyama, M., & Koseki, J. (1996). Performance of soil retaining walls for railway embankments. Soils and Foundations, 36(Special), 311-324.

Transportation Officials. Subcommittee on Bridges. (2002). AASHTO guide specifications for LRFD seismic bridge design.

Veletsos, A. S., & Younan, A. H. (1997). Dynamic response of cantilever retaining walls. Journal of Geotechnical and Geoenvironmental Engineering, 123(2), 161-172.

Vucetic, M., & Dobry, R. (1991). Effect of soil plasticity on cyclic response. Journal of geotechnical engineering, 117(1), 89-107.

Wair, B. R., DeJong, J. T., & Shantz, T. (2012). Guidelines for estimation of shear wave velocity profiles. Pacific Earthquake Engineering Research Center.

Wang, L., Chen, G., & Chen, S. (2015). Experimental study on seismic response of geogrid reinforced rigid retaining walls with saturated backfill sand. Geotextiles and Geomembranes, 43(1), 35-45.

Watanbe, K., Munaf, Y., Koseki, J., Tateyama, M., & Kojima, K. (2003). Behaviors of several types of model retaining walls subjected to irregular excitation. Soils and Foundations, 43(5), 13-27.

Whitman, R. V., & Liao, S. (1985). Seismic design of gravity retaining walls. US Army Corps of Engineers. Washington, USA.

Wilson, P., & Elgamal, A. (2009). Full-scale shake table investigation of bridge abutment lateral earth pressure. Bulletin of the New Zealand Society for Earthquake Engineering, 42(1), 39-46.

Wilson, P., & Elgamal, A. (2015). Shake table lateral earth pressure testing with dense c-ϕ backfill. Soil Dynamics and Earthquake Engineering, 71, 13-26.

Wood, D. M., Crewe, A., & Taylor, C. (2002). Shaking table testing of geotechnical models. International Journal of Physical Modelling in Geotechnics, 2(1), 01-13.

Wood, J. H. (1973). Earthquake-induced soil pressures on structures. Doctoral dissertation, California Institute of Technology, (USA).

Wu, Y., & Prakash, S. (2001). Seismic displacement of rigid retaining walls—state of the art. In Proceedings of 4th international conference on recent Advances in Geotechnical Earthquake Engineering and Soil dynamics. San Diego, CA, paper (No. 7.05).

Yang, K. H., Zornberg, J. G., Liu, C. N., & Lin, H. D. (2012). Backfill stress and strain information within a centrifuge geosynthetic-reinforced slope model under working stress and large soil strain conditions. In GeoCongress 2012: State of the Art and Practice in Geotechnical Engineering, pp. 461-470.

Yazdandoust, M. (2017). Investigation on the seismic performance of steel-strip reinforced-soil retaining walls using shaking table test. Soil Dynamics and Earthquake Engineering, 97, 216-232.

Yazdani, M., Azad, A., & Talatahari, S. (2013). Extended "Mononobe-Okabe" method for seismic design of retaining walls. Journal of Applied Mathematics, 2013.

Yimsiri, S., Soga, K., Yoshizaki, K., Dasari, G. R., & O'Rourke, T. D. (2004). Lateral and upward soil-pipeline interactions in sand for deep embedment conditions. Journal of geotechnical and geoenvironmental engineering, 130(8), 830-842.

A1. Modelling of base soil with brown clay

A1.1. Details of Brown Clay (Mechanics, E. 2005)

Table A1-1. Details of Brown Clay (Mechanics, E. 2005).

Sr. No.	Description	Value (Units)
1	Dry Density	2004 kg/m^3
2	Angle of internal friction	22.8^o
3	Youngs modulus based on UU test data	11 MPa
4	Poisson's ratio	0.4 for low plasticity clay
5	Dilation angle based on UU test data	10^o
6	Rayleigh damping - α_M	0.32
7	Rayleigh damping - β_K	0.0005

A1.2 Calibration of the Mohr Coulomb model with the UU test on Brown Clay (Mechanics, E. 2005)

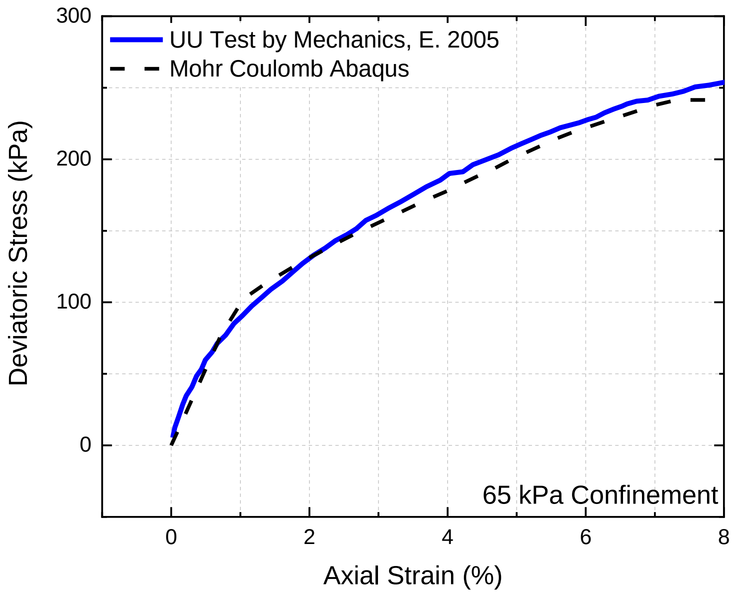

Figure A1-2 Calibration of Mohr Coulomb model with triaxial test data of Brown Clay.

A2. Two dimensional (2D) and three dimensional (3D) behavior of concrete wall

A2.1. FE modelling of reinforced concrete (RC) wall

Figure A2-1 and A2-2 shows 2D and 3D model of reinforced concrete (RC) wall. Reinforcement details for both models have been shown in figure A2-1. Table A2-1 presents the material properties considered for modelling concrete and steel. The pulses shown in figure A2-3 were used as base excitation for both the RC wall models. The non-linear time history analyses have been conducted in the dynamic explicit scheme of finite element (FE) software Abaqus. Figure A2-4 shows the comparison of relative displacements captured at the top of the 2D and 3D RC walls. A good agreement has been observed between the 2D and 3D displacement responses of the RC wall.

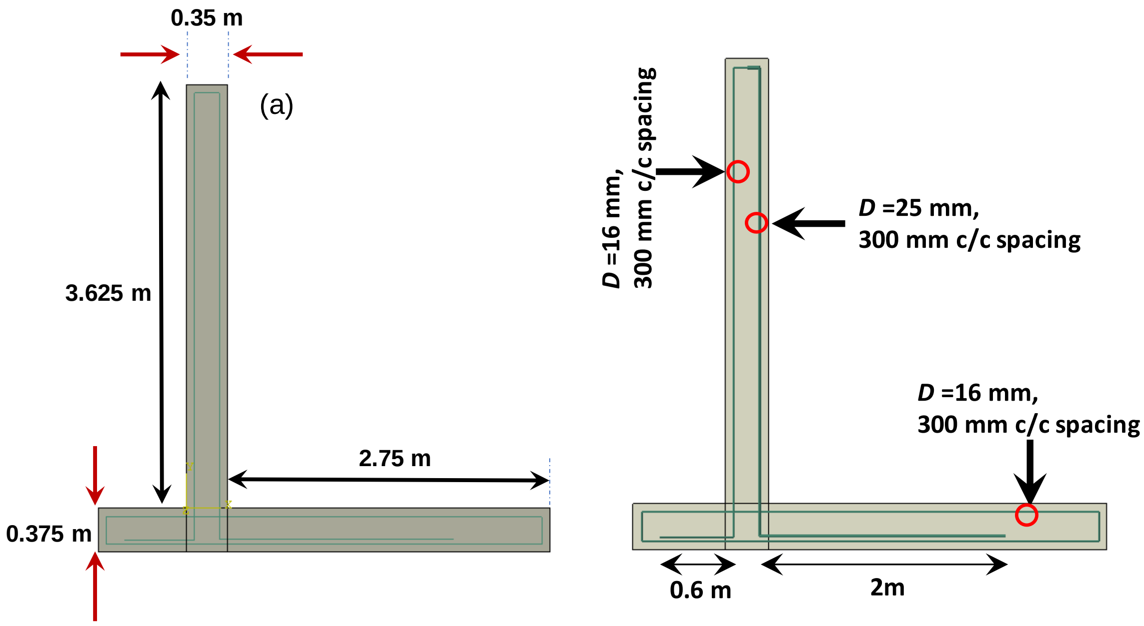

Figure A2-1 2D model of reinforced concrete wall.

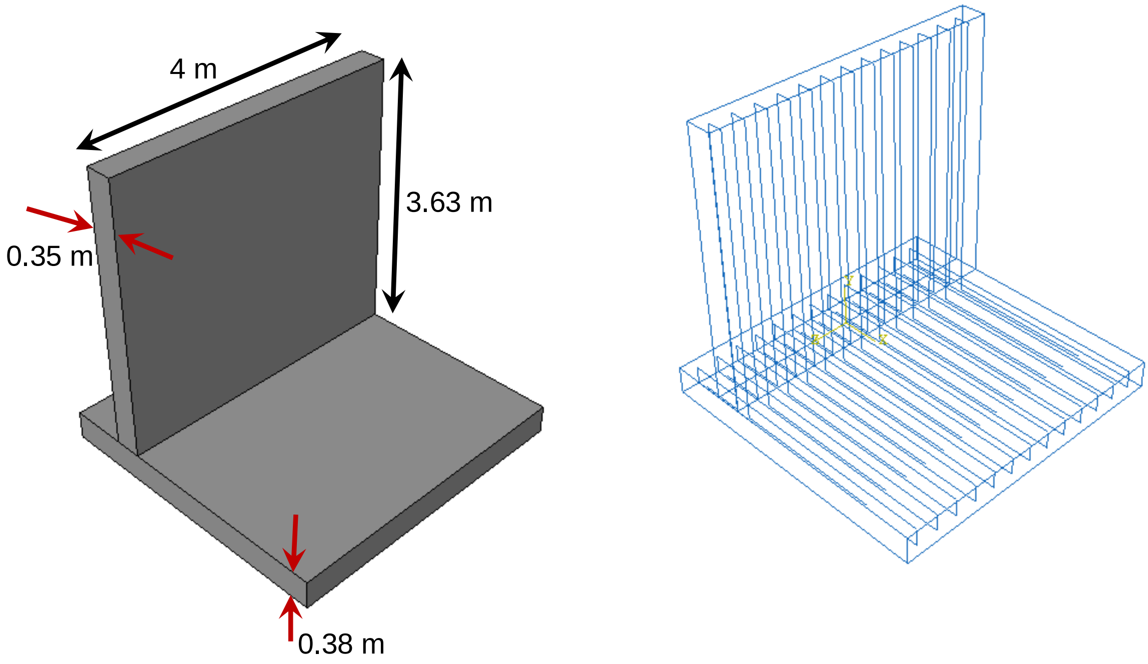

Figure A2-2 3D model of reinforced concrete wall.

Table A2-1 Material properties used to model concrete and steel.

Property – Unit	**Concrete**	**Steel**
Density (ρ) – kg/m^3	2400	7800
Young's modulus - GPa	31.62	200
Poisson's ratio (ν)	0.3	0.3
Maximum strength - MPa	40 (f_{cu})	415 (f_{st})
Plasticity model	Concrete damaged plasticity	von-Mises plasticity

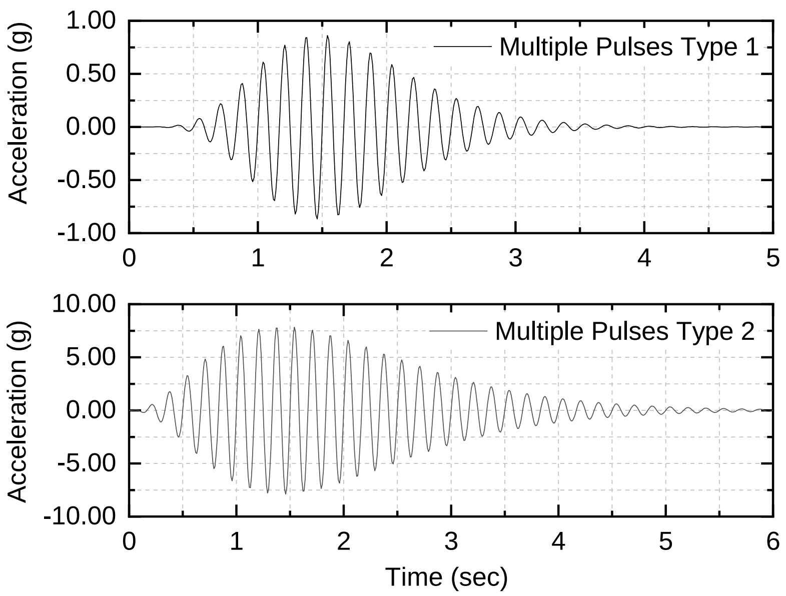

Figure A2-3 Multiple pulses used for the base excitation.

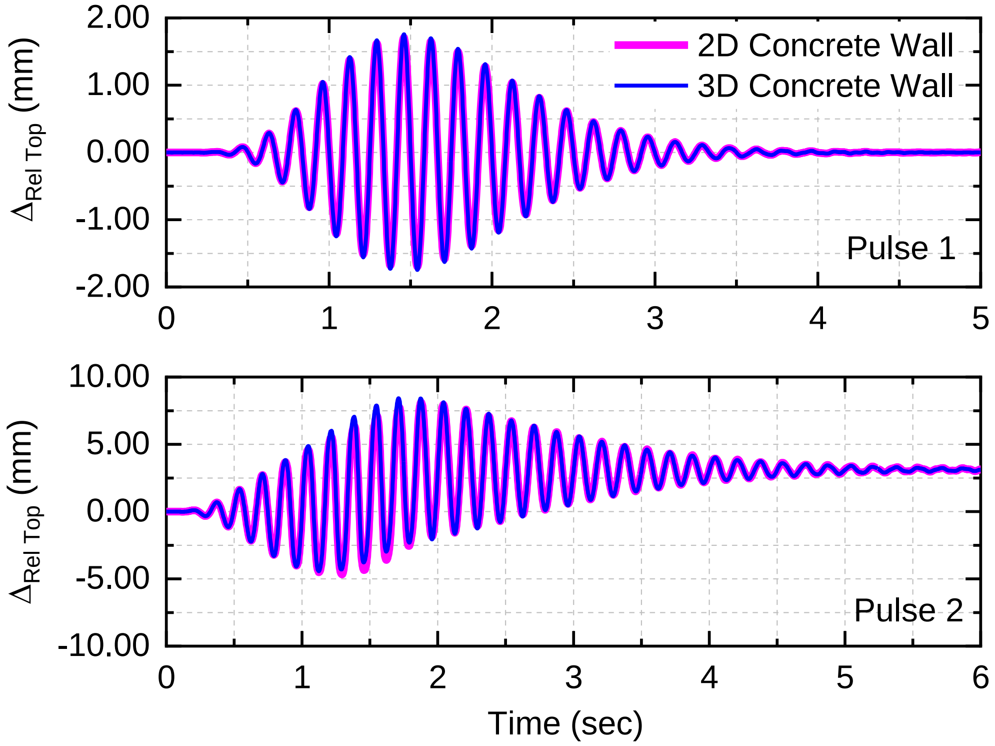

Figure A2 - 4 Comparison of relative displacement at the top of the RC wall observed from 2D and 3D FE models.

A3. Derivations for finding the displacements of base restrained cantilever wall

Case 1 Deflection due to uniformly distributed load

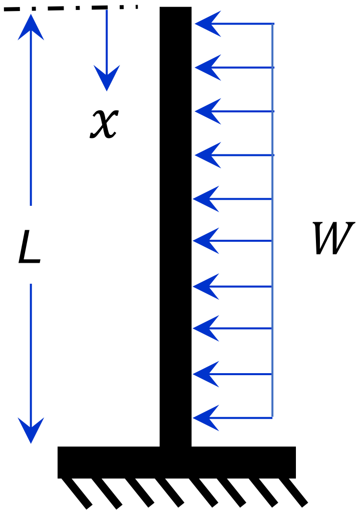

Bending moment distribution, taking $x = 0$ at free end:

$$M_{\mathrm{x,UDL}} = \frac{1}{2}wx^2$$

Theory of simple bending:

$$M_{\mathrm{x}} = -EI\frac{d^2y}{dx^2}$$

Therefore,

$$M_{\mathrm{x}} = \frac{1}{2}wx^2 = -EI\frac{d^2y}{dx^2}$$

$$\frac{d^2y}{dx^2} = \frac{-1}{2EI}wx^2$$

On integration:

$$\frac{dy}{dx} = \frac{-1}{6EI}wx^3 + c_1$$

Slope of the wall at bottom, $x = L$: $\frac{dy}{dx} = 0$.

$$0 = \frac{-1}{6EI}wL^3 + c_1$$

$$c_1 = \frac{1}{6EI}wL^3$$

Therefore,

$$\frac{dy}{dx} = \frac{-1}{6EI}wx^3 + \frac{1}{6EI}wL^3$$

On further integration:

$$y = \frac{-1}{24EI}wx^4 + \frac{1}{6EI}wL^3x + c_2$$

Deflection of the wall at bottom, $x = L$: $y = 0$.

$$0 = \frac{-1}{24EI}wL^4 + \frac{1}{6EI}wL^4 + c_2$$

$$c_2 = -\frac{1}{8EI}wL^4$$

Therefore,

$$y = \frac{-1}{24EI}wx^4 + \frac{1}{6EI}wL^3x - \frac{1}{8EI}wL^4$$

Maximum deflection y_{max} at $x = 0$:

$$y = -\frac{1}{8EI}wL^4$$

Case 2 Deflection due to uniformly varying load

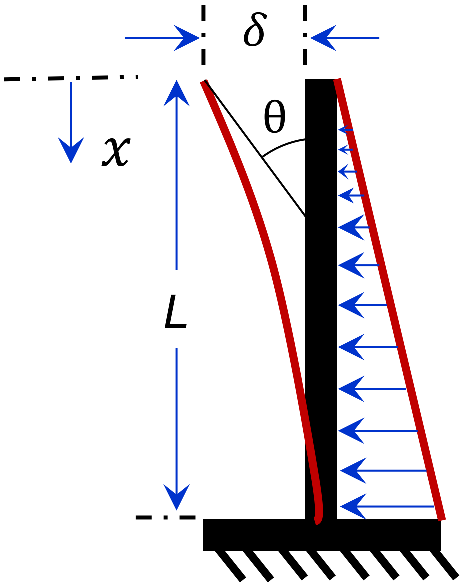

Bending moment distribution, taking $x = 0$ at free end:

$$M_{\mathrm{x,UVL}} = \frac{1}{6L} w_0 x^3$$

Theory of simple bending:

$$M_{\mathrm{x}} = -EI\frac{d^2y}{dx^2}$$

Therefore,

$$M_{\mathrm{x}} = \frac{1}{6L} w_0 x^3 = -EI\frac{d^2y}{dx^2}$$

$$\frac{d^2y}{dx^2} = \frac{-1}{6EIL} w_0 x^3$$

On integration:

$$\frac{dy}{dx} = \frac{-1}{24EIL} wx^4 + c_1$$

Slope of the wall at bottom, $x = L$: $\frac{dy}{dx} = 0$

$$0 = \frac{-1}{24EIL} wL^4 + c_1$$

$$c_1 = \frac{1}{24EI} wL^3$$

Therefore,

$$\frac{dy}{dx} = \frac{-1}{24EIL} wx^4 + \frac{1}{24EI} wL^3$$

On further integration:

$$y = \frac{-1}{120EIL} wx^5 + \frac{1}{24EI} wL^3 x + c_2$$

Deflection of the wall at bottom, $x = L$: $y = 0$

$$0 = \frac{-1}{120EI} wL^4 + \frac{1}{24EI} wL^4 + c_2$$

$$c_2 = -\frac{1}{30EI} wL^4$$

$$y = \frac{-1}{120EIL} wx^5 + \frac{1}{24EI} wL^3 x - \frac{1}{30EI} wL^4$$

Maximum deflection y_{max} at $x = 0$:

$$y = -\frac{1}{30EI} wL^4$$

A4. Station details for the historical accelerograms.

Table A4-1 Recording stations for historical accelerograms.

Sr. No.	Event Name	Year	Recording Station
1.	San Fernando	1971	Fairmont Dam, 326
2.	Fruili	1976	Tarcento, 0
3.	Chuetsu-Oki	2007	Yoitamachi Yoita Nagaoka, EW
4.	Northridge	1994	LA Dam, 64
5.	Tabas, Iran	1978	Tabas, L

A5. Captured displacement of shaking table.

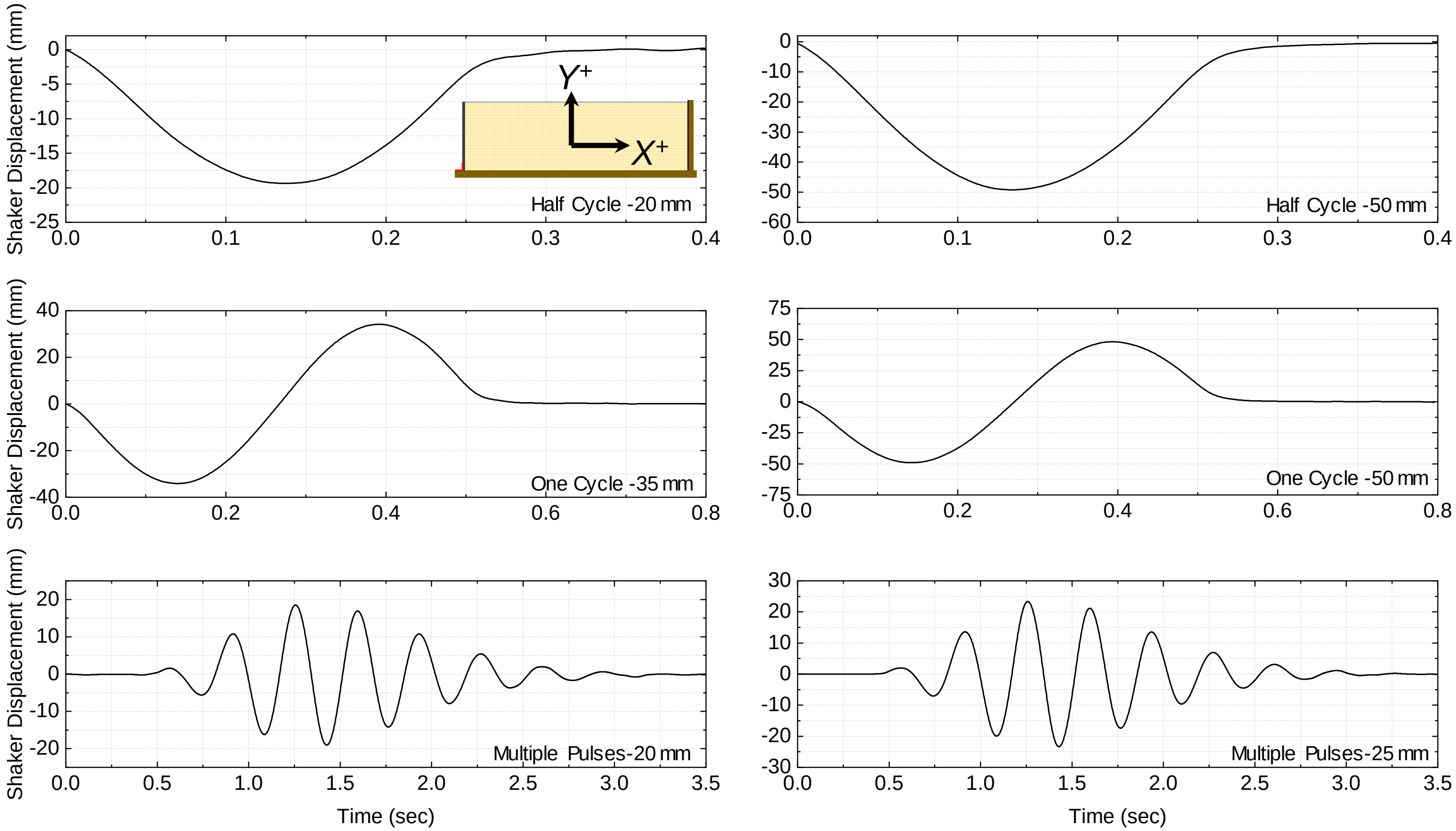

Figure A5 – 1 Captured displacement of the shaking table